UNIVERSITÉ DU LUXEMBOURG

PhD-FSTC-2017-73
The Faculty of Sciences, Technology and Communication

DISSERTATION

Presented on 04/12/2017 in Luxembourg

to obtain the degree of

DOCTEUR DE L'UNIVERSITÉ DU LUXEMBOURG

EN SCIENCES DE L'INGÉNIEUR

by

Michael WEILER
Born on 20 June 1978 in Trier (Germany)

INVESTIGATION OF CRACK DEVELOPMENT IN A FAIR-FACED REPLACEMENT SCREED BASED ON HYBRID FIBRE-REINFORCED CONCRETE

Dissertation defence committee

Dr.-Ing. Andreas Zilian, Chairman
Professor, Université du Luxembourg, Faculté des Sciences, de la Technologie et de la Communication

Dr.-Ing. Luc Courard, Vice-chairman
Professor, Université de Liège, Département des matériaux de construction

Dr.-Ing. Danièle Waldmann, dissertation supervisor
Assistant-Professor, Université du Luxembourg, Faculté des Sciences, de la Technologie et de la Communication

Dr.-Ing. Marc Oudjene,
Assistant-Professor, University of Lorraine, ENSTIB Ecole Nationale des technologies et Industries

Dr.-Ing Reinhard Winzer
Technical Director RMC by Dyckerhoff GmbH

Contents

Für

Elisabeth Weiler

⋆05.11.1921 †08.09.2009

Vorwort

Die vorliegende Arbeit entstand während meiner Tätigkeit als Doktorand am Lehrstuhl „Laboratory of Solid Structures“ der „Faculty of Science, Technology and Communication (FSTC) - Research Unit in Engineering Sciences (RUES)“ an der Universität Luxemburg in dem Zeitraum vom 01.10.2013 bis 31.01.2018.

Mein Dank gilt zunächst Frau Professor Danièle Waldmann für die einmalige Gelegenheit zur Promotion die sich mir geboten hat. Zudem danke ich den Professoren Andreas Zilian (Universität Luxemburg/Luxemburg), Luc Courard (Universität Lüttich/Belgien), Marc Oudjene (Universität Nancy/Frankreich), sowie Herrn Dr. Winzer (Dyckerhoff GmbH Wiesbaden/Deutschland) für die Mitwirkung in meinem Prüfungskomitee.

Darüber hinaus Danke ich meinen Kollegen vom Technical Support, Ed Weyer, Ralph Reiter, Logan Filipe Freitas Moreira, Vicente Reis Adonis und Claude Collé für die tatkräftige Unterstützung der zahlreichen Versuche im Labor der Universität Luxemburg. Außerdem gilt mein Dank den Herrn Gilbert Klein, Claude Collé, Marc Seil (die Kamera war direkt im Eingangsbereich) und Cédric Bruyère (Danke Werner!) für die Vorbereitung und Durchführung der Großversuche auf dem Werksgelände der Dyckerhoff GmbH zu Wiesbaden. Herrn Remi Radinovic und Frau Grace Ligbado danke ich recht herzlich für die moralische Unterstützung.

Meinen Doktoranden-Kollegen Vishojit Bahadur Thapa, Dolgion Erdenebat, Gelen Gael Chewe Ngapeya und Patrick Pereira Dias danke ich für die eine oder andere willkommene Ablenkung im Arbeitsalltag. Euch weiterhin viel Erfolg und wir sehen uns zu eurer Disputation!

Ein besonderer Dank gilt Herrn Yves Staudt. Ich erinnere mich sehr gern an die regelmäßigen interdisziplinären Koordinationsmeetings die wesentlich zum Gelingen der

Arbeit beitrugen (Denke ich...). Letztlich gilt Herrn Ken Adam ein besonderer Dank, mein lieber Ken, ohne Deine Hilfe hätte ich das Projekt sicherlich nicht zum Erfolg führen können – Vielen Dank!

Frau Jeannette Orben (Dyckerhoff GmbH Wiesbaden/Deutschland) danke ich sehr für die Unterstützung in allen Bereichen der Arbeit. Herrn Marco Baum (Dyckerhoff GmbH Wiesbaden/Deutschland) danke ich für die professionelle und umfangreiche Hilfe, sowohl bei der Vorbereitung als auch bei der Durchführung der Großversuche zu Wiesbaden.

Der größte Dank gilt jedoch meiner Frau Johanna und unserer gemeinsamen in 2015 geborenen Tochter Greta. Liebe Johanna, den Wert Deiner Unterstützung kann ich nicht in Worte fassen – darum sage ich einfach nur Danke! Liebe Greta, ich danke dafür dass es Dich gibt, Du bist das Größte das mir jemals passiert ist!

Luxemburg, Januar 2018

Michael Weiler

Zesummefaassung

An dëser Aarbecht gëtt e Bemiessungskonzept fir net arméiert, zementgebonnen Sichtschappen virgestallt. D'Aarbecht konzentréiert sech dobäi op d'Rëssbildung, déi duerch d'Schwinden vum agesate Bëtong verursaacht ginn. Den zentralen Bestanddeel vun dëser Aarbecht ass dobäi e numereschen Modell (Finite Elemente Modell), dat, ënnert der Berécksiichtegung vun allen zäitlech verännerlechen Materialparameter an mat engem einfachen Berechnungsusaz an der Lag ass, Rësspied u schaarfen Aspréng an Abauten ze prognostizéieren. Doriwwer eraus kann mat der Hëllef vun dësem Modell, d'Opschosselen, also d'Deformatioun um Bord vun enger op Folie oder Trennschicht gelagerter Schapp simuléiert ginn.

Fir dësen Zweck goufen déi erfuerderlech, sech zäitlech entwéckelnd Materialparameter (stateschen Elastizitéitsmodul, eenaxesch Zugfestegkeet) ënnert Laboratoiresconditioune ënnersicht a mat Prognosen vun enger disponibeler Software a mat dem analyteschen Usaz no der DIN EN 1992-1-1:2011-01 verglach.

An engem éischten Schrëtt goufen d'Rëssbildung an d'Rëssentwécklung un enger klenger, H-fërmeger Bëtongsprouf ënnersicht a mat engem éischten numereschen Usaz e Rësspad berechent. Dësen éischten numereschen Usaz gouf an der Suite un enger groussformateger Fläch validéiert. Op der Basis vu den groussformategen Versich gouf den numereschen Modell hisiichtlech Opschosselen weiderentwéckelt.

All d'Versich goufen mat dem Usaz vun der Element-Ausfall-Method (EFM) berechent ënnert der Utilisatioun vun der kommerzieller Finite Elemente Software ANSYS®

Komplettéiert gëtt d'Bemiessungskonzept duerch eng Parameteretüd. Mëttels dëser Parameteretüd besteet d'Méiglechkeet, den oder déi Parameter ze identifizéieren, déi maassgeeblech eng Rëssbildung begënschtegen.

Déi virleiend Aarbecht leescht esou eng wichteg Contributioun zu der numereschen Modelléierung vun Schiedegungen an net arméierten Bëtongskonstruktiounen.

SCHLËSSELWIEDER:

Finite Element Method; Beton; Element-Ausfall-Method; Schwinden; Rëssbildung, zaitléech entwéckelnd Materialfestegkeeten; Parameteretüd, Sichtschapp; eenaxesch Zugfestegkeet

Zusammenfassung

In der vorliegenden Arbeit wird ein Bemessungskonzept für unbewehrte, zementgebundene Sichtestrichböden vorgestellt. Die Arbeit konzentriert sich dabei auf Rissbildungen, welche durch Schwinden des verwendeten Betons verursacht werden. Den zentralen Bestandteile der Arbeit bildet dabei ein numerisches Modell (Finite Elemente Modell), das, unter Berücksichtigung aller zeitlich veränderlichen Materialparameter und unter Zuhilfenahme eines einfachen Berechnungsansatzes in der Lage ist, Risspfade an scharfen Einsprüngen und Einbauten zu prognostizieren. Darüber hinaus kann mit der Hilfe des Modells, Aufschüsseln, also das Aufwölben der Ecken eines auf Folie oder Trennschicht gelagerten Estrichfussbodens beschrieben werden.

Zu diesem Zweck wurden die erforderlichen, sich zeitlich entwickelnden Materialparameter (statischer Elastizitätsmodul, einaxiale Zugfestigkeit) unter Laborbedingungen untersucht und mit Prognosewerten einer zur Verfügung stehenden Prognosesoftware und mit dem analytischen Prognoseansatz der DIN EN 1992-1-1:2011-01 verglichen.

In einem ersten Schritt wurde die Rissbildung und Rissentwicklung an einer kleinen, H-förmigen Betonprobe untersucht und mit einem ersten numerischen Ansatz ein Risspfad berechnet. Dieser erste numerische Ansatz wurde in der Folge an großformatigen Flächen validiert. Auf der Basis der großformatigen Versuche wurde das numerische Modell hinsichtlich Aufschüsseln weiterentwickelt.

Alle Versuche wurden mit dem Ansatz der Element-Ausfall-Methode (EFM) berechnet unter Verwendung der kommerziellen Finiten Elemente Software ANSYS®.

Komplettiert wird das Bemessungskonzept durch eine Parameterstudie. Mittels dieser Parameterstudie besteht die Möglichkeit, den oder die Parameter zu identifizieren, die maßgeblich eine Rissbildung begünstigen.

Die vorliegende Arbeit leistet somit einen wichtigen Beitrag zur numerischen Modellierung von Schädigungen in unbewehrten Betonstrukturen.

SCHLÜSSELWÖRTER:

Finite Elemente Methode; Beton; Element-Ausfall-Methode; Schwinden; Rissbildung; zeitliche entwickelnde Materialfestigkeiten; Parameterstudie; Sichtestrich; einachsige Zugfestigkeit

Résumé

Cette thèse présente un concept de dimensionnement pour des sols décoratifs non armés à base cimentaire. Le travail se concentre sur des fissurations qui sont dues à la rétraction du béton utilisé. La partie majeure de la thèse constitue un modèle numérique basé sur la méthode des éléments finis, qui, en prenant compte de l'évolution temporelle des paramètres des matériaux et en utilisant une méthode de calcul simple, peut prédire les chemins de fissure partants d'angles rentrants pointus ou d'autres installations. En plus, la déformation en périphérie d'une chape supportée sur un film plastique ou sur une couche de séparation peut être représentée à l'aide du modèle numérique développé.

À cet effet, les paramètres des matériaux nécessaires (module d'élasticité statique, résistance en traction uniaxiale), qui montrent une évolution en fonction du temps, ont été déterminés sous des conditions de laboratoire et comparés avec les valeurs calculées à l'aide d'un logiciel de prévision ainsi qu'avec l'approche analytique donnée dans la DIN EN 1992-1-1:2011-01.

Dans une première étape, la fissuration et l'évolution des fissures ont été étudiées à l'aide d'échantillons en béton en forme d'un H et le chemin des fissures a été analysé avec un premier modèle numérique. Ce premier modèle analytique a été validé par la suite avec les résultats des tests sur des surfaces grandes. À la base de ces tests à grande échelle, le modèle développé a été étendu en vue de la déformation de la chape en périphérie.

Tous les modèles ont été analysés à l'aide de la «element-failure method» en utilisant le logiciel commercial d'éléments finis ANSYS®.

Cette thèse est une contribution importante en vue de la simulation numérique de la détérioration de structures en béton non armés.

MOTS CLÉS:

Éléments finis; Béton; «Element-failure Method»; Rétraction; Fissuration; Évolution temporelle de la résistance des matériaux; étude paramétrique; sols décoratifs; Résistance en traction uniaxiale

Abstract

In the present study, a design concept for unreinforced, cement-bound concrete floors is presented. The work concentrates on cracking caused by shrinkage of the concrete used. The central components of the work are a numerical model (Finite element model) which, taking into account all time-dependent material parameters and with the aid of a simple calculation approach, is able to predict crack paths on sharp edges. In addition, with the help of the model, it is possible to simulate the curling of the corners of a float mounted concrete floor.

For this purpose, the required material parameters (static elastic modulus, uniaxial tensile strength) were investigated under laboratory conditions and compared with prognosis values of an available prognosis software and with the analytical prognosis approach of DIN EN 1992-1-1: 2011-01.

In a first step, the crack formation and crack development on a small, H-shaped concrete sample were examined and a crack path was calculated using a first numerical approach. This first numerical approach was subsequently validated on large-scale surfaces. On the basis of the large-scale experiments, the numerical model was further developed with regard to curling of concrete floors.

All experiments were calculated with the approach of element failure method (EFM) using the commercial finite element software ANSYS ®.

The design concept is completed by a parameter study. By means of this parameter study, it is possible to identify the parameters which decisively influences cracking.

The present work thus makes an important contribution to the numerical modelling of damage in unreinforced concrete structures.

KEYWORDS:

Finite element method; Concrete; Element-Failure-Method; Shrinkage; Cracking; Evolving material strengths; Parameter study; Cement screed; Uni-axial tensile strength

1 Introduction

1.1 Motivation

Since a few years, fairfaced concrete screeds are enjoying increasing popularity. A fairfaced concrete screed describes a floor, which distinguishes itself by a sanded or polished surface, serving as final surface without any kinds of floor coverings. Besides cleanability and durability, concrete screeds enable nearly unlimited design possibilities regarding the colour design and the surface design of the concrete floors. Furthermore, the economic efficiency must be guaranteed.

In this context, cracking is an important factor. Cracks do not just represent an optical lack, in the worst case, cracks can favour irreparable damage to the entire concrete structure by entrance of pollutants to the bearing structure.

It is of great interest for the cement industry to have the guarantee of a concrete floor, which is crack-free over a period of many years. Within a joint project of the laboratory of solid structures of the University of Luxemburg and the Wilhelm-Dyckerhoff-Institut in Wiesbaden/Germany a design concept was developed, which deals with cracking of unreinforced concrete floors, considering the load independent reasons which lead to cracking.

1.2 Aims

The objective of this work is the development of a new design concept, which allows the planning of new projects such as concrete floors in shopping malls, airports or even private use, and which permits to give a prognosis of crack formation caused by sharp edged corners, obstructions and curling of floating concrete floor screeds. A finite element model, taking account shrinkage and the evolving strength is developed. By using this finite element model, the crack path can be calculated on the previous mentioned

sharp edged corner and/or obstructions as well as it is able to simulate curling of floating concrete floor screeds. On the other hand, the model can be used in the field of concerning claim processing. Cracked concrete screeds, especially during the guarantee period raise the question of the origin of cracking. The main questions which are discussed, within this thesis, are:

- What are the reasons in unreinforced young concrete ($\leq$ 28 days) which lead to cracking?
- How can crack formations be simulated in finite element calculations in a simple and reliable way?
- How is it possible to simulate the effect of curling of float mounted concrete floors?
- What are the parameters which influence an exceedance of the tensile strength in function of the evolving strength properties?

1.3 Outline

The thesis is divided into three parts: A theoretical part (chapter 2 and chapter 3), an experimental part (chapter 4) and a numerical part (chapter 5 and chapter 6). The thesis closes with a conclusion and an outlook. In detail, the respective chapters deal with the following:

- **Chapter 2** gives an overview of the literature concerning the current project and represents the state-of-the-art of the material behaviour of concrete and of numerical modelling of concrete.

  The literature review is divided into five parts. First of all, the reasons of cracking, the form change of young concrete, thermal causes and hygric causes are presented. The next part deals with the prevention, respectively the reduction of cracking induced by a form change of young concrete, thermal causes and hygric causes. Possible measures to prevent or reduce cracking is the use of fibre reinforcement, additives and by applying a suitable curing of concrete. In the third part, material models of concrete are introduced, such as the failure criterion of Willam and Warnke (1974). In the following part, the different methods to simulate a crack within a finite element calculation are given. To complete the literature review

of the behaviour of concrete, the chapter closes with the description of fracture mechanic values, such as the stress intensity factor, the J-Integral and the crack tip opening displacement.

- **Chapter 3** deals with cement and gives, in a first step, some general information about cement. Subsequently, the hardening process of cement is explained. In the last subsection of this chapter, possible influence parameters for the hardening process of cement are given.

- **Chapter 4** presents, in a first step, the determination of the mechanical properties of the concrete which has been used within the thesis. Subsequently, the hygric properties of this concrete are given. Within this chapter, all required material properties, mechanical and hygric, which are used for the numerical model are explained. In the following, small H-shaped shrinkage specimen on which cracking was visually controlled and documented. The chapter closes with in-situ large-scale tests of concrete screeds. In this context, a new, innovative measurement system was tested successfully for the first time.

- **Chapter 5** gives information about the finite element analysis and the reproduction of cracks. First, the finite element method is explained in general. Then, the numerical approach to simulate the crack initiation and the crack development on the basis of the small H-shaped shrinkage specimen is shown. In this context, it is explained, how shrinkage is applied to the finite element model as a thermal load. Furthermore, the developed algorithm to simulate an evolving crack path is explained. Then, this first numerical approach is verified on the basis of large-scale tests. In addition, curling of floating concrete floor screeds is simulated.

- In **Chapter 6** an extensive parameter study is carried out. On the basis of the previous chapter, a numerical model with different support conditions, different environmental conditions and varying lengths and heights of the cement screed is investigated. The findings of Chapter 5 and of Chapter 6 are included in the overall analysis of the results. Furthermore, the results of the parameter study are evaluated using the analysis of variance (ANOVA).

- **Chapter 7** summarises and discusses the results of the thesis and gives an outlook of what can be improved regarding the design concept.

- In **Chapter 8**, it is declared how the design concept is to apply, taking into account its evolving material parameters and its environmental conditions, as well as the numerical model and the statistical evaluation of the parametric study.

In Figure 1.1, a complete overview of the organisation of the thesis is given.

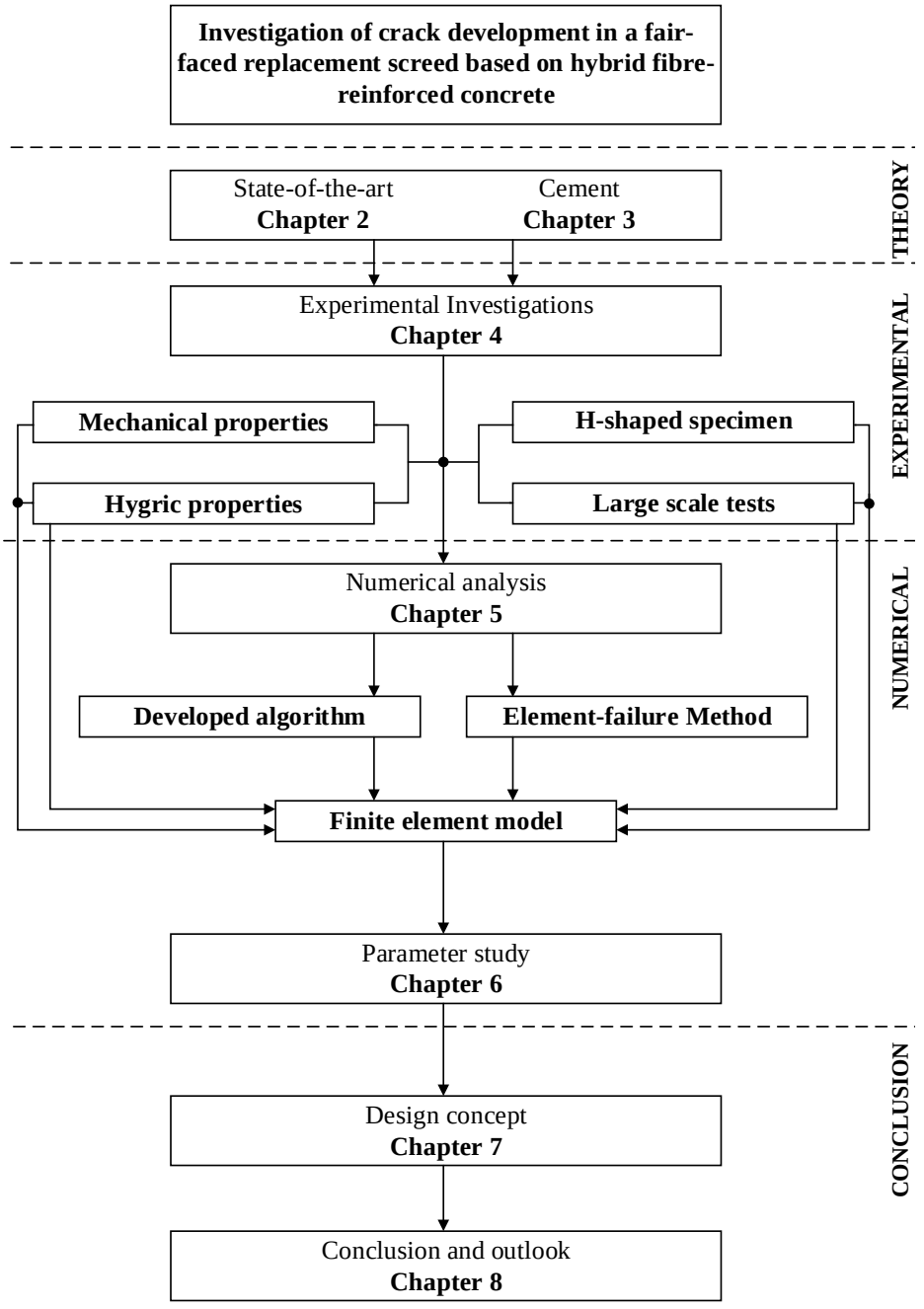

Figure 1.1: Organisation chart of the thesis

2 State of the art

First of all cracks constitute an optical lack, which represents an impairment of the serviceability of a structure. With appropriate measures, cracking can be limited and with a suitable curing of concrete, cracking can be even be completely avoided as described by Bosolt (2014). Within the last years, more and more attention is given to a limitation of cracking of concrete structures as the reputation of concrete structures suffered due to a large number of damage cases. Cracks in a structure favour the development of lasting damage of the reinforcement, respectively the whole component as they allow the penetration of pollutants into a concrete structure. One of the most important reasons of damages, caused by pollutants, is carbonation.

Carbonation describes a chemical reaction which changes the alkaline environment in concrete (normal: $pH - Value \leq 12$) with the consequence that the strength properties of concrete are improved, while the reinforcement corrodes (see Karsten (2003)). Since decades, this effect is the subject of international studies. It was already researched in the late 1980th by Francois and Maso (1988). The main focus was set at this time on the carbonation depth and with this, the damage of the inserted reinforcement, due to mechanical stresses. Subsequently to the work of Francois and Maso (1988) a discussion was carried out in Venecanin (1989). Here, carbonation induced by thermal stresses was investigated. In the following years, mathematical models were created to describe carbonation e.g. in Papadakis et al. (1991). Finite element models were developed such as a simple 2-D model in Saetta et al. (1995). The models were further refined within the next years. In Song et al. (2006) a finite element model was developed which could predict the carbonation depth very precisely. The studies were carried out on a cylindrical concrete specimen during the tensile splitting test. Today, there is a huge number of research projects which deal with carbonation. The mathematical model is ongoing further developed (see Zhang (2016) and Kashef-Haghighi et al. (2015), as well as the numerical models (see Wang et al. (2016)).

Name	**chemical formula**	**mineral. comp.**	**acronym**
tri-calcium-silicate	Ca_3SiO_5	$3\ CaO \cdot SiO_2$	C_3S
di-calcium-silicate	Ca_2SiO_4	$2\ CaO \cdot SiO_2$	C_2S
tri-calcium-aluminate	$Ca_3Al_2O_6$	$3\ CaO \cdot Al_2O_3$	C_3A
calcium-aluminate-ferrite	$Ca_2Al_2Fe_2O_{10}$	$2\ CaO \cdot (Al_2O_3, Fe_2O_3)$	$C_2(A, F)$

Table 2.1: Names and chemical formula inspired by Karsten (2003), Oehmischen (2010) and Bosold and Pickhardt (2014)

2.1 Cement

2.1.1 General informations

It is known to each civil engineer, that cement was already used by the Romans in the 3rd century before Christ. In these days cement was labelled as "Opus Caementicium". The breakthrough of the use of cement only came at the end of the 19th century. The historical development of cement can be read in a range of different books (Stark and Wicht (1999), Locher (2000), Stark and Wicht (2012)).

By definition, cement is an inorganic, non-metallic finely milled hydraulic binder. After addition of water to cement, cement solidifies automatically in a chemical reaction whether to air or in water. The hardening of cement is in general due to bindings of calcium-silicate-hydrates. The reaction of hardening of cement is an exothermic reaction (see Bosold and Pickhardt (2014)).

Cement consists of natural minerals and is obtained from lime ($CaCO_3$), marl (mixture of clay, sand and lime or magnesium carbonate) and clay (Al_2O_3). In general the raw material mix used to produce Portland cement consists of natural components such as calcium oxide (CaO), silicium oxide (SiO_2), aluminium oxide (Al_2O_3) and iron oxide (Fe_2O_3). Only a small amounts of magnesium oxide (MgO), potassium oxide (K_2O), sodium oxide (Na_2O), sulphur oxide (SO_3) and other oxides of small importance(Mn_2O_3, TiO_2) are contained (see van Breugel (1991), Tacke (2002), Karsten (2003) and Bützer (2009))(see Table 2.2).

It should be noted, that the names used for the respective components are a common spelling in construction chemistry. The correct chemical designation is shown in Table 2.1.

	Portland cement	Portland slag cement	Blast-furnace cement	Pozzolanic cement	Portland slate cement
CaO	61.0 - 69.0	52.0 - 66.0	43.0 - 60.0	53.0 - 48.0	53.0 - 58.0
SiO_2	18.0 - 24.0	19.0 - 26.0	23.0 - 32.0	25.0 - 28.0	24.0 - 28.0
Al_2O_3	4.0- 8.0	4.0 - 10.0	6.0 - 14.0	6.0 - 7.0	5.0 - 7.0
Fe_2O_3	1.0 - 4.0	1.0 - 4.0	0.5 - 3.0	2.5 - 3.5	3.0 - 6.0
Mn_2O_3	0.0 - 0.5	0.0 - 1.0	0.1 - 2.5	0.1 - 0.3	0.1 - 0.3
MgO	0.5 - 4.0	0.5 - 5.0	1.0 - 9.5	1.0 - 3.0	1.5 - 2.5
SO_3	2.0 - 3.5	2.0 - 4.0	1.0 - 4.0	2.0 - 3.0	2.5 - 3.5

Table 2.2: Chemical composition of cement in % from Karsten (2003)

To produce mortar or concrete, water must be added to the cement. Mortar and concrete are in general the same, the difference lies in the size of aggregates, up to 4.0 mm for mortar and up to 32.0 mm for concrete. After adding of water to cement an exothermic chemical reaction starts, in which hydrate phases (CSH phases) form.

According to DIN EN 197-1:2011-11 (2011), DIN 1164-1 and according to Karsten (2003), the following kinds of cement are standardised.

CEM I: Portland cement; with at least 95% of portland cement clinker

CEM II: Portland-composite cement; different kinds of cement, besides portland cement mostly granulated slag, puzzolanes and fly ash

CEM III: Blast-furnace cement; three kinds of cement with 36% - 95% granulated slag

CEM IV: Pozzolanic cement; two cements which contain, besides 11% - 55 % portland cement clinker, also puzzolanes

CEM V: Composite cement; cement with 18% - 50 % granulated slag, portland cement clinker and other proportions

The processing of cement and his production is shown in Figure 2.1. The raw material is extracted in quarries and is subsequently crushed. After that, the raw material is homogenized and stored in blending bed silos.

From the blending bed the material is transferred to a grinding and drying plant. Then, the raw meal is transferred to a rotary kiln, where the material is heated up to $2000°C$. Here, the material begins to sinter, that means it starts to melt partially and leaves the rotary kiln as clinker. From the rotary kiln, the clinker is stored and homogenized in silos. During burning of the raw material to clinker, the clinker phases develop, which are necessary for hydraulic hardening of cement.

To get a material which can to react, the material will be milled and stored. The cement produced will be bagged and is ready to use.

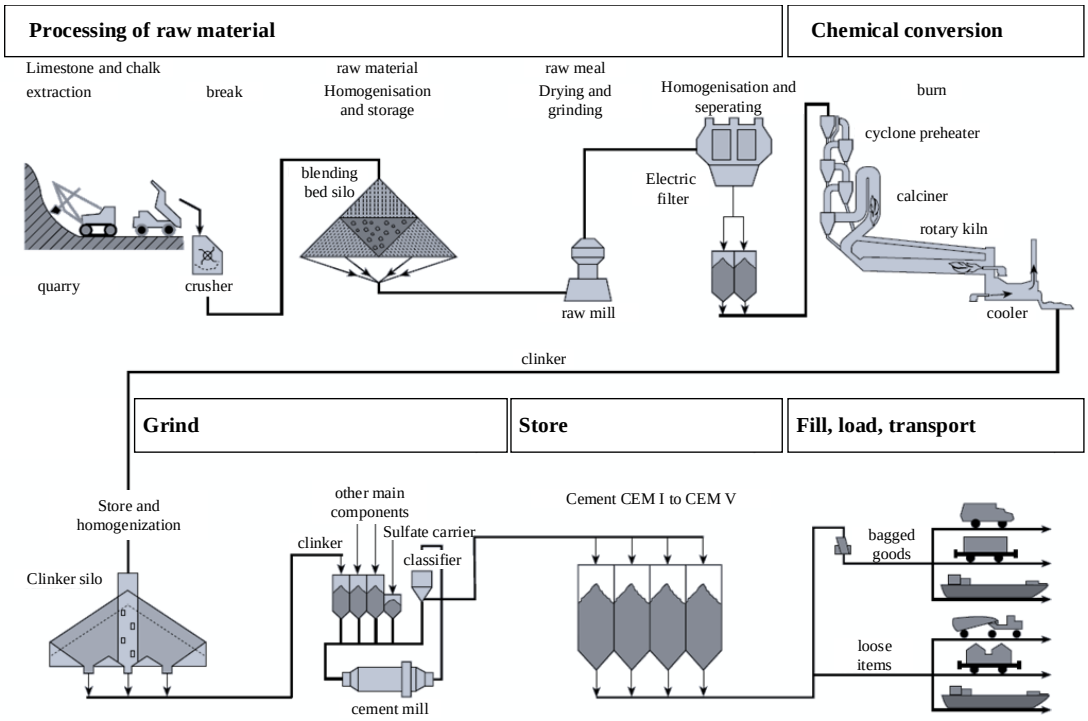

Figure 2.1: Scheme drawing of cement production inspired by Bosold and Pickhardt (2014)

2.1.2 Hardening of cement

Hardening of cement is on basis of a development of a stable structure due to hydration products of the cement (see Locher (2000)).

For a complete hydration of cement, a theoretical amount of water of 38% as described in Richartz (1969) up to 40% as described in Verlag Bau+Technik (2008) and in Wischers (1981) of the cement weight is sufficient. For an amount of 40% which corresponds to a water-cement-ratio of 0.40, 25% of mixing water is chemically bound and 15% of mixing water is physically bound.

In general, three different states of hydration have to be differentiated. The sequence of hydration is described i.a in Richartz (1969), Wischers (1981), Tacke (2002) and in Verlag Bau+Technik (2008) and is shown in Figure 2.2.

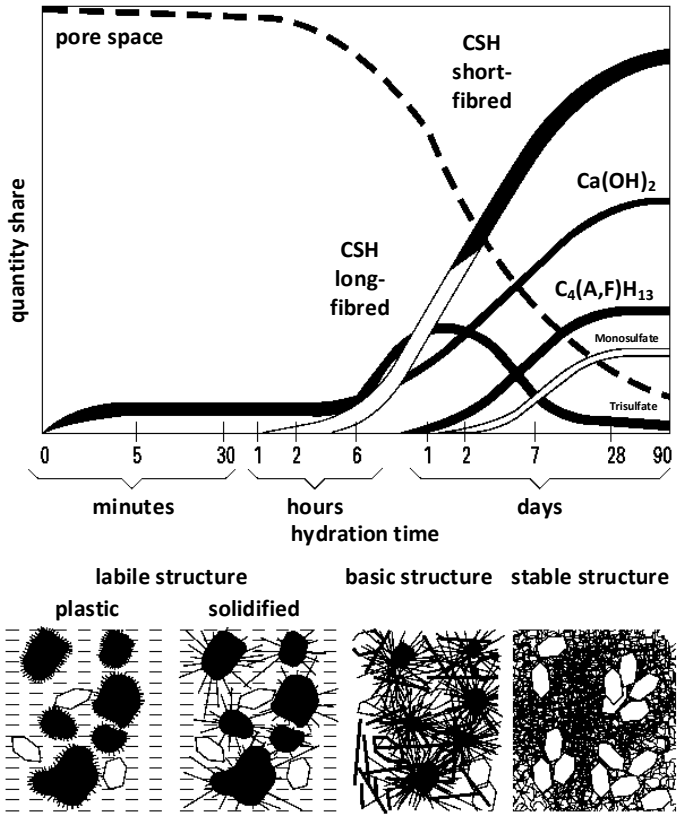

Figure 2.2: Hydratphases inspired by Verlag Bau+Technik (2008)

The first hydration phase, the stiffening with a period of up to 30 minutes after adding of water to cement, is characterized by formation of calcium hydroxide and ettringite. In this period solidification as well as a rise of hydration heat cannot be observed. The mixture of water and cement is known as cement paste, the hardened cement paste as cement stone.

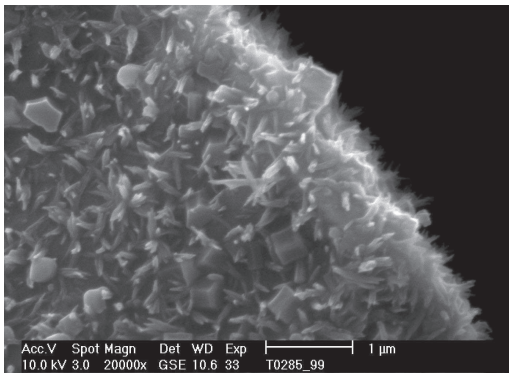

Figure 2.3: CSH-phase after three hours by Verlag Bau+Technik (2008)

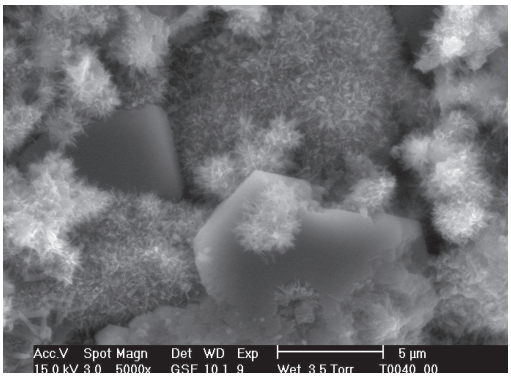

Figure 2.4: CSH-phase after 24 hours by Verlag Bau+Technik (2008)

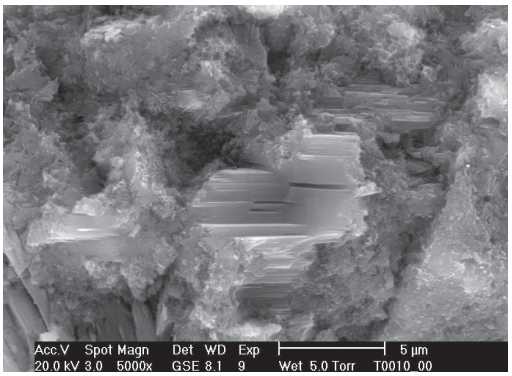

Figure 2.5: CSH-phase after 28 days by Verlag Bau+Technik (2008)

The second hydration phase (Figure 2.3 and Figure 2.4), the solidification phase lasting from one hour to 24 hours after adding of the water to the cement, is characterized by formation of very fine calcium-silicate-hydrate crystalline (CSH). Hydration heat reaches its maximum during this period. At the end of the second hydration phase, the temperature in the concrete caused by hydration aligns to the environmental temperature. Due to the fact that the water filled spaces between the cement particles still have the

same size as at the beginning of hydration, calcium-silicate-hydrates and ettringite has the chance to grow long-fibred. With this, the pores are bridged and a basic structure is build. The strength of mortar or concrete is expected to be higher, the higher the amount of long-fibred calcium-silicate-hydrate. According to this, it is clear that the strength development is decisively influenced in this period of solidification. The formation of ettringite is finished at the end of the second hydration phase and the added gypsum was used.

In the last period of hydration (Figure 2.5), the hardening phase, which takes place from one day up to complete hydration, is characterized by filling up of existing pores by hydration products. The structure is getting more and more stable. Instead of ettringite, tetra-calcium-aluminate-hydrates ($4CaO \cdot Al_2O_3 \cdot 13H_2O$) occur, in which a part of clay is replaced by iron oxide. The duration of respective hydration phases can be influenced by changing of hydration conditions. As a result, the structure development as well as strength development can be influenced decisively.

2.1.3 Factors influencing the hardening of cement

Different factors can influence the hardening of cement. Delayed and accelerated hardening can be distinguished. First, the delayed hardening is described.

The long time strength development (age > month/years) is influenced, intentionally or unintentionally, by change of environmental temperature. In Figure 2.6 it can be seen, that for the same time (t=48 hours), the predicted value of compressive strength, for an environmental temperature of only $5°C$, is $\approx$ 4.0 MPa and for an environmental temperature of $30°C \approx$ 16.0 MPa. This effect was investigated in Bonzel (1961), in Tschernjawski (1967) and explained in Richartz (1969). Nevertheless, for practical use, the period of 28 days or 56 days is influenced insofar, that a low initial temperature causes a low strength after 28 days and a high initial temperature causes a high strength after 28 days (see Figure 2.6).

For lower temperatures as $20°C$, the reaction of cement with water is slower and less hydration products occur. This reaction delay causes a longer duration of hydration phases according to 2.2. Especially in the second hydration phase, a basic structure with a higher amount of long-fibred calcium-silicate-hydrates can form. Therefore, far-reaching connections with a higher amount of contact surfaces will occur. Finally, this

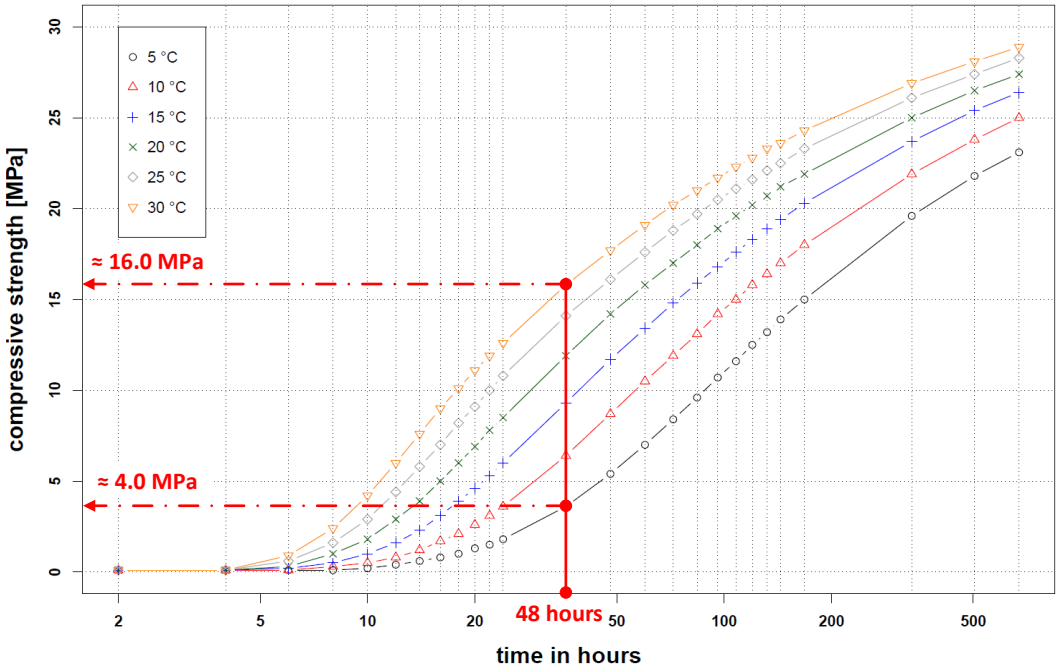

Figure 2.6: Different hardening due to different environmental temperatures

structure will lead to a higher final strength.

Similar changes of the structure and strength development compared to hardening under lower temperature are produced by chemical additives which delay the hardening of cement. In Lieber (1967) it was found out, that the early strength decreased, compared to concrete without additives, however the final strength increased. On the other hand, hardening of cement can be influenced by a higher environmental temperature, by the use of setting accelerator and by an increase of fineness-of-grind of cement.

Higher temperatures encourage an increase of crystal growth induced by a spontaneous nucleation. This reaction is caused by faster and stronger hydration reaction, which forms a supersaturated pore solution. Thus, only few calcium-silicate crystals can grow long-fibred within the second hydration phase. The cement structure, which forms during faster hardening, contents Mainly, short-fibred calcium-silicate hydrates. The early strength of cement of a faster hardening is higher than the early strength under normal conditions, however the final strength is lower than for a normal hardened

cement (see Richartz (1969)).

The same result can be produced by using accelerators. The early strength is in this case higher than the early strength of normal cement but the final strength is lower (see Richartz (1969)).

For fine milled cements (PZ 475 as referred in Richartz (1969)), a lower strength after 90 days is to be expected whereas a coarse milled cement lead to higher strength after 90 days. This is due to the fact that the spaces between the fine milled cement particles are smaller than the spaces between the coarse milled cement particles. Here, short fibres are sufficient to bridge these pore spaces to get a stable structure.

2.1.4 Summary

Hardening of cement is influenced by a range of different reasons. In general, two different effects can be observed during hardening; a hardening with high early strengths and lower final strength and hardening with low early strengths and higher final strengths.

High early strengths and lower final strengths are induced by a high environmental temperature during hardening phase (compared to a reference temperature of 20 $°C$). Accelerators and super-plasticizers have the same effect to hardening of cement as very fine milled cements have.

The hardening behaviour of cement with low environmental temperatures or retarders for concrete have the opposite effect. The early strengths are lower and the final strength are higher, compared to a hardening at the reference temperature of $20°C$.

In any case, it is hard to find an adequate admixture, because environmental temperature can only be influenced partially and using additives runs the risk of unintended effects as described in Richartz (1969).

2.2 Reasons of cracking

As one of the first, Wischers and Manns (1972) identified the most determining reasons which can lead to cracking. These are beside the form change of young concrete

($age \leq 28\ days$) and thermal causes, hygric causes such as shrinkage.

Furthermore, an inadequate use of the concrete screed, respectively the bearing structure and unscheduled stresses can also lead to cracking in concrete.

2.2.1 Change of shape of young concrete

During hardening, young concrete changes its tensile strain behaviour. After two hours, the tensile strain capability is very high ($\approx$ 2.00 mm/m), due to the fact, that the young concrete is not yet hardened (see Figure 2.7, black coloured ordinate axis). The tensile strain of the concrete decreases in the following hours and reaches the minimum tensile strain after eight hours, according to Eifert (2006). At this time the tensile strain is less than 0.05 mm/m ($\approx$ 1/3 of tensile strain after 28 days) whereas The tensile strength at this time (see Figure 2.7, red coloured ordinate axis) is still only 0.25 MPa ($\approx$ 1/10 of tensile strength after 28 days)[see Figure 2.7].

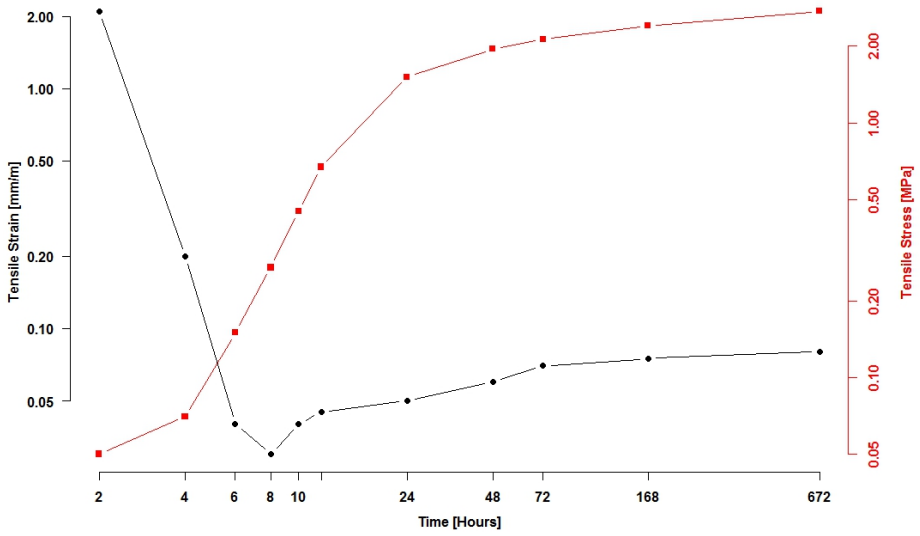

Figure 2.7: Fracture strain versus tensile strength inspired by Eifert (2006) and Thienel (2015)

With respect to Figure 2.7, the work of Weisner and Richter (2016) reports a minimum tensile strain of $\approx$ 0.045 mm/m. The precise value and the chronological development of the tensile strain varies, depending on the concrete composition.

At this early time, a form change caused by external stresses bears the risk of cracking. These changes of shape of young concrete could be e.g. caused by a premature removal of the supports (props) of the bearing structure.

2.2.2 Thermal reasons

As a thermal reason of crack initiation, the development of hydration heat is to mention. Hydration describes an exothermic reaction in which a part of the mixing water is chemically bound. Already in the mid of 1970s, investigations were carried out to measure the heat development as a result of hydration. The measurement of heat development of cement at an early age by using a reaction calorimeter was described in Adams (1976). The calorimeter is a device, which measures the quantity of heat, as a result of chemical, physical or biological processes. Further researches on the heat development were performed in the following years. In Kamiński and Zielenkiewicz (1982), nine different types of cement were tested, the thermal output and the hydration heat of the cement were determined with thermochemical analysis. Subsequently, calculation models were developed which accurately predict the hydration heat development such as Cervera et al. (2002) and Buffo-Lacarrière et al. (2007). Particularly noteworthy is the forecast software KINFEST of the COBET GmbH. Not only the hydration heat development but also, on the basis of the hydration heat development, the strength developments of concrete can be predicted.

The fresh concrete temperature and the environmental temperature are decisive factors which affect the hydration heat development: the higher the environmental temperature the higher the hydration heat development. With appropriate measures such as e.g. protection against solar radiation, the environmental temperature can be influenced. The temperature of fresh concrete $T_{c,fr}$ can be calculated according to Biscoping and Beck (2014) by using the following Equation.

$$T_{c,fr} = \frac{0.84 \cdot (z \cdot T_z + g \cdot T_g + f \cdot T_f) + w \cdot T_w}{0.84 \cdot (z + g + f) + 4.2 \cdot w} \quad [^\circ C] \tag{2.1}$$

z, g, w, f: weight of cement, gravel, water, additives $[kg/m^3]$
T_z, T_g, T_w, T_f: temperature of cement, gravel, water, additives $[^\circ C]$

Another approximation formula to estimate the temperature of fresh concrete with a content of cement of 300 kg/m^3 is provided by Weisner and Richter (2016).

$$T_{c,fr} = 0.1 \cdot T_z + 0.2 \cdot T_w + 0.7 \cdot T_g \quad [^\circ C] \tag{2.2}$$

T_z: cement temperature $[^\circ C]$
T_w: water temperature $[^\circ C]$
T_g: temperature of gravel $[^\circ C]$

The temperature development $\Delta T_n(t)$ in the core of a component can be calculated by Equation 2.3 according to Biscoping and Beck (2014).

$$\Delta T_n(t) = \frac{z \cdot H_n(t)}{c_B \cdot \rho_B} \quad [^\circ C] \tag{2.3}$$

z: quantity of cement $[kg/m^3]$
$H_n(t)$: hydration heat due to figure 2.8 $[kJ/kg]$
c_B: specific heat capacity of concrete ≈ 1.0 $[kJ/kg \cdot K]$
ρ_B: density of concrete ≈ 2350 $[kg/m^3]$

The reason why hydration heat has a practical significance for crack initiation is shown in Figure 2.9. This Figure shows the stress state and the temperature development due to hydration for a concrete with restrained deformations. In accordance with Bosolt (2014), five states of hardening are distinguished:

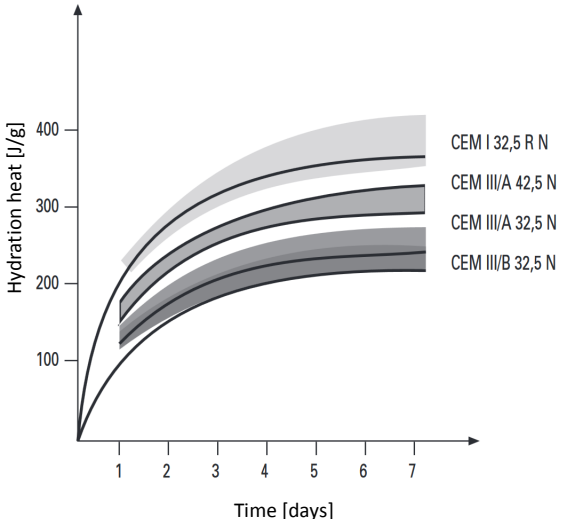

Figure 2.8: Hydration heat of different types of cement from Verlag Bau+Technik (2008)

- **Stage I** (0 hours to 2 hours) presents the initial stage without any significant temperature changes.
- **Stage II** (2 hours to 6 hours) is characterised by a temperature rise due to the hydration heat development. The tensions in young concrete are still not measurable. The reached temperature at the end of this stage is commonly referred to as "first zero-stress temperature" (T_{01}). At this time, the stresses increase as a result thereof.
- **Stage III** (6 hours to 9 hours) shows a continuous warming up to the maximum concrete temperature. The maximum temperature (T_{max}) of the concrete also marks the maximum value of the compressive stresses in the concrete.
- **Stage IV** (9 hours to 11 hours) is characterised by a decreasing concrete temperature. The compressive stress is reduced to zero. At the end of this stage, the concrete reaches the "second zero stress temperature" (T_{02}). Within the next hours the tensile stress in concrete will increase.
- **Stage V** (11 hours to 15 hours) are considered as particularly critical as the young concrete only develops his strength with increasing age. For a C20/25 concrete, the tensile strength at this time is only about 0.20 MPa, thus about 1% of its final compressive strength. The concrete releases at this time continuously heat. This can be hindered or limited by external influences such as the environmental

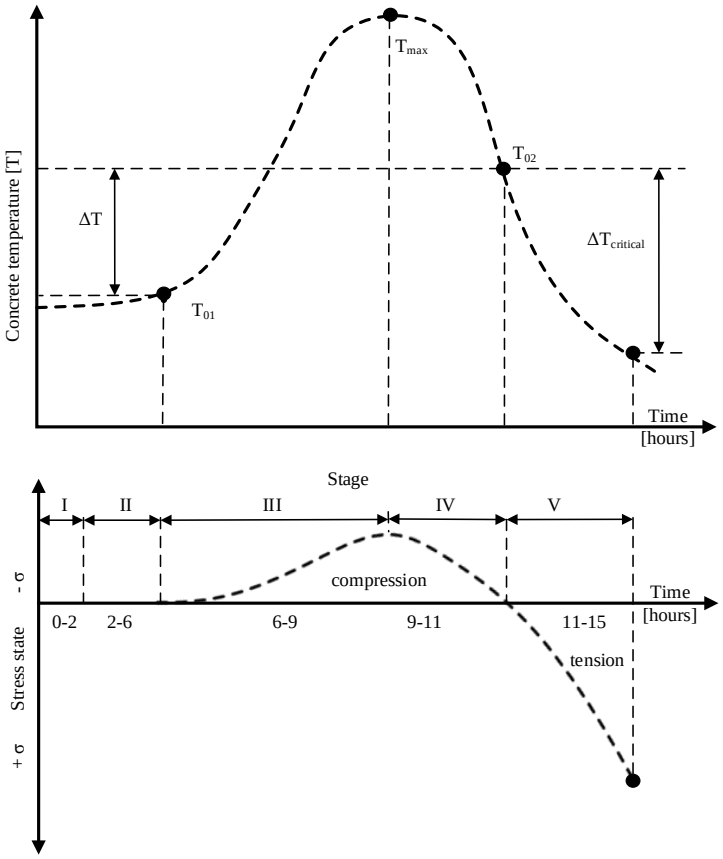

Figure 2.9: Temperature and stress development on a concrete with restrained deformations inspired by Springenschmid and Nischer (1973), Hilsdorf and Reinhardt (2000), Thienel and Hintzen (1994) and by Bosolt (2014)

temperature and if then the resulting stresses are exceeding the developed tensile strength cracking will occur.

2.2.2.1 Thermal induced deformation of concrete

Another important thermal parameter represents the temperature variation of the concrete implied by the environmental temperature. Any material undergoes a change in volume due to temperature changes. An increase in temperature causes an increase in volume, while a temperature decrease will cause a reduction in volume. Regarding a completely free deformable plate, a length change can be calculated with equation 2.4.

$$\Delta l = \alpha_T \cdot l \cdot \Delta T \quad [mm] \tag{2.4}$$

Δl: length change $[mm]$
α_T: coefficient of thermal expansion $[1/K]$
ΔT: temperature difference $[K]$

However, a cement screed cannot be considered as a free deformable plate as there is friction between the concrete screed and the load bearing structure. This friction causes a reduced elongation compared to a completely free deformable screed. This reduced deformation can be calculated with equation 2.5.

$$\Delta l = \alpha_T \cdot l \cdot \Delta T - \frac{\gamma \cdot \mu \cdot l^2}{4 \cdot E} \quad [mm] \tag{2.5}$$

γ: density of concrete $[N/mm^2]$
μ: coefficient of friction $[-]$
1.6 first movement on concrete ground (see Stenzel (2005))
0.8 repeated movement on concrete ground (see Stenzel (2005))
0.8 first movement on foil (see Stenzel (2005))
(other values can be found in Deutscher Ausschuß für Stahlbetonbau (1996))
E: Young's Modulus $[N/mm^2]$

In summary, the hydration heat development and the changing environment temperature were noted as thermal causes. Hydration heat causes tensions in the cross-section of the plate, whereas the changing environmental temperature causes stresses in the panel plane.

2.2.3 Hygric reasons

In concrete, two different kinds of hygric induced processes can occur: Swelling and shrinkage. Swelling describes a volume increase due to water absorption, e.g. during a storage of concrete specimen under water. For building constructions, the effect of swelling is negligible. Shrinkage, on the other hand, is a reduction of the volume of the

concrete and is more detailed explained in the following.

If a free shrinkage of an element is hindered due to e.g. bearing constraints, crack initiation and crack development are most probable. Components with a very high ratio of surface to volume are particularly affected, such as cement screeds. There are several types of shrinkage which can occur in young concrete, as well as in hardened concrete. The distinction

- capillary shrinkage (also early shrinkage or plastic shrinkage)
- drying shrinkage
- chemical shrinkage
- carbonation shrinkage
- thermal shrinkage

The first four different types of shrinkage, their temporal occurrence and their respective shrinkage degree were investigated in Grube (1991). "Bleeding" was mentioned in connection with capillary shrinkage (see Figure 2.10). It designates the settling of water on the surface of a structural component. If water has been removed from a suspension by vaporising, the volume of this suspension decreases. Capillary shrinkage occurs in young concrete caused by a loss of water on the surface of the component. Due to this loss of water, capillary forces arise, depending on the fineness and distribution of solid particles. This is a purely physical process. By stirring the mixture and adding again the lost water content, the process is completely reversible. Furthermore, it is noted, that the capillary shrinkage could be considerably reduced by a prevention of water loss by e.g. covering of fresh concrete with foil.

Drying shrinkage is a decrease of volume in cement stone, caused by the change of the moisture conditions. Factors which influence negatively the drying shrinkage are a low relative humidity, a high water-cement ratio, a high surface to volume ratio, the grain size of cement (the finer the worst) and the age at which the drying shrinkage starts (the earlier the worst). However, the drying shrinkage is unavoidable but could be reduced by varying the aforementioned factors.

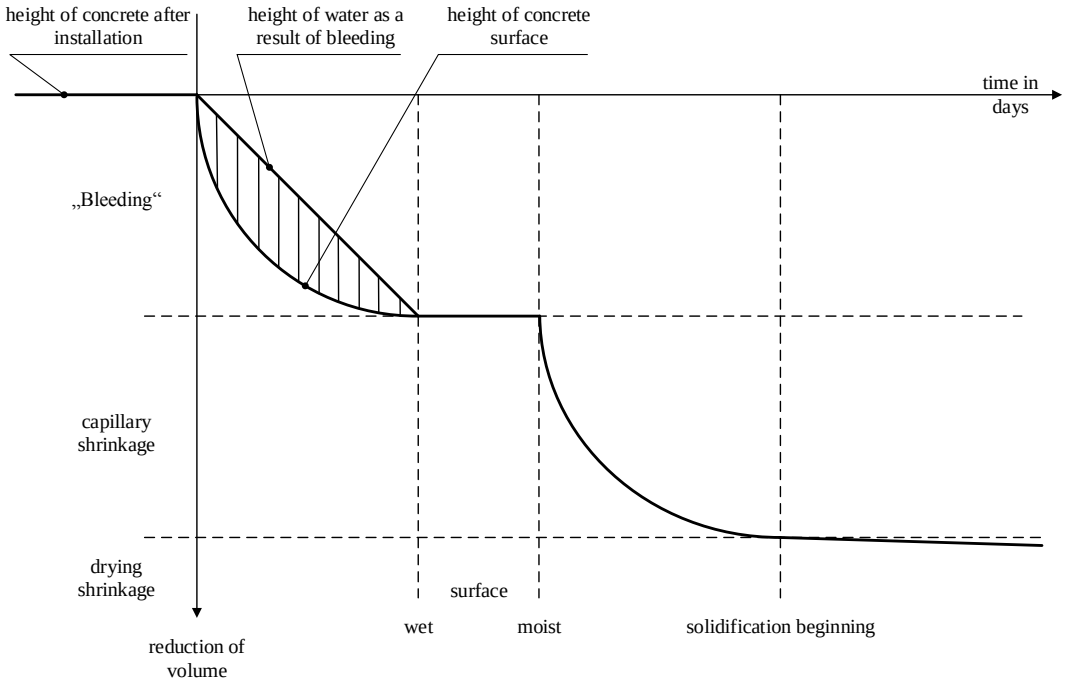

Figure 2.10: Shematic representation of bleeding of concrete inspired by Lura (2011)

During hydration of cement stone, the sum of cement volume and water volume is higher than the volume of hydrates.

Carbonation shrinkage occurs especially on external vertical components, which are rarely watered but often illuminated by the Sun. The carbonation shrinkage concerns generally only a fraction of the whole component and remains thus for the total deformation without meaning.

Thermal shrinkage, as described by Šahinagić-Isović et al. (2012), occurs within the first days after adding water to the cement and is due to temperature changes causes by hydration heat development (see Chapter 2.2.2). Depending on the type of cement and depending on the concrete mixture, thermal shrinkage can reach a value of 0.40 mm/m to 0.50 mm/m. For components with a thickness of less than 20 cm, the effect of thermal shrinkage is nearly zero.

In Schwarz (2000) the practical importance of shrinkage regarding cracking and the definition for shrinkage was described. Shrinkage causes residual stresses, which increase

the risk of cracking on a concrete with restrained deformations. Schwarz (2000) dealt also with the four different kinds of shrinkage. These different kinds of shrinkage were detailed with their occurrence and evolution over time. Recommendations were given how shrinkage can be reduced. These are the use of high-performance plasticisers, which achieve a low water/cement ratio, a suitable post-treatment and an early impregnation of industrial floors.

In Jacobs et al. (2008) the reasons of shrinkage were explained. Compressive strength tests were carried out on the specimen with different grain size distribution of the aggregates (maximum grain size 16 mm and 32 mm) and with different plasticisers and the degree of shrinkage was measured. In addition, a correlation between the compressive strength and degree of shrinkage was established. Overall, eight different concrete mixtures were tested. Moreover, the different kinds of shrinkage were discussed. The timing when shrinkage occurred and the evaluated degree of shrinkage were documented. The results showed that the degree of shrinkage is mainly influenced by the initial cement paste volume. The smaller the maximum grain size the higher the degree of shrinkage. With the use of plasticisers, the degree of shrinkage could be reduced. As no relation between compressive strength and shrinkage was found, it was stated that the compressive strength of concrete cannot be used as a parameter to predict the degree of shrinkage.

All the results of Grube (1991) and of Jacobs et al. (2008) were summarised in Table 2.3 which gives a complete overview of the occurrence of the respective kind of shrinkage as well as the degree of shrinkage in function of the hardening time.

To have an order of magnitude of shrinkage, a formula to calculate shrinkage, considering the cement used and the respective compressive strength class, is provided by DIN EN 1992-1-1:2011-01 (2011) and by Fédération internationale du béton (2013).

Table 2.3: Types of shrinkage from Grube (1991) and of Jacobs et al. (2008)

Type of shrinkage	**Timing**	**Strain**	**Comment**
Capillary shrinkage	2 to 8[1)]hours	up to -4 mm/m	An adequate curing can reduce capillary shrinkage to zero.
Drying shrinkage	initial setting time	+0.1 mm/m	Stored in water
		-0.1 mm/m	Stored at 90% rel. hum.
		-0.3 mm/m	Stored at 70% rel. hum.
		-0.5 mm/m	Stored at 50% rel. hum.
Chemical shrinkage	first days	0.0 mm/m up to -0.3 mm/m	Normally included in drying shrinkage
Carbonation shrinkage	from month	-0.01 mm/m up to -0.1 mm/m	Generally refers only to a part of the entire component and has therefore no significance for overall shrinkage

[1)]Depends on initial setting time

$$\varepsilon_{cds}(t) = \varepsilon_{cd}(t) + \varepsilon_{ca}(t) \quad [-] \tag{2.6}$$

This formula consists of two factors, with $\varepsilon_{cd}(t)$ the strain due to drying shrinkage and $\varepsilon_{ca}(t)$ the strain due to autogenous shrinkage.
Strain due to drying shrinkage can be calculated with:

$$\varepsilon_{cd}(t) = \frac{(t-t_s)}{(t-t_s+0.04\cdot\sqrt{h_0^3})} \cdot k_h \cdot 0.85 \cdot [(220+110\cdot\alpha_{ds1}) \cdot e^{\left(-\alpha_{ds2}\cdot\frac{f_{cm}}{f_{cm0}}\right)}] - 10^{-6} \cdot 1.55 \cdot \left[1-\left(\frac{RH}{RH_0}\right)^3\right] \tag{2.7}$$

Strain due to autogenous shrinkage can be calculated with:

$$\varepsilon_{ca}(t) = 1 - e^{(-0.2\cdot\sqrt{t})} \cdot 2.5 \cdot (f_{ck}-10) \cdot 10^{-6} \tag{2.8}$$

t:	regarded time [d]
t_s:	age of concrete at the end of curing [d]
$h_0 = 2 \cdot A_c/u$:	effective component thickness $[mm]$
	A_c: concretes cross sectional area $[mm^2]$
	u: perimeter $[mm]$
k_h:	empirical coefficient which depends on h_0, see Table 2.4
α_{ds1}:	coefficients to considerate a cement type due to Table 2.5
α_{ds2}:	coefficients to considerate a cement type due to Table 2.5
f_{cm}:	average cylindrical compressive strength N/mm^2
f_{cm0}:	10 N/mm^2
RH:	relative humidity [%]
RH_0:	100%
f_{ck}:	compressive strength of the respective concrete

Table 2.4: k_h values in accordance to h_0 from DIN EN 1992-1-1:2011-01 (2011)

$h_0[mm]$	k_h
≤ 100	1.00
200	0.85
300	0.75
≥ 500	0.70

Table 2.5: k_h values in accordance to h_0 from DIN EN 1992-1-1:2011-01 (2011)

Cement type	α_{ds1}	α_{ds2}
S	3	0.13
N	4	0.12
R	6	0.11

Shrinkage causes deformations in the slab plane and is the reason of curling of concrete floors which are float mounted on concrete floors as described in Georgin et al. (2008) and in Fluckinger (2016). The following reasons of curling were identified by Fluckinger (2016).

- Due evaporation, the upper side of the cement screed shrinks more than the lower side.
- The screed dries only on the upper side as the lower side is covered by the formwork during hardening.
- Due to segregation effects the more heavy aggregates will be at the lower part of

the element whereas the more light cement past will be at the upper part of the element.

- Because of this different dryings and because of the difference in shrinkage, the upper side greatly shrinks more in length than the lower side and as a consequence, the corners of the concrete floor will curl in the following.
- The degree of curling is a result of the difference between the degree of shrinkage on the upper side and the degree of shrinkage on the lower side. Furthermore, it is influenced by the Young's Modulus, the dead weight of the concrete screed and the insulation layer.
- The maximum deformation due to curling can be approximated by five millimetres on a distance of one meter.
- The higher the Young's Modulus, the higher the curling (see Equation 4.4).

2.2.4 Traffic loads

Traffic loads depend on the use of the concrete floor, e.g. industrial floors, floors in shopping centres or airports. In the case of a shopping centre, the different loads, which have to be taken into account, are not very extensive. These are loads caused by live loads, lightweight partition walls, load bearing walls and racking loads. The characteristic values of these loads can be found in DIN EN 1991-1-1:2002 + AC:2009 (2009).

In the case of industrial floors and floors on airports, loads from forklifts and small vehicles must be taken into account. Forklifts are divided, according to their own weight, dimensions and stacking loads, in six classes (FL-classes) (see DIN EN 1991-1-1:2002 + AC:2009 (2009)).

Table 2.6: Dimensions of forklifts due to FL-classes

Class of forklift	**Own weight (netto)**	**Stacking loads**	**Wheel distance**	**Vehicle width**	**Vehicle length**
			a	b	l
$[-]$	$[kN]$	$[kN]$	$[m]$	$[m]$	$[m]$
FL1	21	10	0.85	1.00	2.60
FL2	31	15	0.95	1.10	3.00
FL3	44	25	1.00	1.20	3.30
FL4	60	40	1.20	1.40	4.00
FL5	90	60	1.50	1.90	4.60
FL6	110	80	1.80	2.30	5.10

Table 2.7: Axle loads of forklifts

Class of forklift	**axle load**
	Q_k
$[-]$	$[kN]$
FL1	26
FL2	40
FL3	63
FL4	90
FL5	140
FL6	170

The axle loads Q_k, as shown in table 2.7, of forklifts depends on the FL-classes as given in table 2.6

The value Q_k should be increased with a dynamic factor φ as shown in equation 2.9. Thereby, the dynamic factor φ takes into account the inertial effects as a result of acceleration and deceleration of the stacking loads.

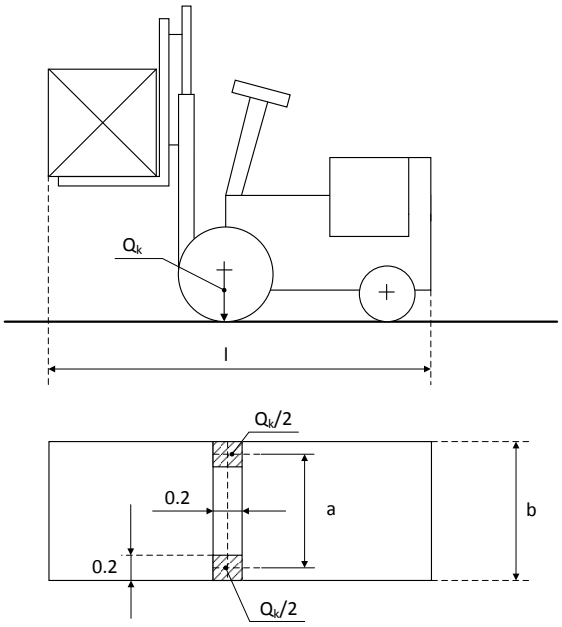

Figure 2.11: Dimensions of forklifts due to DIN EN 1991-1-1:2002 + AC:2009 (2009)

$$Q_{k,dyn} = \varphi \cdot Q_k \tag{2.9}$$

$Q_{k,dyn}$: dynamic characteristic value
φ: dynamic magnification factor
φ= 1.40 pneumatic tyre
φ= 2.00 solid rubber tyres
Q_k: static characteristic value

Furthermore, the influence of different load positions, for a cement screed supported on a damp course, must be taken into account. Due to Westergaard (1926) and Eisenmann and Leykauf (1987), the different stresses, caused by different load positions, can be calculated with equation 2.10 to equation 2.12.

Load position in the middle of the slab (bending tensile stresses below):

$$\sigma_i = \frac{0.275 \cdot Q}{h^2} \cdot (1+\mu) \cdot \left[lg\left(\frac{E_c \cdot h^3}{k \cdot b^4}\right) - 0.436) \right] \quad [N/mm^2] \tag{2.10}$$

Load position at the edge of the slab (bending tensile stresses below):

$$\sigma_r = \frac{0.529 \cdot Q}{h^2} \cdot (1+0.54 \cdot \mu) \cdot \left[lg\left(\frac{E_c \cdot h^3}{k \cdot b^4}\right) + \left(\frac{b}{1-\mu^2}\right) - 2.48) \right] \quad [N/mm^2] \tag{2.11}$$

Load position in the corner of the slab (bending tensile stresses above):

$$\sigma_e = \frac{3 \cdot Q}{h^2} \cdot \left[1 - \left(\frac{12 \cdot (1-\mu^2) \cdot k}{E_c \cdot h^3}\right)^{0.3} \cdot \left(a \cdot \sqrt{2}\right)^{1.2} \right] \quad [N/mm^2] \tag{2.12}$$

E_c:	Young's Modulus of concrete $[N/mm^2]$
h:	thickness of floor slab $[mm]$
$a = \sqrt{\frac{Q}{\pi \cdot p}}$:	radius of load circle
	p = contact pressure $[N/mm^2]$
	Q= wheel load $[N]$
b:	$\sqrt{1.6 \cdot a^2 + h^2} - 0.675 \cdot h \; for \; a \leq 1,724 \cdot h \;\; [mm]$
b:	$a \; for \; a \geq 1,724 \cdot h \;\; [mm]$
k	bedding modulus $[N/mm^3]$
μ	Poisson's ratio of concrete

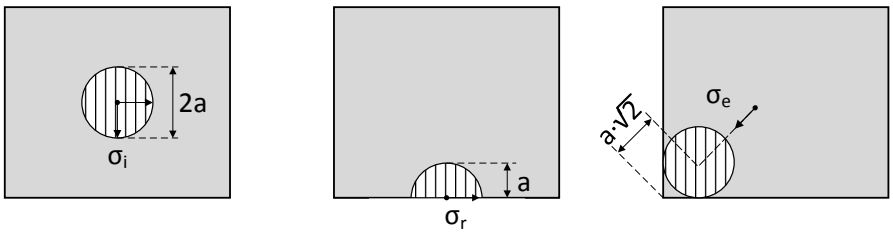

Figure 2.12: Load positions according to Westergaard (1926) and Eisenmann and Leykauf (1987)

2.3 Prevention/Reduction of cracking

2.3.1 Prevention/Reduction of thermal induced cracking

As described in Chapter 2.2.2, the fresh concrete temperature as well as the temperature of the environment influence decisively hydration heat development.

The fresh concrete temperature can be reduced as much as it is possible to reduce the temperature of the single aggregates. Calculation examples showing how fresh concrete temperature can be influenced by reducing the temperature of the aggregates, are described in Biscoping and Beck (2014) (see also Equation 2.1 and Equation 2.2).

According to Pickhardt and Schäfer (2014), a temperature change between surface and core of a component causes stresses. These temperature changes could be implied by e.g. an increase of the surface temperature due to sun radiation or a decrease of the surface temperature due to heavy rain. Both kinds of the temperature change cause stresses in the cross section of the concrete element as described in Figure 2.13. Longitudinal stresses provoke cracks whereby warping stresses cause surface cracks.

Different environmental temperatures lead to different hardening processes. Figure 2.14 shows the qualitative progression of six different hardening profiles, caused by six different environmental temperature, whereby the fresh concrete temperature is for all six cases the same. It can be clearly seen, that a low environmental temperature, e.g. $5°C$, causes lower strengths compared to the profile of the environmental temperature of $30°C$. The difference between the environmental temperature of $5°C$ ($f_{ck} \approx 23.0$ MPa) and the environmental temperature of $30°C$ ($f_{ck} \approx 28.5$ MPa)is, after 28 days about 5.5 MPa.

2.3.2 Prevention/Reduction of hygric induced cracking

In general, cracking cannot be prevented. Thus, with a suitable curing of concrete, shrinkage can be reduced to a minimum (see Table 2.3). In the following, suitable measures to reduce cracking, caused by shrinkage, are presented.

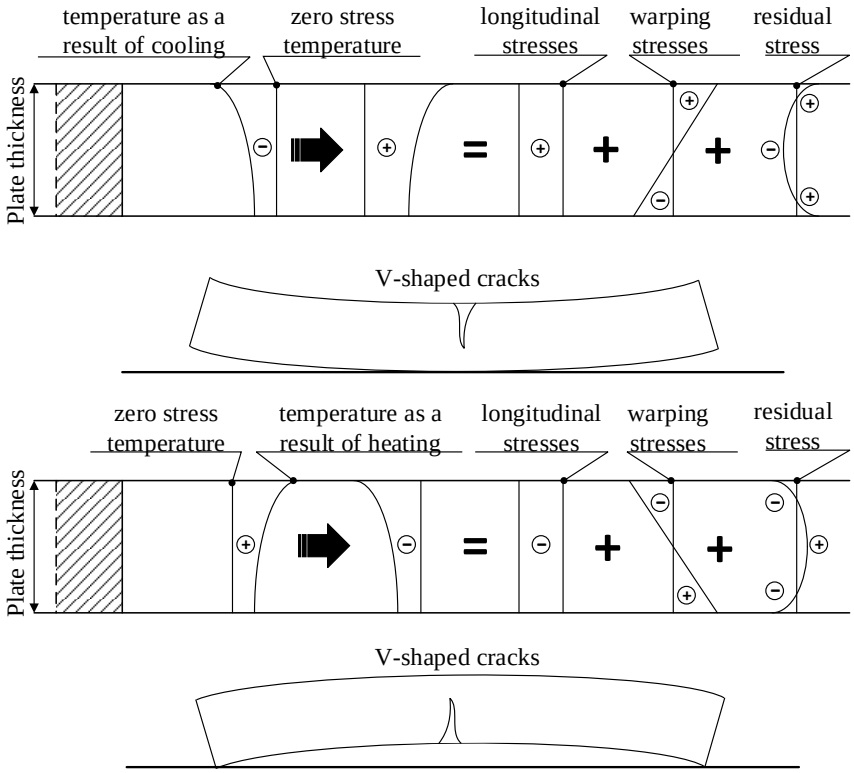

Figure 2.13: Temperature stresses according to Eisenmann and Leykauf (1987) and Foos (2005) for cooling, respectively heating of the surface of the plate

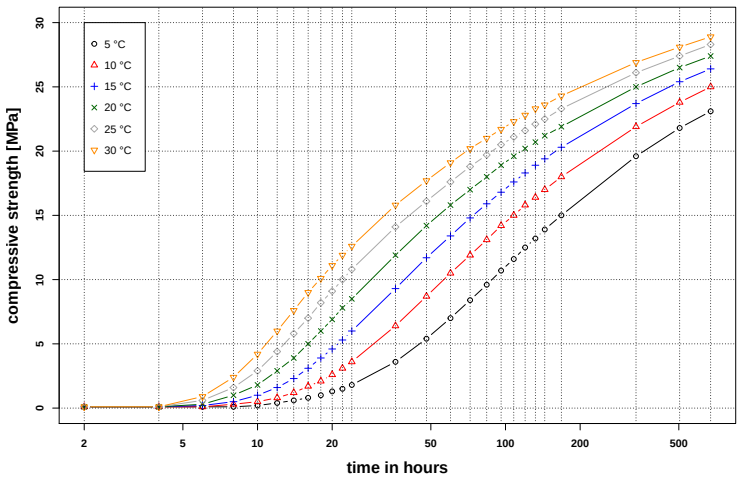

Figure 2.14: Different hardening due to different environmental temperatures

2.3.2.1 Fibre reinforcement

The reduction of hygric induced cracking is the subject of many works. One promising method to reduce cracking is the use of a fibre reinforcement in concrete. Already in the 1970's, the use of fibre reinforced concrete was investigated by Wischers (1974) and Dahms (1978). First, Wischers (1974) found out, that a fibre reinforcement does not improve the tensile strength but it does improve the shaping capability. But in the following work of Dahms (1978) it has been concluded, that the tensile strength and the resistance to dynamic stress were improved. In the following years, the improvement of the shrinkage behaviour caused by a steel fibre reinforcement was tested by Chern and Young (1989). It was found that fibre reinforcement was able to reduce significantly shrinkage as well as creeping of concrete. Further research dealt with the improvement of the material strength properties by using different kinds of fibre reinforcement (steel-fibres, carbon-fibres, polypropylene-fibres) and different volume contents of fibre reinforcement (see Banthia and Sheng (1996)). At the beginning of the 21st century, hybrid-fibre reinforcement, a mixture of the different fibre kinds and lengths and the effect on crack growth and strength improvement were investigated by Banthia and Nandakumar (2003) and by Yao et al. (2003), as well as the influence of shrinkage behaviour in Banthia and Gupta (2006) and in Banthia and Sappakittipakorn (2007). In all studies, the mechanical properties, namely the compressive strength of concrete was improved, while the shrinkage behaviour of the respective concrete was reduced.

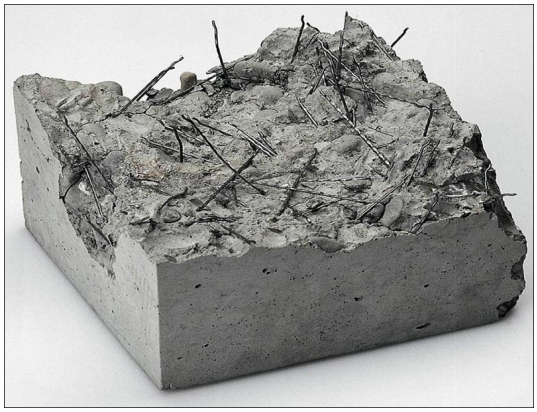

Figure 2.15: Fibre orientation from Helm (2010)

Figure 2.16: Fibre nest from Klischke (2012)

2.3.2.2 Additives

In DIN EN 934-2:2012-08 (2012), the different kinds of additives as well as the requirements concerning additives of concrete are defined. In general, seven different kinds of additives such as e.g. plasticiser and stabiliser, accelerators and retarders are available.

To prevent, respectively to reduce hygric cracking, the use of concrete plasticisers or super-plasticisers is a good measure. The positive effect of a super-plasticiser is its ability to lower the needed water content and thus, the water/cement ratio which leads finally to a lower degree of total shrinkage.

2.3.2.3 Curing of concrete

The purpose of the curing of concrete is to protect the young concrete against evaporation and against extreme temperatures and temperature changes (see Pickhardt and Schäfer (2014)). Evaporation is favoured by high wind speeds, high temperatures and by a low relative humidity. An amount of evaporation is given in 2.17. Starting with the air temperature and considering the relative humidity, the concrete temperature and the wind speed, Figure 2.17 shows very precisely the amount of evaporated water.

A suitable measure, to reduce evaporation, is to cover the young concrete with a foil, respectively to moistening the young concrete or a mixture of both. An indication for an order of magnitude of how long the post-treatment must be applied is given in Table 2.8 and in Table 2.9. The values in the tables are given in days. According to 2.8, the curing time of concrete, considering the temperature and the strength development of concrete, ranges from one day up to 15 days, whereas for table 2.9, the curing time of concrete ranges from one day up to 14 days.

2.4 Material models for concrete

To determine the failure of a material, failure models were developed already since the beginning of the last century. One of the first approaches is the shape modification hypothesis of von Mises (see Figure 2.18). To describe the stress state in a structural component, the stress tensor is needed, which consists of six different stress values $(\sigma_x,\ \sigma_y,\ \sigma_z,\ \tau_{xy},\ \tau_{xz},\ \tau_{yz})$.

According to Equation 2.13, the description of the general stress state follows to:

$$\sigma_{v,M} = \sqrt{\sigma_x^2 + \sigma_y^2 + \sigma_z^2 - \sigma_x \cdot \sigma_y - \sigma_x \cdot \sigma_z - \sigma_y \cdot \sigma_z + 3 \cdot (\tau_{xy}^2 + \tau_{xz}^2 + \tau_{yz}^2)} \qquad (2.13)$$

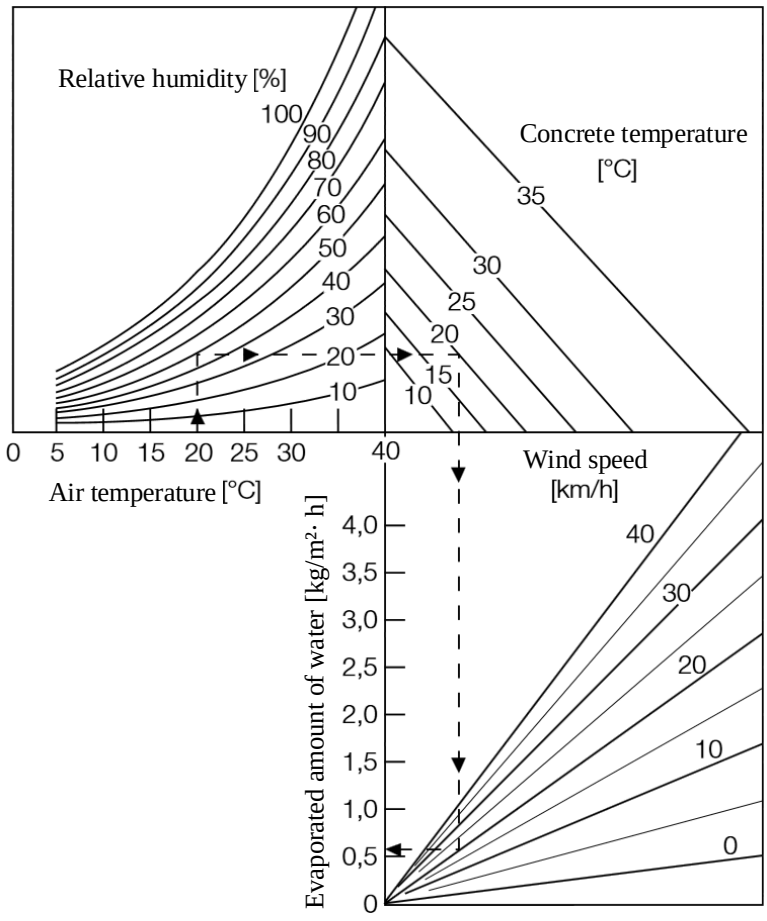

Figure 2.17: Evaporation of concrete depending on temperature, relative humidity and wind speed according to Pickhardt and Schäfer (2014)

If the limit value $\sigma_{v,M}$ is reached, the structural component will fail.

In the following years, the failure models were further developed, e.g. the failure model of Drucker and Prager (1952). Drucker and Prager describe a yield surface in the general stress state 2.19. The yield-criterion is a pressure dependent material model which works well for concrete and other pressure dependent materials (e.g. rocks). The formulation of the yield-criterion is shown in Equation 2.14,

Table 2.8: Minimum curing time in days due to DIN EN 13670/DIN 1045-3, for all exposure classes expect X0, XC1 and XM, taken from Pickhardt and Schäfer (2014)

Surface temperature ϑ [°C]	Minimum curing time in days Strength development of concrete $r = f_{cm2}/f_{cm28}$			
	fast $r \geq 0.50$	middle $r \geq 0.30$	slow $r \geq 0.15$	very slow $r < 0.15$
$\vartheta \geq 25$	1	2	2	3
$25 > \vartheta \geq 15$	1	2	4	5
$15 > \vartheta \geq 10$	2	4	7	10
$10 > \vartheta \geq 5$	3	6	10	15

Table 2.9: Alternative procedure based on exposure classes: Minimum curing time in days according to DIN EN 13670/DIN 1045-3, for exposure classes XC2, XC3, XC4 and XF1, taken from Pickhardt and Schäfer (2014)

Temperature of fresh concrete ϑ_t at the time of concrete poured into place [°C]	Strength development of concrete $r = f_{cm2}/f_{cm28}$		
	fast $r \geq 0.50$	middle $r \geq 0.30$	slow $r \geq 0.15$
$\vartheta \geq 15$	1	2	4
$15 > \vartheta \geq 10$	2	4	7
$10 > \vartheta \geq 5$	4	8	14

$$\sigma_v = \frac{m-1}{2} \cdot (\sigma_1 + \sigma_2 + \sigma_3) + \frac{m+1}{2} \cdot \sqrt{[(\sigma_1 - \sigma_2)^2 + (\sigma_2 - \sigma_3)^2 + (\sigma_3 - \sigma_1)^2]} \quad (2.14)$$

with $m = \frac{\sigma_c}{\sigma_t}$, where σ_c is the boundary stress of the compressive strength and σ_t is the boundary stress of the tensile strength.

Another failure model is the failure criterion of Willam and Warnke (1974). This failure model is a further development of the Drucker and Prager (1952) failure model. In opposite to the Drucker-Prager model, the failure criterion of Willam and Warnke (1974) is only developed for concrete. In the next subsection, the failure criterion is explained extensively.

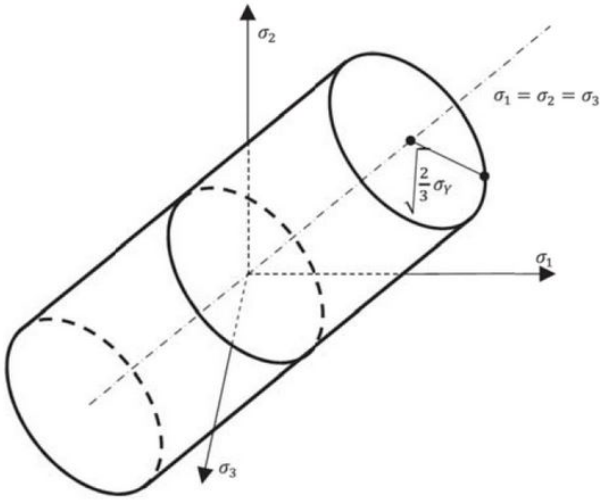

Figure 2.18: von Mises yield surface from Samer (2017)

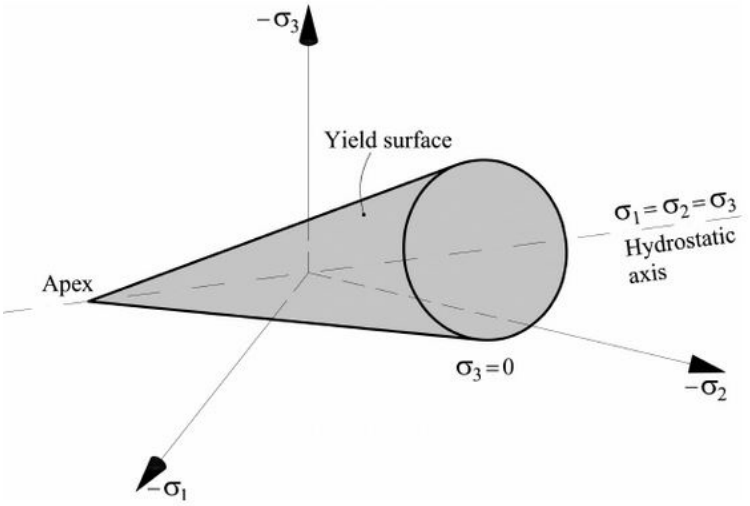

Figure 2.19: Drucker-Prager yield surface from Cervera et al. (2015)

2.4.1 Failure criterion of Willam and Warnke

For a finite element simulation of concrete using ANSYS$^{\text{ő}}$ software, a solid element, SOLID65 is available. The SOLID65 element is able to represent a crack in a solid concrete structure. The material model which is applied during a simulation using the SOLID65 element is the failure criterion of Willam and Warnke (1974). This failure criterion was developed, by the two German engineers K.J. Willam and E.P. Warnke, in the 1970th (see also Schümann (2006) and ANSYS Inc. ANSYS Europe (2013)).

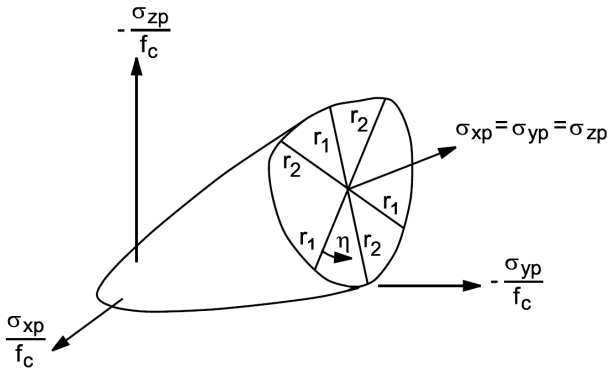

Figure 2.20: Willam-Warnke yield surface from ANSYS Inc. ANSYS Europe (2013)

Willam and Warnke (1974) assumed four requirements to describe the yield surface for a triaxial stress state.

- **good accordance with experimental data**
  Willam and Warnke (1974) made the following demands concerning a good accordance with experimental data »*A close approximation of the concrete data is reached if the failure surface depends on the hydrostatic as well as the deviatoric state, whereby the latter should distinguish different strength values according to the direction of deviatoric stress. Therefore, the failure envelope must be basically a conical surface with curved meridians and a non-circular base section. In addition, in the tensile regime the failure surface could be augmented by a tension cut-off criterion in the form of a pyramid with a triangular section in the deviatoric plane.*«

- **simple determination of model parameter from standardised tests**
  Willam and Warnke (1974) explained this requirement as follows: »*Simple identification means that the mathematical model of the failure surface is defined by a very small number of parameters wich can be determined from standard tests data, e.g. uniaxial tension, uniaxial compression, biaxial compression tests, etc. The description of the failure surface should also encompass simple failure envelopes for specific model parameters. In other words, the cylindrical von Mises and the conical Drucker-Prager model should be special cases of the sophisticated failure formulation.*«

- **constant surface with continuously variable tangential plane (smoothness)**
  The smoothness is, according to Willam and Warnke (1974) important for two reasons: »*From a computational point of view, it is very convenient if a single description of the failure surface is valid within the stress space under consideration. From the theoretical point of view, the proposed failure surface should have a unique gradient for defining the direction of the inelastic deformations according to the 'normal principle'. The actual nature of concrete failure mechanics also supports the concept of a gradual change of strength for small variations in loading. Geometrically, the smoothness condition implies that the failure surface is continuous and has derivates. Therefore, the deviatoric trace of the failure surface must pass through* r_1 *and* r_2 *with tangents* t_1 *and* t_2 *at* $\theta = 0°$ *and* $\theta = 60°$ [see Figure 2.21]. *Recall that for isotropic conditions only a sextant of the stress space has to be considered,* $0° \leq \theta \leq 60°$.«

- **monotonously curved surface without turning points (convexity)**
  According to Willam and Warnke (1974), »*Convexity is an important property since it assures stable material behaviour [...] if the 'normality' principle determines the direction of inelastic deformations. Stability infers positive dissipation of inelastic work during a loading cycle according to the concepts of thermodynamics.* «

The condition that must be fulfilled for a failure to occur on tension or pressure is:

$$\frac{F}{f_c} - S \geq 0 \tag{2.15}$$

If Equation 2.15 is satisfied, the concrete fails due to tension or pressure. In Equation 2.15, F is the function of the principal stress state $(\sigma_{xp}, \sigma_{yp}, \sigma_{zp})$, f_c is the uniaxial compressive strength of the concrete, and S is the failure area in the three-dimensional main stress space.

Material properties

For the determination of the failure area, the two following input parameters have to be determined, the uniaxial compressive strength (f_c) and uniaxial tensile strength (f_t). The other required parameters, the two-axial compressive strength (f_{cb}), the compressive strength for biaxial pressure (f_1) and the compressive strength for uniaxial pressure (f_2) can be calculated according to Equation 2.16, Equation 2.17 and Equation 2.18.

$$f_{cb} = 1.200 \cdot f_c \tag{2.16}$$

$$f_1 = 1.450 \cdot f_c \tag{2.17}$$

$$f_2 = 1.725 \cdot f_c \tag{2.18}$$

The preceding parameters are only valid for stress states following the condition:

$$|\sigma_h| \leq \sqrt{3} \cdot f_c \tag{2.19}$$

with

$$\sigma_h = hydrostatic\ stress\ state = \frac{1}{3} \cdot (\sigma_{xp} + \sigma_{yp} + \sigma_{zp}) \tag{2.20}$$

The factors F and S are described by the principle stress states.

$$\sigma_1 = max(\sigma_{xp}, \sigma_{yp}, \sigma_{zp}) \tag{2.21}$$

$$\sigma_3 = min(\sigma_{xp}, \sigma_{yp}, \sigma_{zp}) \tag{2.22}$$

and

$$\sigma_1 \geq \sigma_2 \geq \sigma_3 \tag{2.23}$$

The failure of concrete is divided into four possible areas:

1. $0 \geq \sigma_1 \geq \sigma_2 \geq \sigma_3$ $(compression - compression - compression)$
2. $\sigma_1 \geq 0 \geq \sigma_2 \geq \sigma_3$ $(tension - compression - compression)$
3. $\sigma_1 \geq \sigma_2 \geq 0 \geq \sigma_3$ $(tension - tension - compression)$

4. $\sigma_1 \geq \sigma_2 \geq \sigma_3 \geq 0 \;\; (tension - tension - tension)$

In every single area, F (the function of the principal stress state $(\sigma_{xp}, \sigma_{yp}, \sigma_{zp})$) and S (the failure area in the three-dimensional principle stress space) are described independently.

Mathematical description

2.4.1.1 Domain 'compression - compression - compression'

$0 \geq \sigma_1 \geq \sigma_2 \geq \sigma_3$

The function F_1 of the general stress state is calculated according to Formula 2.24 and corresponds to average shear stress.

$$F_1 = \frac{1}{\sqrt{15}} \cdot \sqrt{(\sigma_1 - \sigma_2)^2 + (\sigma_2 - \sigma_3)^2 + (\sigma_3 - \sigma_1)^2} \tag{2.24}$$

The failure area in the three-dimensional stress space follows the following Formula:

$$S_1 = \frac{2 \cdot r_2 \cdot (r_2^2 - r_1^2) \cdot cos\eta + r_2 \cdot (2 \cdot r_1 - r_2) \cdot \sqrt{4 \cdot (r_2^2 - r_1^2) \cdot cos^2\eta + 5 \cdot r_1^2 - 4 \cdot r_1 \cdot r_2}}{4 \cdot (r_2^2 - r_1^2) \cdot cos^2\eta + (r_2 - 2 \cdot r_1)^2} \tag{2.25}$$

with

$$cos\eta = \frac{2 \cdot \sigma_1 - \sigma_2 - \sigma_3}{\sqrt{2} \cdot \sqrt{(\sigma_1 - \sigma_2)^2 + (\sigma_2 - \sigma_3)^2 + (\sigma_3 - \sigma_1)^2}} \tag{2.26}$$

$$r_1 = a_0 + a_1 \cdot \xi + a_2 \cdot \xi^2 \tag{2.27}$$

$$r_2 = b_0 + b_1 \cdot \xi + b_2 \cdot \xi^2 \tag{2.28}$$

$$\xi = \frac{\sigma_h}{f_c} = \frac{\sigma_1 + \sigma_2 + \sigma_3}{3 \cdot f_c} \tag{2.29}$$

The undetermined coefficients a_0, a_1, a_2, respectively b_0, b_1, b_2 are calculated with Formula 2.30

$$\begin{bmatrix} 1 & \xi_t & \xi_t^2 \\ 1 & \xi_c b & \xi_c b^2 \\ 1 & \xi_1 & \xi_1^2 \end{bmatrix} \cdot \begin{bmatrix} a_0 \\ a_1 \\ a_2 \end{bmatrix} = \begin{bmatrix} \frac{F_1(\sigma_1=f_t,\sigma_2=\sigma_3=0)}{f_c} \\ \frac{F_1(\sigma_1=0,\sigma_2=\sigma_3=-f_{cb})}{f_c} \\ \frac{F_1(\sigma_1=-\sigma_h^a,\sigma_2=\sigma_3=-\sigma_h^a-f_1)}{f_c} \end{bmatrix} \tag{2.30}$$

with

$$\xi_t = \frac{f_t}{3 \cdot f_c}, \xi_c b = -\frac{2 \cdot f_{cb}}{3 \cdot f_c}, \xi_1 = -\frac{\sigma_h^2}{f_c} - \frac{2 \cdot f_1}{3 \cdot f_c} \tag{2.31}$$

respectively with Formula 2.32

$$\begin{bmatrix} 1 & -\frac{1}{3} & \frac{1}{9} \\ 1 & \xi_2 & \xi_2^2 \\ 1 & \xi_0 & \xi_0^2 \end{bmatrix} \cdot \begin{bmatrix} b_0 \\ b_1 \\ b_2 \end{bmatrix} = \begin{bmatrix} \frac{F_1(\sigma_1=\sigma_2=0,\sigma_3=-f_c)}{f_c} \\ \frac{F_1(\sigma_1=\sigma_2=-\sigma_h^a,\sigma_3=-\sigma_h^a-f_2)}{f_c} \\ \frac{F_1(\sigma_1=\sigma_2=\sigma_3=0)}{f_c} \end{bmatrix} \tag{2.32}$$

with

$$\xi_2 = -\frac{\sigma_h^2}{f_c} - \frac{f_2}{3 \cdot f_c} \tag{2.33}$$

Due to the fact that the two parables intersect on the common hydrostatic axis in the point $\xi = \xi_0$, a constraint condition arises:

$$r_1(\xi_0) = r_2(\xi_0) = 0 \tag{2.34}$$

ξ_0 can be calculated according to Equation 2.35, respectively Equation 2.36 and is rep-

resented in Figure 2.21.

$$r(\xi_0) = a_0 + a_1 \cdot \xi_0 + a_2 \cdot \xi_0^2 = 0 \tag{2.35}$$

$$\xi_0 = \frac{-a_1 - \sqrt{a_1^2 - 4 \cdot a_0 \cdot a_2}}{2 \cdot a_2} \tag{2.36}$$

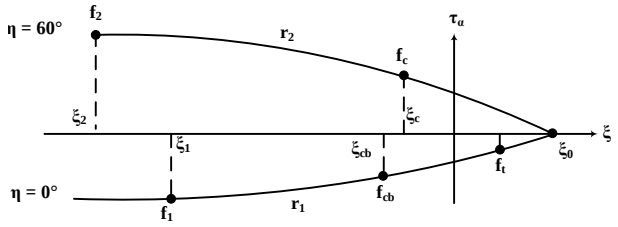

Figure 2.21: Meridian of failure surface from ANSYS Inc. ANSYS Europe (2013)

To ensure a convexity of the failure surface, the relation of r_1 to r_2 must satisfy the condition due to Equation 2.37.

$$0.50 < \frac{r_1}{r_2} < 1.25 \tag{2.37}$$

Furthermore, for the coefficients a_0, a_1, a_2, b_0, b_1 and b_2 the following conditions must be fulfilled.

$$a_0 > 0, a_1 \leq 0, a_2 \leq 0 \tag{2.38}$$

$$b_0 > 0, b_1 \leq 0, b_2 \leq 0 \tag{2.39}$$

By determining of selecting parameters, the material model of Willam and Warnke Willam and Warnke (1974) can be transferred into simple material models such as the failure criterion of von Mises

$$a_0 = b_0, a_1 = b_1 = a_2 = b_2 = 0 \tag{2.40}$$

or the failure criterion of Drucker-Prager Drucker and Prager (1952).

$$a_0 = b_0, a_1 = b_1, a_2 = b_2 = 0 \tag{2.41}$$

2.4.1.2 Domain 'tensile - compression - compression'

$$\sigma_1 \geq 0 \geq \sigma_2 \geq \sigma_3$$

For the domain 'tensile - compression - compression', the formulation is modified, compared to the previous formulation. The function F_2 is then described according to Equation 2.43 and the failure surface S_2 due to Equation 2.44,

$$F_2 = \frac{1}{\sqrt{15}} \cdot \sqrt{(\sigma_2 - \sigma_3)^2 + \sigma_2^2 + \sigma_3^2} \tag{2.42}$$

$$S_2 = \left(1 - \frac{\sigma_1}{f_t}\right) \cdot \frac{2 \cdot p_2 \cdot (p_2^2 - p_1^2) \cdot cos\eta + p_2 \cdot (2 \cdot p_1 - p_2) \cdot \sqrt{4 \cdot (p_2^2 - p_1^2) \cdot cos^2\eta + 5 \cdot p_1^2 - 4 \cdot p_1 \cdot p_2}}{4 \cdot (p_2^2 - p_1^2) \cdot cos^2\eta + (p_2 - 2 \cdot p_1)^2} \tag{2.43}$$

with $cos\eta$ as already described in Equation 2.26 and p_1 and p_2 according to Equation 2.44 and Equation 2.45, where χ can be calculated with Equation 2.46.

$$p_1 = a_0 + a_1 \cdot \chi + a_2 \cdot \chi^2 \tag{2.44}$$

$$p_2 = b_0 + b_1 \cdot \chi + b_2 \cdot \chi^2 \tag{2.45}$$

$$\chi = \frac{\sigma_2 + \sigma_3}{3} \tag{2.46}$$

To complete the formulation of the material modell of Willam and Warnke (1974), the domain 'tensile - tensile - compression' and the domain 'tensile - tensile - tensile' are described in subsection 2.4.1.3, respectively in subsection 2.4.1.4.

2.4.1.3 Domain 'tensile - tensile - compression'

$$\sigma_1 \geq \sigma_2 \geq 0 \geq \sigma_3$$

$$F_3 = \sigma_i \quad i = 1, 2 \tag{2.47}$$

$$S_3 = \frac{f_t}{f_c} \cdot \left(1 + \frac{\sigma_3}{f_c}\right) \tag{2.48}$$

If the failure criterion for σ_1 and for σ_2 is fulfilled, the concrete cracks perpendicular to the principle stress directions σ_1 and σ_2. If the failure criterion is only satisfied for σ_1, the concrete will only crack perpendicular to the plane σ_1 direction.

2.4.1.4 Domain 'tensile - tensile - tensile'

$$\sigma_1 \geq \sigma_2 \geq \sigma_3 \geq 0$$

$$F_4 = \sigma_i \quad i = 1, 2, 3 \tag{2.49}$$

$$S_4 = \frac{f_t}{f_c} \tag{2.50}$$

2.4.2 Summary

In general, the choice of a failure criterion depends on the chosen technique to represent a crack path. For the representation of crack paths, different techniques are available as described in section 2.6.

2.5 Fracture-mechanic characteristics

The previously mentioned, most common material models gives an overview of when, respectively under which circumstances a material will fail. In the case of concrete, the failure of the material is accompanied by cracking. In the following subsections, different fracture-mechanic values are introduced, which allow the calculation of a crack.

2.5.1 Stress Intensity Factor (K-factor)

The stress intensity factor K, describes, within the limits of the linear-elastic material laws (linear-elastic fracture-mechanic [LEFM]), a decreasing stress level at the crack tip. In general, the stress intensity factor can be calculated with Equation 2.51 for all crack problems.

$$K_I = \sigma_n \cdot \sqrt{\pi \cdot a} \cdot g \tag{2.51}$$

where σ_n is the representative stress, a is the crack length and g describes a function for the influence of the crack geometry (edge crack; slanted crack), the influence of the specimen geometry (infinity plate; thin plate) and the elastic material properties.

According to Langenberg (2015), the the value of the stress intensity factor is limited by the size of the plastic zone. The assumption of the linear elastic behaviour is only

for very small plastic zones. Apart from that, the fracture-mechanic characteristics for elastic-plastic fracture mechanics (EPFM) must be used.

2.5.2 J-Integral

The J-Integral is one of the elastic-plastic fracture-mechanical (EPFM) characteristics. This approach is based on continuum mechanics. Using the energy balance, the J-Integral can be calculated for a line integral which runs around the crack tip (see Figure 2.22).

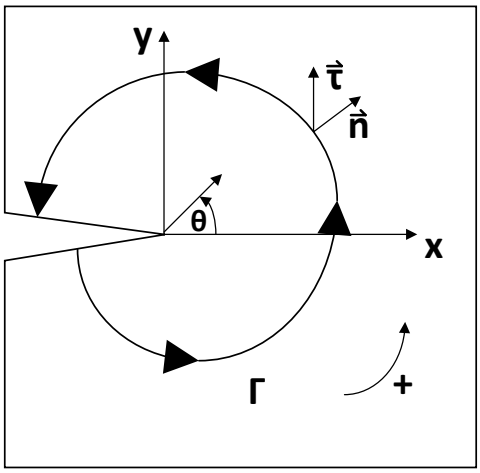

Figure 2.22: J-Integral inspired by Langenberg (2015)

The J-Integral can be calculated with Equation 2.52,

$$J = \frac{\delta U}{\delta a} \cdot \frac{1}{B} \tag{2.52}$$

where U is the potential energy, B is for the thickness of the specimen and a is the fatigue crack length. The J-Integral is suitable for steel and other ductile metals, but was also used by Mindess et al. (1977) for concrete .

2.5.3 Crack tip opening displacement (CTOD)

The crack tip opening displacement (CTOD) is also a characteristic of elastic-plastic fracture-mechanical (EPFM). The CTOD describes the displacement of the edge of the crack in the area of the crack tip. Thereby, the CTOD can be calculated with equation 2.53,

$$CTOD(\delta) = \delta_{el} + \delta_{pl}$$

$$CTOD(\delta) = \frac{K_I^2 \cdot (1-\nu^2)}{2 \cdot R_{pl,2} \cdot E} + \frac{r \cdot (W-a) \cdot \nu_{pl}}{r \cdot W + 0.6 \cdot a + Z} \tag{2.53}$$

with:

r: rotation factor
ν_{pl}: plastic component of clip gauge displacement
W: width of specimen
a: fatigue crack length
Z: edge spacing
ν: Poisson's ratio

The CTOD is usually used in offshore areas. For solid structures, the CTOD does not represent an alternative and is only represented here to give a complete overview of fracture-mechanic characteristics.

2.6 Representation of a crack path

To represent a crack path, different techniques are available. The most common methods are the technique of node splitting and the technique of element modification. These techniques are represented in the following.

2.6.1 Node splitting technique

The node splitting technique represents the simplest way to simulate a crack path (see Kuna (2010)). In general, it can be noted, that the node which meets a chosen failure criterion is split, respectively another node is created.

In Fagerholt et al. (2012), tensile strength tests were performed on single-edge notched steel specimens and Fagerholt et al. (2013) dealt with mesh adaption techniques for the node-splitting method. The numerical simulation, using node splitting method, of ductile fractures was investigated in Gruben et al. (2014) with a modified Arcan test.

The technique of node splitting is only applicable when the crack path is already known. The elements of the mesh must be arranged concerning their size and their orientation. Otherwise, the method is strongly mesh dependent.

2.6.2 Element modification technique

2.6.2.1 Element splitting technique

A much more powerful, but on the other hand, a very extensive method to represent a crack path is the element splitting technique. Using different splitting algorithms, the crack path can be predicted very precisely. An example of different kinds of split algorithms is given in Figure 2.23.

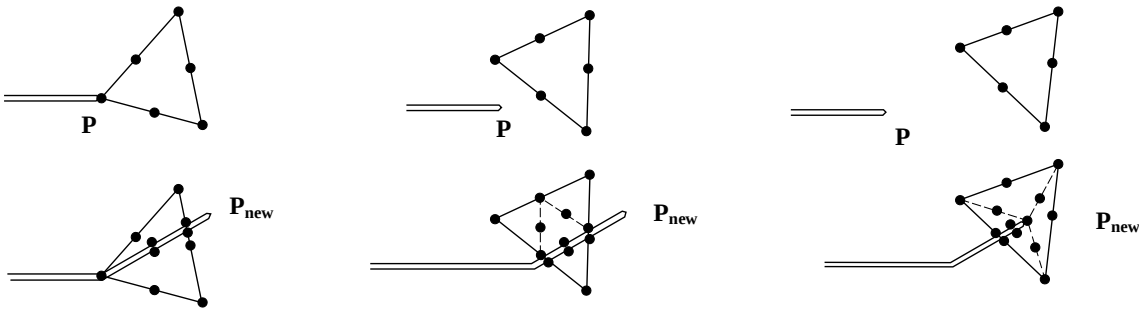

Figure 2.23: Different split algorithms by Kuna (2010)

One of the element splitting techniques is the extended finite element method (XFEM) Which has been developed in 1999 and published in the work of Belytschko and Black (1999). The XFEM is a net independent method to simulate and to represent discontinuities. The discontinuities inside the elements are represented through extending of the initial functions by adding degrees of freedom as well as enhancing functions.

Today, many works deal with the extended finite element method such as the work of Wang et al. (2012), Pathak et al. (2013) and of Wen and Tian (2016). Wang et al. (2012)

dealt with the crack growth of brittle, particle-reinforced composites. In Pathak et al. (2013) three-dimensional fatigue crack growth and in Wen and Tian (2016), dynamic crack growth was investigated.

2.6.2.2 Element-failure method

The element failure method (EFM) determinates the crack growth by eliminating all elements which are highly loaded, according to a chosen failure criterion. As a failure criterion, the operator can choose between strength theory of strength and fracture mechanics.

In Kuna (2010), the EFM was described in general. Beissel et al. (1998) developed an algorithm for dynamic crack propagation in general directions. A concept for dynamic fracture and delamination on a composite laminate subjected to a three-point bending test is represented in Tay et al. (2005) and Sun et al. (2011) described the progressive failure analysis of fibre reinforced laminates.

The element-failure method was used in the past to simulate delamination effects on composite laminate subjects. For the glue layer, a suitable failure criterion was assigned. Furthermore, the element-failure method was used, to calculate a crack path for brittle materials, such as cast iron structures. The crack path, caused by air pockets was simulated very precisely. In the current work, the simulation of a crack path using element-failure method is carried out for the first time for concrete.

2.6.2.3 Summary

Besides the previously mentioned techniques, there is a number of other techniques or representations of cracks in solid structures, such as the moving crack tip elements, as researched in Ozkan et al. (2010); Fujimoto and Nishioka (2010) and the smeared crack model, as described in Beshara (1993) and in Edalat-Behbahani et al. (2017). The smeared crack model is further implemented in the SOLID65 element (see subsection 2.4.1), which was presented in de Schutter (1996, 2002).

Within a design concept and for the choice of a technique to simulate a crack path in a concrete structure, the following requirements must be fulfilled: the technique should be reliable, simple to use and the required material parameters, should be determined in a simple way.

2.6.3 Present design methods

To design a unreinforced concrete floor, different design methods can be used. It distinguishes between analytical approaches, standardised procedures and numerical calculations (FEM). Thereby, the durability and the serviceability, namely the cracking of concrete floors, is a very important factor.

The analytical approach of Lohmeyer and Ebeling (2012) regards rectangular concrete floors. The floors are dimensioned, taking into account the bedding module of the base course, single loads and traffic loads. Load independent load cases (shrinkage versus evolving material properties) are considered in a simplified manner. An interaction of concrete floor and bearing structure, due to deflection of the bearing structure, is not considered.

The standardised procedures combine experiences gathered in practice with results from scientific tests. For the planning of unreinforced concrete floors, recommendations are given by Betonstein Handwerk (2011) and by Schäfer and Beck (2015). Here, the ratio between length and width and the maximum size of the area is regulated, as well as the hight of the concrete floor.

Numerical concepts for the calculation of concrete floors are represented by Martinola et al. (1996) and by Foos (2005). Martinola et al. (1996) developed a two-dimensional numerical model, which is able to simulate cracking due to drying of a cementitious coat. Furthermore, the detaching of a cementitious coat can be simulated. Foos (2005) developed a design concept for unreinforced concrete pavements, considering weather conditions and traffic loads.

Fair-faced concrete screeds serving as final surface represent an interesting alternative to conventional floor systems. The challenge while designing a fair-faced screed is in the possible cracking of the concrete used. Herewith, the evolving material parameters used, such as mechanical and hygric properties, need to be considered. Furthermore, effects such as curling and the interaction between bearing structure and screed have to be taken into account. Currently, no existing numerical model is able to consider all these mentioned factors. The current work represents a design concept, which closes this research gap. A design concept has to be developed, which considers the previously

mentioned points. Besides extensive experimental investigations, a numerical model serves as the starting point for the development of a design concept. A parameter study, on the basis of the experimental tests and the numerical model, completes the design concept.

3 Experimental investigations

3.1 Objectives

To simulate the crack initiation and crack growth in a concrete structure as function of time, the evolving material strengths, as well as the hygric material behaviour must be determined in function of time. The following chapter deals with experimental investigations to determine the material properties, such as mechanical behaviour and hygric behaviour and to determine cracking behaviour of a C20/25 concrete. The findings of material properties in this chapter are the basis for the finite element model. Crack initiation and crack development of H-shaped concrete specimen and of large scale tests are used to calibrate and to verify the developed finite element model and calculation algorithm.

First, all important material properties are represented. After this, tests on small H-shaped shrinkage specimen are described, which show the cracking behaviour of an obstructed component. Concluding large scale tests are represented to show cracking behaviour on large concrete floors with different boundary conditions, such as floors fixed on foil and floors in direct connection to the bearing structure.

3.2 Mechanical properties

For the simulation of concrete in its hardening phase and beyond, material behaviour and development of material properties of concrete have to be known. On one hand it is important to know evolving material properties over time, such as compressive strength, Young's Modulus and tensile strength and on the other hand hygric properties such as shrinkage and moisture release must be determined.

To determine the material properties in its hardening phase, different methods are applied: the prognosis software KINFEST, a test set-up as well as analytical approaches

according to DIN EN 1992-1-1:2011-01 (2011) and according to Fédération internationale du béton (2013) were used. Finally, the results of these three different approaches are compared. For hygric properties, shrinkage was investigated on shrinkage drains and compared to the analytical approaches of DIN EN 1992-1-1:2011-01 (2011) and Fédération internationale du béton (2013). Moisture release was investigated on small specimen using humidity sensors.

3.2.1 KINTEMP/KINFEST

KINTEMP/KINFEST was developed i.a. by Prof. Dr Gebauer and is distributed by COBET Software company in Germany. First practical applications were made in the 1990th of the last century and were published by Oecknick (1996) and by Weise (1996). KINTEMP/KINFEST predicts evolving material properties of various concrete mixtures with various boundary conditions.

KINTEMP estimates the temperature development caused by hydration heat based on a tremendous number of experimental tests, for one defined point in a structure, as shown in Figure 3.1. KINTEMP takes into account the composition of the concrete mixture, the boundary conditions such as the fresh concrete temperature, the transition conditions (type of formwork; environmental temperature) and the geometry of structure. The concrete mixture can be optimized according to the national standard code using the additional module BEPRO. Basis for the calculations in KINTEMP is the date when hydration starts as well as 12 hours and 72 hours values of the hydration heat of the used cement. The calculated temperature profile (Figure 3.2; see also Figure 3.3 to Figure 3.5) due to hydration is then the basis for the calculations in KINFEST.

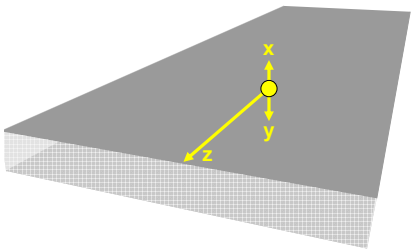

Figure 3.1: Orientation of coordinate system in KINTEMP

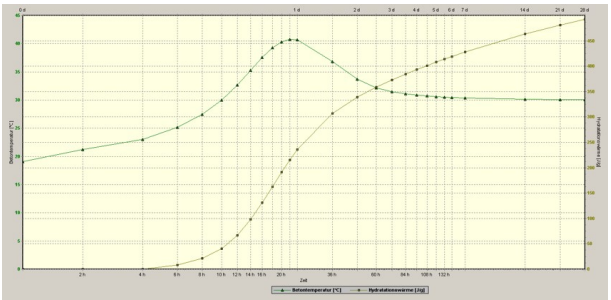

Figure 3.2: Hydration development and calculated temperature profile from KINTEMP

KINFEST calculates the hardening process as a function of time. Usually time steps from two hours up to 672 hours (28 days) are represented, as shown in Table 4.1 but also setting times up to 180 days can be represented. KINFEST is tested for nearly all kinds of cements and all kinds of additives, water-cement ratios from 0.20 to 1.00 and pore contents of fresh concrete from 0% to 12%. Concrete temperatures from $0°C$ to $80°C$ can be considered.

time in hours	2	4	6	8	...	336	504	672
compressive strength [MPa]	0.1	0.2	0.6	1.1	...	27.0	27.6	28.0

Table 3.1: Extract of predicted compressive strength values from KINFEST for C20/25 concrete in tabular form

Besides the compressive strength, KINFEST is able to calculate following material properties:

- tensile splitting strength
- bending tensile strength
- tensile strength
- Young's Modulus

Basis for calulations in KINFEST is the initial setting time and the value of two-days and of 28-days cement strength. The profiles of hydration heat development, hydration degree and strength development is always mathematically described as S-shaped.

In the following three parts, three different types of concrete has been investigated by using KINTEMP for the prediction of the hydration heat development and compared to experimental measurements. These mixture are:

- a common C20/25 concrete
- a C20/25 concrete with steel fibres
- Terraplan concrete

Terraplan is a self-developed concrete by the Dyckerhoff company, which is based on a CEM I 42.5 R white cement according to DIN EN 206:2017-01 (2017). This concrete permits to generate a Terrazo-like surface when it is grinded. Terraplan is able to develop high strengths at the early age.

Temperature development of C20/25 concrete

As previously mentioned, the temperature profile of the hydration heat development represents an important input information for the prediction of the material properties in KINFEST. To this reason, measurements of the hydration heat development were carried out on polystyrene-cubes for the three different types of concrete used: C20/25 concrete; C20/25 concrete with steel fibres; Terraplan concrete.

For the C20/25 concrete, the maximum temperature of the average value from the measurements was recorded after 16.0 hours (see Figure 3.3). The maximum temperature measured was $38.0°C$. The maximum temperature, predicted by KINTEMP was $38.0°C$, recorded after 18.0 hours. The predicted and the measured temperature profile of the hydration heat development show a good agreement, as well in the value of the maximum temperature as in the time of occurrence.

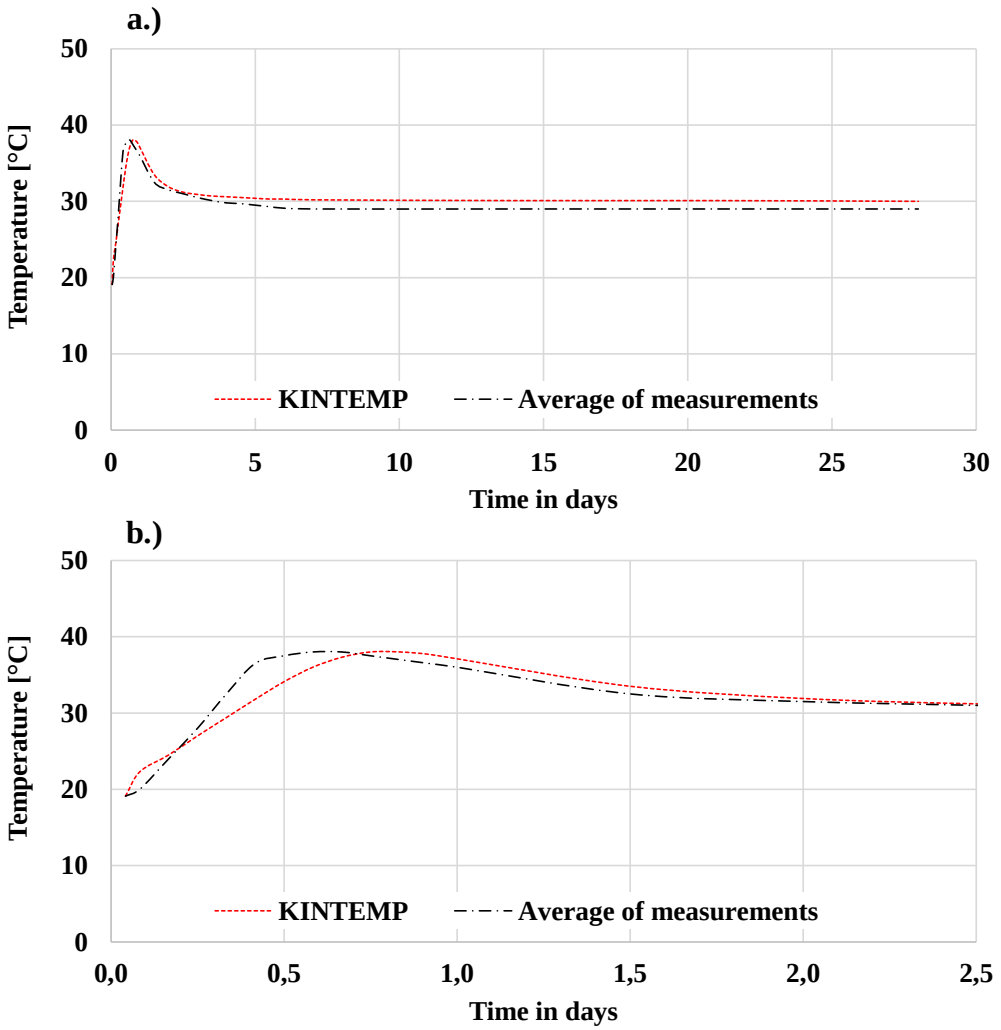

Figure 3.3: Measured hydration heat development versus predicted hydration heat development by KINTEMP for a C20/25 concrete*
a.) Temperature profile for a period of 28 days
b.) Temperature profile for the first 2.5 days with maximum temperature
*the boundary conditions has been changed after this test from 30°C and 50% relative humidity to 20°C and 50% relative humidity

Temperature development of C20/25 concrete with steel fibres

In Figure 3.4, the hydration heat development of a C20/25 concrete with steel fibres is represented. The maximum temperature within the three tests was recorded after 16.1 hours with a value of 38.8°C. KINTEMP predicted a maximum temperature of 40.3°C after 20.0 hours. The prediction in KINTEMP shows a deviation of 3.8% for the maximum temperature, the time of occurrence varies 3.9 hours. Thus, the predicted

temperature profile shows a good correlation compared to the measured values.

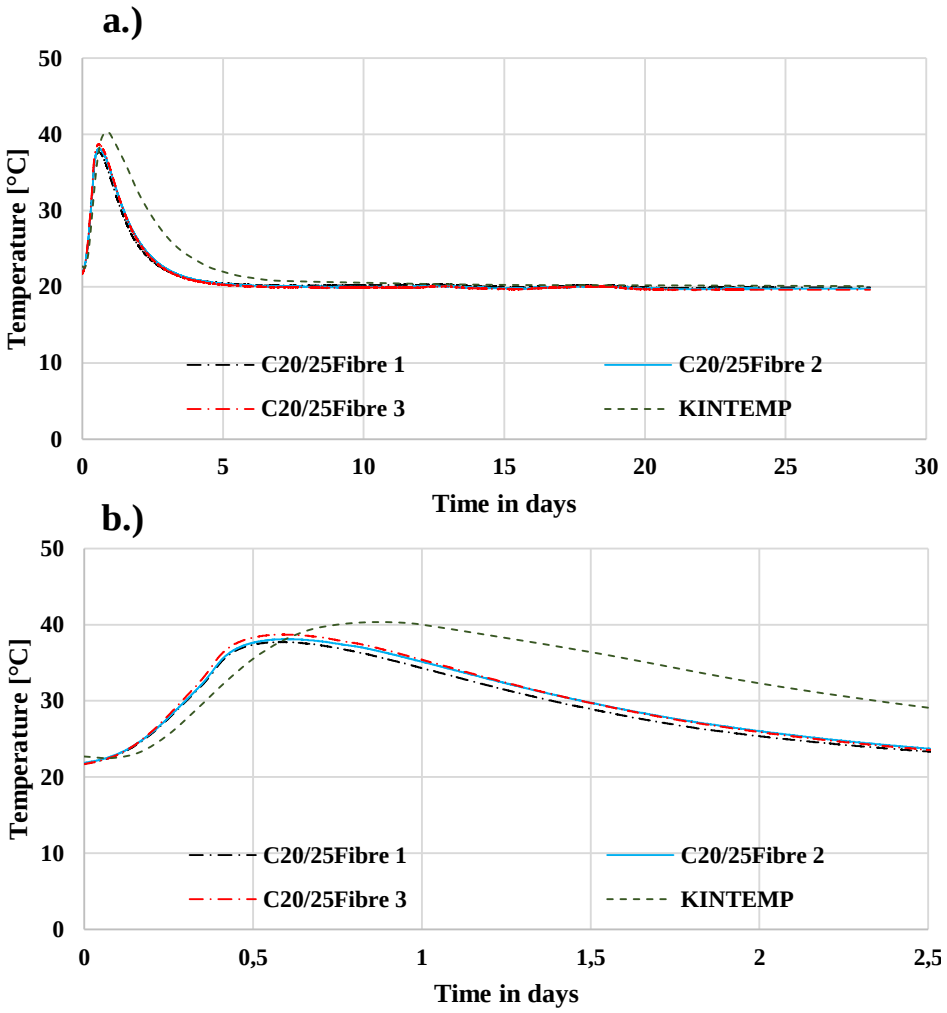

Figure 3.4: Measured hydration heat development versus predicted hydration heat development by KINTEMP for a C20/25 concrete with steel fibres
a.) Temperature profile for a period of 28 days
b.) Temperature profile for the first 2.5 days with maximum temperature

Temperature development of Terraplan concrete

As well as for the C20/25 concrete and for the C20/25 concrete with steel fibres, shows the predicted temperature profile by KINTEMP an excellent accordance to the measured values of the hydration heat development. The maximum temperature predicted by KINTEMP was after 7.0 hours with a value of 52.6°C (see Figure 3.5). During the

measurements, a maximum temperature of 50.7°C was recorded after 5.2 hours. The predicted and the measured maximum temperature varies only 3.8%. The predicted temperature profiles of the hydration heat development as well as the measured values serves as a good basis for the calculation of the material properties.

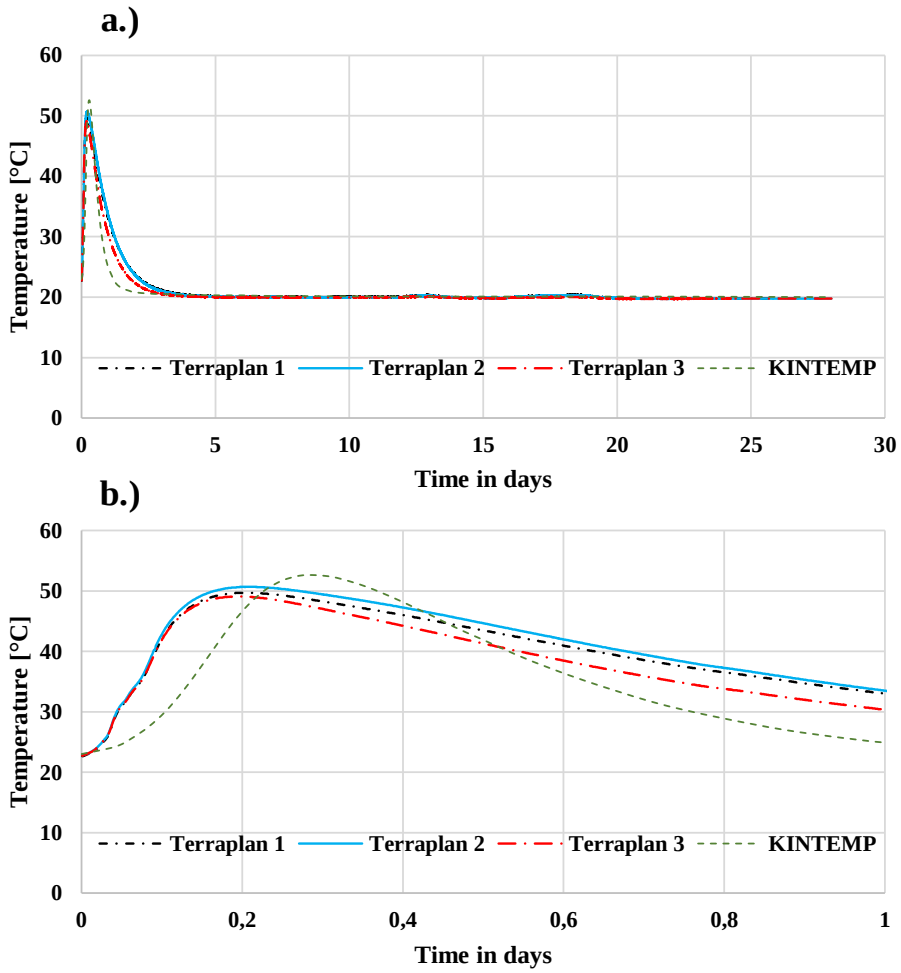

Figure 3.5: Measured hydration heat development versus predicted hydration heat development by KINTEMP for a Terraplan concrete
a.) Temperature profile for a period of 28 days
b.) Temperature profile for the first day with maximum temperature

3.2.2 Compressive strength according to DIN EN 1992-1-1:2011-01

The compressive strength is one important indicator for the choice of the appropriate concrete mixture as the tensile strength directly depends on it. There are different pos-

sibilities to determine or predict compressive strength. First of all, compressive strength can be determined with the compressive strength test according to DIN EN 1992-1-1:2011-01 (2011). In general, two different kinds of specimen can be used, cylinders and cubes. The dimensions of cylinder are ∅ 150 mm × 300 mm and the dimensions of cubes are 150 mm × 150 mm × 150 mm.

Figure 3.6: Compression testing machine

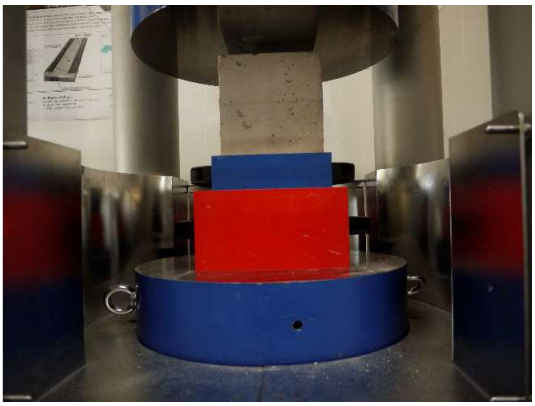

Figure 3.7: Cube before compressive test

For the tests in this work, cubes were used because of the sake of simplicity. For cylinders, their bottom and top side must be smoothed before testing whereas for cubes due to their form-work two plane-parallel smooth surfaces are available.

The compressive strength is calculated with equation 3.1. Here, six series of compressive strength tests were performed respectively after 2 days, 7 days and 28 days.

$$f_{ck} = \frac{F}{A_c} \quad [MPa] \tag{3.1}$$

f_{ck}: characteristic compressive strength [MPa]
F: maximum applied Force [N]
A_c: cross section [mm^2]

Another possibility to predict compressive strength is using the approach according to DIN EN 1992-1-1:2011-01 (2011) and Fédération internationale du béton (2013), as described with equation 3.2.

$$f_{cm}(t) = 1.25 \cdot f_{cm} \cdot e^{s \cdot [1 - \sqrt{28/t}]} \quad [MPa] \tag{3.2}$$

1.25: calculation factor for cube compressive strength
f_{cm}: average cylinder compressive strength after 28 days [MPa]
t: concrete age in days
s: hardening coefficient of cement type due to table 3.2.2

type of cement due to DIN EN 197-1:2011-11 (2011)	s
CEM III, CEM I (32.5 N), CEM II/B-S (42.5 N)	0.38
CEM II (32.5 R; 42.5 N; 42.5 R), CEM I (32.5 N; 32.5 R; 42.5 N)	0.25
CEM I (42.5 R; 52.5 N; 52.5 R)	0.20

Table 3.2: Hardening coefficient s of cement type due to DIN EN 197-1

The disadvantage of the previous approach is, that environmental temperature influence cannot be considered. These effects are respected by the prognosis software KINFEST which is able to take into consideration the environmental temperature and to predict the strength development for the first hours up to 180 days.

The results of the compressive strength tests are compared to values produced by KINFEST and to values calculated according to DIN EN 1992-1-1:2011-01 (2011). The boundary conditions in all tests were identical (20°C; 50%).

C20/25 concrete

In Figure 3.8 the values predicted by KINFEST and the results from the six experimental test series were compared. The results can be seen in Figure 3.8 and in Table 3.4. After one day, the prognosis of KINFEST compared to the average value of the measurements show a deviation of 3.7%, whereby KINFEST overestimates the measured values. After seven days, the predicted and the average of the measured values of the compressive strength agree. After 28 days, the predicted values in KINFEST overestimate the average measured values. The deviation from KINFEST to the measurements is 4.4%. The prognosis software KINFEST describes very precisely the strength development of the C20/25 concrete. The composition of the C20/25 concrete can be seen in Table 3.3.

Table 3.3: Material weights (kg/m^3)

Rhine Sand	Gravel 2/8	Gravel 8/16	CEM II/A LL 42.5 N	Water
671.7	218.5	924.5	300.0	196.0

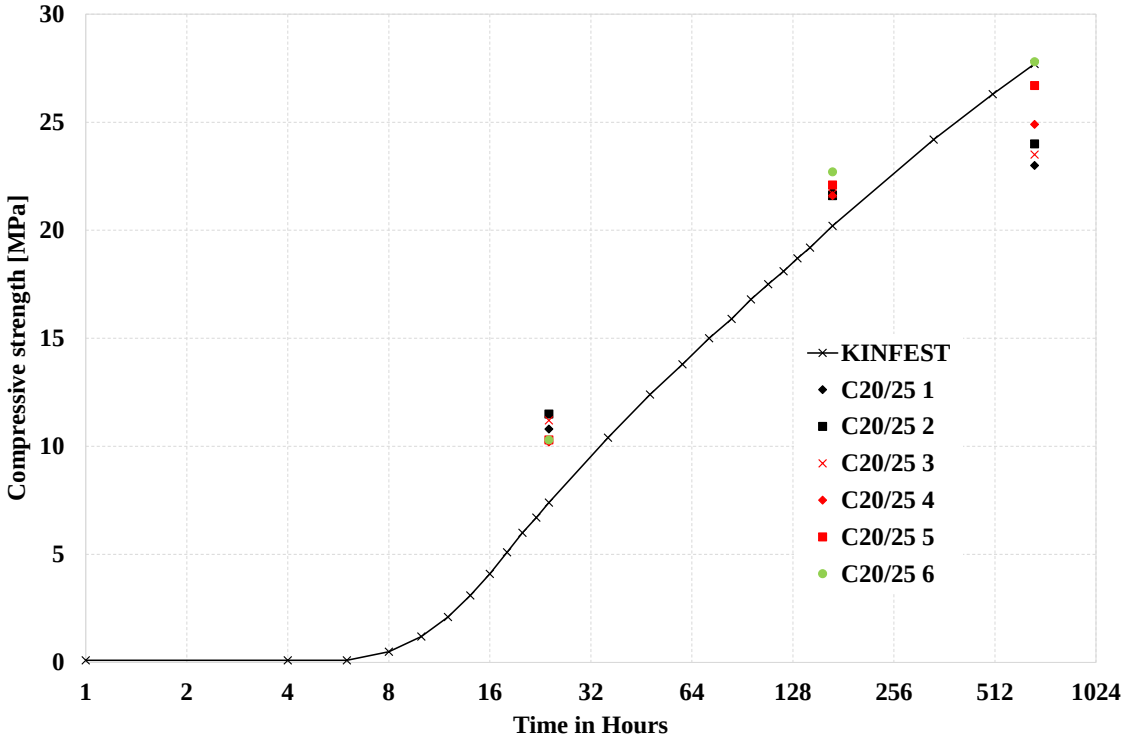

Figure 3.8: Predicted and measured compressive strength of C20/25 concrete

C20/25 concrete with steel fibres

Figure 3.9 and Table 3.6 shows the compressive strength development of a C20/25 concrete with steel fibres predicted by KINFEST versus the actual measured values. After one day, the prognosis of KINFEST deviates from 14.0% to the average value of the three test series. At the time two days, the predicted value of KINFEST and the average value of the measurements vary from 8.8% and after seven days they vary from 12.2%. In all these three cases, KINFEST overestimates the actual measured values. After 28 days, KINFEST underestimates the average value of the compressive strength from 6.5%. The reason, why the predicted values and the measured values vary such strong, can be due to the fact, that KINFEST does not consider fibres in the concrete. The steel fibres used (Arcelor Mittal), have a diameter of 1.0 mm and a length of 50

Table 3.4: Results from compressive strength test of C20/25 concrete versus predicted values by KINFEST and predicted values by DIN EN 1992-1-1:2011-01 (2011)

Time	[h]	24	168	672
$C20/25_{1-I}$	[MPa]	10.8	21.8	23.0
$C20/25_{2-I}$	[MPa]	11.5	21.6	24.0
$C20/25_{3-I}$	[MPa]	11.2	21.7	23.5
$C20/25_{1-II}$	[MPa]	10.2	21.6	24.9
$C20/25_{2-II}$	[MPa]	10.3	22.1	26.7
$C20/25_{3-II}$	[MPa]	10.3	22.7	27.8
Average ø	**[MPa]**	**10.7**	**21.9**	**25.0**
KINFEST	[MPa]	11.1	21.9	26.1
Δ KINFEST to ø	[%]	-3.7	$\pm$ 0.0	-4.4

mm. Both ends of the steel fibre are cranked S-shaped.

Table 3.5: Material weights (kg/m^3)

Rhine Sand	Gravel 2/8	Gravel 8/16	CEM II/A LL 42.5 N	Water	Steel fibre
667.0	216.0	919.0	300.0	196.0	30.0

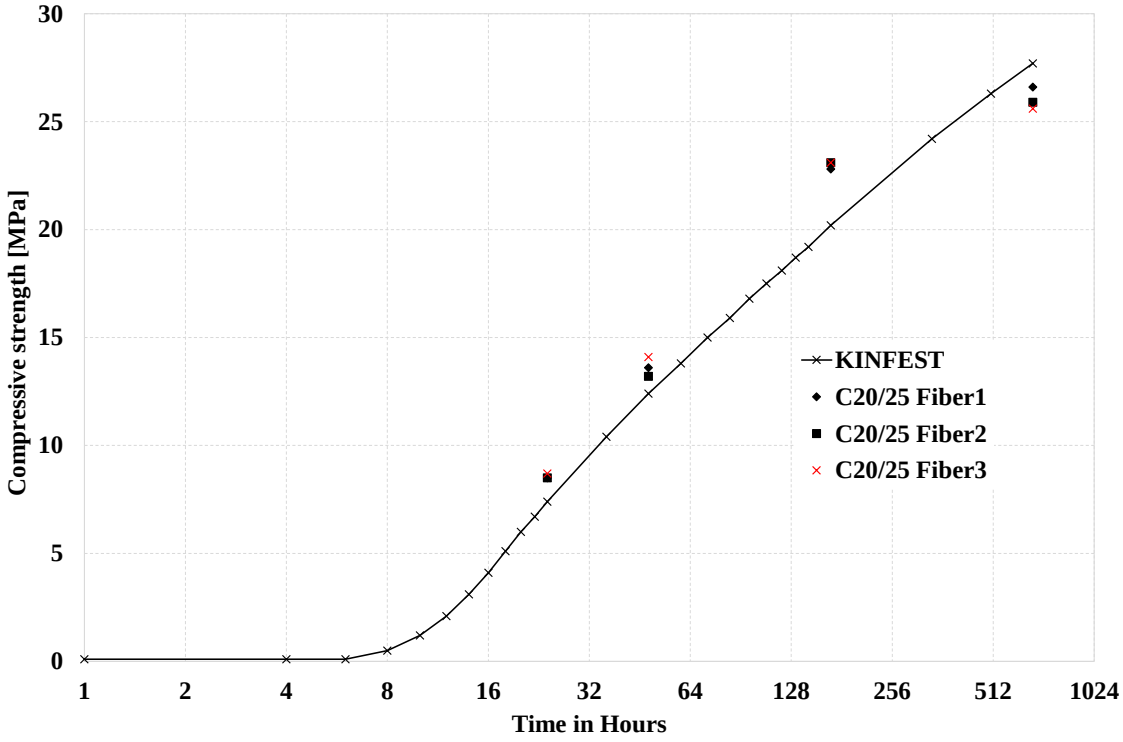

Figure 3.9: Predicted and measured compressive strength of C20/25 concrete with steel fibres

Table 3.6: Results from compressive strength test of C20/25 concrete with steel fibres versus predicted values by KINFEST

Time	[h]	24	48	168	672
$C20/25_{Fiber1}$	[MPa]	8.5	13.6	22.8	26.6
$C20/25_{Fiber2}$	[MPa]	8.5	13.2	23.1	25.9
$C20/25_{Fiber3}$	[MPa]	8.7	14.1	23.1	25.6
Average ø	**[MPa]**	**8.6**	**13.6**	**23.0**	**26.0**
KINFEST	[MPa]	7.4	12.4	20.2	27.7
Δ KINFEST to ø	[%]	+14.0	+8.8	+12.2	-6.5

Terraplan

The predicted values of the compressive strength by KINFEST for the Terraplan concrete and the results from the six test series are shown in Figure 3.10 and in Table 3.7. The predicted values after one day, show a deviation of 1.9% to the average of the measured values. After seven days, the difference of the predicted compressive strength of KINFEST to the average of the measurements is only 0.2%. In both cases, the prediction of KINFEST underestimates the actual values slightly. At the time 28 days, a deviation of 1.2% was recorded, whereby the predicted values of KINFEST overestimate the average of the measured values. All in all, the predicted compressive strength development from KINFEST gives excellent results.

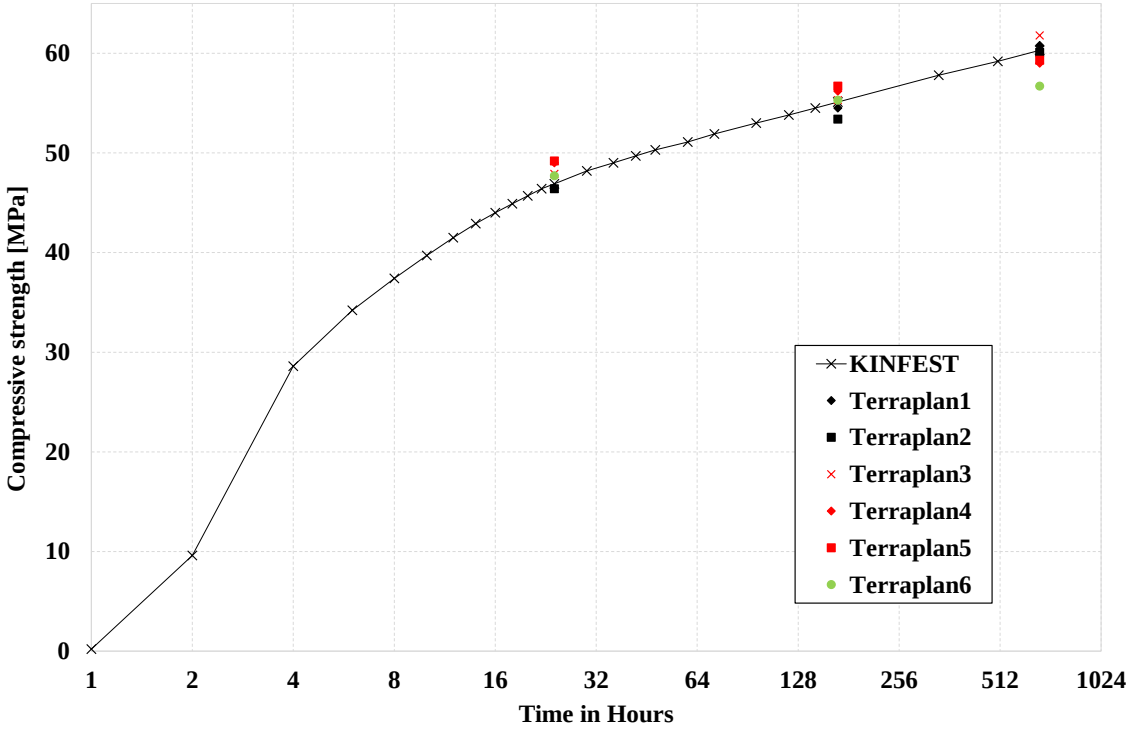

Figure 3.10: Predicted and measured compressive strength of Terraplan concrete with steel fibres

Table 3.7: Results from compressive strength test of Terraplan concrete versus predicted values by KINFEST

Time	[h]	24	168	672
$Terraplan_{1-I}$	[MPa]	46.5	54.5	60.8
$Terraplan_{2-I}$	[MPa]	46.4	53.4	60.1
$Terraplan_{3-I}$	[MPa]	47.9	55.3	61.8
$Terraplan_{1-II}$	[MPa]	49.0	56.2	59.0
$Terraplan_{2-II}$	[MPa]	49.2	56.7	59.3
$Terraplan_{3-II}$	[MPa]	47.7	55.3	56.7
Average ø	**[MPa]**	**47.8**	**55.2**	**59.6**
KINFEST	[MPa]	46.9	55.1	60.3
Δ KINFEST to ø	[%]	+1.9	+0.2	-1.2

3.2.3 Young's Modulus according to DIN EN 12390-13:2014-06

For simulation of concrete, Young's Modulus is another important parameter which also depends on an evolving strength development. To determine Young's Modulus, tests can be carried out or/and the prognosis values of KINFEST can be used.

Young's Modulus (E) is the relation between stress and strain and describes material's behaviour within the limits of linear elasticity (see Figure 3.11). For concrete, a linear relationship between stresses and strains can be assumed up to a compression stress level of 40% of the ultimate compression stress.

Young's Modulus is defined according to equation 3.3:

$$E = \frac{F \cdot (l - l_0)}{A \cdot l_0} = constant \quad [MPa] \tag{3.3}$$

F: Force [N]
A: cross section [mm^2]
l: deformed length, length of the deformed specimen [mm]
l_0: initial length [mm]

With $\sigma = F/A$, and with $\Delta l = l - l_0$ and $\varepsilon = \Delta l / l_0$, equation 3.3 can be written to:

$$E = \frac{\sigma}{\varepsilon} = constant \quad [MPa] \tag{3.4}$$

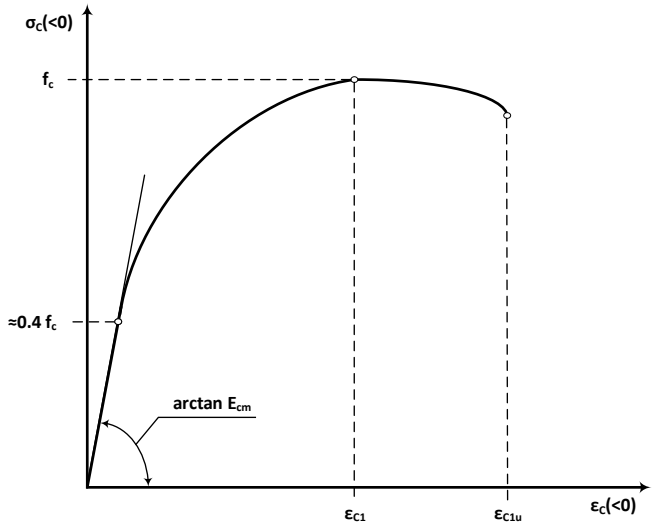

Figure 3.11: Stress strain diagram of concrete

Besides mentioned equation 3.4 to calculate Young's Modulus, Young's Modulus can be determined according to DIN EN 1992-1-1:2011-01 (2011) with a cyclic test as seen in Figure 3.12.

Figure 3.12: Cylindrical specimen

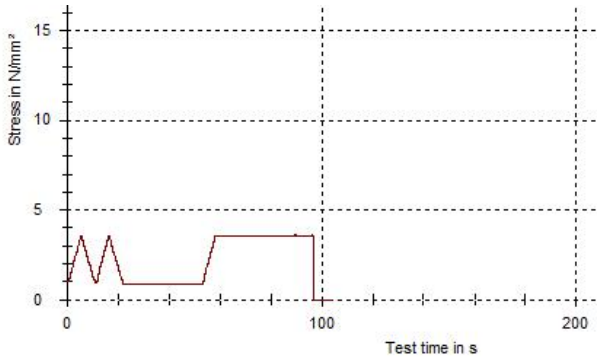

Figure 3.13: Cyclic Young's Modulus test

During the cyclic testing, upper-stress level is measured as well as strain level at fixed intervals (see Figure 3.13). According to this test set-up, Young's Modulus is calculated using equation 3.5.

$$E_c = \frac{\sigma_{c,o} - \sigma_{c,u}}{\varepsilon_{c,o} - \varepsilon_{c,u}} \quad [MPa] \tag{3.5}$$

$\sigma_{c,o}$: upper test stress $(1/3 \cdot f_{c,e})$ [MPa]
$f_{c,e}$ = expected compressive strength [MPa]
$\sigma_{c,u}$: 0.5 [MPa]
$\varepsilon_{c,o}$: strain after third load [-]
$\varepsilon_{c,u}$: strain after second relieve [-]

The test result must be declared with an accuracy of 100 [MPa].

The second possibility to determine Young's Modulus is the analytical approach of DIN EN 1992-1-1:2011-01 DIN EN 1992-1-1:2011-01 (2011), as given in equation 3.6.

$$E_{cm}(t) = [f_{cm}(t)/f_{cm}]^{0.3} \cdot E_{cm} \quad [MPa] \tag{3.6}$$

$f_{cm}(t)$: medium compressive strength [MPa]
f_{cm}: medium compressive strength after 28 days [MPa]
E_{cm}: medium Young's Modulus after 28 days [MPa]

C20/25 concrete

The results of the prognosis of KINFEST and the measured values are shown in Figure 3.14 and in Table 3.8. In total, three series of Young's Modulus tests were performed on the C20/25 concrete. The tested cylinders for the C20/25 concrete, and in the following also for the C20/25 concrete with steel fibres and for the Terraplan concrete, have a diameter of 150 mm and a height of 300 mm. The specimens were stored in a climate chamber at $20°C$ and 50% relative humidity. The respective Young's Modulus was tested according to DIN EN 12390-13:2014-06 (2014).

At the time two days, the average of the measurements deviates from the predicted values by 29.8%. The prognosis from KINFEST overestimates the actual measured values. After seven days, again an overestimation of KINFEST by 14.4% to the average value of the measurements of Young's Modulus can be regarded. The predicted values by KINFEST after 28 days deviates by 7.8% to the average value of the measurements. The influence of these strong deviations has to be investigated within calculation in the finite element program.

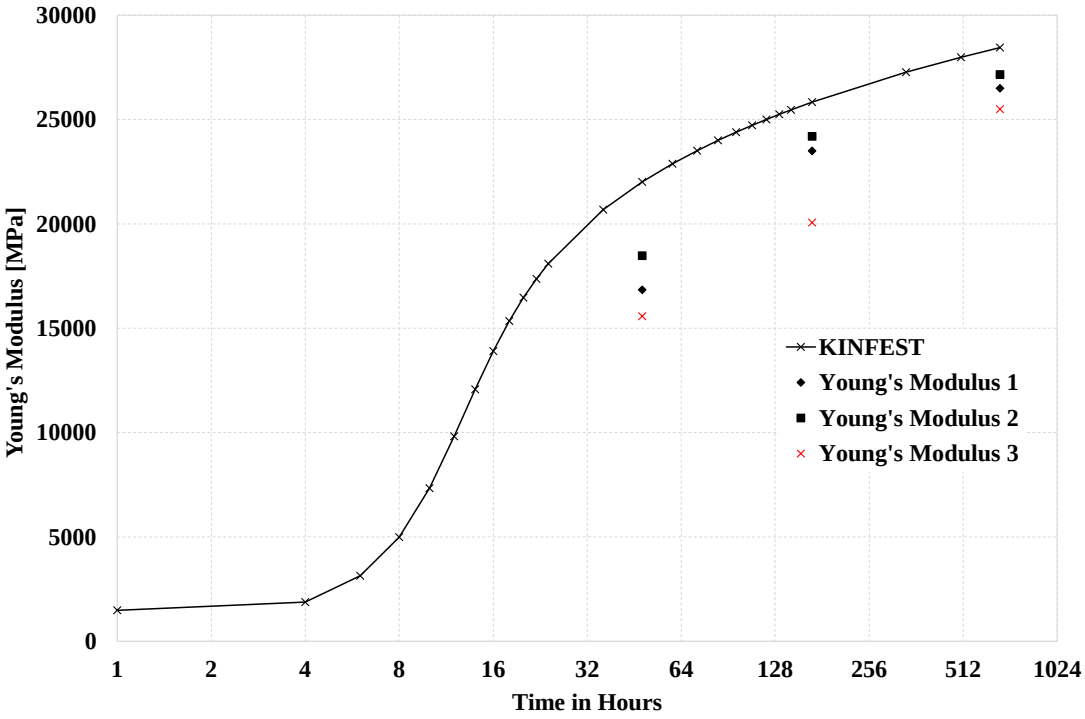

Figure 3.14: Predicted and measured Young's Modulus of C20/25 concrete

Table 3.8: Results from Young's Modulus test of C20/25 concrete versus predicted values by KINFEST

Time	[h]	48	168	672
$C20/25_1$	[MPa]	15570	20063	25501
$C20/25_2$	[MPa]	16847	23499	26494
$C20/25_3$	[MPa]	18476	24192	27160
Average ø	**[MPa]**	**16964**	**22585**	**26385**
KINFEST	[MPa]	22015	25834	28449
Δ KINFEST to ø	[%]	-29.8	-14.4	-7.8

C20/25 concrete with steel fibres

The results of the measured values of Young's Modulus for a C20/25 concrete with steel fibres and the predicted values by KINFEST can be seen in Figure 3.15 and in Table 3.6. The deviation of the predicted values by KINFEST to the average of the measurements is 18.6%, after two days. Thereby, the prognosis software KINFEST overestimates the average value. After seven days, the deviation from KINFEST to the average value

of the measurements is only 2.0%. KINFEST overestimates the average value of the measurements again. At the time 28 days, KINFEST overestimates the average value of the measurements by 4.6%. The development of Young's Modulus of a C20/25 concrete with steel fibres gives very good results.

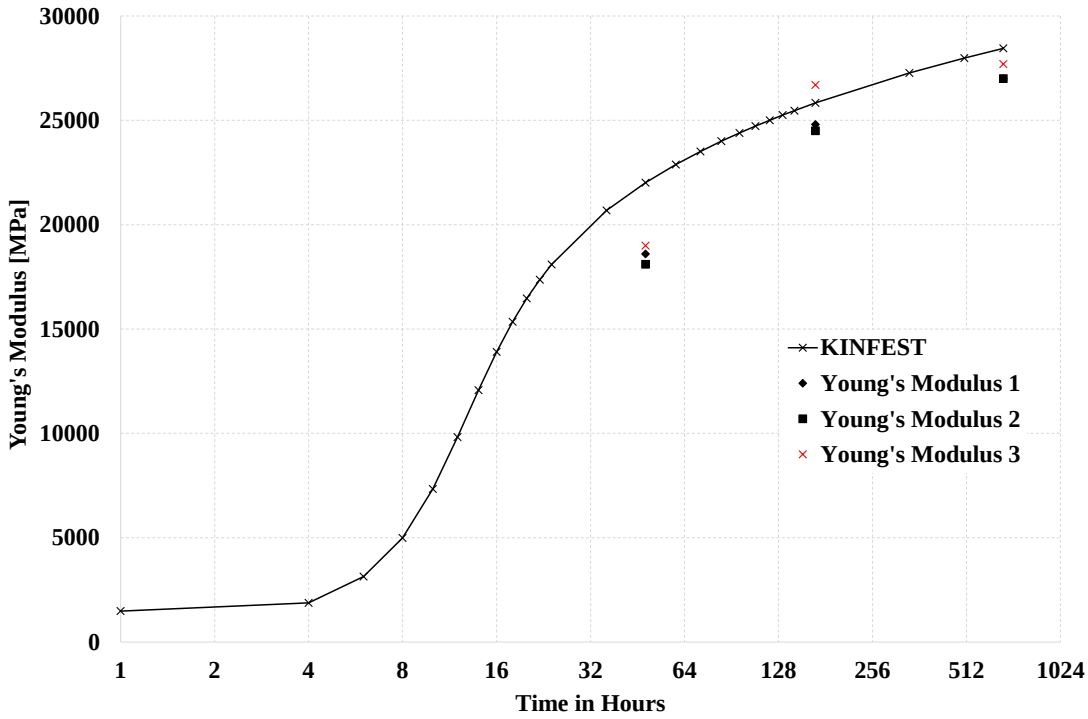

Figure 3.15: Predicted and measured Young's Modulus of C20/25 concrete with steel fibres

Table 3.9: Results from Young's Modulus test of C20/25 concrete with steel fibres versus predicted values by KINFEST

Time	[h]	48	168	672
$C20/25_{Fiber1}$	[MPa]	19000	26700	27700
$C20/25_{Fiber2}$	[MPa]	18600	24800	27000
$C20/25_{Fiber3}$	[MPa]	18100	24500	26900
Average ø	**[MPa]**	**18567**	**25333**	**27200**
KINFEST	[MPa]	22015	25834	28449
Δ KINFEST to ø	[%]	-18.6	-2.0	-4.6

Terraplan

The predicted values of Young's Modulus by KINFEST for the Terraplan concrete and the results from the three test series are shown in Figure 3.16 and in Table 3.10. The predicted development of Young's Modulus overestimates the actual value of the average of the measurements at each time step. The deviation after two days is 11.0%, after seven days 15.6% and after 28 days 17.2%.

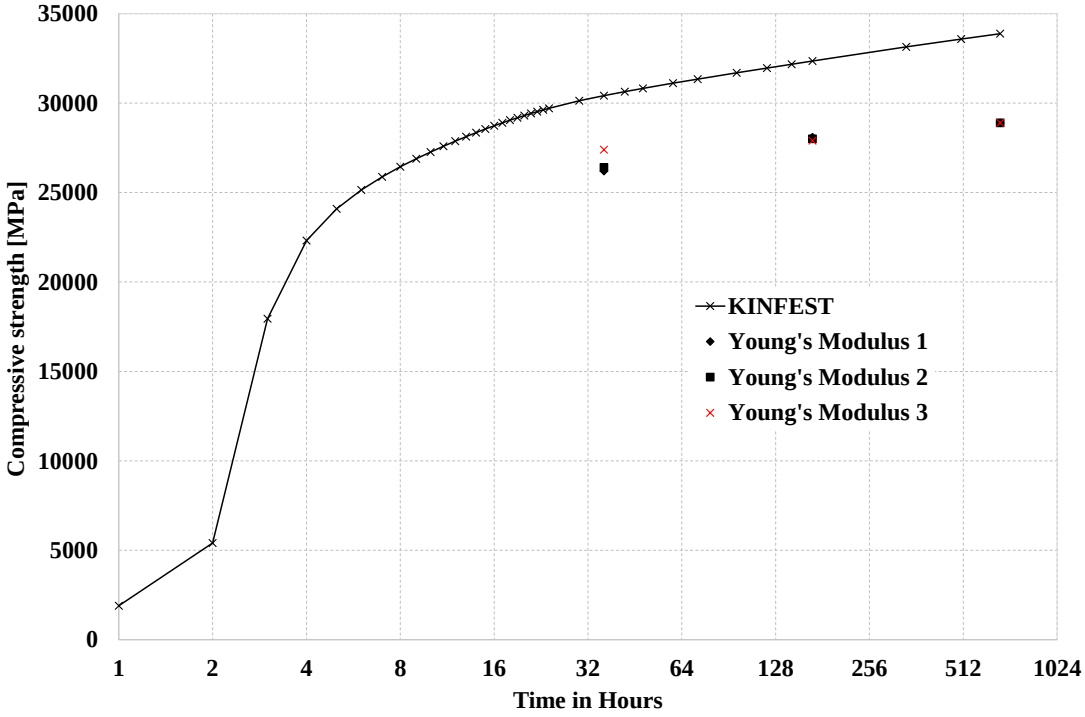

Figure 3.16: Predicted and measured Young's Modulus of Terraplan concrete

Table 3.10: Results from Young's Modulus test of Terraplan concrete versus predicted values by KINFEST

Time	[h]	48	168	672
$Terraplan_1$	[MPa]	27700	27900	28900
$Terraplan_2$	[MPa]	27800	28000	28900
$Terraplan_3$	[MPa]	27800	28100	28900
Average ø	**[MPa]**	**27767**	**28000**	**28900**
KINFEST	[MPa]	30824	32354	33879
Δ KINFEST to ø	[%]	-11.0	-15.6	-17.2

3.2.4 Uniaxial tensile strength

As the uniaxial tensile strength determines the cracking behaviour of fair-faced screeds is one of the most important parameters in the current study. It is used as failure criterion at the respective time step. Similar as for the compressive strength and Young's Modulus, the tensile strength can be predicted by KINFEST and by an analytical approach according to DIN EN 1992-1-1:2011-01 (2011). To test the tensile strength, different methods are available.
According to DIN EN 1992-1-1:2011-01 (2011), two different formulas are given to calculate the tensile strength.

$$f_{ctm}(t) = 0.30 \cdot f_{ck}(t)^{2/3} \quad [MPa] \tag{3.7}$$

$$f_{ctm}(t) = [\beta_{cc}(t)]^{\alpha} \cdot f_{ctm} \quad [MPa] \tag{3.8}$$

f_{ctm}:	medium tensile strength after 28 days [MPa]
$\beta_{cc}(t) =$	$e^{s \cdot [1-\sqrt{28/t}]}$
α:	1 for t $\leq$ 28 days
	2/3 for t $\geq$ 28 days
s	hardening coefficient see table 3.2.2

Apart from the predicted analytical values of the uniaxial tensile strength and apart from the prognosis values of the uniaxial tensile strength from KINFEST, a test set-up to determine the uniaxial tensile strength was developed.

Usually, the uniaxial tensile strength test is carried out while at both ends of the specimen a device is glued, which is then clamped in the testing machine (see Akita et al. (2003), Wu et al. (2012) and dos Santos and Rodrigues (2016)). The disadvantage of this method is that it cannot be applied to test the tensile strength at early age. Another method consists in inserting an anchoring at the ends of the specimen as described in Alhussainy et al. (2016), Choi et al. (2014) and in Shen et al. (2016), or in testing the specimen in a horizontal lying direction as described in Roziere et al. (2015). But these methods are very extensive.

A better way to test the uniaxial tensile strength is to clamp both ends of the specimen with the use of a special device (see Graybeal and Baby (2013) and Brameshuber (2016)). The form of the developed specimen is given in Figure 3.17. The specimen has a total length of 500 mm and a width at the ends of the specimen of 100 mm. The middle edge parallel area of the specimen has a constant cross section of 50 mm × 50 mm.

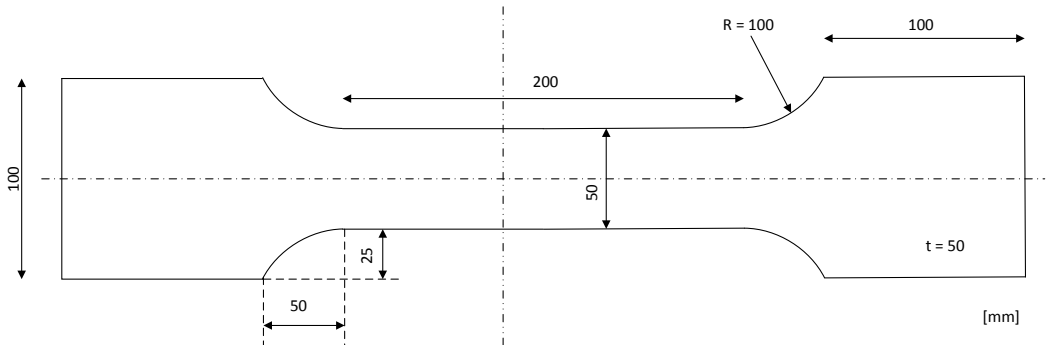

Figure 3.17: Drawing and dimensions of the tensile specimen

Using the clamping device (Figure 3.18 and Figure 3.19) it was possible to test the concrete used at the very early time of only eight hours. The test speed was 0.4 mm/min, the specimen was tested until failure (see Figure 3.20). The results of the three test series of this very simple but effective tensile strength test are shown in Figure 3.21.

The results of the tensile strength tests are compared to the results of the prognosis of the analytical approach according to DIN EN 1991-1-1:2002 + AC:2009 (2009) and to the predicted values by KINFEST.

The earliest time to test the concrete specimen was after eight hours. The values of the tests range between the results of the prognosis software KINFEST and the analytical prognosis values of the standard.

After 48 hours, the results from the tests lie between the prognosis of KINFEST and the predicted values of DIN EN 1992-1-1, where the highest values meet the prognosis of KINFEST and the lowest values are close to the values predicted by DIN EN 1992-1-1. After 144 hours (7 days), the values from DIN EN 1992-1-1 as well as the values of KINFEST are close to the test results. After 336 hours (14 days) and after 672 hours (28 days) the test results agree very well with the prognosis values of DIN EN 1992-1-1 and KINFEST. It is worth noting that the profiles of the prognosis of DIN EN 1992-1-1 and the profile of the predicted values of KINFEST approach at this time.

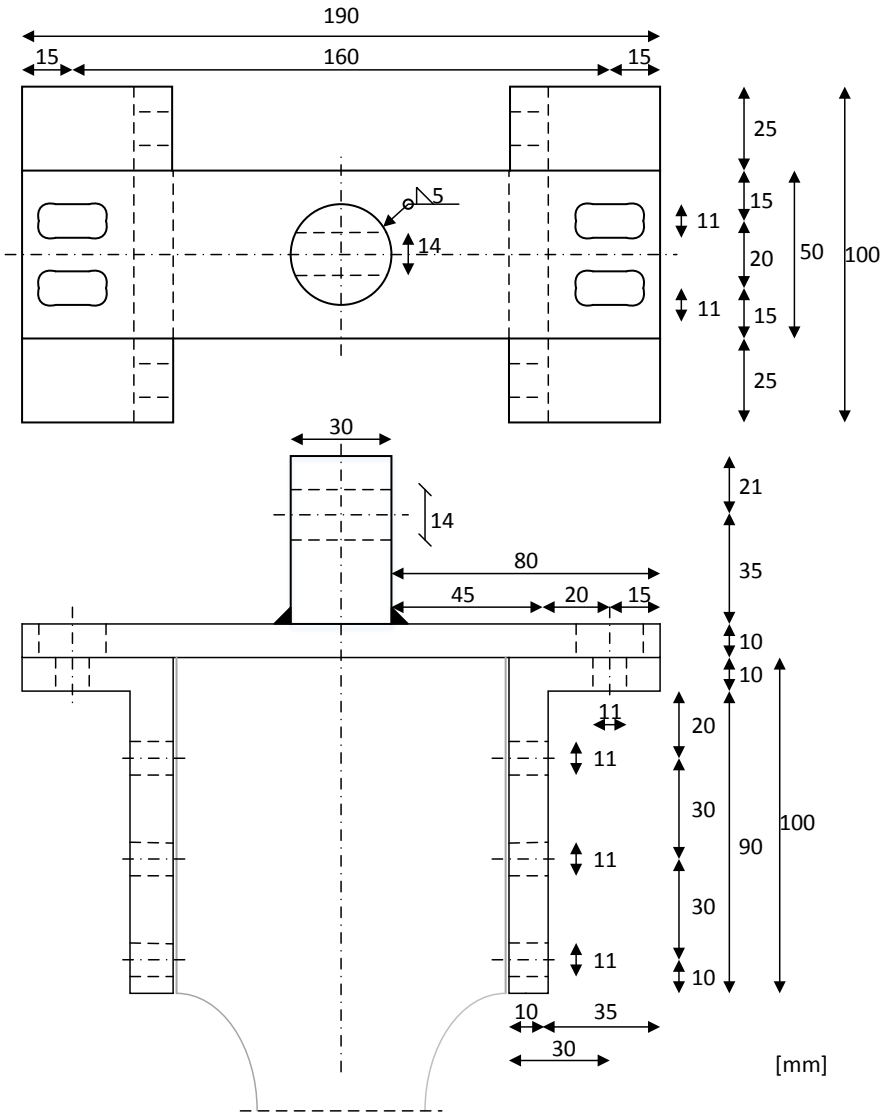

Figure 3.18: Drawing of the clamping device to test the tensile strength

Figure 3.19: Clamping device fixed at one end of the tensile specimen

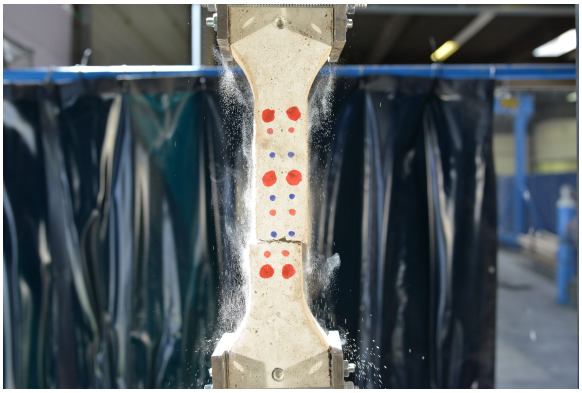

Figure 3.20: Tensile specimen at the moment of tensile failure

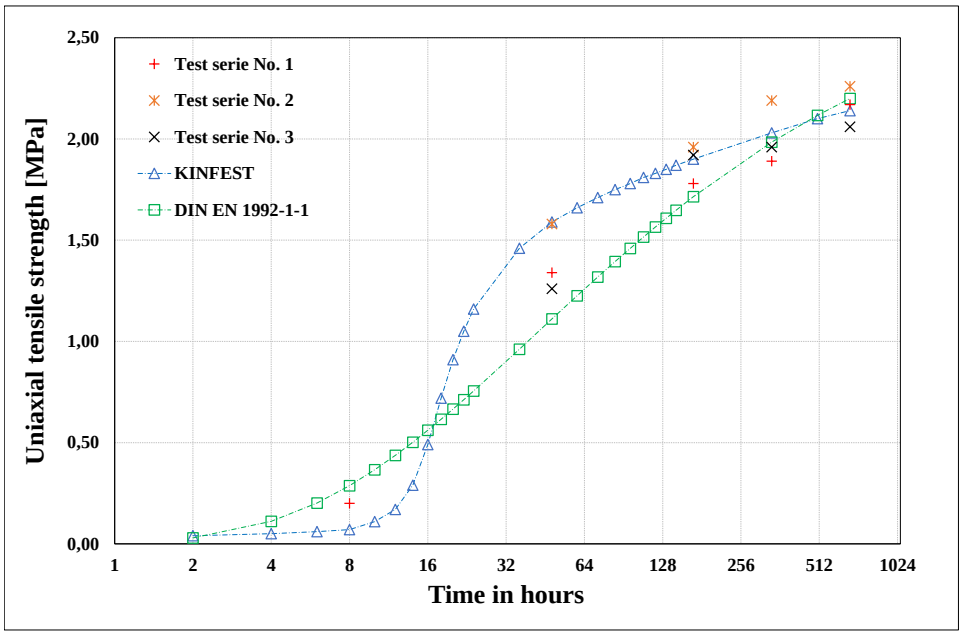

Figure 3.21: Measured values from three test series versus prognosis values of tensile strength from KINFEST and DIN EN 1992-1-1:2011-01 (2011)

3.3 Hygric properties

3.3.1 Shrinkage

Shrinkage was already mentioned in Chapter 2.2.3. Within the test series, the degree of shrinkage was determined by a test setup using a shrinkage drain and the results were compared to the analytical approach according to DIN EN 1992-1-1:2011-01 (2011) and Fédération internationale du béton (2013). In total, three shrinkage drains (Figure 3.22) were filled with the concrete which has been used later for all the analysis. The shrinkage drains have the following dimensions: length 1000 mm × width 100 mm × height 60 mm. To reduce the sliding contact between concrete and the steel drain, a neoprene layer was inserted. The concrete is fixed in the drain with steel hooks, whereby one side of the shrinkage drain is movable. The movable end of the shrinkage drain is in touch with a displacement transducer which records all displacement within a range of 2 mm (Figure 3.23). This ensures a constant measuring during the whole period of the test. The sample rate during the test was one value every two minutes. The shrinkage drains were stored in one room, in which temperature and humidity were recorded during the whole test period (see Figure 3.24).

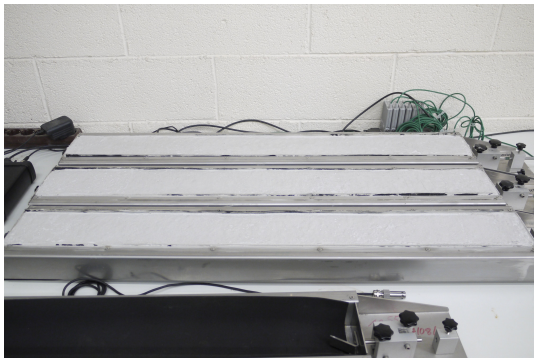

Figure 3.22: Shrinkage drain

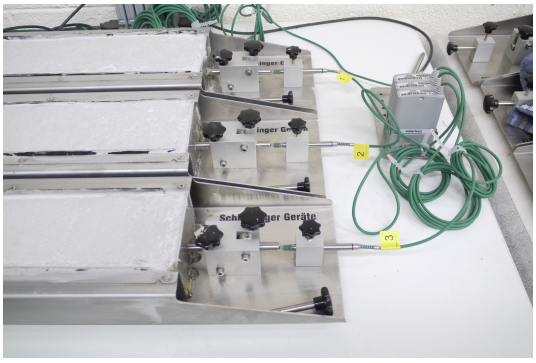

Figure 3.23: Displacement transducer

In the following, the results from the tests, respectively from the shrinkage drains are compared to the analytical approach (see equation 3.9) according to DIN EN 1992-1-1:2011-01 (2011) and Fédération internationale du béton (2013). The different elements of the Formula have been already explained in Formula 2.7 and in 2.8 in Chapter 2.2.3.

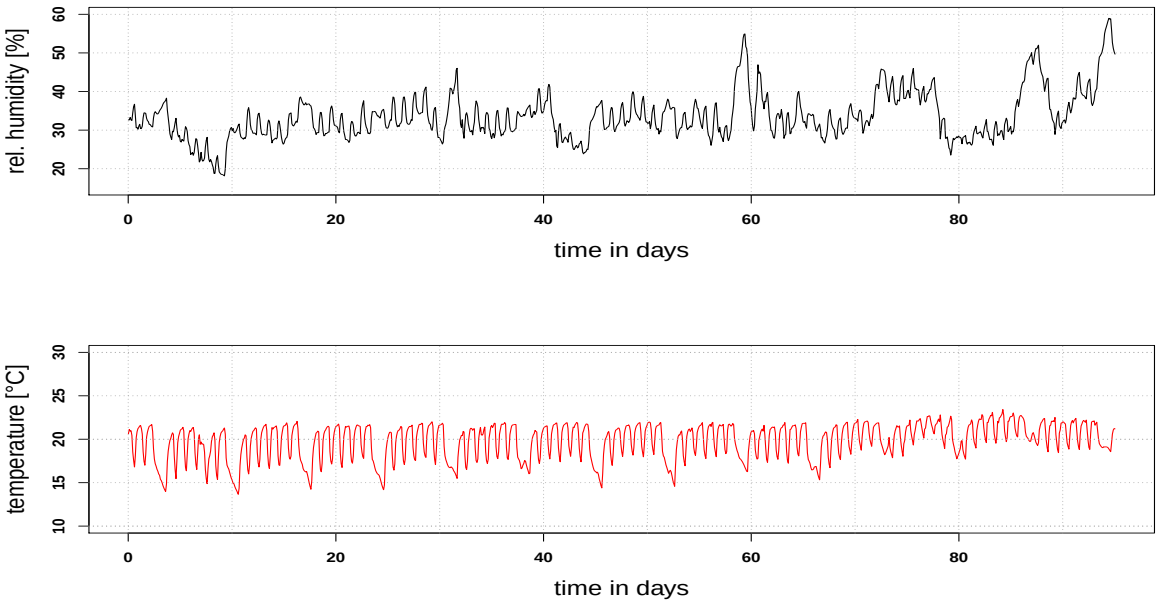

Figure 3.24: Recorded relative humidity and recorded temperature

$$\varepsilon_{cds}(t) = \varepsilon_{cd}(t) + \varepsilon_{ca}(t) \quad [-] \tag{3.9}$$

Figure 3.25 shows the predicted degree of shrinkage compared to the measured degree of shrinkage over a period of 95 days for a C20/25 concrete. Compared to the average values of shrinkage drains, the predicted values according to DIN EN 1992-1-1:2011-01 (2011) and Fédération internationale du béton (2013) show a very high accordance. As part of a design concept, the predicted values can be used without any restriction.

The same can be stated for the measured and predicted values for a Terraplan concrete, which can be seen in Figure 3.26. Here, in addition, a period of curing of concrete of seven days was taken into account.

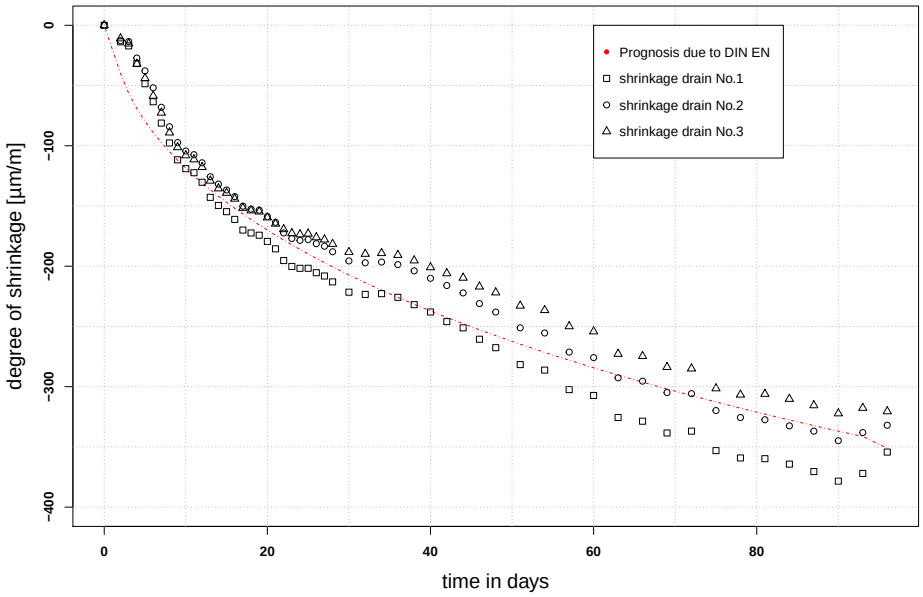

Figure 3.25: Measured and predicted degree of shrinkage

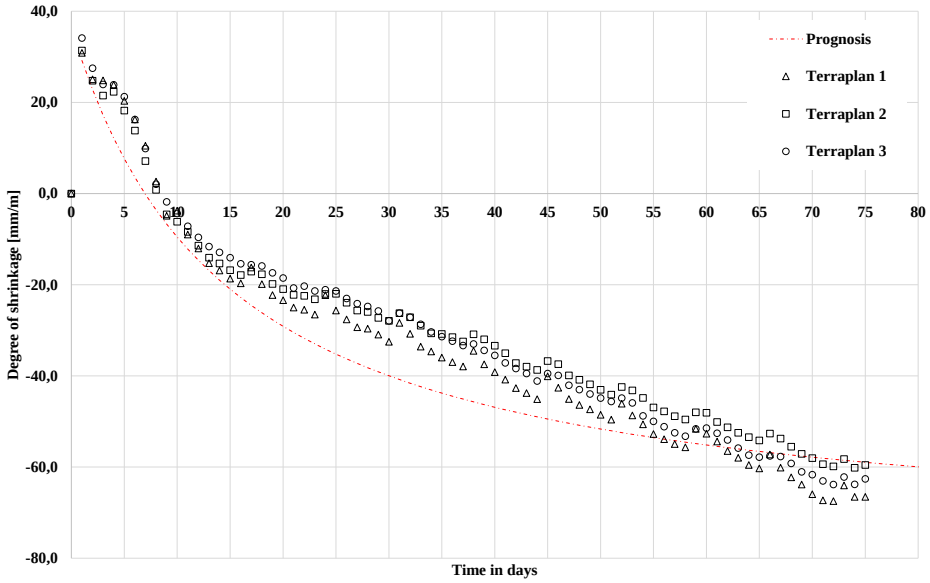

Figure 3.26: Measured and predicted degree of shrinkage of Terraplan concrete

3.3.2 Moisture release

To have an order of magnitude of the moisture release, humidity sensors were encased in a C20/25 concrete as shown in Figure 3.27. For this purpose the sensors (see Figure 3.28) were placed in the joint between the base plate and the concrete (see Figure 3.29). The used sensors are in-house developed sensors of University of Luxembourg. The dimensions of the sensors are 2.0 cm of width, 1.5 cm of length and 1.0 cm of thickness. The accuracy of measuring is $\pm$ 2.0 $°C$. The measurements were carried out over a period of 28 days and started four hours after addition of water.

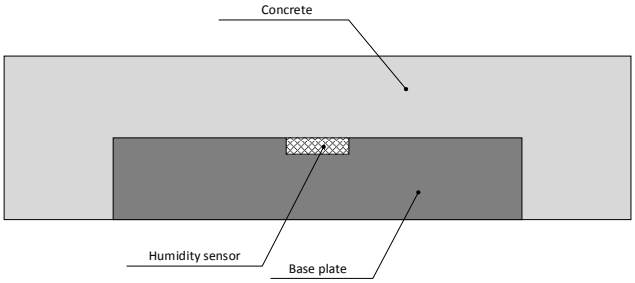

Figure 3.27: Schematic drawing of the base plate with humidity sensor (side view)

After a rapid decrease of humidity, which could be observed within the first hours (see Figure 3.30 and Figure 3.31), humidity adjusts itself to a value of around 90%. This result corresponds to the findings of Avak and Glaser (2007). Measurements on construction components with a thickness of more than 50 cm showed, after years, a humidity inside the construction component of around 90%.

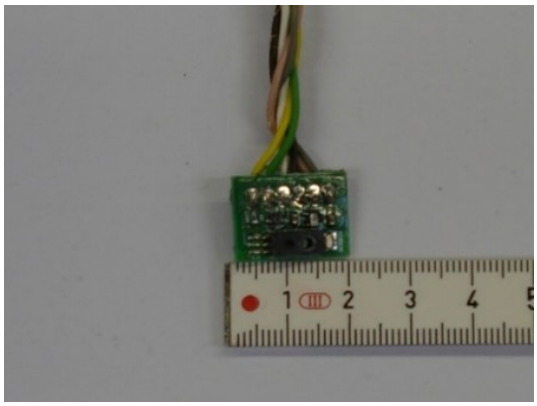

Figure 3.28: Temperature and humidity sensor

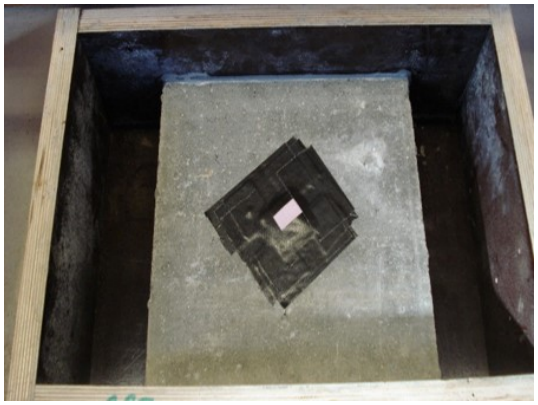

Figure 3.29: Placement of sensor

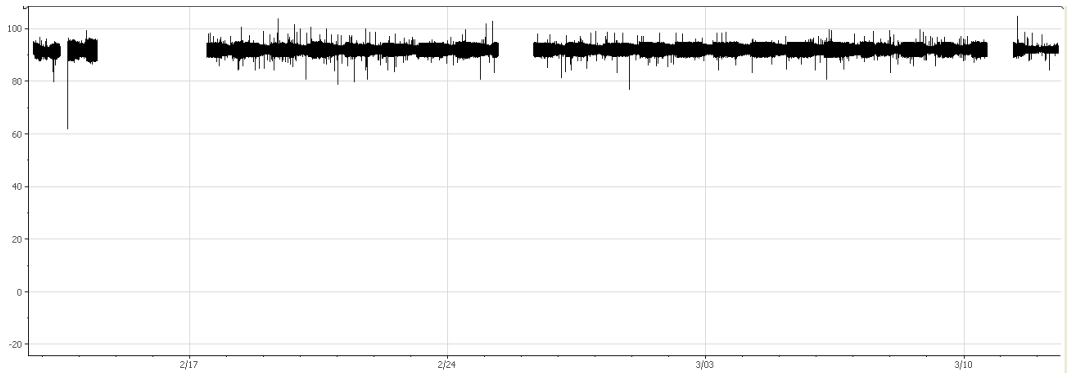

Figure 3.30: Results of sensor 11

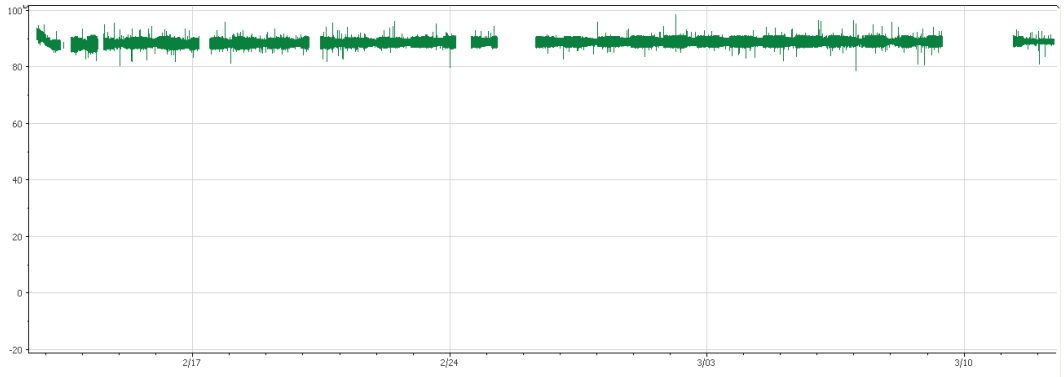

Figure 3.31: Results of sensor 12

3.4 H-shaped concrete specimen

The H-shaped concrete specimen is manufactured to understand the crack initiation and crack development of unreinforced concrete specimen induced by shrinkage. Using this specimen, the comparison between different types of concrete is possible. Furthermore, different environmental conditions, such as relative humidity and temperature can be considered. The H-shaped concrete specimen is the basis for the numerical model.

3.4.1 Experimental setup

First of all, a concrete specimen has to be developed, which causes cracks in any case. Therefore, an H-shaped concrete specimen was developed, on which the concrete layer was obstructed during shrinkage. As shown in Figure 3.32, the obstruction was realized by two symmetrically arranged steel tubes with welded steel plates. The length of the

specimen is 1700 mm, the width 400 mm. The two re-entrant corners, where the steel tubes with welded steel plates were inserted, have a length of 1500 mm and a width of 100 mm. The height of the shrinkage specimen is constant with 50 mm. On this shrinkage specimen with the previously mentioned dimensions, a C20/25 concrete was investigated

Later on, three different kinds of concrete, a C20/25 concrete, a C20/25 concrete with steel-fibres and a Terraplan concrete were tested. The dimensions of the specimen were downscaled. The aim was to have a comparison between the three different kinds of concrete regarding cracking.

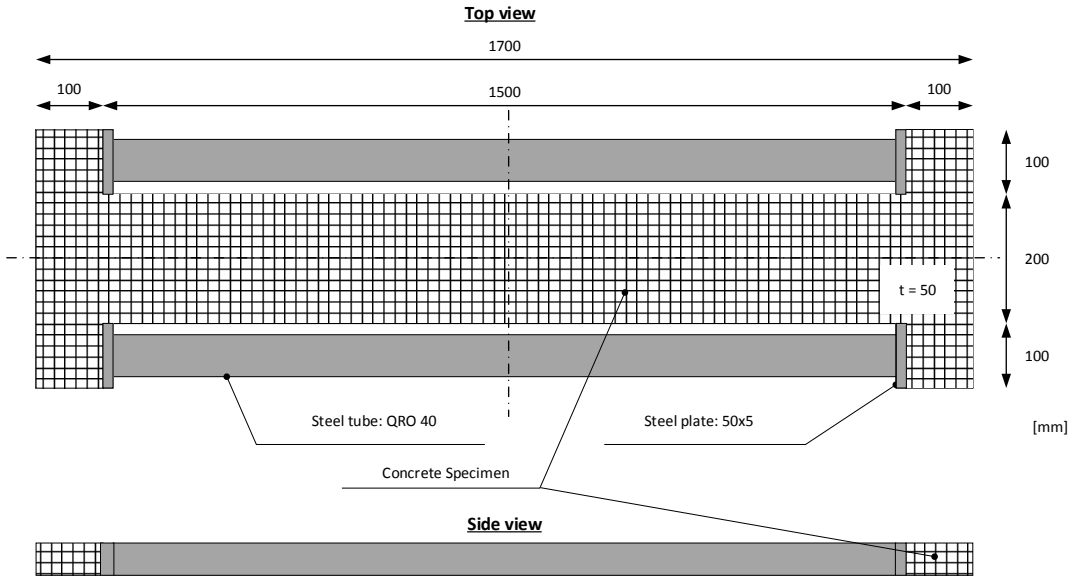

Figure 3.32: H-shaped shrinkage specimen

The concrete specimen were fixed on a wooden ground plate which was spanned with foil to ensure that there is no friction or interaction between concrete and wood.

3.4.2 Preparation of samples

As mentioned in the beginning, three different kinds of concrete were tested. First, a C20/25 concrete with no additives, such as fibres and no admixtures, such as plasticisers was used.

After addition of water to the aggregates and to the cement, the fresh concrete temperature was measured. Then, the flow spread was checked, directly after mixing, ten minutes after addition of water and 30 minutes after addition of water.

The wooden formwork, except the ground plate, was removed already one day, after casting of the specimen.

3.4.3 Experimental procedure

After casting of concrete, the specimen was stored in a large climate chamber with a constant relative humidity of 50 % and a constant temperature of 20°C. Cracking were controlled twice a day, using a scale loupe and a crack width ruler.

Figure 3.33: Scale loupe

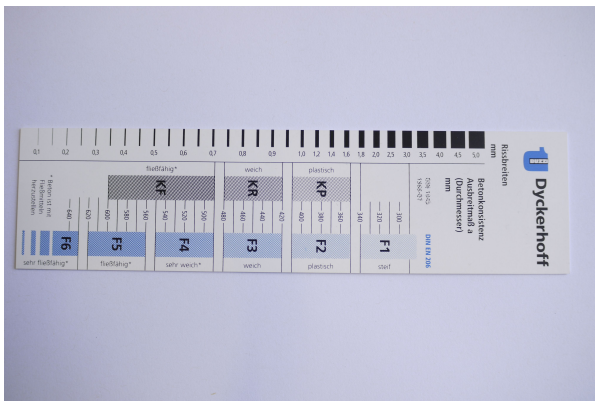

Figure 3.34: Crack width ruler

3.4.4 Test evaluation

The corners of H-shaped concrete specimen are orientated as seen in Figure 3.35.

The fully cracked states of the different corners are shown in Figure 3.36 to 3.39. The date of crack initiation and crack development of the different corners are shown in table 3.11. The first observed crack initiation was in corner 2 after 14 hours. After

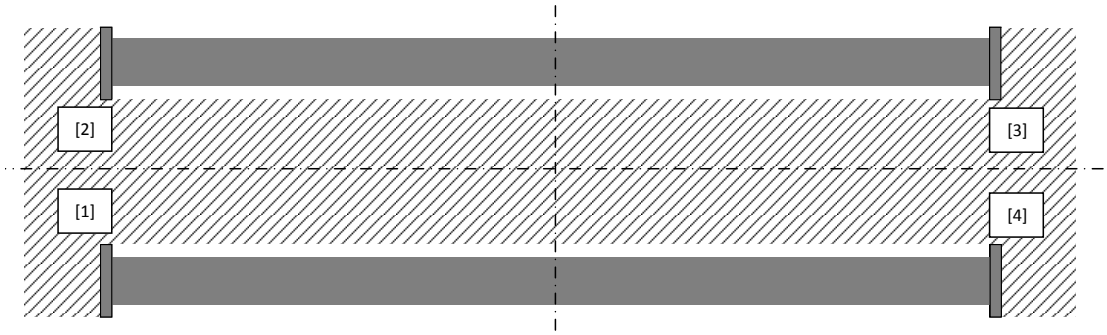

Figure 3.35: Orientation of corners of H-shaped shrinkage specimen

one day the first cracks appeared also in corner 3. Cracking in corner 1 and in corner 4 started after three days. After the first cracks appear in the four corners, the crack length remained constant for a while and continued only to grow after six days in corner 1 and in corner 3. Cracking in corner 2 continued then after 20 days and in corner 3 after 30 days whereas cracking in corner 1 was finished after 12 days and cracking in corner 3 after ten days. In corner 2, cracking was finished after 42 days and in corner 4 after 43 days.

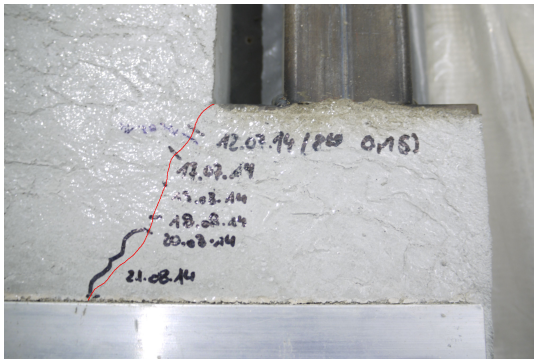

Figure 3.36: Corner 1 with cracking path

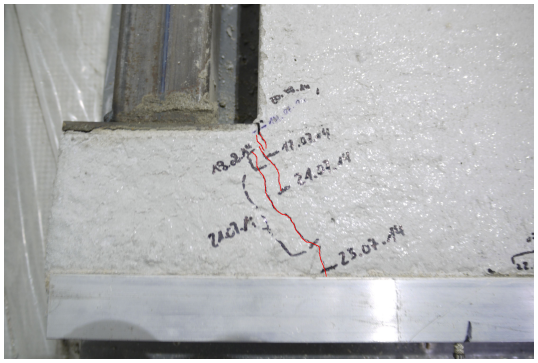

Figure 3.37: Corner 2 with cracking path

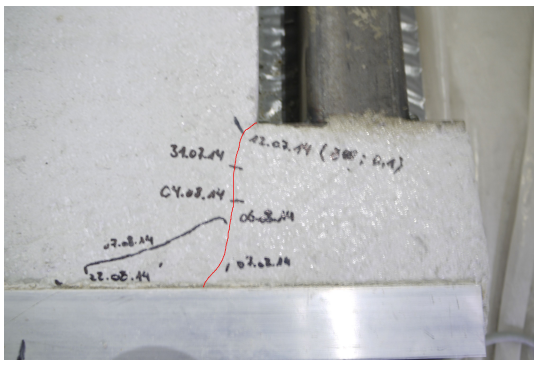

Figure 3.38: Corner 3 with cracking path

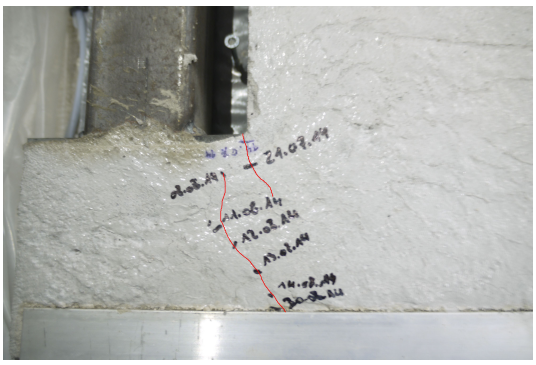

Figure 3.39: Corner 4 with cracking path

Table 3.11: Measured crack length of corner 1 to corner 4

time [d]	corner 1 [mm]	corner 2 [mm]	corner 3 [mm]	corner 4 [mm]
0.5	0	5	0	0
1.0	0	5	10	0
3.0	10	5	10	5
4.5	10	5	10	5
5.0	10	5	10	5
6.0	20	5	20	5
7.0	20	5	65	5
10.0	35	5	100	5
12.0	100	5	100	5
20.0	100	25	100	5
24.0	100	35	100	5
30.0	100	35	100	30
31.0	100	35	100	50
42.0	100	100	100	50
43.0	100	100	100	100

With the use of the H-shaped shrinkage specimen, the desired crack initiation and crack development could be observed and documented. The findings of the cracking path of H-shaped concrete specimen served as a basis for the self-developed finite element model.

3.4.5 Small scaled H-shaped concrete specimen

To compare the cracking behaviour of the different concrete mixture used within the tests, small scaled H-shaped concrete specimen were produced. The total length is 500 mm, the total width 200 mm and the height is constant 50 mm. The re-entrance corners have a length of 300 mm and a width of 50 mm.

C20/25 concrete

The numbering of the corner areas is the same than for the previous tests 3.35. The numbering of the specimen, as seen in Figure 3.40, is 'one' for the upper specimen, 'two' for the middle specimen and 'three' for the lower specimen. The first crack for specimen 'one' could be documented after 12 days. Cracking for specimen 'two' was recorded after 6 days and for specimen 'three' after 9 days.

Figure 3.40: Small scaled H-shaped concrete specimen of C20/25 concrete

C20/25 concrete with steel fibres

For specimen 'one', the first crack was observed after 13 days. Specimen 'two' cracked after 6 days and specimen 'three' after 13 days.

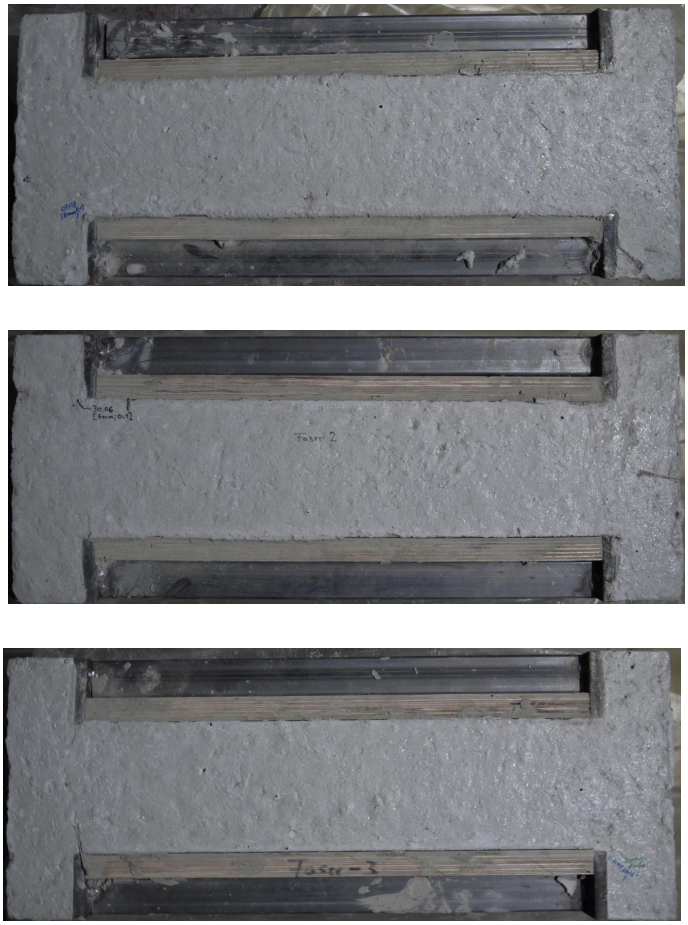

Figure 3.41: Small scaled H-shaped concrete specimen of C20/25 concrete

Terraplan concrete

For the small scaled H-shaped Terraplan concrete specimen, crack initiation could be recorded after 14 days, for specimen 'two' and for specimen 'three'. Within the test period of 28 days, no cracking could be observed for specimen 'one'.

Figure 3.42: Small scaled H-shaped concrete specimen of C20/25 concrete

The investigation and comparison of the three concrete mixtures showed no significant differences regarding cracking. Thus the degree of shrinkage of a C20/25 concrete is higher than the degree of shrinkage of a Terraplan concrete (see Figure 3.25 and Figure 3.26), the time of crack initiation is approximately equal.

3.5 Large scale tests

After the cracking behaviour was observed on small H-shaped shrinkage specimen, a finite element model, taking into account the material properties which were determined in the tests, was developed. Now, to transfer the numerical findings from the H-shaped shrinkage specimen to a concrete floor with realistic dimensions and realistic boundary conditions, large-scale tests were carried out.

3.5.1 Experimental setup

At the plant of Wilhelm Dyckerhoff company in Wiesbaden/Germany, a suitable slab structure was found where large-scale tests could be performed. The slab has a length of about 35 meters and a width of about 3.50 meters as shown in Figure 3.43. At the wall, the slab is constantly supported. At the free edge, the slab is supported by a concrete beam, which is supported by concrete supports for his part. The span length from the wall to the free edge is 3.28 meters, the span length of the concrete beams among each other in length direction is 3.50 meters.

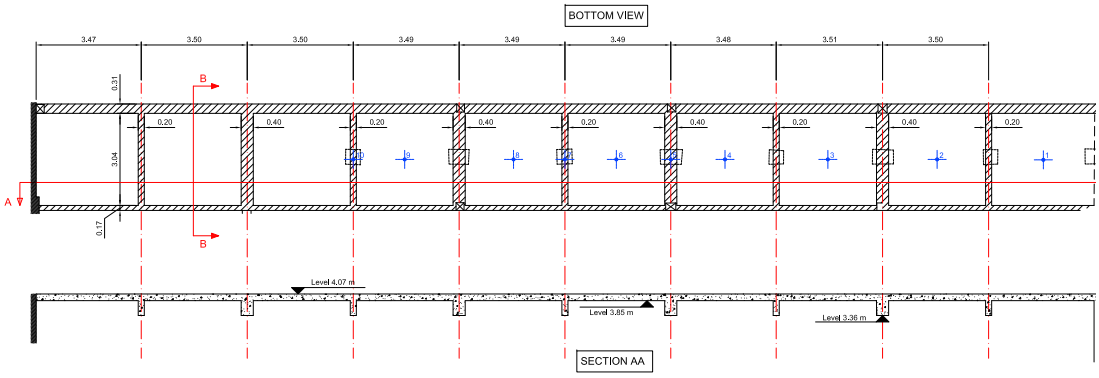

Figure 3.43: Top view and section view of the slab for large scale tests

In total, two tests areas were chosen: on the first area the fair-faced screed was cast in direct connection to the load bearing structure and on the second area a foil was inserted between the screed and the load bearing structure. The dimensions of the areas which are supported on three axes are: 6.00 m of length × 2.50 m of width × 0.08 m of height. (see grey areas in Figure 3.44).

In the centre of the areas, rectangular steel frames are inserted to produce constraint points in form of re-entrance corners (Figure 3.45) within the concrete screed. These

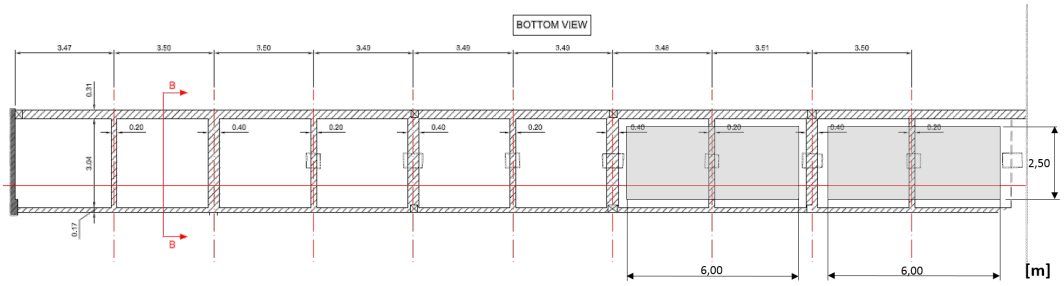

Figure 3.44: Slab with testing areas in grey

steel frames have the dimensions of 50 cm × 50 cm and a height of 8 cm. The frames are dowelled on the load bearing structure to ensure that they do not shift during the casting of the concrete.

Figure 3.45: Steel frame

3.5.2 Preparation of areas

The concrete was a C20/25 as described in Table 3.7. The concrete was mixed on site with a truck mixer and pumped to the prepared areas with a concrete pump.

3.5.3 Experimental procedure

After the casting of the fair-faced concrete screeds on the testing areas, cracking was visually controlled and documented every day. Besides, shrinkage deformation, environmental temperature and humidity variations as well as the displacement of slabs were

Figure 3.46: Truck mixer with concrete pump

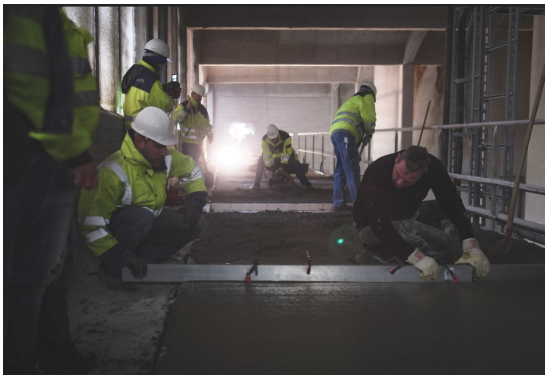

Figure 3.47: Realisation of the concrete screed on the test areas

continuously recorded. In the following it will be explained how the measurement of the displacements of the slabs has been performed.

3.5.4 Measurement technology

To measure the displacement of the slabs during the entire test, a new measurement technique has been elaborated. To compare the novel measurement technique to traditional measurement techniques, the displacement of the slabs has in addition been measured by using digital levelling.

Usually, to measure displacements of a slab, a complex sub-structure to fix the measuring devices must be installed in short vertical distance to the structure. These structures are very time-consuming when putting them in place and they are also very material intensive. Furthermore, they are sensible against wind, vibrations and temperature change which lead to an inaccuracy of the test results. Therefore a new method has been developed which is simple to be installed and for which the temperature influence is easy to be considered.

The new measuring system consists of a steel cable, which is dowelled under the slab. At the end of the steel cable a steel weight is fixed to stabilise the steel cable and the steel weight functions also as surface where the displacement transducer can measure against. The displacement transducer and the steel weight are enclosed in a protective cover, to protect the measuring equipment and the steel weight from environmental influences. The principle of the measuring system is shown in Figure 3.50.

Figure 3.48: Tubular construction

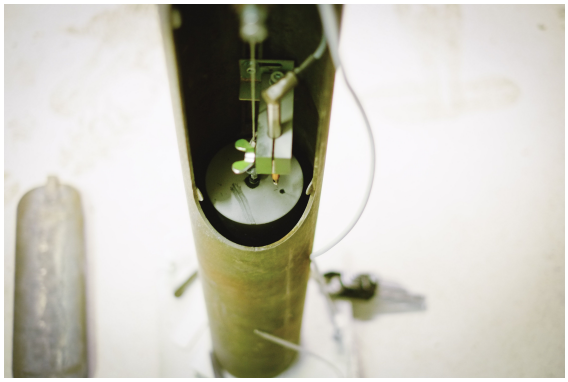

Figure 3.49: New measuring method

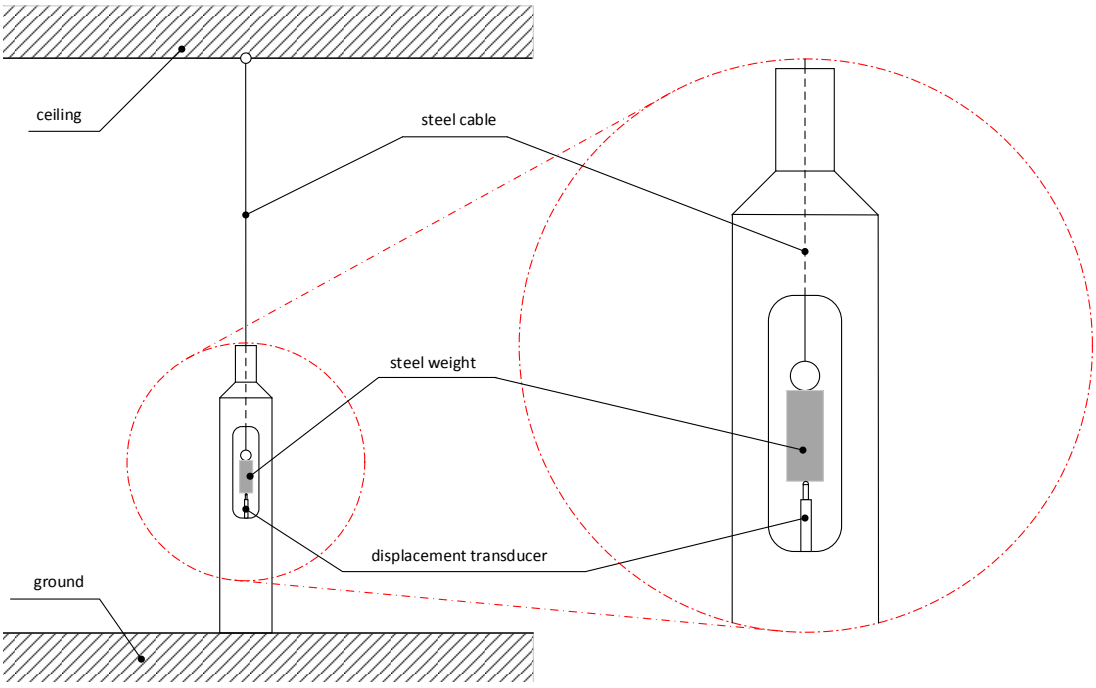

Figure 3.50: Schematic drawing of the new measuring system

The measuring of displacement of slab started at the moment when the first areas was casted. Values of the displacement were recorded over a period of 77 days. The sample rate was one value every minute. The measuring points can be seen, analogue to Figure 3.43, in Figure 3.51.

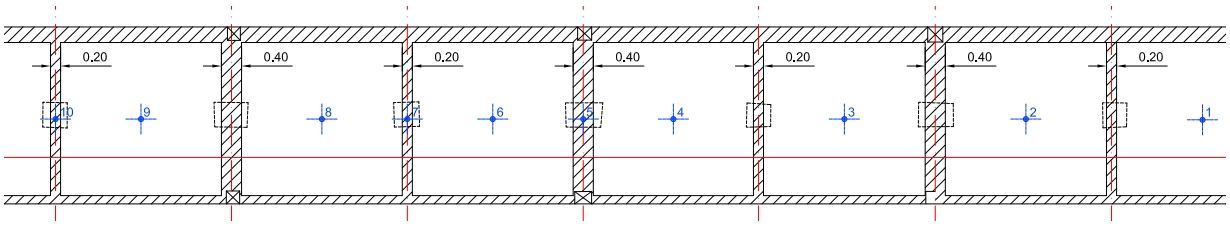

Figure 3.51: Overview of the measuring points No. 1 to No. 9 of the digital levelling and of the new measurement technique

The additional measuring of the displacement using digital levelling was realised directly before and directly after the casting of concrete.

Besides measuring of the displacement, one shrinkage drain was filled with the used concrete to document the shrinkage behaviour. The sample rate for the measurement of shrinkage was one value every two minutes.

Furthermore, the temperature and humidity were recorded as well as the compressive strength development on concrete cubes according to DIN EN 1992-1-1:2011-01 and the development of Young's Modulus on concrete cylinders according to DIN EN 12390-13:2014-06 as well as the heat development due to hydration on concrete cubes. In total, 12 cylinders and 12 cubes were tested. The sample rate for temperature and humidity was one value every minute, compressive strength and Young's Modulus were tested after one day, two days, seven and 28 days.

3.5.5 Discussion of the results of the large-scale tests

In a first step, the cracking behaviour of the two areas is evaluated. After this, the recorded displacement of the slabs is shown. In a further step, the material behaviour such as strength development and shrinkage are described.

The cracking behaviour is evaluated for the two different areas: at one area a foil has been inserted between the screed and the load bearing structure and on the other area the screed has been directly connected to the load bearing structure. For the screed lying on foil, no cracking could be observed within a period of at least seven months whereas the screed directly connected to the load bearing structure showed a completely different behaviour. The crack initiation and crack development for this is shown in Table 3.12. The four corners are labelled according to Figure 3.52.

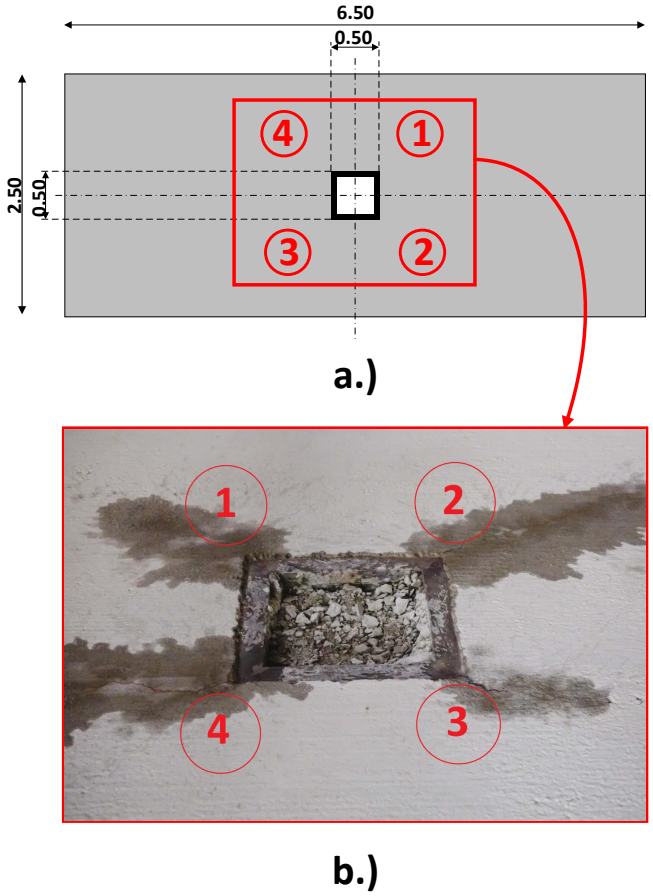

Figure 3.52: a.) View on the slab with orientation and labelling of the corners
b.) Image with numbering of the cracked corners

The first cracks started, two days after casting of concrete, in corner 1 and in corner 2, with a length of 3 mm (corner 1) respectively 5 mm (corner 2). The first crack in corner 3 could be observed after three days with a length of 2 mm. In corner 4, the first crack, with a length of 8 mm, started after eight days. Cracking was finished in corner 4 after 47 days. Even after 77 days, cracking in corner 1, corner 2 and corner 3 was not completed.

The crack pattern (see Figure 3.53) of the large scale tests is similar to the crack pattern found for the H-shaped shrinkage specimen. In the first days, cracking started consecutively at all corners. Afterwards, cracks propagate in diagonal direction. This could also be observed for the large scale tests for the corners 2 and 4.

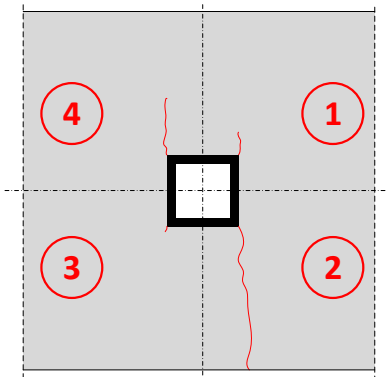

Figure 3.53: Schematic view of the crack pattern after 77 days for the slab with direct contact to the load bearing structure

Table 3.12: Measured crack length of the corners 1 to 4 for the slab with direct contact to the load bearing structure

time [d]	corner 1 [mm]	corner 2 [mm]	corner 3 [mm]	corner 4 [mm]
0	0	0	0	0
1	0	0	0	0
2	3	5	0	0
3	3	5	2	0
4	3	5	2	0
5	3	5	2	0
6	3	10	6	0
7	6	10	6	8
8	6	13	8	18
9	11	30	10	35
13	35	55	16	120
14	35	70	36	170
15	35	70	41	170
16	35	70	41	180
20	35	95	45	200
23	50	1000	45	315
30	35	1000	45	390
37	110	1000	45	510
47	145	1000	45	510

The maximum displacement measured with the new measuring system was 0.38 mm after 77 days. The deflection directly measured with digital levelling after casting of concrete was, 0.15 mm. In Figure 3.54a to Figure 3.54d, the displacement of four different points, measured with the new measuring system, within 77 days is shown. In every signal, a constant increase of the displacement can be observed. This is due to creeping effects of the bearing structure. Further variations in the signals are due to temperature change. The sample rate was one value every minute.

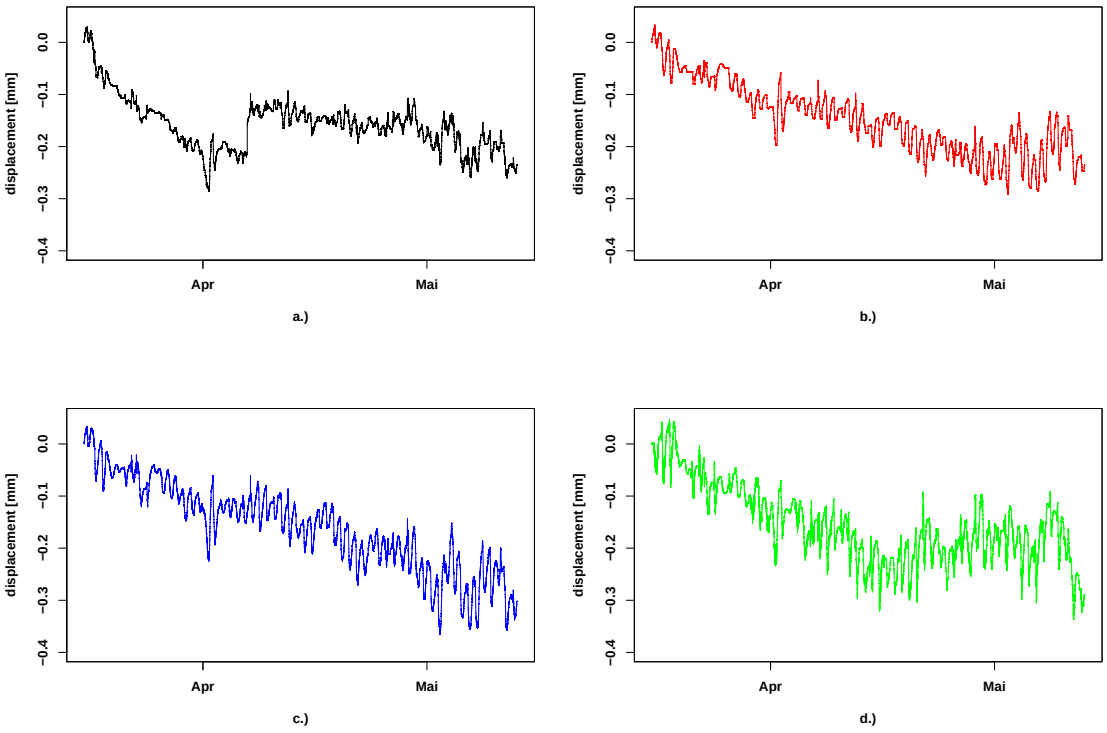

Figure 3.54: Displacement of slab after concreting a.) Point No. 1 b.) Point No. 3 c.) Point No. 4 d.) Point No. 5

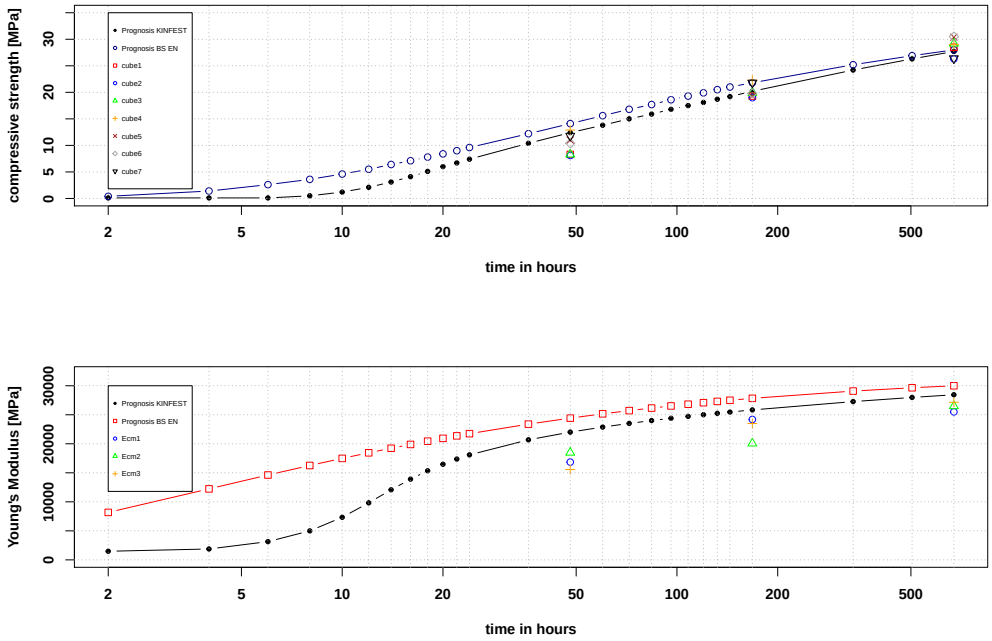

Figure 3.55: Compressive strength and Young's Modulus compared to KINFEST and DIN EN 1992-1-1:2011-01 (2011)

For the simulation of large scale tests, the material properties of the used concrete, such as compressive strength and Young's Modulus, have to be known. The material strength evolution is provided by KINFEST. The prognosis values from KINFEST has to be verified in order to use them in a numerical simulation. By this reason, compression strength tests and tests to measure Young's Modulus are again carried out after two, seven and 28 days.

As seen in Figure 3.55, the compressive strength evolution predicted with KINFEST as well as predicted with DIN EN 1992-1-1:2011-01 (2011) show very good results compared to the measured compressive strength values. The values predicted by KINFEST takes into account hydration temperature development as well as environmental temperature. Young's Modulus predicted with KINFEST, compared to test results, show very good results whereas the values predicted with DIN EN 1992-1-1:2011-01 (2011) show a large deviation especially within the first 48 hours.

Shrinkage, as one of the most important reasons that can cause cracking in concrete

structures, was also documented. The measurement was carried out over a period of 77 days. The test was finished after 77 days, no significant changes regarding crack growth could be observed. Afterwards, the measured values are compared to values predicted with DIN EN 1992-1-1:2011-01 (2011). The predicted and measured values show a very high accordance so that the analytical approach due to DIN EN 1992-1-1:2011-01 (2011) can be used as the basis for shrinkage within a design concept.

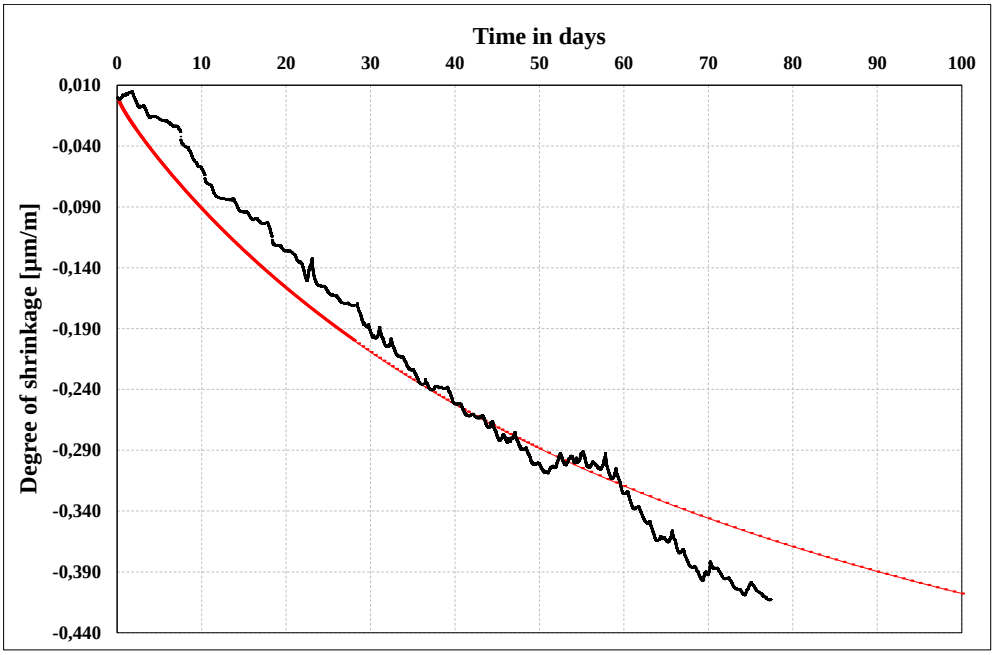

Figure 3.56: Measured and predicted shrinkage

3.6 Summary

The aim of the current chapter was the determination of the required mechanical and hygric material properties. Besides, the cracking behaviour on small scale H-shaped shrinkage specimen as well as the cracking behaviour on large scale specimen with different boundary conditions was investigated.

Within a design concept for fair faced concrete screeds, the material behaviour (mechanical and hygric) of the concrete has to be known. To avoid extensive test set-ups, it has been proven by the current analysis that the analytical approaches as well as the prediction software KINTEMP/KINFEST can be used to determine the mechanical material behaviour of the concrete used within this project.

Shrinkage represents one of the most important factors provoking cracking of young concrete. The determination of shrinkage of the concrete by measuring the degree of shrinkage within shrinkage drains is a time consuming process. It has been shown that the analytical approach due to DIN EN 1992-1-1:2011-01 (2011); Fédération internationale du béton (2013) provides excellent results, and thus, provides sufficiently accurate results. Thus, the determination of the hygric material properties for the concrete investagted within this thesis can be done by these analytical approaches.

Besides the testing of the material properties, a novel measurement technique was tested. This technique provides excellent results compared to results from digital levelling. This technique is a promising method to measure displacements on slab systems and could also be used for measuring bridge deformations.

Crack initiation and crack development on small scale H-shaped concrete specimen and on large scale concrete surfaces were documented. The findings of cracking as well as the findings from the determination of the material properties serves as a basis for a self-developed finite element model, which is described in the following chapter.

4 Numerical analysis

In this chapter, a numerical model is represented, which is able to predict the crack initiation and the crack growth on unreinforced cement screeds, with different boundary conditions.

To this reason, a first model for cracking of the H-shaped shrinkage specimen was developed, using ANSYS^{ő} Finite Element Software. The findings of the material behaviour from the performed mechanical and hygric tests, as well as the predicted values from KINFEST and the, with the analytical approach due to DIN EN 1992-1-1:2011-01 (2011) and Fédération internationale du béton (2013), predicted degree of shrinkage, were taken into account. Furthermore, the findings from cracking of the small scale H-shaped shrinkage specimen served as a basis to calibrate and to validate the numerical model.

For the H-shaped shrinkage specimen, the crack initiation and the crack development is calculated with the numerical model as well the crack distribution over the screed surface as the crack evolution in function of time. For the large-scale tests, the crack distribution over the screed surface and the crack evolution in function of time is evaluated with the numerical model as well as curling of the concrete screed. Curling is a very important aspect, which leads to cracking in the corner areas of a float mounted concrete screed.

Finally, the self-developed numerical model serves a basis for an extensive parameter study. Within this parameter study, the maximum possible dimensions of a concrete floor (length; width; height), concerning the bearing system, the relative humidity and the interactions of the mentioned parameters are investigated. The parameter study will be presented in detail in the next chapter.

4.1 Preparation of simulation and general informations

In the previous chapter, evolving material properties were determined such as compressive strength, Young's Modulus, tensile strength and shrinkage behaviour. Besides, moisture release and cracking of concrete floors was investigated. The decisive findings, which influence crack initiation and crack development, will be taken into account in the following in order to create a finite element model for numerical analysis.

The sequence of the finite element simulation is divided into three parts; preprocessing, solving and post-processing. In the first part, in the preprocessor, units for calculation have to be defined. The finite element software ANSYS$^{\circledcirc}$ does not operate with default units. In general, it is recommended to use SI-Units. For the gradual calculation of cracking, external data are required. These external data, such as Young's Modulus, poisson's ratio, tensile strength and temperature were provided in csv.data files. In a next step, the element types have to be defined. The elements for structural analysis used are shown in Figure 4.1. Then, material properties depending on the element type need to be defined. For the calculation with the SOLID185 element, Young's Modulus, Poisson's ratio and thermal expansion factor as well as density of the material must be set. Thereupon, geometry of the model is created. The model was parametrized, symmetry conditions were use. In a last step of the pre-processor, the model is meshed. Hexahedral elements and tetrahedral elements were used to mesh the created model.

In the solution section boundary conditions (support conditions; symmetry axes) have to be defined. As support conditions, all types of support, rigid support, spring support or rigid clamping are possible. Furthermore all types of load cases, thermal as well as structural, can be represented.

In the post-processor, stress states, strain states and deformations of the calculated model can be represented. In the case of the element failure method (see Chapter 2.6.2.2), the calculated model with failed elements, respectively the calculated crack path, can be represented.

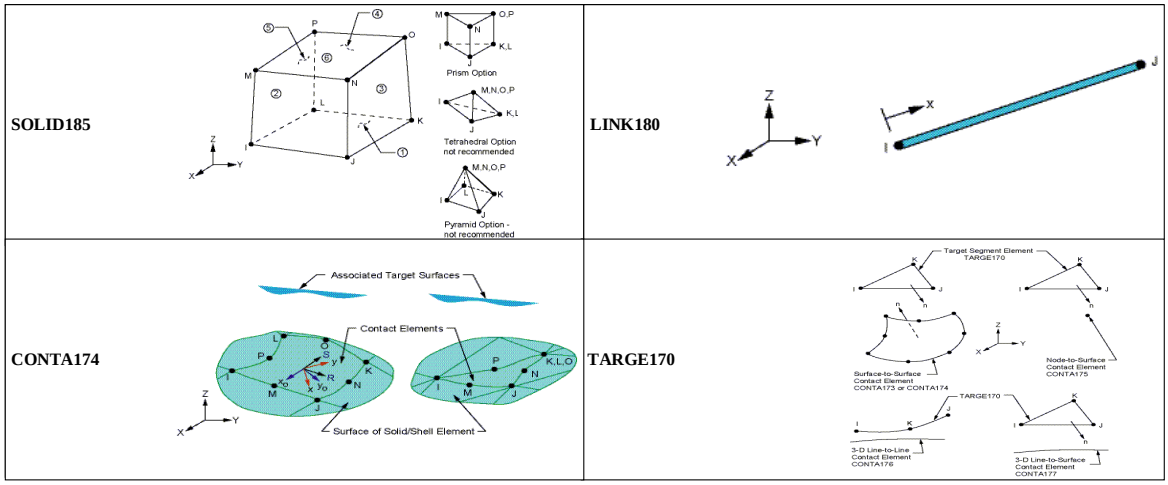

Figure 4.1: Elements used for structural analysis ANSYS Inc. ANSYS Europe (2013)

4.2 Objectives and Methodology

The aim of the finite element model is to calculate crack initiation and crack development of an unreinforced cement-bound concrete screed on a reinforced load bearing slab structure. In a first step, a model of a small-scale H-shaped concrete specimen was created. On this small-scale concrete specimen, a first numerical approach to calculate crack initiation and crack growth in unreinforced concrete structures was developed. In a further step, the model was verified on large scale test areas.

4.3 Finite element model of H-shaped concrete specimen

4.3.1 Model design

As already mentioned, ANSYS does not work with predefined units, the units used are to be defined, here for length millimetres [mm], for forces Newton [N] and for temperatures degree in Celsius [°C]. In a next step, the model is parametrized as seen in Figure 4.2. The respective dimensions of the different areas are substituted by variables, so that a change of the dimensions can be carried out easily. This allows on one hand to generate various geometries and on the other hand, the parametrization is extremely valuable within a parameter study.

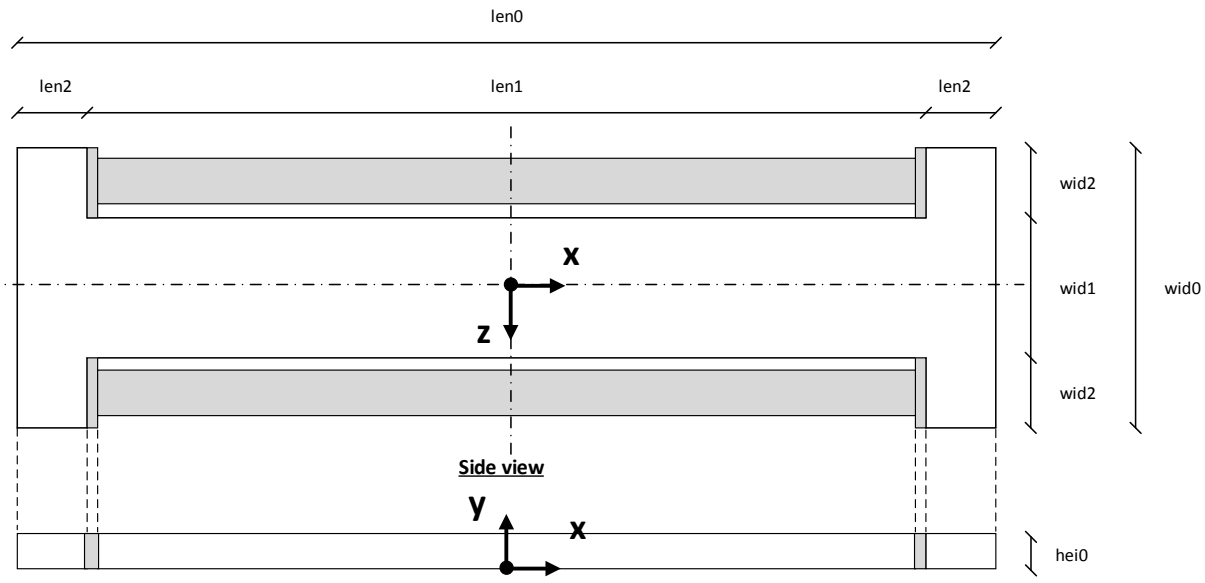

Figure 4.2: Overview of the parametrized model

After parameterizing the model, external csv.data are provided such as tensile strength, equivalent temperature, Poisson's ratio and Young's Modulus. These material properties evolve as a function of time. The evolution of the material properties will be considered within simulation.

Uniaxial tensile strength serves as failure criterion. Thereby, the tensile strength at the respective time is compared to the stresses in the X-Z-plane. The equivalent temperature, to represent shrinkage as described in DIN Fachbericht 104 (2009), is calculated with equation 4.1.

$$\varepsilon_{cds}(t) = \alpha_T \cdot \Delta T \quad [-] \tag{4.1}$$

$\varepsilon_{cds}(t)$: shrinkage strain [-] (see equation 2.6 in chapter 2.2.3)
α_T: coefficient of thermal expansion $= 12 \cdot 10^{-6}$ [1/K]
ΔT: $T_E - T_S$ [K]
T_E: end temperature [K]
T_S: initial temperature (here: reference temperature) [K]

The Young's Modulus is varied respecting its strength development during hardening

by attributing a data table to the respective equivalent properties at each time step (see Figure 4.3). Attributing e.g. the Young's Modulus to a data table has the effect, that the Young's Modulus is varied gradually in function of the evolving compressive strength of concrete. Here it was possible to take into account the evolving shrinkage behaviour as well as an evolving Young's Modulus and tensile strength during simulation of concrete.

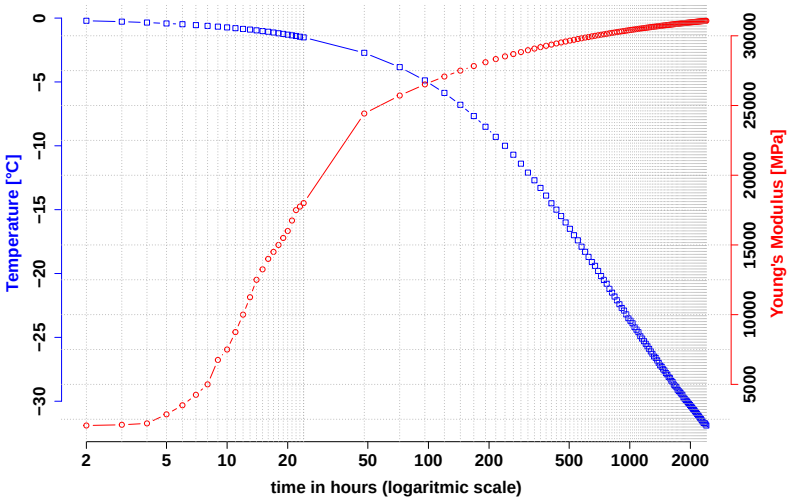

Figure 4.3: Young's Modulus and Δ T versus time

In the following, the model is meshed with the 3D brick element SOLID185. SOLID185 has eight nodes (I,J,K,L,M,N,O,P) with three degrees of freedom (UX, UY, UZ) for every node. The shape of the used elements is a tetrahedral shape, which is used because of a smoothing of the sharp edges of the internal corners.

The reason for smoothing of the edges is to reduce singularities in the corner area. Singularities in finite element simulations were described in Bröske (2010), in Cheng et al. (2016) and in Staudt et al. (2016). Bröske (2010) investigated two different types of two-dimensional cantilevers. One cantilever with the dimensions: length 50 mm $\times$ height 10 mm and a thickness of 1 mm and an L-shaped cantilever with the dimensions: length of 50 mm $\times$ height 10 mm $\times$ a thickness of 1 mm with an additional angle-leg with the dimensions: length 10 mm $\times$ height 10 mm. The material used is steel and the load is a single load of 100 N. Concluding can be stated, that the smaller the elements size, under the same loading, the higher the stresses in the corner area.

For a cantilever with 100 elements, a von Mises stress of 298 MPa is documented, for a cantilever with 400 elements a von Mises stress of 604 MPa and for a cantilever with 25000 elements a von Mises stress of 4938 MPa was documented. For the L-shaped cantilever a maximum von Mises stress of 216 MPa for 125 elements, a maximum von Mises stress of 361 MPa for 650 elements and a maximum von Mises stress of 1414 MPa for 50000 elements was documented.

The entire model is supported in Y-direction. This support ensures that the model is able to slide during simulation, as it does in the tests, where concrete was fixed on foil. The obstruction, which is guaranteed in the experimental investigations by steel tubes with welded steel plates, is represented within the finite element calculation by blocks. The blocks are fixed in X-, Y- and Z-direction (orientation of coordinate system see Figure 4.2). Between the blocks and the concrete specimen, a contact surface is defined, which allow sliding in Z-direction, considering a coefficient of friction of $\mu = 0.8$ (coefficient of friction between concrete and steel). Due to the fact that the blocks are fixed in X-, Y- and Z-direction, a displacement in -X-direction is oppressed, while a displacement in X-direction is possible.

4.3.2 Verification of the model

To verify the chosen mesh size, only a quarter of H-shaped shrinkage specimen was modelled using the double symmetry (see Figure 4.4) of the model. Symmetry axes are defined along the XY-plane and XZ-plane.

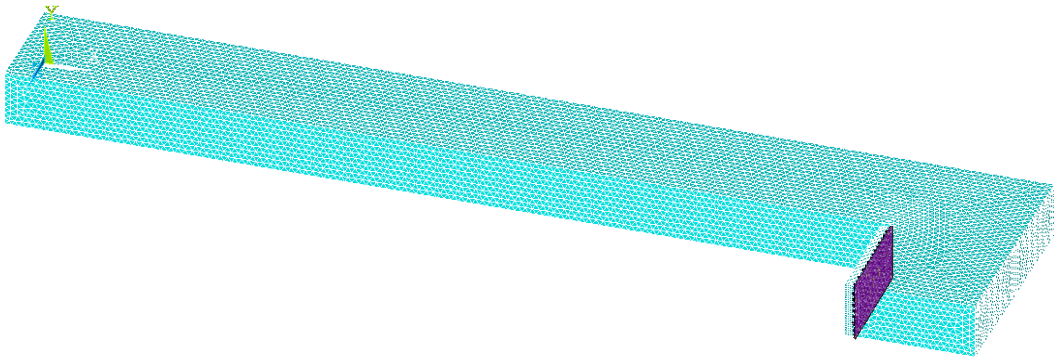

Figure 4.4: FE-model of H-shaped specimen with contact surface (drawn in purple)

The mesh size was reduced successively, starting with a mesh size of 20 mm (Figure 4.5), until the calculated crack path converged with the crack path from the test, regarding its spatial development.

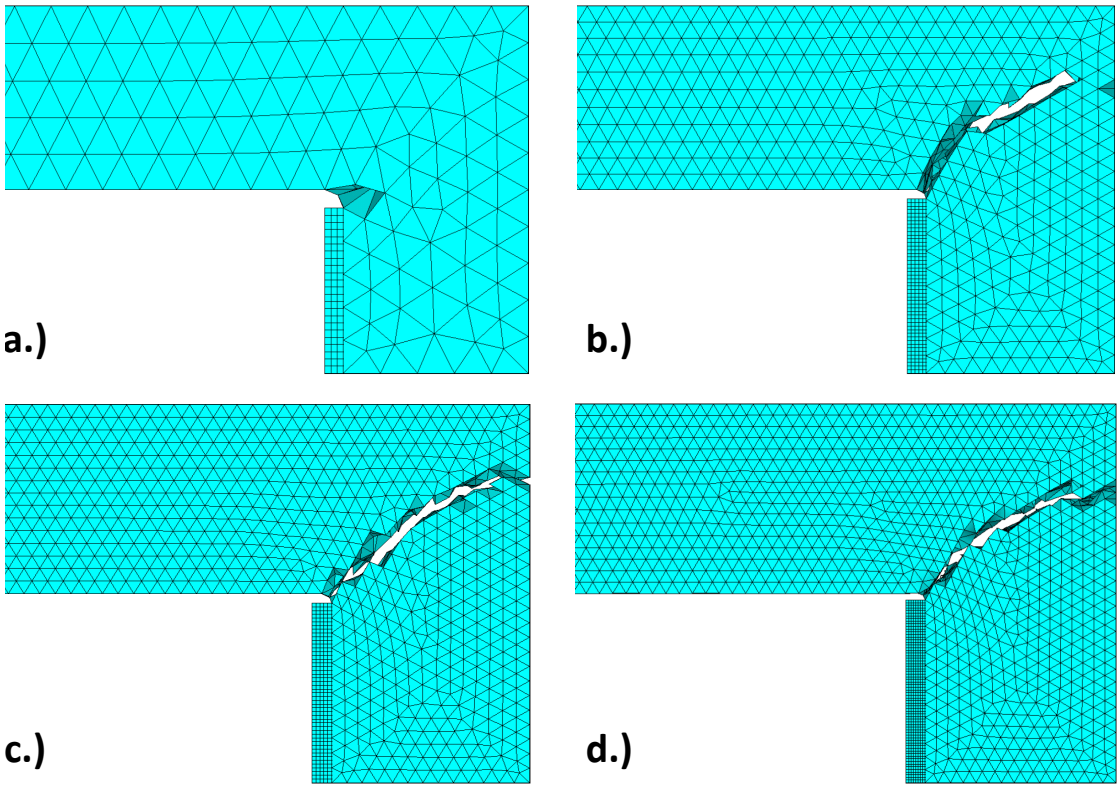

Figure 4.5: a.) FE- model with element size of 20 mm
b.) FE- model with element size of 10 mm
c.) FE- model with element size of 8 mm
d.) FE- model with element size of 7 mm

Figure 4.5 shows crack paths for 20 mm, 10 mm, 8 mm and 7 mm element sizes. The element size of 20 mm does not represent the crack path by far. The crack path for an element size of 10 mm is a substantial improvement compared to the 20 mm element size, but it is still not sufficiently precise enough. An element size of 8 mm, reproduces the crack path from the experiments with a very high accuracy. The element size of 7 mm does not represent an improvement of the crack path compared to the result from 8 mm element size.

The following step consisted in verifying the number of load steps. The choice of a high number of load steps ensures, within the simulation, a slow increase of the load. The importance of a high number of load steps is shown in Figure 4.6 and in Figure 4.7. Figure 4.6 shows the calculated crack path with 50 load steps. The calculated crack path is not precise enough. The crack path, calculated with 250 load steps (Figure 4.7), shows a very high accordance to the crack path observed in the experiments.

The simulation of the H-shaped shrinkage specimen has been done with an element size of 8 mm and a number of 250 load steps which constitutes a good compromise between calculation time and accuracy of the resulting crack path. For a first assumption of the mesh size, the number of load steps can be calculated with equation 4.2.

$$n_{LS} \approx \frac{T_E}{0,05} \quad [-] \tag{4.2}$$

n_{LS}: Number of load steps
T_E: End temperature according to equation 4.3 [K]
0.05: Step of temperature increase [K]

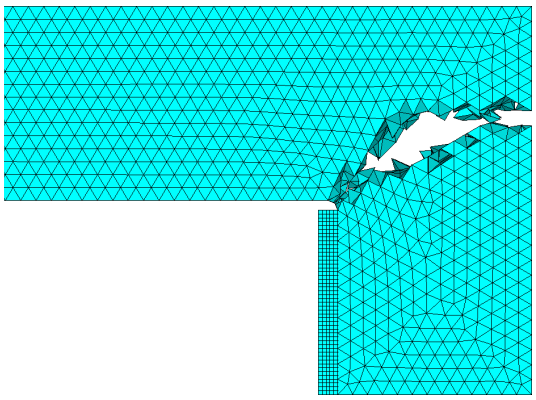

Figure 4.6: Fully cracked state of the Fe-model using 50 load steps

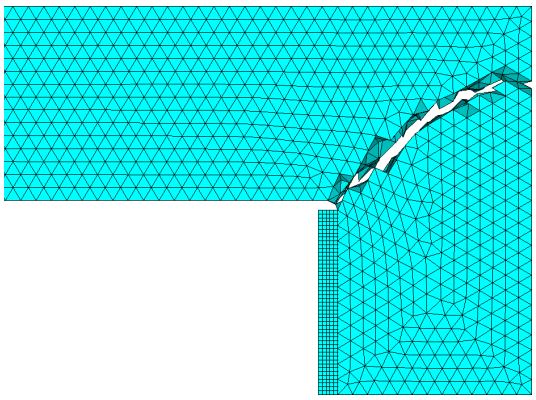

Figure 4.7: Fully cracked state of the Fe-model using 250 load steps

4.3.3 Description of developed algorithm

Using Element Failure Method (EFM), the model is able to calculate crack initiation and crack development considering evolving material strengths. The calculation is carried out in a loop. First, an equivalent temperature (see equation 4.3) is set on every node of the model.

$$T_E(t) = \frac{\varepsilon_{csd}(t)}{\alpha_T} \quad [K] \tag{4.3}$$

This temperature to simulate shrinkage causes a contraction of the concrete layer and thus, generates tensile stresses. At the end of every loop run, the algorithm checks which nodes satisfy the chosen failure criterion (here: uniaxial tensile strength) i.e. at which nodes the uniaxial tensile strength of the concrete at this time step is exceeded. For the current simulation the chosen failure criterion, the uniaxial tensile strength at the respective time step, is compared to the stresses in the X-Z-plane. An element only fails if all of its eight nodes satisfy the failure criterion. In the case an element fails, the stiffness of the respective element is set to zero. The element is no longer displayed but it is still part of the entire model (Figure 4.8 and Figure 4.9).

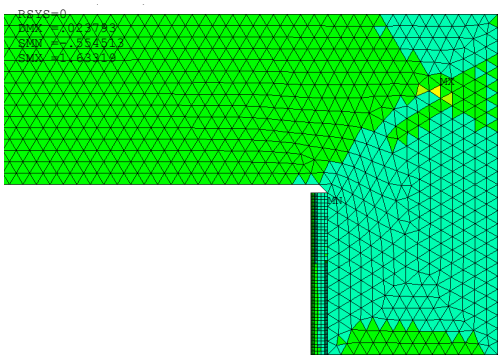

Figure 4.8: FE- model at load step 125 with “representation of element failure” off

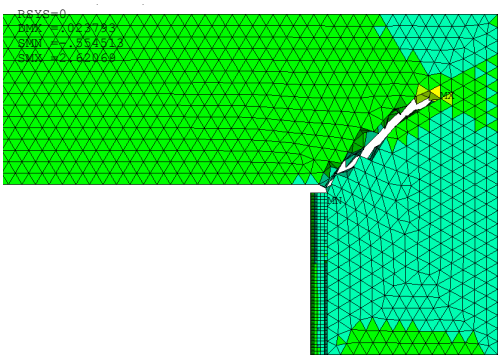

Figure 4.9: FE-model at load step 125 with “representation of element failure” on

The model with failed elements serves as basis for the next loop run. The simulation showed that the tensile strength at the respective time step serving as failure criterion delivers suitable results compared to the experiments. The sequence of the entire simulation is shown in Figure 4.10.

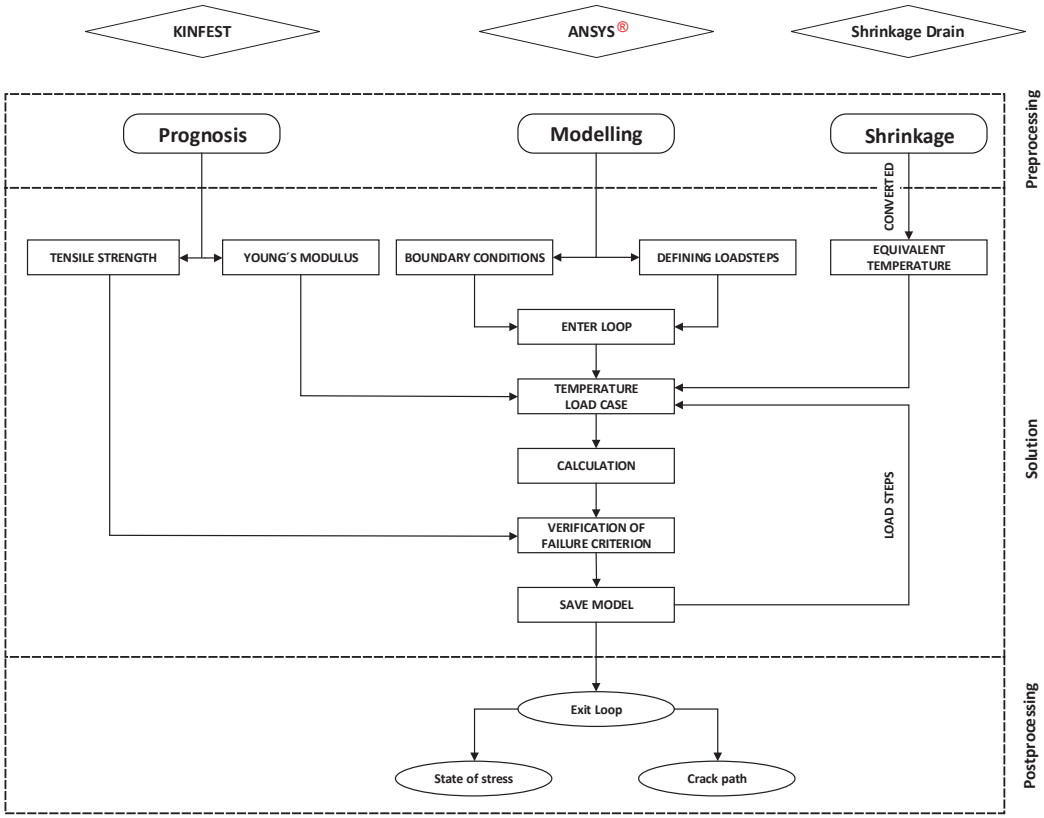

Figure 4.10: Flowchart sequence of calculation

A mesh dependency can be excluded by using very fine load steps as described in Weiler and Waldmann (2016). This assumption was also proven on the H-shaped shrinkage specimen. The conclusion was, the finer the mesh the more load steps are required (see Equation 4.2). This is clearly illustrated in Figure 4.6 and Figure 4.7.

4.3.4 Analysis of numerical results

Because the cracking behaviour is different from a quarter model compared to a full model, a full model is calculated in the following. Indeed, the mesh of the full model seems double-symmetrically in the top-view, but over the hight of the 3D-model, especially for the rounded corner areas, the mesh is different for each corner area. As a consequence thereof, elements in one corner area within the numerical calculation will fail first. In Figure 4.12 the crack path evolution of the numerical model is shown. The numbering of the corners has been chosen according to Figure 4.11.

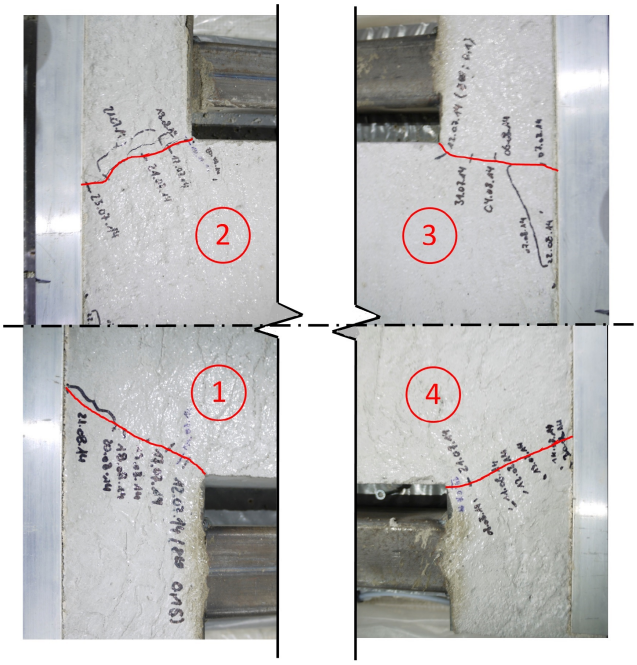

Figure 4.11: Representation of the four cracked corners of the specimen at t = 43 days

Figure 4.12a shows the crack path starting after 12 hours with failed elements in the corners of the structure. In Figure 4.12b, a crack path growth in corner 1 and in corner 3 can be observed after 72 hours. In Figure 4.12c, the evolution of the calculated crack path is shown after 108 hours. Corner 1 and corner 3 are fully cracked after 120 hours (see Figure 4.12d). In the finite element simulation, the model can be regarded as completely cracked after 240 hours (see Figure 4.12e).

In Table 4.1, the chronological evolution of the calculated crack path is compared to the measured cracking path of the experimental tests. Within the simulation, the

start of cracking with the failure of the first elements can be noted after 12 hours, whereas depending on the different corners the earliest cracks in the experiments were observed after 14 hours and the latest after 66 hours. Since during the experiments the specimens were only controlled every 12 hours, it is possible that the first crack in the test appeared earlier than noticed. The end of cracking in the finite element simulation was observed depending again on the different corners after 5 days and up to 10 days (Table 4.1). When cracking in corner 1, corner 2 and corner 3 was completed, the simulation was no longer able to converge. The discrepancies of the cracking end in the tests and in the finite element simulation may be due to the fact that a crack in a concrete structure only becomes gradually visible. To chart the precise development of a crack in a cementitious structure, detection methods such as the acoustic emission method can be used as described in Hu et al. (2013) and in Kocur et al. (2016).

Table 4.1: Measured crack path evolution versus calculated crack path evolution

time [**d**]	Crack length [**mm**]							
	Corner 1		Corner 2		Corner 3		Corner 4	
	FE	Test	FE	Test	FE	Test	FE	Test
0.5	8	0	8	5	8	0	8	0
1.0	8	0	8	5	8	10	8	0
3.0	16	10	8	5	10	10	16	5
4.5	25	10	8	5	40	10	40	5
5.0	100	10	50	5	100	10	40	5
6.0	100	20	50	5	100	20	40	5
7.0	100	20	50	5	100	65	40	5
10.0	100	35	100	5	100	100	40	5
12.0	100	100	100	5	100	100	40	5
20.0	100	100	100	25	100	100	40	5
24.0	100	100	100	35	100	100	40	5
30.0	100	100	100	35	100	100	40	30
31.0	100	100	100	35	100	100	40	50
42.0	100	100	100	100	100	100	40	50
43.0	100	100	100	100	100	100	40	100

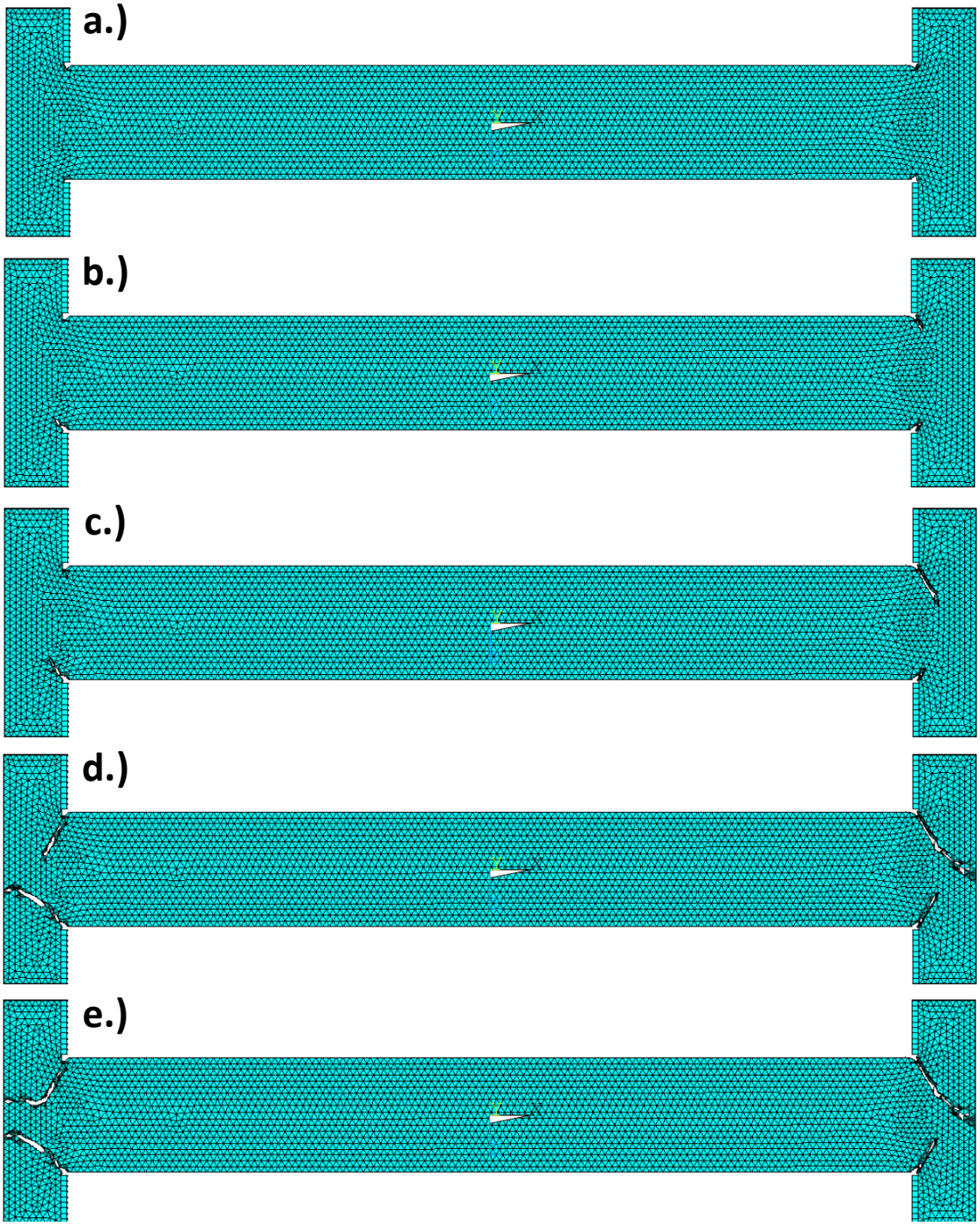

Figure 4.12: a.) Crack path within the FE-model after 12 hours
b.) Crack path within the FE-model after 72 hours
c.) Crack path within the FE-model after 108 hours
d.) Crack path within the FE-model after 120 hours
e.) Crack path within the FE-model after 240 hours

4.4 Finite element model of large scale tests

4.4.1 Model design

The design of the model is for the large scale tests similar as for the H-shaped concrete specimen. The same units were used. The model for the large-scale tests can be seen in Figure 4.13.

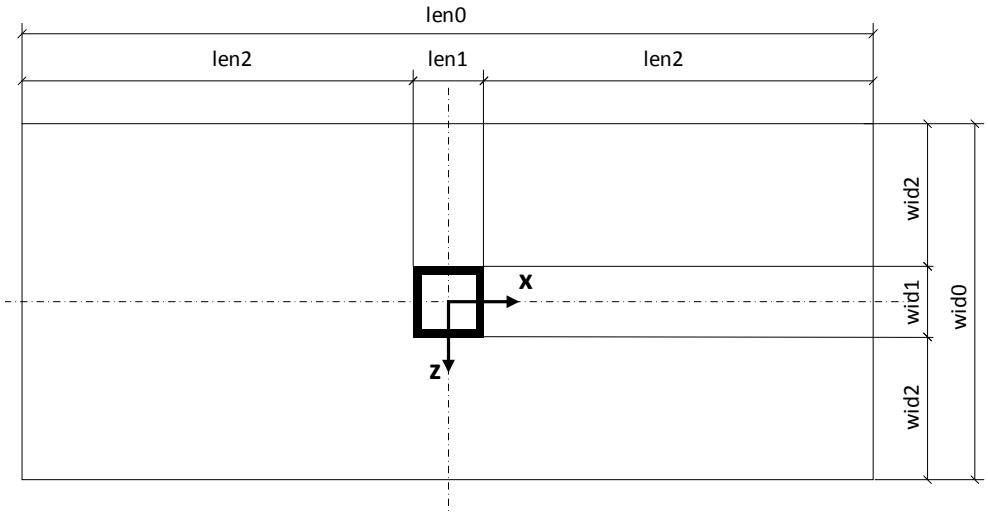

Figure 4.13: Parametrized large scale model

The input data are again the same as for the H-shaped concrete specimen. The shrinkage behaviour, as well as the evolving material properties of the corresponding concrete serves as basis input data.

To simulate a concrete floor on a bearing structure, it is necessary to take the interaction, respectively the contact between concrete floor and bearing structure into account. Here, two different kinds of support condition are simulated: a concrete floor directly fixed to the bearing structure and a concrete floor fixed on foil to ensure sliding of the concrete floor.

The concrete screed has again been modelled by SOLID185 elements. Compared to the small scale H-specimen, a main difference for the large scale model is based on the fact that the contact between bearing structure and concrete screed has to be modelled. This is needed as the bearing structure has in contrast to the small scale H-shaped shrinkage

specimen, an influence on the concrete screed. This influence is the deformation of the bearing structure in function of the respective support system. The contact conditions are simulated by LINK180 elements. LINK180 elements are 3-D spar or truss elements. The LINK180 element is a uniaxial compression-tension element which consists of two nodes with three degrees of freedom in X-, Y-and Z-direction. The LINK180 element can fail under compression or as required in the current application, it can fail under tension. Using LINK180 elements makes it possible to simulate a screed floating on foil as well as in direct bond to the screed by providing with the vertical LINK180 elements a compression strength in vertical direction and with the diagonal LINK180 elements a friction strength in horizontal direction. These both vertical LINK180 elements allow also the representation of curling of the concrete screed as it is known for concrete floor fixed on foil (see Schnell (1987), Lorenz and Schmidt (1998) and Georgin et al. (2008)) (see Figure 4.14).

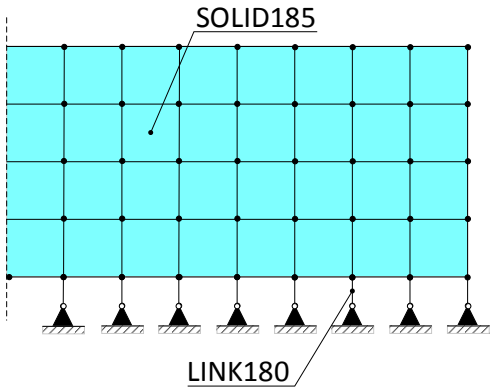

Figure 4.14: Vertikal LINK180 Elements

Diagonal LINK180 Elements simulate the bond between bearing-structure and concrete screed (see Figure 4.15).

Associated with curling of concrete floors, the term of "shrinkage depth" needs to be explained. The shrinkage depth is related to the moisture release of concrete as described in Chapter 3. According to the fact that moisture between the bearing structure and the cement screed is still at 90 % months or years after casting Avak and Glaser (2007), a moisture gradient occurs in the cross section of concrete floor. This moisture gradient implies that the surface of the concrete floor shrinks according to the relative humidity of the surrounding air, whereas the bottom of the concrete floor with a humidity of at

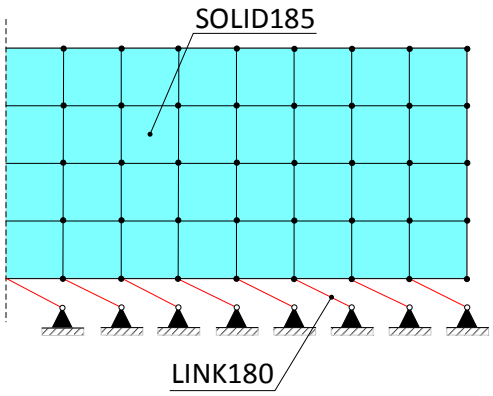

Figure 4.15: Diagonal LINK180 Elements

least 90%, shrinks only hardly. This is highlighted by Figure 4.16 where shrinkage is represented by a thermal load case as already mentioned in subsection 4.3.3.

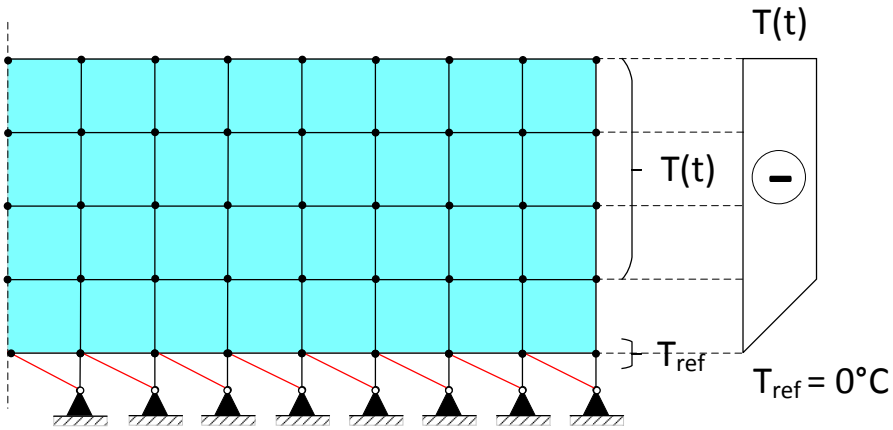

Figure 4.16: Temperature distribution for the model with vertical and diagonal LINK180 Elements. $T(t)$ is the equivalent cooling temperature and T_{ref} is the reference temperature within simulation

In the following, if the chosen failure criterion (maximum allowable concrete expansion) for LINK180 Elements is fulfilled, the concrete floor will curl within simulation.

For simulation of contact between bearing structure and concrete floor, diagonal LINK180 Elements are used. The failure criterion is the same than for the vertical LINK180 Elements.

4.4.2 Verification of the model

To verify the mesh size of the finite element model for the direct bond case, a quarter of the large scale tests, considering again the symmetry axes, was modelled. Symmetry axes are defined, similar to the model of the H-shaped specimen, along XY-plane and along XZ-plane. The model consists of a bearing structure, represented by a thin slab, and of the cement screed on top of the bearing structure.

The bearing structure itself is supported in UX-, UY- and in UZ-direction. The steel frame (see Figure 3.45 in Chapter 3.5.1) is represented by a contact area in the entrance of the model. The conditions (support-conditions; contact-conditions) of this contact area are similar to the contact area of the H-shaped concrete specimen (see Chapter 4.3.1).

The mesh size of the large-scale FE-model was reduced gradually starting with a mesh size of 80 mm (Figure 4.17 a). To calculate the crack path of the large scale tests, a mesh size of 40 mm (Figure 4.17 b) was not precise enough. The mesh size was reduced as long as the calculated crack path converged to the measured results from large-scale tests.
Finally a mesh size of 25 mm (Figure 4.17 c) showed a good compromise between calculation time and accuracy of resulting crack path, especially as a mesh size of 20 mm (Figure4.17 d) does not show any improvement.

Figure 4.18 a to Figure 4.18 h show the evolving calculated crack paths of the large scale tests. Crack started after 152 hours (6.25 days), represented by a first element failure in corner 1 and in corner 3 as represented in Figure 4.18 a. The end of the crack paths in corner 1 and in corner 3 was after 444 hours (18.5 days). At this time the model can be regarded as fully cracked. In corner 2 and corner 4 no crack path did develop.

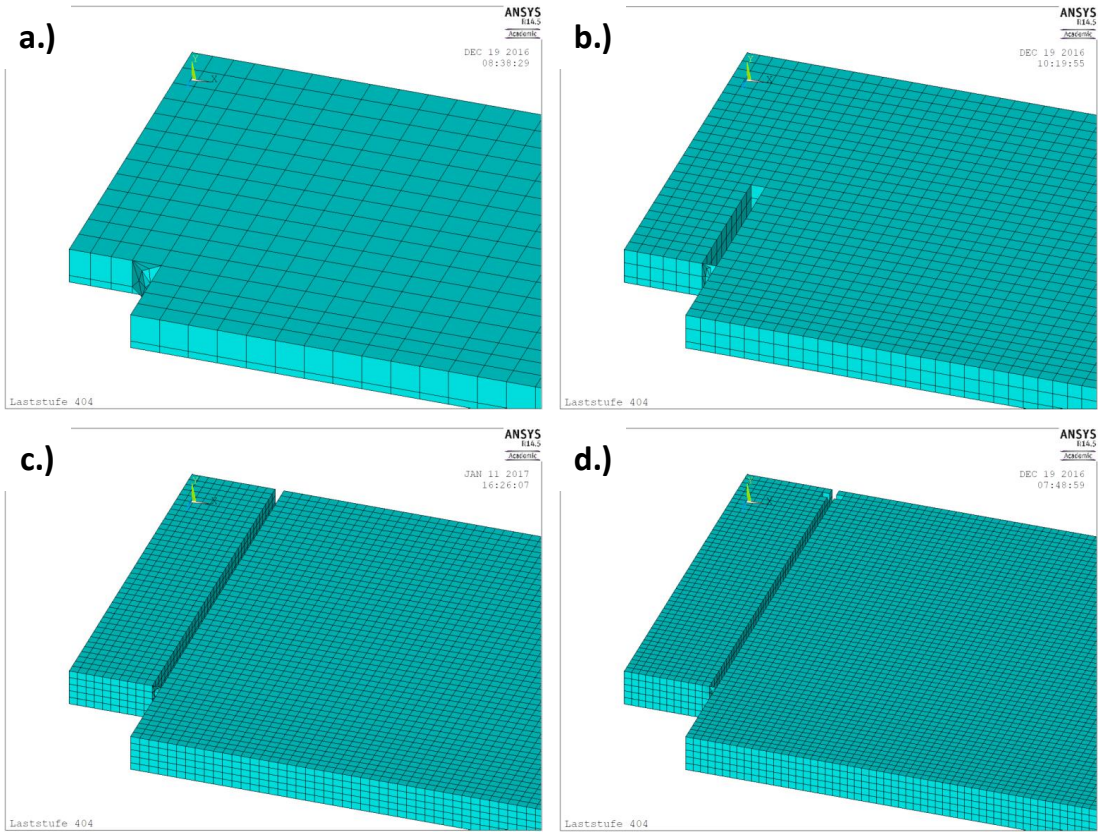

Figure 4.17: a.) FE-Model of the large-scale tests with an element size of 80 mm b.) FE-Model of the large-scale tests with an element size of 40 mm c.) FE-Model of the large-scale tests with an element size of 25 mm d.)FE-Model of the large-scale tests with an element size of 20 mm

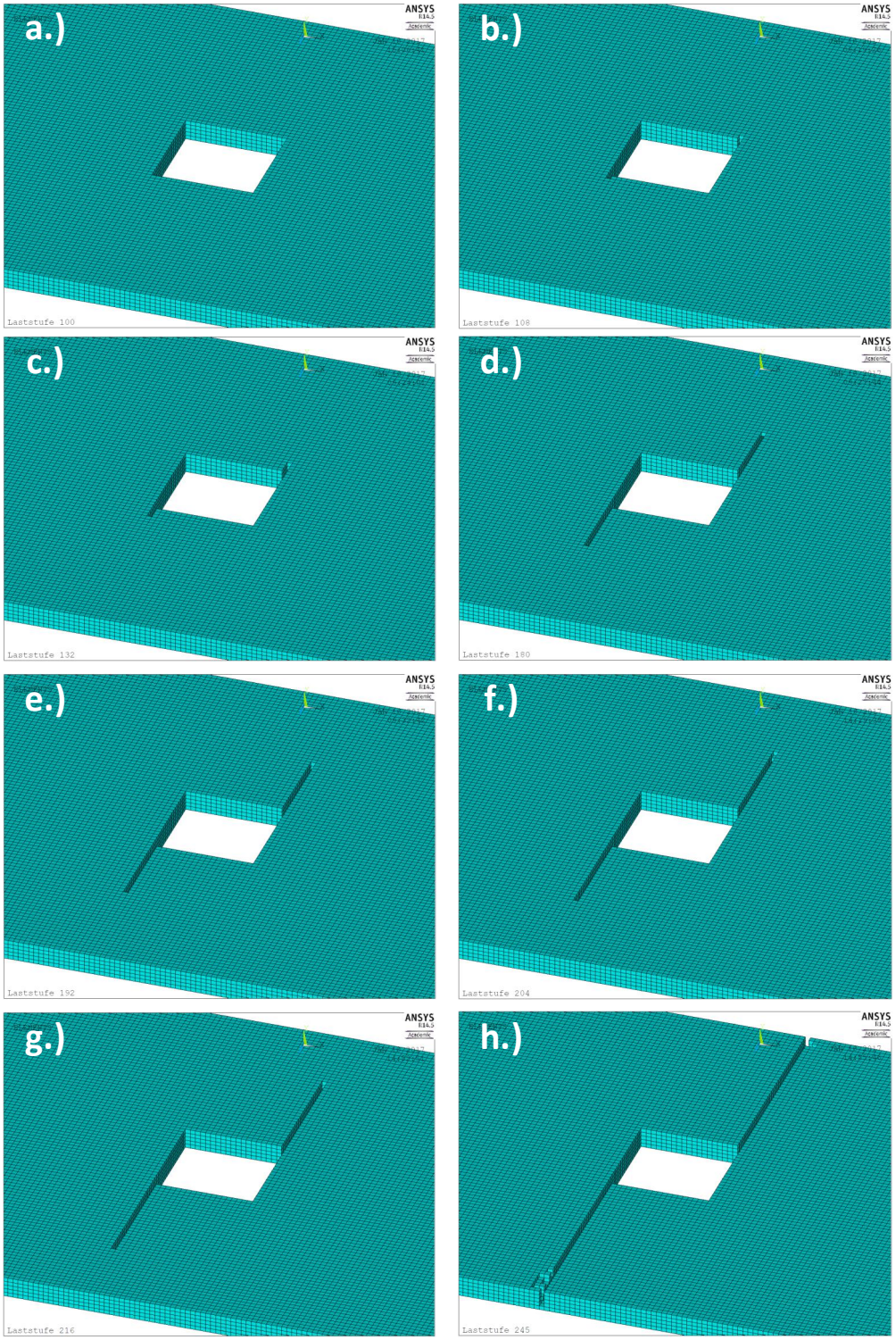

Figure 4.18: a.) Crack path within the FE-model after 12 hours b.) Crack path within the FE-model after 72 hours c.) Crack path within the FE-model after 108 hours d.) Crack path within the FE-model after 120 hours e.) Crack path within the FE-model after 240 hours f.) Crack path within the FE-model after 108 hours g.) Crack path within the FE-model after 120 hours h.) Crack path within the FE-model after 240 hours

Table 4.2 shows the measured crack path evolution of the large-scale tests (Figure 3.52 in Chapter 3.5.5) compared to the calculated crack paths from simulation. The corners are numbered as seen in Figure 4.19. During the tests, the first crack appeared in corner 1 and in corner 2 after two days. The length of the cracks was 3 mm respectively 5 mm. In corner 4 a first crack could be observed after four days (2 mm) and in corner 3 after seven days (8 mm). Within the simulation, the crack path grows during the first sixth day in corner 1 and in corner 3. In the simulation the model could be regarded as fully cracked at 18.5 days, as well in corner 1 as in corner 3. In the experimental in-situ tests, the fully cracked state of corner 1 was recorded after 20 days. Due to the fact, that the last visual control was at day 16 after casting of the areas, it could be possible, that corner 1 was already fully cracked earlier.

All in all, the chronological evolution as well as the spatial appearance of the simulated crack path compared to the crack path of the experimental in-situ tests shows a very good accordance.

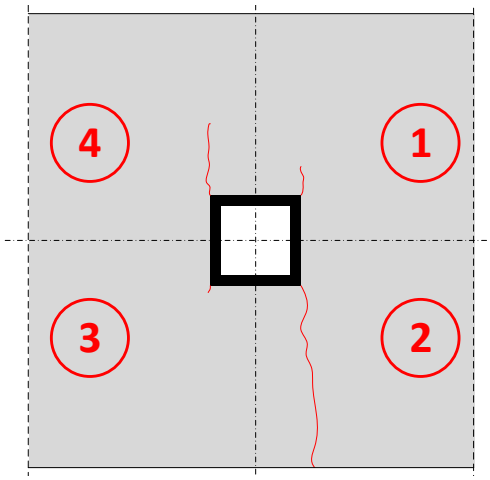

Figure 4.19: Representation of cracking of the experimental in-situ test

Table 4.2: Measured crack evolution versus calculated crack path evolution of large scale tests

time	time	Crack length [**mm**]							
time [**d**]	time [**h**]	Corner 1		Corner 2		Corner 3		Corner 4	
		FE	Test	FE	Test	FE	Test	FE	Test
0	0	0	0	0	0	0	0	0	0
1	24	0	0	0	0	0	0	0	0
2	48	0	5	0	3	0	0	0	0
3	72	0	5	0	3	0	0	0	0
4	96	0	5	0	3	0	0	0	2
5	120	0	5	0	3	0	0	0	2
6	144	0	10	0	3	0	0	0	2
7	168	25	10	0	6	25	8	0	6
8	192	25	13	0	6	25	18	0	6
9	216	75	30	0	11	75	35	0	8
13	312	350	55	0	35	350	120	0	10
14	336	425	70	0	35	425	170	0	16
15	360	525	70	0	35	525	170	0	36
16	384	600	95	0	35	600	180	0	41
20	480	1000	1000	0	35	1000	200	0	41
23	552	1000	1000	0	50	1000	315	0	45
30	720	1000	1000	0	50	1000	390	0	45
37	888	1000	1000	0	110	1000	510	0	45
47	1128	1000	1000	0	145	1000	510	0	45

4.4.3 Numerical results of curling

Curling of floating concrete floors represents one very important factor which results in a damage of the concrete floor. Due to this damage, the serviceability and the durability of a concrete floor are no more given. Thereby, curling describes a detaching of the edges of a rectangular concrete floor. This effect is caused by an uneven drying of the concrete floor: the surface dries due to evaporation, while the lower area has still a high moisture inside the concrete, which leads to a shrinkage of the surface, while the lower area does not shrink.

An analytical approach of curling of floating concrete floors was already developed in the 1990s by Eisenmann and Leykauf (1991). The basis for this analytical approach was an elastically bedded beam. The degree of curling (f_{max}; see Figure 4.20) is to calculate with Equation 4.5 and with Equation 4.4.

$$f_{max} = 0.75 \cdot \frac{t \cdot \varepsilon_s \cdot (h-t) \cdot (l_{krit})^2}{h^3} - 2.25 \cdot 10^{-6} \cdot \frac{(l_{krit})^4}{E \cdot h^2} \quad \text{[mm]} \tag{4.4}$$

$l < l_{krit}$: l_{krit} as length
$l > l_{krit}$: effective plate length l as length

$$l_{krit} = 409.06 \cdot \sqrt{\frac{t \cdot \varepsilon_s \cdot (h-t) \cdot E}{h}} \quad \text{[mm]} \tag{4.5}$$

l_{krit}: critical length (see Figure 4.20)
t: depth of shrinkage [mm]
ε_s: degree of shrinkage [-]
h: thickness of the plate [mm]
E: Young's Modulus [N/mm^2]

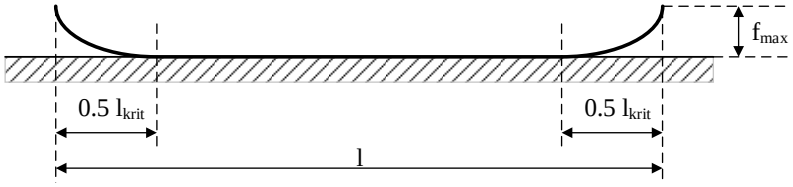

Figure 4.20: Curling due to shrinkage as decribed in Eisenmann and Leykauf (1991) inspired by Foos (2005)

The critical length l_{krit} (see Figure 4.20) can be calculated with Equation 4.5 and describes the area of a concrete floor which risks to curl due to shrinkage (see Figure 4.20).

According to Eisenmann and Leykauf (1991) and Eisenmann (1996), the depth of shrinkage can have a value of 40 mm to 60 mm. The influence of shrinkage depth to curling of concrete floors is shown in Figure 4.21 for a screed thickness of 80 mm.

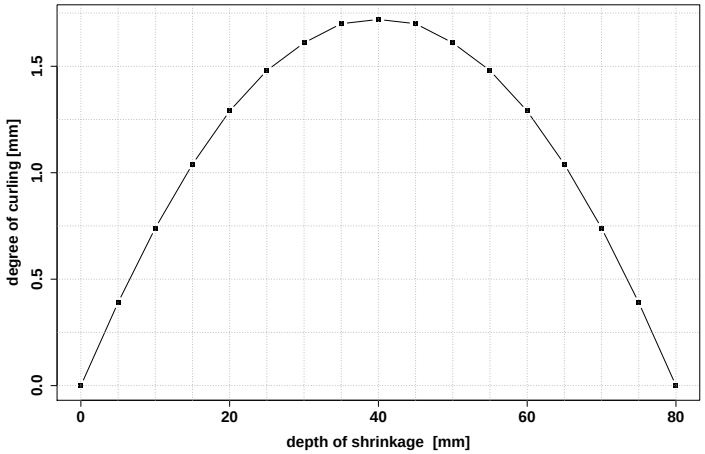

Figure 4.21: Degree of curling f_{max} due to depth of shrinkage for t=∞ and for a plate thickness of 80 mm

For concrete screeds fixed on foil, a maximum curling of 1.72 mm occurred due to shrinkage which can be calculated with Equation 4.4. The finite element model was calibrated by adjusting the calculated displacement (1.72 mm) of the corners of concrete floor on the value of the analytical approach (see Figure 4.22). The depth of shrinkage was 40 mm and is represented by a thermal load, as shown in Figure 4.23.

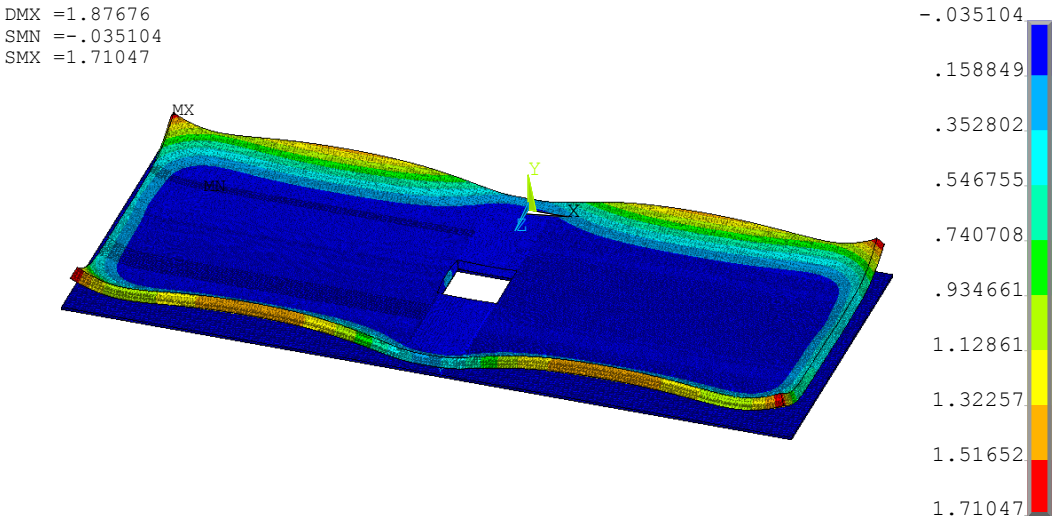

Figure 4.22: Degree of curling due to depth of shrinkage for t=∞

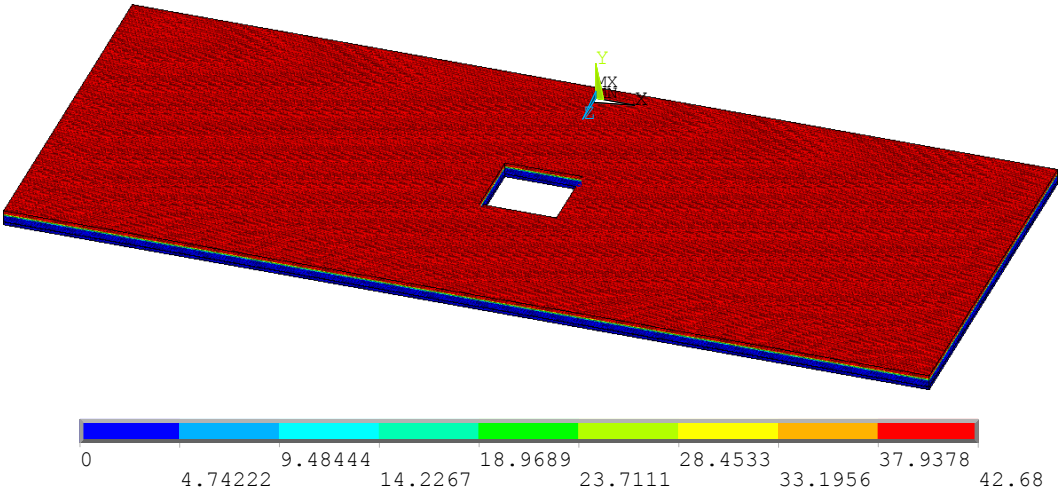

Figure 4.23: Depth of shrinkage for t=∞ represented by a thermal load case in [$°C$]

4.5 Summary

In the current chapter, a finite elements model was developed, which can calculate a crack path in a concrete floor due to shrinkage of the concrete used, considering its material properties such as the uniaxial tensile strength and Young's Modulus. To this reason, an H-shaped concrete specimen was developed, which was obstructed during the shrinkage process by two inserted steel tubes with welded on steel plates. In a further step, the approach chosen to calculate a crack path, the element failure method, was applied to large scale tests. In both cases, the finite element model was calibrated, regarding the element failure. In addition, the large-scale slab was calibrated in respect of curling. To this reason, the contact between bearing structure and cement screed was simulated by LINK-Elements. Using 'shrinkage depth' for the cement screed (see Eisenmann and Leykauf (1991) and Eisenmann (1996)) and a suitable failure criterion for the LINK-Elements, curling was simulated for the first time. This model serves in the current chapter as a basis for an extensive parameter study.

5 Parameter study

The aim of the parametrical study is to identify the limits of possible dimensions of rectangular cement screeds regarding its length, height and width in function of varying boundary conditions such as relative humidity and support conditions. To avoid cracking in a concrete floor, the parametrical study will give important hints while planning new projects concerning the maximum possible dimensions of a cement screed. Furthermore, the model can be used to analyse the reasons of cracking of existing concrete screeds.

In a first step, the parameter study is prepared. To exclude possible shortcomings in the modelling of the finite element model, the ANSYS® model is verified by another finite element software named RFEM. As an indicator of the accuracy of the ANSYS$^{\circ}$ model, the maximum displacement of the entire structure (bearing structure and cement screed) caused by a traffic load is compared to the results from the displacements calculated with RFEM finite element software. RFEM is a finite element software developed by Dlubal Company for structural engineering applications. This comparison is carried out for a model with support on three axes slab and a flat slab.

In a further step, the parameters which will be varied are defined. The parameters are of two different types: geometrical parameters and environmental parameters. The geometrical parameters are the length of the cement screed and the height of the cement screed. The width was set constant. One of the environmental parameters, the relative humidity, influences the shrinkage behaviour decisively. Furthermore, in addition to these different parameters the chronological evolution of the material properties of the used concrete was taken into account.

In a first part the different parameters will be defined, the sequence of the parameter study is described. The current chapter closes with the evaluation of the parameter study and the summary of the chapter.

5.1 Preparation of the parameter study

5.1.1 ANSYS® Model

The model was created respecting its double symmetry, only a quarter of the model is calculated and the results are extruded later on to a full model. To verify the ANYSY FE-model the results of the maximum displacements are compared with a simplified finite element analysis on two different support conditions, a slab with support on three axes and a flat slab. The loads which induce the displacement are, besides the dead weight of the structure, a traffic load of 5.0 kN/m^2. This traffic load corresponds to the traffic loads according to DIN EN 1991-1-1:2002 + AC:2009 (2009) and to Goris (2010) for the use as sales room. The simulated slab has a length of 7000 mm, a width of 3500 mm and a height of 80 mm. For the slab with support on three axes, the structure is supported at the outer edges in Z-direction and additionally in the middle of the structure (see Figure 5.1 and 5.2). The flat slab lies at the four corners of the slab on single supports. Furthermore, the point supports are arranged on the outer edges in Y-direction at mid-span in X-direction (see Figure 5.3 and 5.4)

5.1.2 RFEM Model

Whereas in Ansys only one quarter of the structure is modelled, in the RFEM calculation the entire structure is simulated. Here, also a traffic load of 5.0 kN/m^2 is applied and the dimensions of the entire structure, as well as the support conditions, remain unchanged compared to the boundary conditions of the ANSYS® simulation.

5.1.3 Results

The results of the maximum displacement of ANSYS® simulation and of RFEM simulation are shown in Figure 5.1 and in Figure 5.4. The maximum displacements for the slab supported on three axes of the two different simulations are each 0.6 mm (Figure 5.1), (Figure 5.2)..

Also the maximum displacement for the point-support shows with 1.4 mm the same result for the simulation done with ANSYS® (Figure 5.3)as for the simulation done with RFEM (Figure 5.4).

Another indicator, to exclude a mistake in modelling is the profile of the displacement: They are absolutely identical. Thus, the ANSYS® finite element model is calibrated and verified.

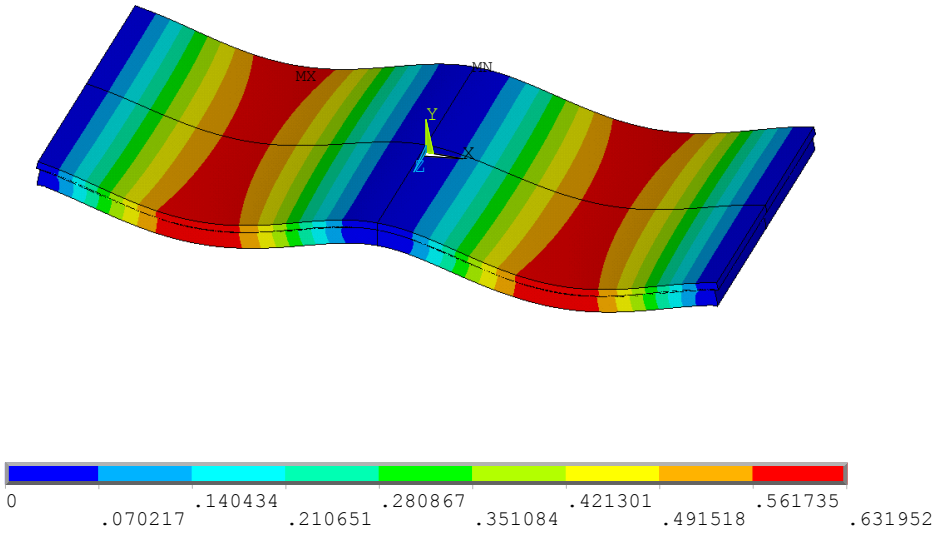

Figure 5.1: Displacement of slab supported on three axes simulated by ANSYS® Model; max. w=0.6 mm

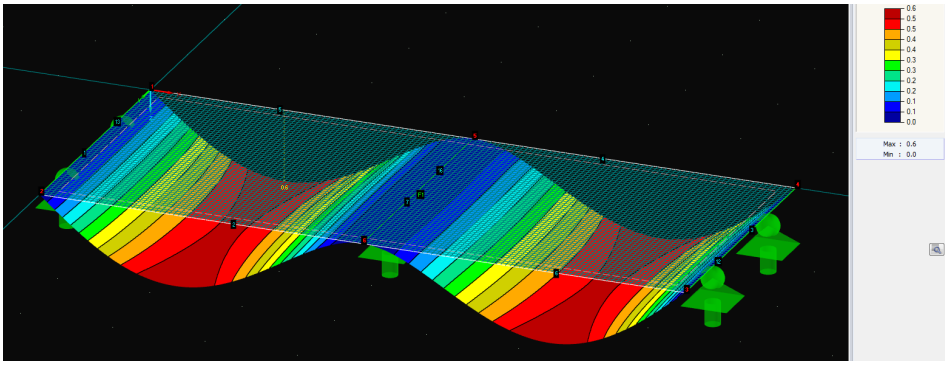

Figure 5.2: Displacement of slab supported on three axes simulated by RFEM Model; max. w=0.6 mm

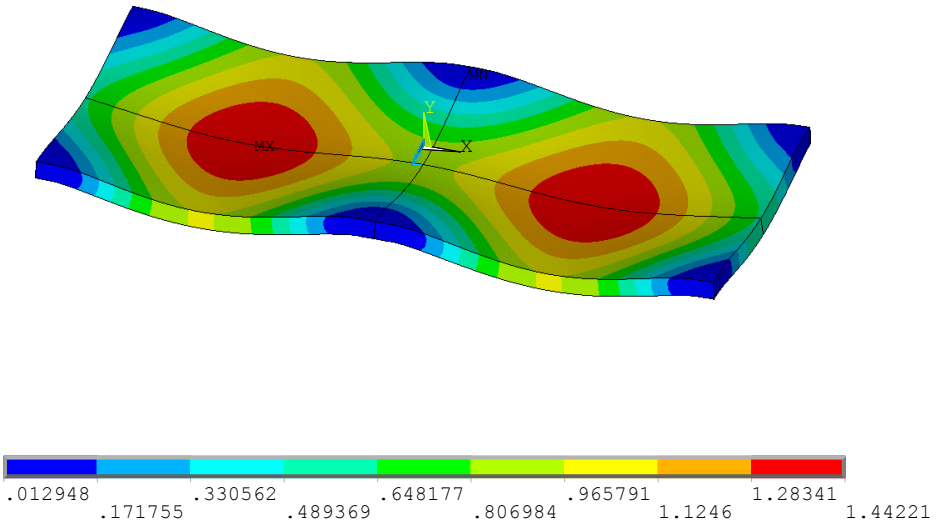

Figure 5.3: Displacement of point-supported structure simulated by ANSYS$^{\circ}$ Model; max. w=1.4 mm

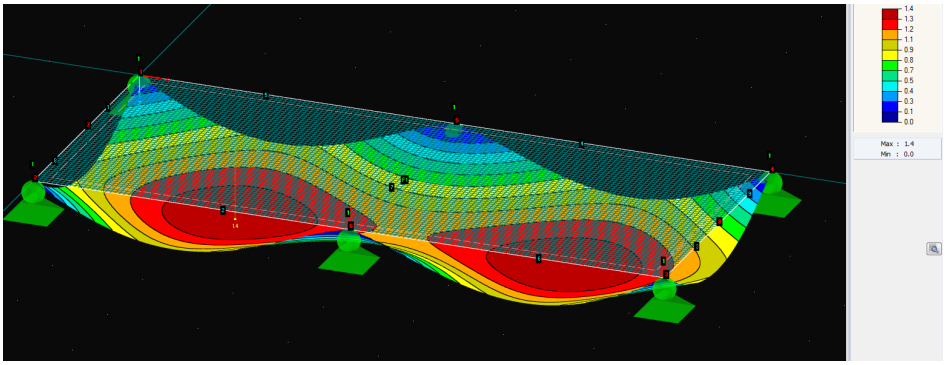

Figure 5.4: Displacement of point-supported structure simulated by RFEM Model; max. w=1.4 mm

5.2 Definition of parameters

This subsection determines the parameters used within the parametrical study. Besides different support conditions and different dimensions of the slab, environmental conditions which influence material properties have to be defined.

5.2.1 Boundary conditions

Three different kinds of support conditions will be investigated. The first one is a full-surface support, such as industrial floors founded directly on the ground. The two others

are the already mentioned slab supported on three axes and the point support.
Besides the support conditions, the dimensions of the slab will be varied according to Formula 5.1 with recommendations of Betonstein Handwerk (2011) and of Schäfer and Beck (2015). These two references describe that to avoid cracking in cement screeds, the relation width to length, according to Formula 5.1, should have a value of 1/3 to 2/3 but may not be greater than 35 m^2 Betonstein Handwerk (2011), respectively 45 m^2 Schäfer and Beck (2015).

$$\frac{width}{length} = \frac{1}{3} \ to \ \frac{2}{3} \ \leq 35m^2 \ to \ 45m^2 \tag{5.1}$$

The length of the slab is varied in the following simulations from 6000 mm up to 9000 mm and the width is kept constant at 4000 mm. The increment of length change is 1000 mm. The height is varied from 50 mm to 80 mm within the simulations with an increment of 10 mm. It is described in Schäfer and Beck (2015), that the height of the concrete screed is an important factor which influences its bearing capacity decisively. This is clearly explained in Formula 5.2 and in Formula 5.3 from Schäfer and Beck (2015).

$$\sigma_{FS} = \frac{1.5 \cdot F_{break} \cdot l}{w \cdot h^2} \quad [MPa] \tag{5.2}$$

$$F_{break} = \frac{\sigma_{FS} \cdot w \cdot h^2}{1.5 \cdot l} \quad [N] \tag{5.3}$$

σ_{FS}:	flexural strength [MPa]
F_{break}:	breaking load [N]
l:	length of screed [mm]
w:	width of screed in break [mm]
h:	height of screed [mm]

5.2.2 Material data

The material data which are needed for the parametrical study are Young's Modulus and the tensile strength. These data are varied over time for 24 hours, 48 hours, 168 hours, 28 days, 100 days and for five years. The changing material values, provided by KINFEST Gebauer (2016), are shown in Table 5.1.

Table 5.1: Material data of C20/25 concrete used for parameter study

Time in hours	12	24	48	168	672	2400	43800
Tensile strength [MPa]	0.44	0.75	1.11	1.65	2.20	2.47	2.82
Young's Modulus [MPa]	9800	17700	24400	26500	30000	31100	32000

Furthermore, the material properties vary as much as the relative humidity varies and influences as a consequence the shrinkage behaviour of the concrete. According to own measurements of the ambient relative humidity over a period of one year, relative humidity is varied from 20% to 65% (see Figure 5.5), with an additional step of 42.5 %.

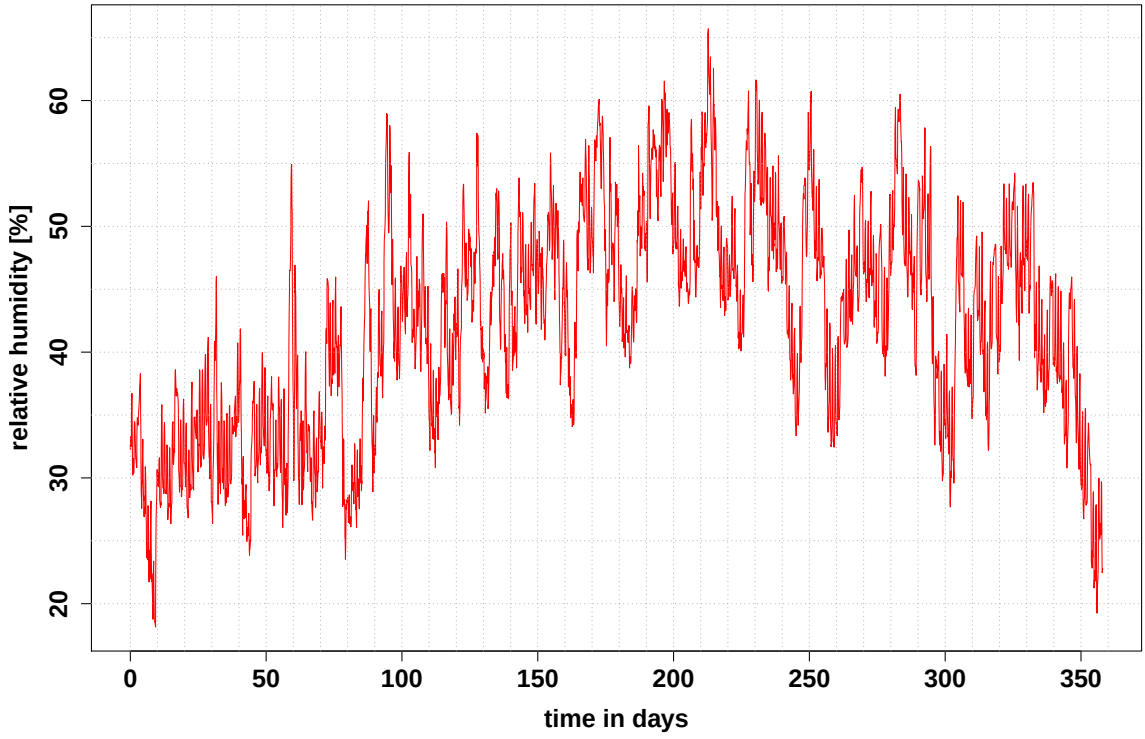

Figure 5.5: Development of relative humidity over a period of one year

The maximum degree of shrinkage (t=∞) is reached to 95 % after 1000 hours ($\approx$ 42

days) and the profile of the degree of shrinkage approaches asymptotically a final value (see Figure 5.6). After 5800 hours (≈ 242 days), the maximum degree of shrinkage is reached, no more significant changes in the profile of the degree of shrinkage can be registrated.

The previously mentioned can be clearly seen in Figure 5.6. The profile of the degree of shrinkage for a cement screed with a constant height of 50 mm, 20.0 % of relative humidity and a width of 4000 mm is given. The only difference constitutes the length of the screed which varies from 6000 mm to 9000 mm in 1000 mm steps.

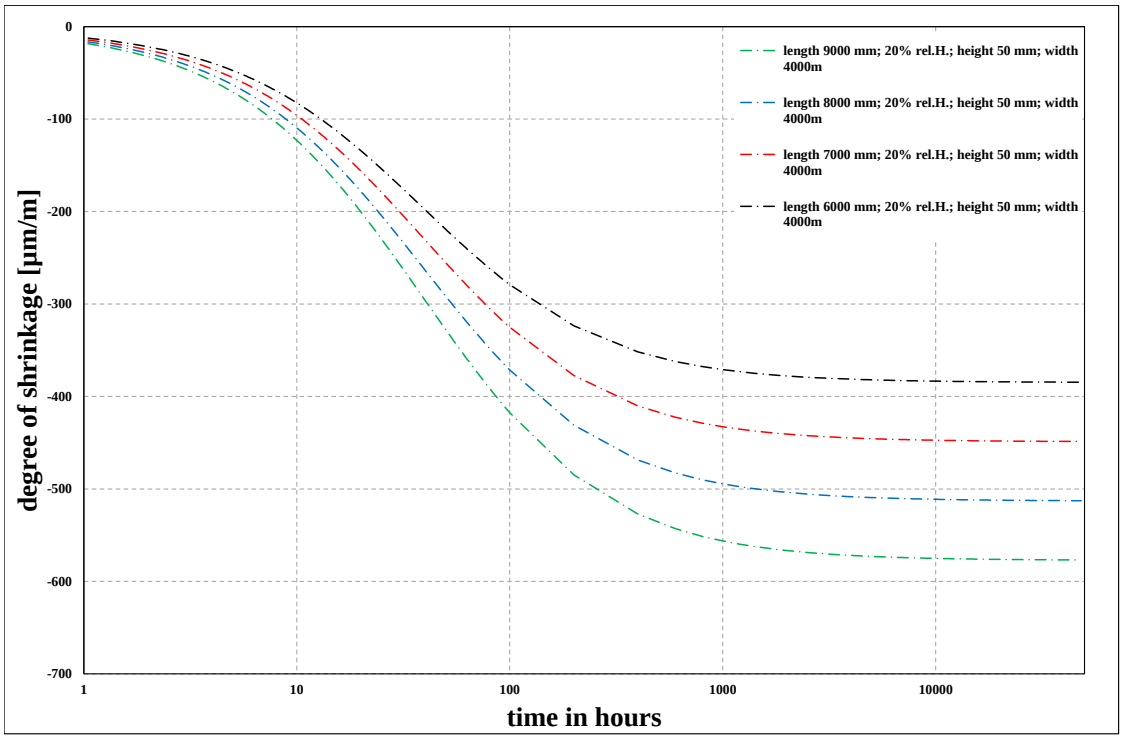

Figure 5.6: Profiles of shrinkage for a cement screed with a constant height of 50 mm, a constant relative humidity of 20.0%, a constant width of 4000 mm and different length of 6000 mm to 9000 mm.

5.2.3 Sequence of parameter study

During the parametrical study, the length and the height of the cement screed is varied as well as the relative humidity and the support conditions, all as a function of time. The individual values of the respective parameters are given in the following list:

• **Time**	• **Length**	• **Height**	• **relative humidity**	• **Support condition**
–24 h	–6000 mm	–50 mm	–20.0 %	–supported on three axes
–48 h	–7000 mm	–60 mm	–42.5 %	–full support
–168 h	–8000 mm	–70 mm	–65.0 %	–point support
–672 h	–9000 mm	–80 mm		
–2400 h				
–43800 h				

Every possible combination of the parameters is carried out in a simulation, to get the maximum existing stress in X-Z-plane.

5.3 Results of parameter study

Figure A.1 to Figure A.54 show the results from the parametrical study seperately for the different support conditions and the varying relative humidity [%] as a function of time in form of 3D-Barplots. In Figure 5.7 all the resulting stress states in X-Z-plane (see Figure 4.2) are shown as a function of time. Here, all interactions between the parameters are drawn in one diagram. Figure 5.12 to Figure 5.15 show the results separately for the different parameters.

Figure 5.8 to Figure 5.11 show the tensile stress evolution for different lengths (Figure 5.8), different heights (Figure 5.9) and different support conditions (Figure 5.11) of the analysed slab as a function of time.

For a better view, the X-axis is represented with a logarithmic scale. Furthermore, the maximum admissible tensile strength, predicted by KINFEST, is given in every single Figure.

Figure 5.8 to Figure 5.11 show the results seperately for the different parameters length (Figure 5.8), height (Figure 5.9), relative humidity (Figure 5.10) and support conditions

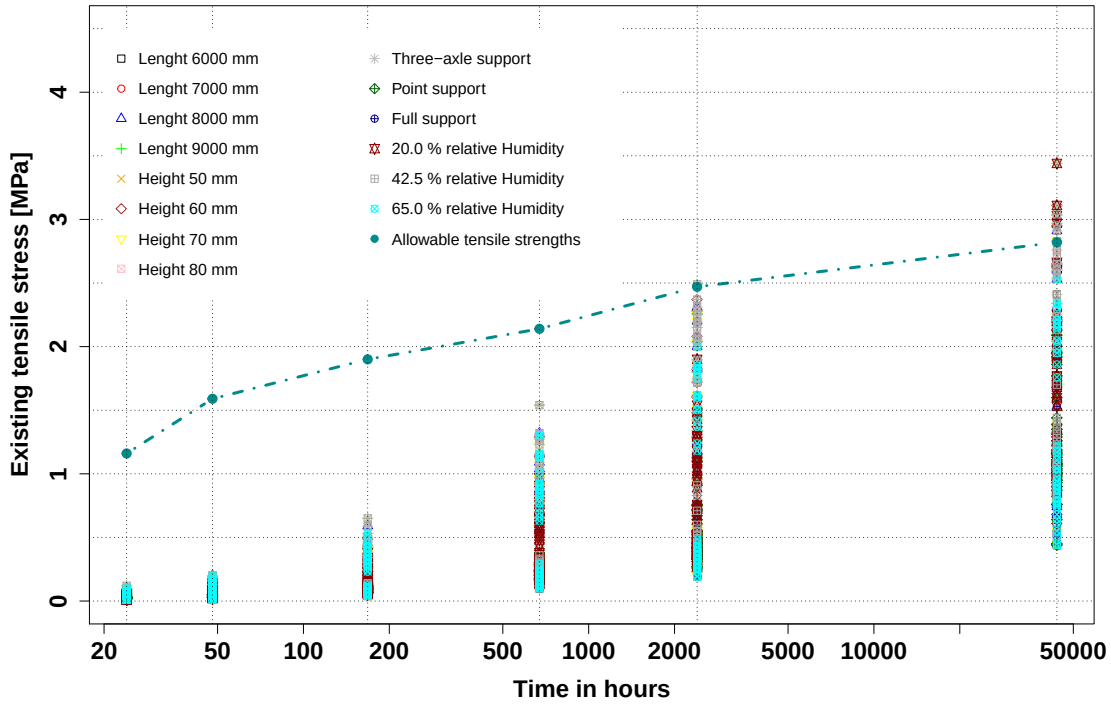

Figure 5.7: Resulting tensile strengths of the simulation versus the admissible tensile strength as a function of time

(Figure 5.11). It can be stated for all diagrams, that time 43800 hours (five years) is the critical time where the existing tensile strength exceeds the admissible tensile strength.

Therefore, Figure 5.12 to Figure 5.15 show the stresses only for time $t = 43800\ hours$. Figure 5.12 shows the stresses for the different lengths. It can be clearly seen, that only a length of 8000 mm and a length of 9000 mm cause an exceedance of the maximum admissible tensile strength, which is drawn in a green dot-dashed line. In Figure 5.13 the different investigated heights are illustrated. Each height has an influence (see Equation 5.2 and Equation 5.3) on the exceedance of the maximum admissible tensile strength. The three different relative humidities are shown in Figure 5.14. Only the relative humidity of 20.0 % and 42.5 % cause high stresses. Finally, in Figure 5.15, the influence to the existing tensile stresses according to the support conditions are illustrated. The slab supported on three axes is the only support system which causes an exceedance of the maximum admissible tensile strength.

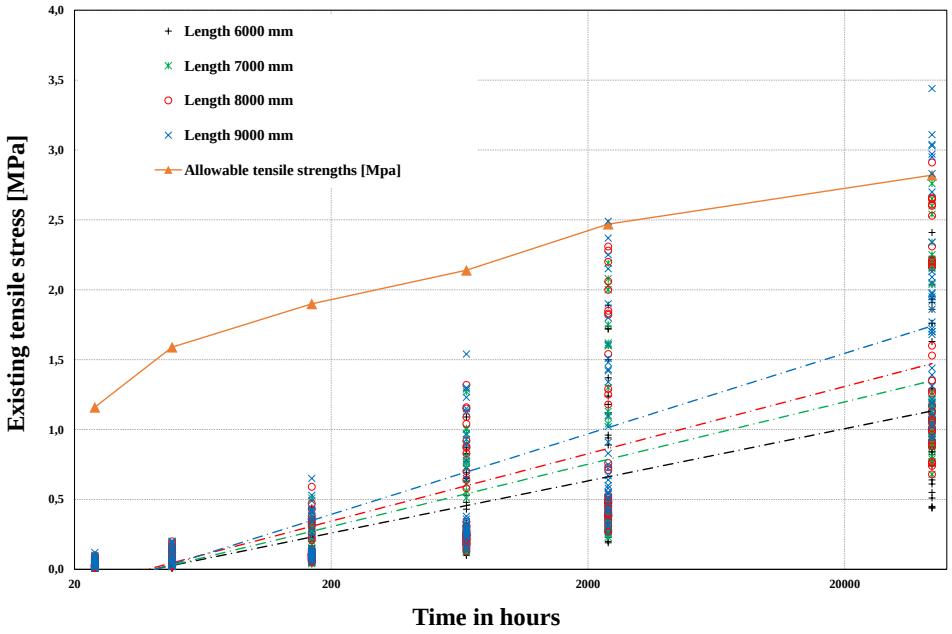

Figure 5.8: Tensile stress development in function of time for different slab lengths

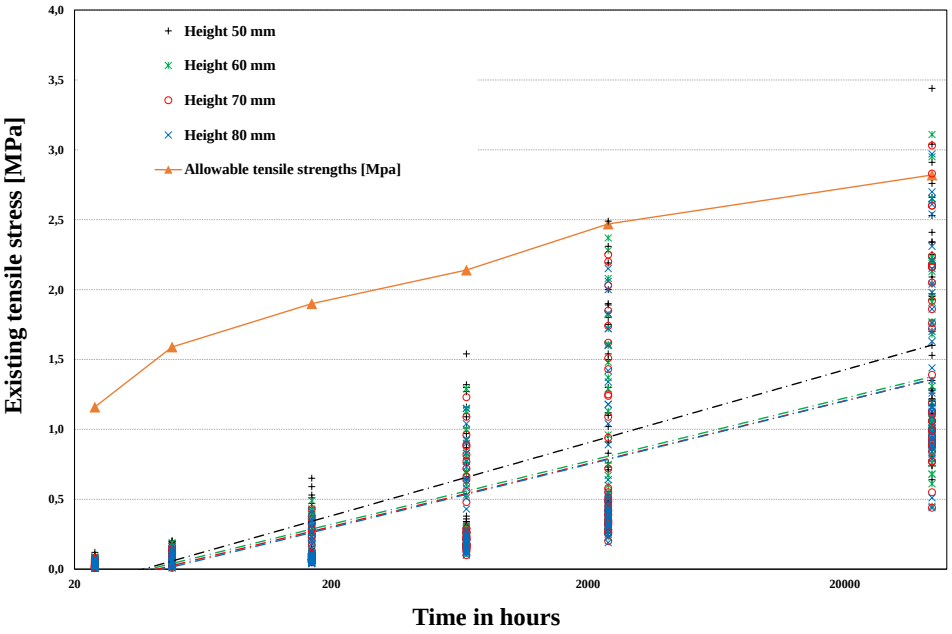

Figure 5.9: Tensile stress development in function of time for different slab heights

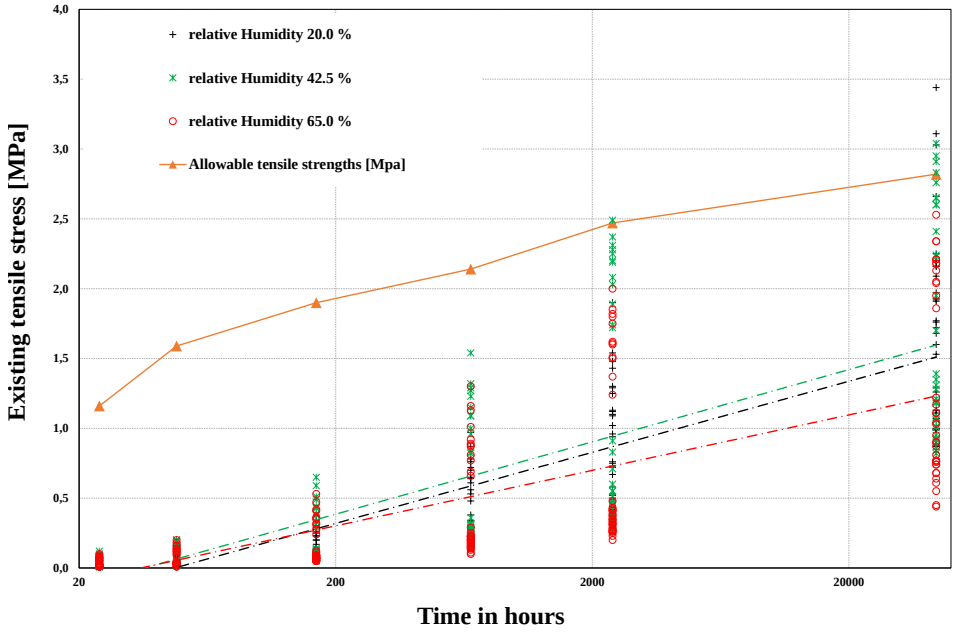

Figure 5.10: Tensile stress development in function of time for different relative Humidities

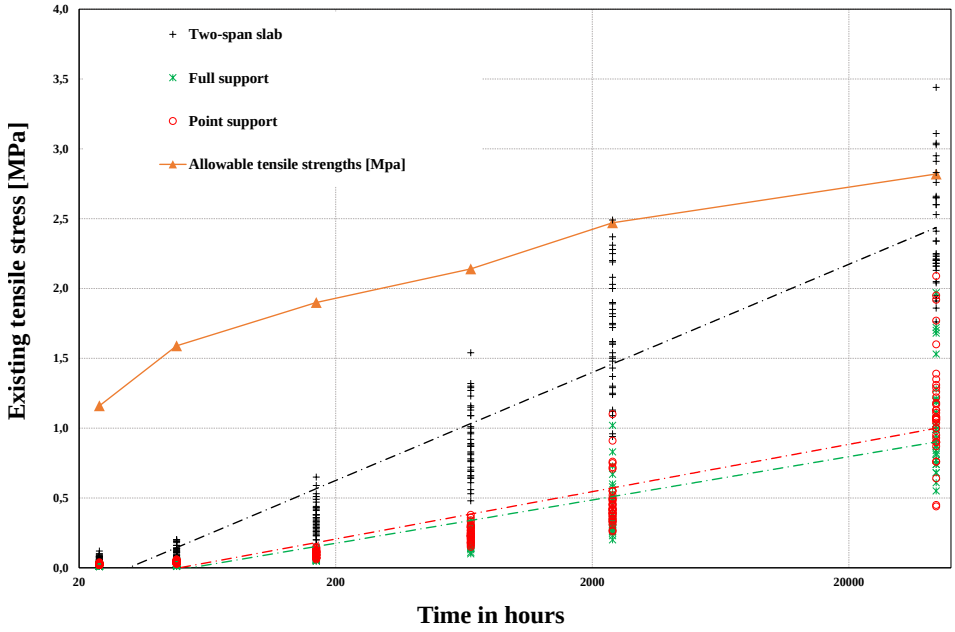

Figure 5.11: Tensile stress development in function of time for different support conditions of the slab

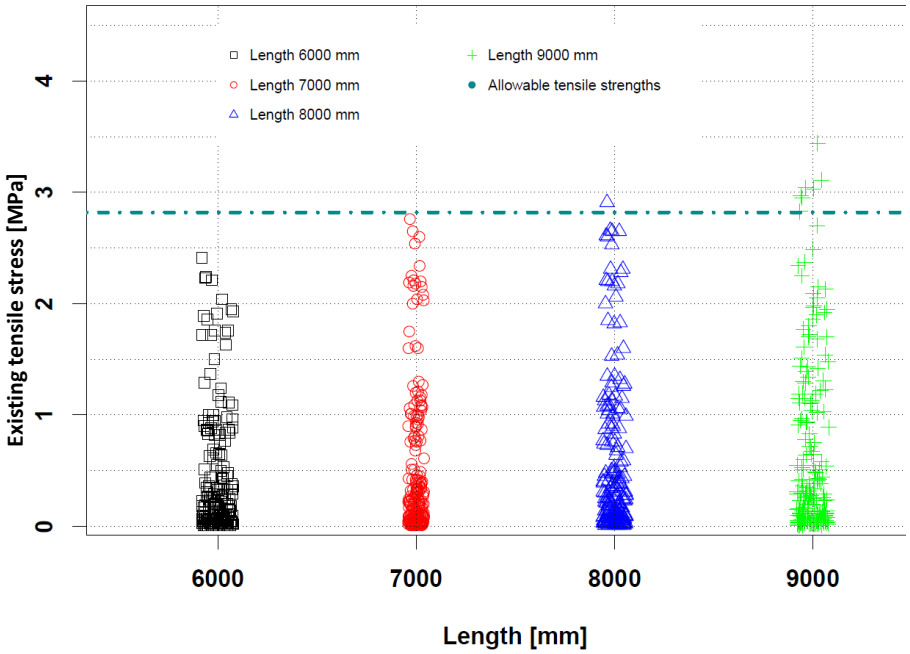

Figure 5.12: Tensile strength development at time $t = 5$ *years* for different lengths of the concrete screed

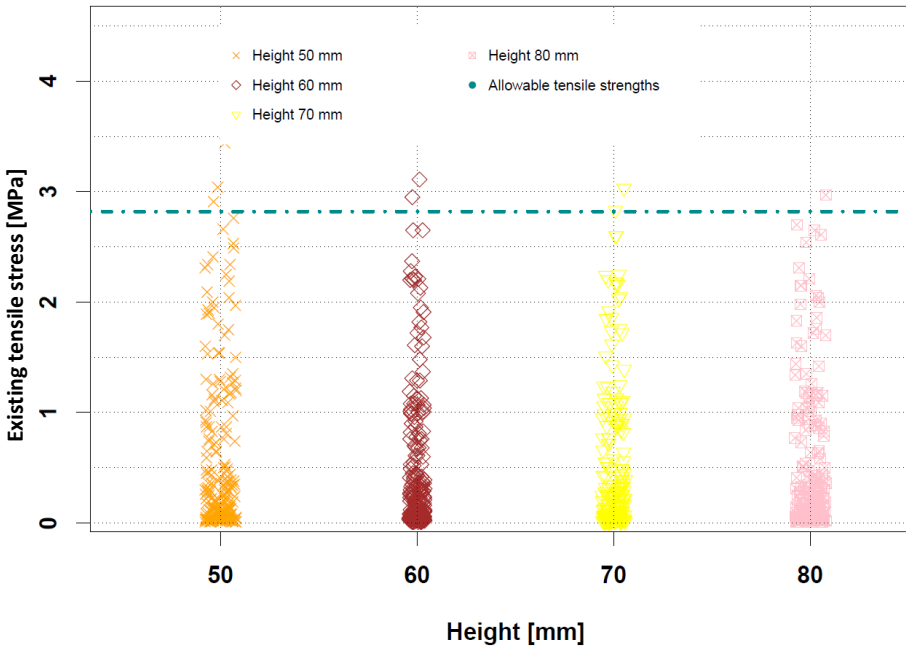

Figure 5.13: Tensile strength development at time $t = 5$ *years* for different heigths of the concrete screed

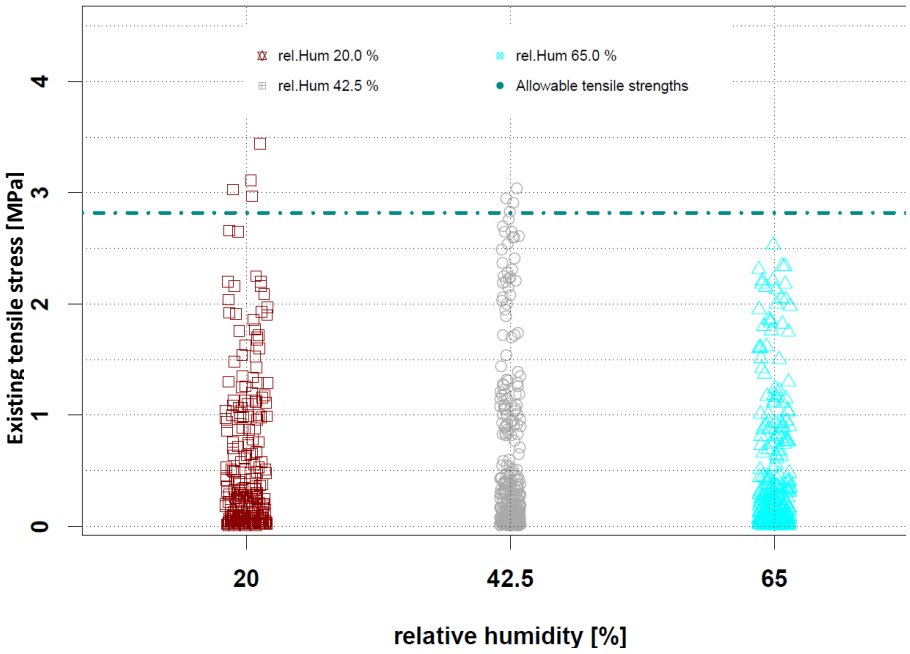

Figure 5.14: Tensile strength development at time $t = 5$ *years* for different relative humidity

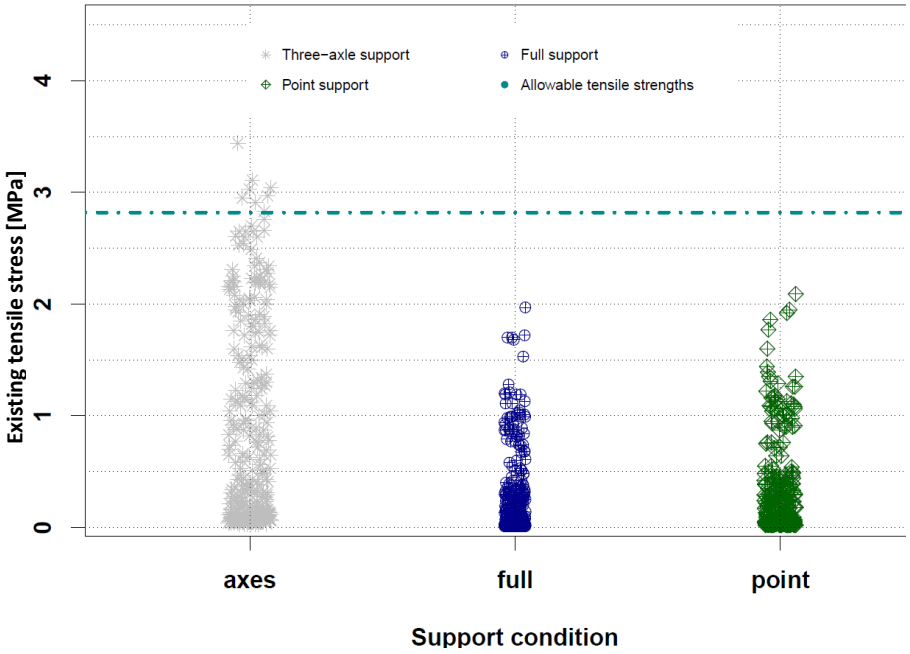

Figure 5.15: Tensile strength development at time $t = 5$ *years* for different support conditions

The parameters, which influence decisively the exceedance of the maximum admissible tensile strength can be reduced to a minimum As follows:

• **Time**	• **Length**	• **Height**	• **relative humidity**	• **Support condition**
–43800 h	–8000 mm	–50 mm	–20.0 %	–supported on three axes
	–9000 mm	–60 mm	–42.5 %	
		–70 mm		
		–80 mm		

In the following subsection, it will be clarified with the help of a statistical evaluation which parameter or which group of parameters have a high impact to produce high stresses.

5.4 Statistical evaluation

In order to determine the impact of one or more parameters (here: length, height, relative humidity, support conditions) on cracking, whereby each parameter could have a different impact level, the analysis of variance is a suitable tool. According to Tutz (2007), the analysis of variance provides variance analytical models which are able to represent dependencies between different parameters.

In the previous subsection, the parameters, which cause an exceedance of the maximum admissible tensile stresses in X-Z-plane were identified. The parameters have already been reduced in order to minimize the parameters to a minimum number. This reduction was carried out by a comparison of the produced tensile stresses within the FE-model and admissible tensile stresses according to the strength development of the concrete. In the current subsection, the parameters, which have a decisive influence to the exceedance of the maximum admissible tensile stresses in X-Z-plane, are not just identified: an order of magnitude is given of how strong the effect of the respective parameter and how strong the interaction of different parameters is. In advance, some necessary and important terms and definitions have to be presented. Besides this, the sequence of an analysis of variances is demonstrated as described in Tutz (2007). The subsection closes with the information, which group of parameters has a main impact to an exceedance of the maximum admissible tensile strength.

The first term is the binding target Figure which is in the present case the maximum

tensile stresses in X-Z-plane of the FE simulation. The target Figure is named with Y. Other relevant elements are the factor level and the investigation unit. The factor describes in the current case the different parameters (length, height, relative humidity, support conditions). The factor levels are then with 6000 mm, 7000 mm, 8000 mm, 9000 mm) the different lengths of the concrete screed. The investigation unit is the number of the respective level. The factor levels and the investigation unit can be written in a table as general notification as follows.

Table 5.2: General notification of a two factor variance analysis with I levels of factor A, J levels of factor B and K observations for each factor combination according to Tutz (2007)

		Factor B with levels				
		1	...	j	...	J
Factor A	1	y_{111} y_{112} $\vdots$ y_{11K}				
with	$\vdots$					
	i			y_{ij1} y_{ij2} $\vdots$ y_{ijK}		
levels	$\vdots$					
	I					

To get a model for the variance analysis, the target Figure must be described in accordance with the respective cause variable. Two different approaches are distinguished. In the model formulation (I), the target Figure is described in accordance with the respective factor combination, caused by the average value of all different variations μ_{ij}, which is superimposed by ε_{ijk}, an individual error term respecting the present observation(see Equation 5.4).

$$Y_{ijk} = \mu_{ij} + \varepsilon_{ijk}, \quad \varepsilon_{ijk} \sim N(0, \sigma^2) \tag{5.4}$$

$$i = 1, ..., I, \quad j = 1, ..., J \quad k = 1, ...K$$

This model has the substantial disadvantage that no analysis concerning the interactions are possible. In model formulation (II), the interaction between the factors can be taken into account. The general formulation of model (II) is shown in equation 5.5 as follows:

$$Y_{ijk} = \mu + \alpha_i + \beta_j + (\alpha\beta)_{ij} + \varepsilon_{ijk}, \quad \varepsilon_{ijk} \sim N(0, \sigma^2) \tag{5.5}$$

$$i = 1, ..., I, \quad j = 1, ..., J \quad k = 1, ...K$$

For the current parameter study the length = α, height = β, the relative humidity = γ and the support conditions = δ, model formulation (II) is:

$$\begin{aligned} Y_{ijk} = \mu + \alpha_i + \beta_j + \gamma_k + \delta_l + (\alpha\beta)_{ij} + (\alpha\gamma)_{ik} + (\alpha\delta)_{il} + (\beta\gamma)_{jk} + (\beta\delta)_{jl} + (\gamma\delta)_{kl} + \\ (\alpha\beta\gamma)_{ijk} + (\alpha\beta\delta)_{ijl} + (\beta\gamma\delta)_{jkl} + (\alpha\gamma\delta)_{ikl} + (\alpha\beta\gamma\delta)_{ijkl} + \varepsilon_{ijklm} \end{aligned} \tag{5.6}$$

$$i = 1, ..., I, \quad j = 1, ..., J \quad k = 1, ...K \quad l = 1, ..., L \quad m = 1, ..., M$$

In accordance to the single factor analysis of variance, the single parameters result to: The global mean value, or grand mean, is referred to as μ.

$$\mu = \frac{1}{IJKL} \sum_{i=1}^{I} \sum_{j=1}^{J} \sum_{k=1}^{K} \sum_{l=1}^{L} \mu_{ijkl}$$

The grand mean μ within parameter study becomes $\mu = \frac{1}{144} \sum_{i=1}^{4} \sum_{j=1}^{4} \sum_{k=1}^{3} \sum_{l=1}^{3} \mu_{ijkl}$. The main effects of the respective parameters $\alpha_i, \beta_i, \gamma_i$ and δ_i are described in the following. The effect for the factor A (length: 6.0 m; 7.0 m; 8.0 m; 9.0 m) is described as

$$\alpha_i = \mu_i... - \mu$$

with $\mu_i... = \frac{1}{JKL} \sum_{j=1}^{J} \sum_{k=1}^{K} \sum_{l=1}^{L} \mu_{ijkl}$,

and for the factors B (height: 50 mm; 60 mm; 70 mm; 80 mm), C (relative humidity: 20.0%; 42.5%; 65.0%) and D (support condition: support on three axes; point support; full support), the effects are described to

$$\beta_j = \mu_{.j..} - \mu$$

with $\mu_i... = \frac{1}{IKL} \sum_{i=1}^{I} \sum_{k=1}^{K} \sum_{l=1}^{L} \mu_{ijkl}$,

$$\gamma = \mu_{..k.} - \mu$$

with $\mu_i... = \frac{1}{IJL} \sum_{i=1}^{I} \sum_{j=1}^{J} \sum_{l=1}^{L} \mu_{ijkl}$,

$$\delta = \mu_{...l} - \mu$$

with $\mu_i... = \frac{1}{IJK} \sum_{i=1}^{I} \sum_{j=1}^{J} \sum_{k=1}^{K} \mu_{ijkl}$.

Furthermore, the different effects of the parameters are a function of time and thus the whole analysis must be repeated for each time step. The results of the respective effect is shown from Figure 5.16 to Figure 5.19. The X-axis is for the respective time [h] and the Y-axis is for the main effect [-].

In Figure 5.16 the effect of the parameter 'length' is shown. With regards to the global mean value, at time 43800 hours a length of 6000 mm has a positive influence on an existing tensile strength and a length of 9000 mm has an adverse influence on an existing tensile strength. This means that the difference of -0.31, for a length of 6000 mm at time 43800 hours, has a lower mean value, compared to the global mean value of all lengths at time 43800 hours. Because of the lower value, the difference is stated as positive. For a length of 9000 mm for the time 43800 hours, an exceedance of the tensile strength of +0.35 can be recorded. This difference is stated as adverse because the existing tensile strengths are higher than the global mean value.

Figure 5.17 shows the main effect for the parameter 'height'. It is obvious, that a height of 50 mm has an adverse influence at all times. The heights 60 mm, 70 mm and 80 mm, on the other hand, have a positive influence on the global mean value.

The effect of the parameter 'relative humidity' is given in Figure 5.18. From time

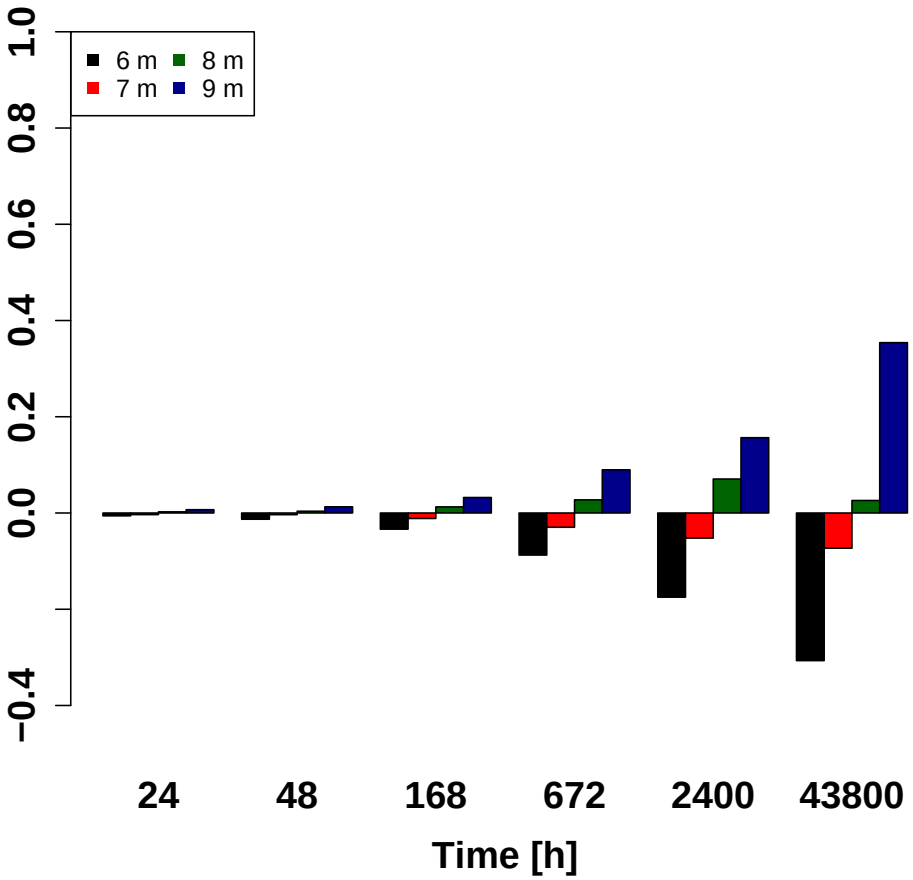

Figure 5.16: Main effect of parameter 'length' as a function of time

24 hours to 2400 hours, only a relative humidity of 42.5 % has an adverse influence regarding the tensile strength. At the time 43800 hours, a relative humidity of 20.0 % has an adverse influence on high tensile strengths. However, the impact is not as serious as compared to the other effects of 'length' and 'support condition'.

In Figure 5.19, the effect of the parameter 'support condition' is shown. It can be clearly stated, that the support condition 'Axes' for the slab supported on three axes, has an adverse influence at each time step. The previous diagrams did only show each single parameter in function of time. An interaction of the respective parameters is shown in the following.

In the next step, the interactions of the respective factors (length, height, relative humidity, support condition) are investigated. Therefore, interaction parameters are es-

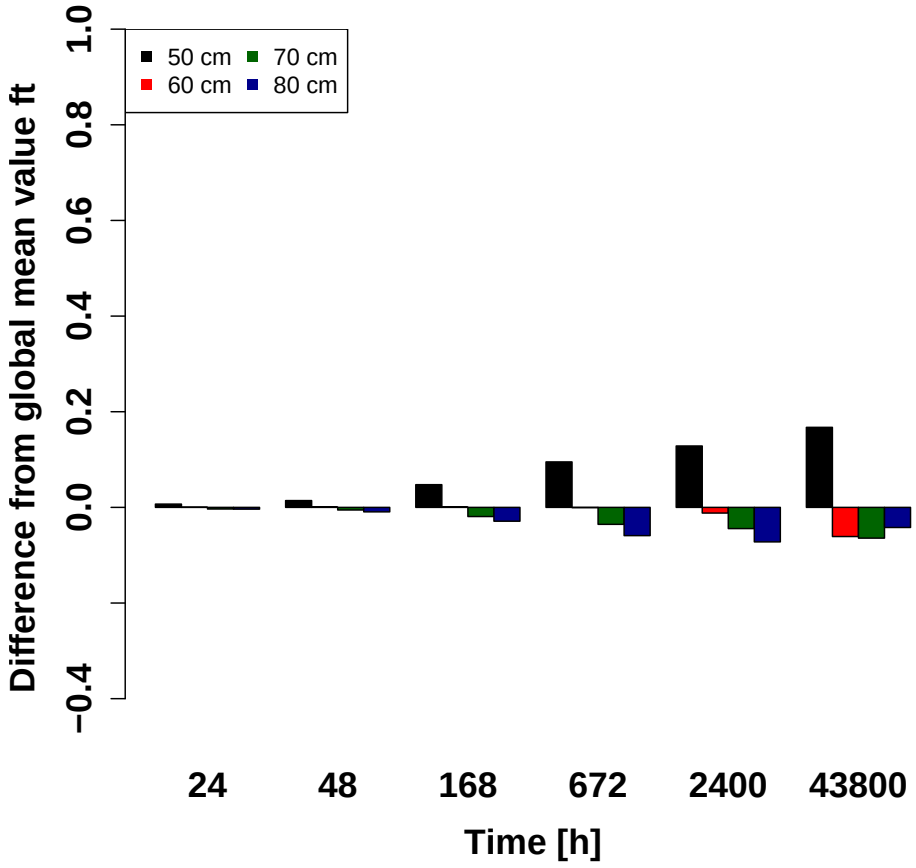

Figure 5.17: Main effect of parameter 'height' as a function of time

timated for the time 43800 hours. The respective interaction of the different parameters were estimated as follows.

$$\widehat{(\alpha\beta)} = \bar{Y}_{ij\ldots} - (\hat{\mu} + \hat{\alpha}_i + \hat{\beta}_j)$$

with $\bar{Y}_{ij\ldots} = \frac{1}{M}\sum_{m=1}^{M} Y_{ijklm}$.

$$\widehat{(\alpha\gamma)} = \bar{Y}_{i.k.} - (\hat{\mu} + \hat{\alpha}_i + \hat{\gamma}_k)$$

with $\bar{Y}_{i.k.} = \frac{1}{M}\sum_{m=1}^{M} Y_{ijklm}$.

$$\widehat{(\alpha\delta)} = \bar{Y}_{i..l} - (\hat{\mu} + \hat{\alpha}_i + \hat{\delta}_l)$$

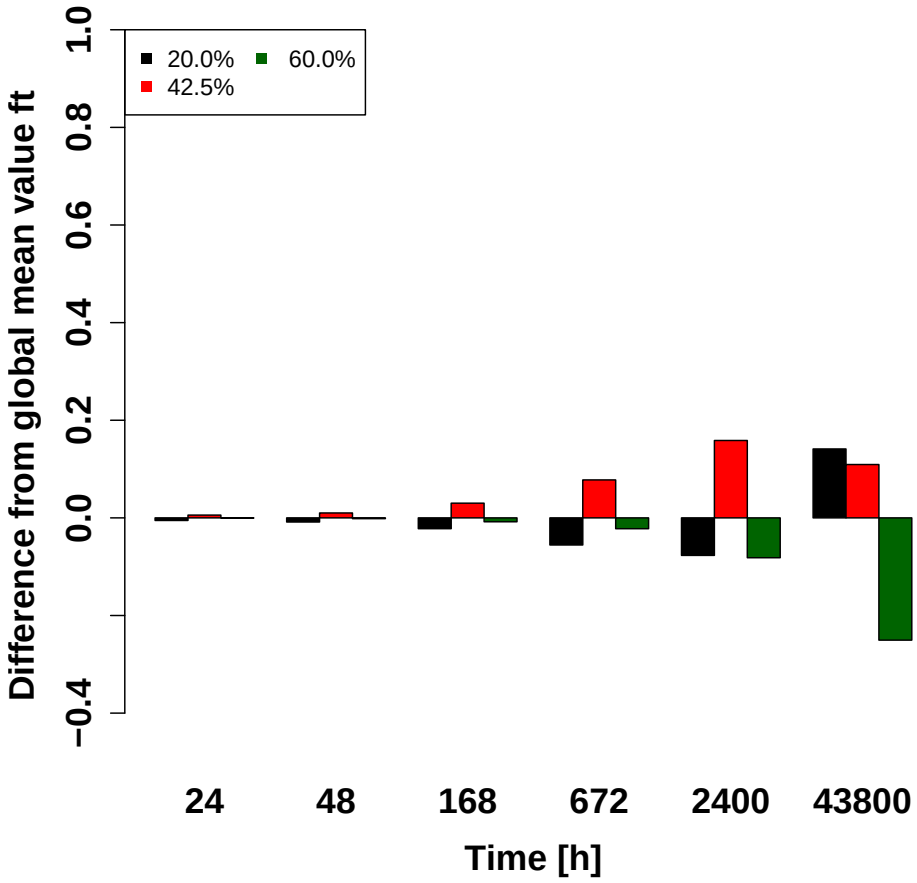

Figure 5.18: Main effect of parameter 'relative humidity' as a function of time

with $\bar{Y}_{i..l.} = \frac{1}{M}\sum_{m=1}^{M} Y_{ijklm}$.

$$(\widehat{\beta\gamma}) = \bar{Y}_{.jk..} - (\hat{\mu} + \hat{\beta}_j + \hat{\gamma}_k)$$

with $\bar{Y}_{.jk..} = \frac{1}{M}\sum_{m=1}^{M} Y_{ijklm}$.

$$(\widehat{\beta\delta}) = \bar{Y}_{.j.l.} - (\hat{\mu} + \hat{\beta}_j + \hat{\beta}_l)$$

with $\bar{Y}_{.j.l.} = \frac{1}{M}\sum_{m=1}^{M} Y_{ijklm}$.

$$(\widehat{\gamma\delta}) = \bar{Y}_{..kl.} - (\hat{\mu} + \hat{\gamma}_k + \hat{\delta}_l)$$

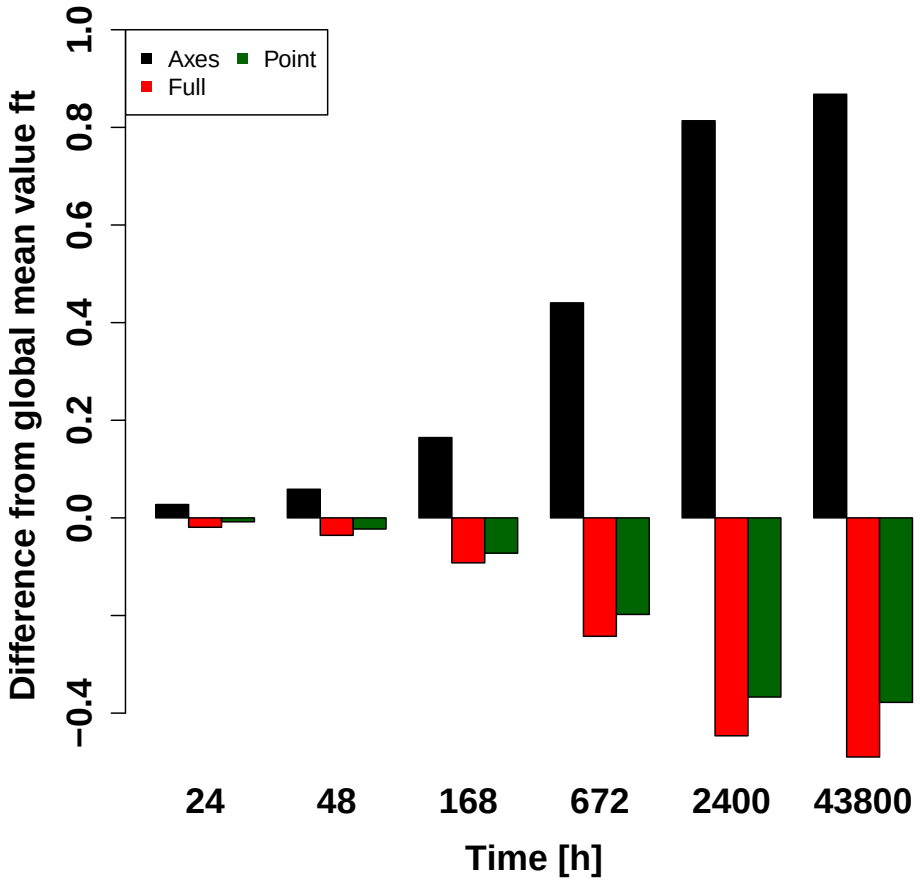

Figure 5.19: Main effect of parameter 'support condition' as a function of time

with $\bar{Y}_{..kl.} = \frac{1}{M} \sum_{m=1}^{M} Y_{ijklm}$.

In total, six interaction diagrams are shown from Figure 5.21 to Figure 5.26. For the interpretation of the diagrams (see Figure 5.20), three different possibilities can be applied according to Tutz (2007).

In the left diagram of Figure 5.20 can be seen, that the two graphs are in parallel. This means, that there is no interaction. In the middle diagram of Figure 5.20, the two graphs cross. This means, that there is a full interaction. Finally, in the right diagram no clear hint for an interaction can be noticed within the considered range.

Within Figure 5.20 it becomes obvious that an interaction between the parameters 'length' and 'height' is existing (see Figure 5.21). The same could be observed for the parameters 'length' and 'relative humidity' (Figure 5.22).

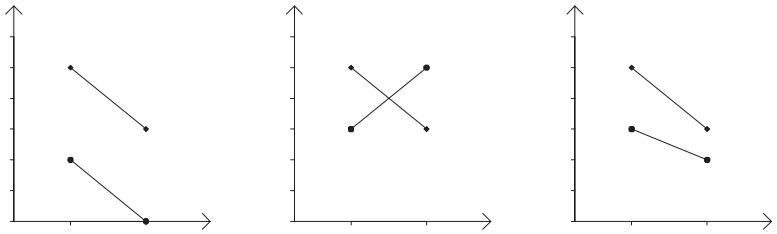

Figure 5.20: Graphical illustration of a diagram (left) without interaction, diagram (middle) with full interaction and diagram (right) with main effects and interaction from Tutz (2007)

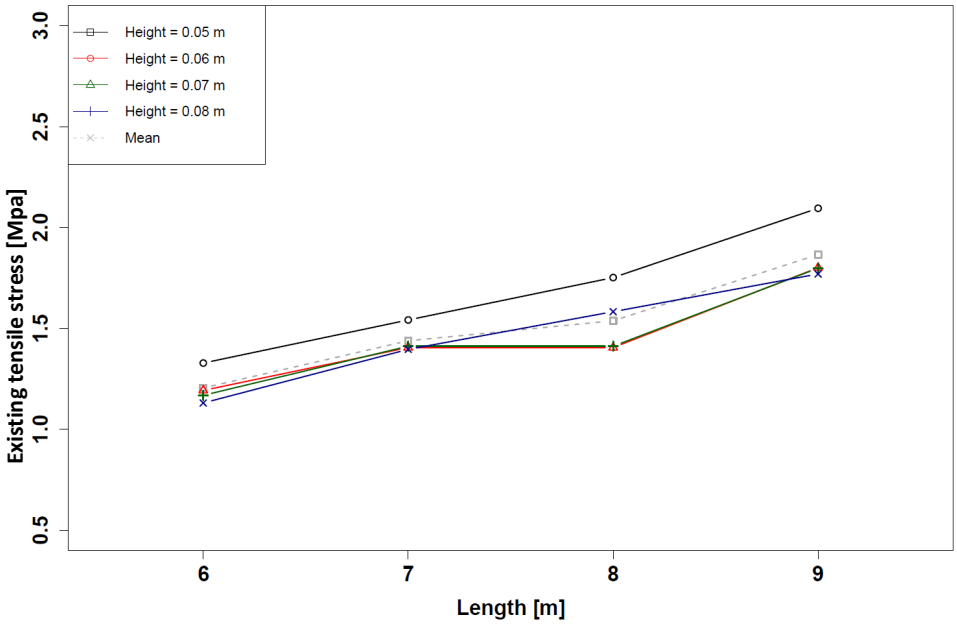

Figure 5.21: Estimated interaction between length and height at t=43800 hours

In Figure 5.23, Figure 5.24, Figure 5.25 and in Figure 5.26 there is no obvious interaction between the respective parameters.

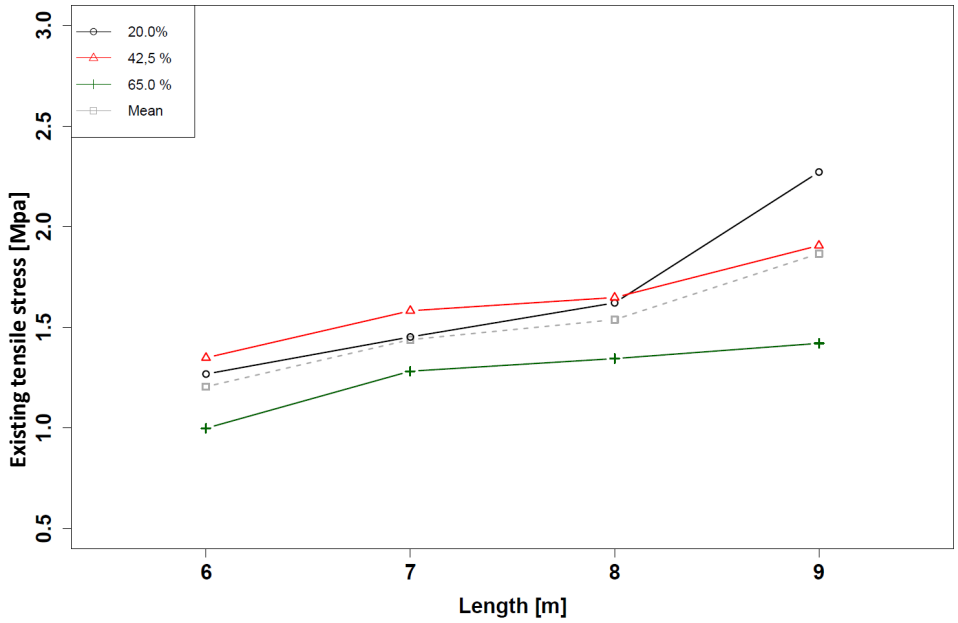

Figure 5.22: Estimated interaction between length and relative humidity at t=43800 hours

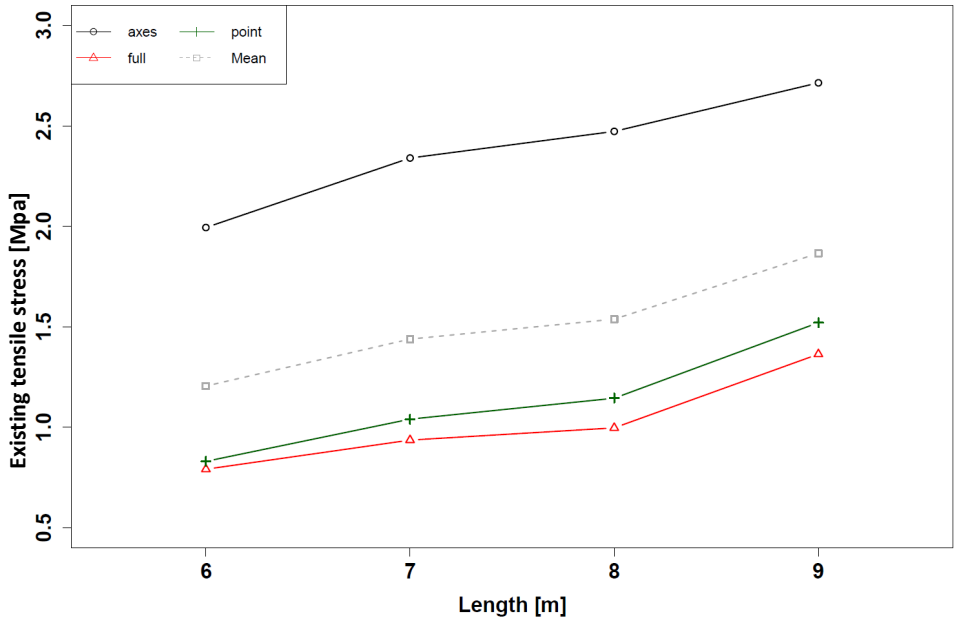

Figure 5.23: Estimated interaction between length and support condition at t=43800 hours

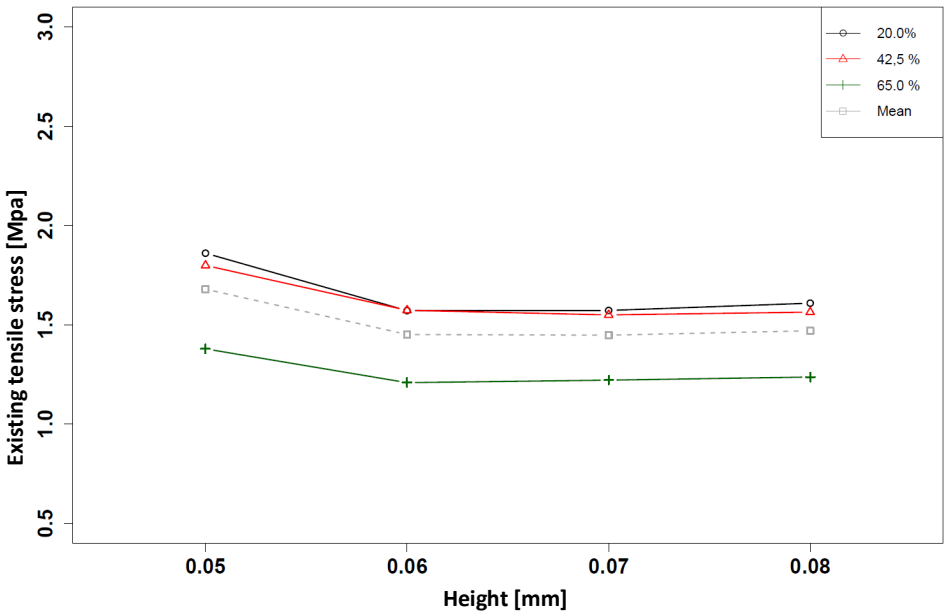

Figure 5.24: Estimated interaction between height and relative humidity at t=43800 hours

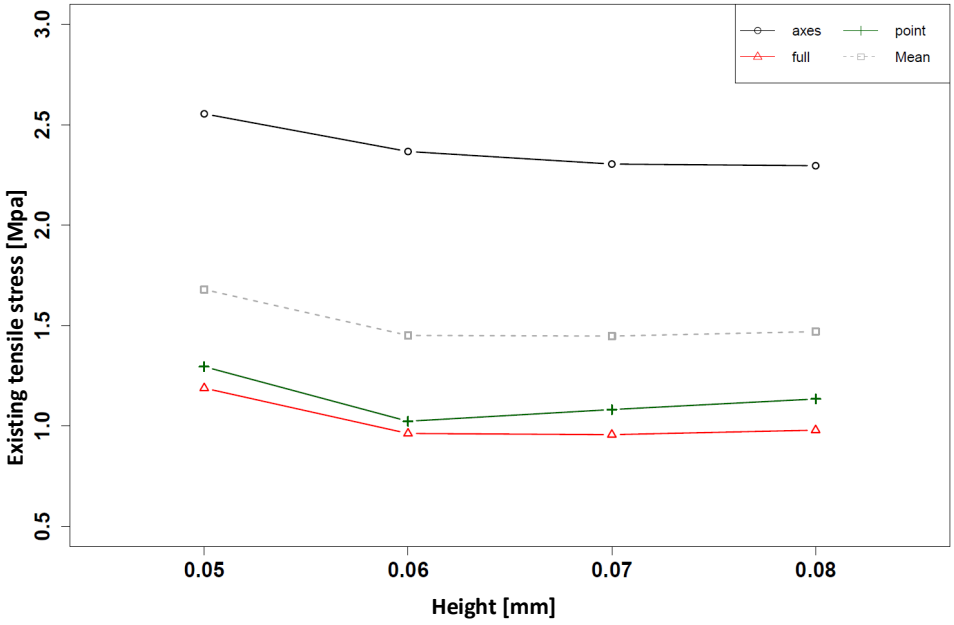

Figure 5.25: Estimated interaction between height and support condition at t=43800 hours

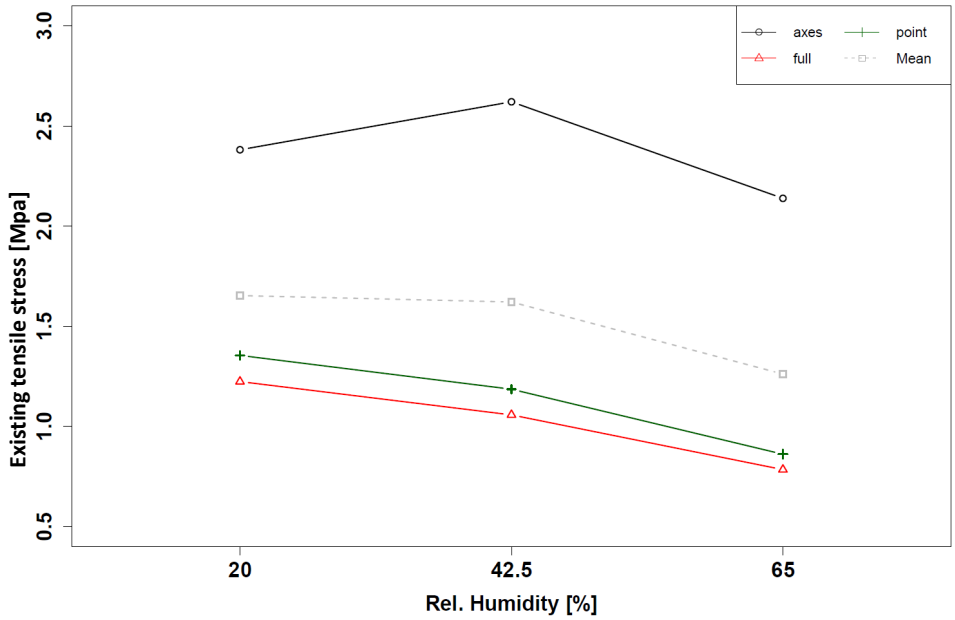

Figure 5.26: Estimated interaction between relative humidity and support condition at t=43800 hours

In the following, three different types of null hypothesises will be proven. The analysis of variance provides statistical tests to proof these hypotheses. First, it is checked if there is an interaction between the chosen parameters. The test problem for this check is, in general, represented by the following equation.

$H_0^{A\times B} : (\alpha\beta)_{ij} = 0$ for all $i, j, \quad i = 1, ..., I, \quad j = 1, ..., J$ or

$H_1^{A\times B} : (\alpha\beta)_{ij} \neq 0$ for at least two pairs of (i, j).

The null hypothesis implies, that all interactions are zero, while the alternative implies that interaction exists.
Furthermore, it should be examined if some of the different analysed parameters have an influence to the target Figure. In this case some parameter dominate on others. The general formulation for this problem is, according to Tutz (2007), as follows.
Main effect caused by parameter A:

$H_0^A : \alpha_i = 0$ for all $i = 1, ..., I$ or

H_1^A : for at least two α_i *with* $\alpha_i \neq 0$

Main effect caused by factor B:

$H_0^B : \beta_j = 0$ for all $j = 1, ..., J$ or

H_1^B : for at least two β_j *with* $\beta_j \neq 0$

The variance decomposition is used for the derivation of suitable test values. The variance decomposition stipulates in general, that the total deviation (SQT) is the sum of the deviation caused by factor A (SQA), the deviation of factor B (SQB), the deviation of the interaction of factor A and of factor B ($SQ(A \times B)$) and the residuum (SQR).

$$SQT = SQA + SQB + (SQ(A \times B)) + (SQR) \tag{5.7}$$

In the current case of the parameter study, formula 5.7 is given as:

$$SQT = SQI + SQJ + SQK + SQL + (SQ(I \times J)) + (SQ(I \times K)) + (SQ(I \times L)) + (SQ(J \times K)) + (SQ(J \times L)) + (SQ(K \times L)) + (SQR)$$

For the general case of a variance decomposition of two factors A and B, the respective terms of equation 5.7 results to:

$$SQT = \sum_{i=1}^{I} \sum_{j=1}^{J} \sum_{k=1}^{K} (Y_{ijk} - \bar{Y}_{...})^2$$

$$SQA = K \cdot J \cdot \sum_{i=1}^{I} (\bar{Y}_{i..} - \bar{Y}...)^2 = K \cdot J \cdot \sum_{i=1}^{I} \hat{\alpha}_i^2$$

$$SQB = K \cdot I \cdot \sum_{j=1}^{J} (\bar{Y}_{.j.} - \bar{Y}...)^2 = K \cdot I \cdot \sum_{j=1}^{J} \hat{\beta}_i^2$$

$$SQ(A \times B) = K \cdot \sum_{i=1}^{I} \sum_{j=1}^{J} (\bar{Y}_{ij.} - \bar{Y}i.. - \bar{Y}_{.j.} + \bar{Y}...)^2 = K \cdot \sum_{i=1}^{I} \sum_{j=1}^{J} \widehat{\alpha\beta}_{ij}^2$$

$$SQR = \sum_{i=1}^{I} \sum_{j=1}^{J} \sum_{i=k}^{K} (Y_{ijk} - \bar{Y}_{ij.})^2 = \sum_{i=1}^{I} \sum_{j=1}^{J} (K-1) S_{ij}^2$$

The scattering of the interactions $SQ(A \times B)$, caused by the factors A and B are set in relation to the remaining scattering SQR, whereby the scattering of the interactions is additionally divided by the corresponding degrees of freedom. The resulting test values of the respective null hypothesis have an F-distribution with the corresponding related degrees of freedom. In detail, the test value for the first test problem concerning the interactions is:

$$F_{A \times B} = \frac{SQ(A \times B)/(I-1)(J-1)}{SQR/IJ(K-1)}$$

The null hypothesis will be rejected to the level α, if the value of the test value is greater than the $(1-\alpha)$-Quantiles of the F-distribution with $(I-1)(J-1)$ degrees of freedom and $IJ(K-1)$ degrees of freedom for the case that $F > F_{1-\alpha}((I-1)(J-1),\ IJ(K-1))$.

The null hypothesis concerning the main effects of A is rejected, if

$$F_A = \frac{SQA/(I-1)}{SQR/IJ(K-1)}$$

the $(1-\alpha)$-Quantiles of the F-distribution with $(I-1)$ degrees of freedom and $IJ(K-1)$ degrees of freedom exceeds, if $F_A > F_{1-\alpha}(I-1,\ IJ(K-1))$.

Analogue to factor A, the null hypothesis for factor B is rejected, if

$$F_B = \frac{SQB/(J-1)}{SQR/IJ(K-1)}$$

the $(1-\alpha)$-Quantiles of the F-distribution with $(I-1)$ degrees of freedom and $IJ(K-1)$ degrees of freedom exceeds, if $F_B > F_{1-\alpha}(J-1,\ IJ(K-1))$.

The test values are merged into a table of analysis of variance (see Table 5.3).

Table 5.3: Table of analysis of variance inspired by Tutz (2007)

cause of variability	variability	degrees of freedom	mean square error	test value
Factor A	SQA	$I-1$	$MQA = \frac{SQA}{I-1}$	$F_A = \frac{MQA}{MQR}$
Factor B	SQB	$J-1$	$MQB = \frac{SQB}{J-1}$	$F_B = \frac{MQB}{MQR}$
Interactions $A \times B$	$SQ(A{\times}B)$	$(I-1)(J-1)$	$MQ(A \times B) = \frac{SQ(A\times B)}{(I-1)(J-1)}$	$F_{A\times B} = \frac{MQ(A\times B)}{MQR}$
Residuals	SQR	$IJ(K-1)$	$MQR = \frac{SQR}{IJ(K-1)}$	
Total	SQT	$n-1$		

With the help of these statistical tests it can be checked, if significant interactions and main effects exist.

For the current parameter study, the table of analysis of variance results to:

Table 5.4: Table of variance analysis for t=43800 hours

cause of variability	variability	degrees of freedom	mean square error	test value
Factor I	8.12	3	2.706	79.59
Factor J	1.35	3	0.452	13.29
Factor K	4.54	2	2.271	66.79
Factor L	54.53	2	27.264	801.88
Interactions				
$I \times J$	0.34	9	0.038	1.12
$I \times K$	1.86	6	0.310	9.12
$I \times L$	0.27	6	0.045	1.32
$J \times K$	0.01	6	0.002	0.06
$J \times L$	0.10	6	0.017	0.50
$K \times L$	0.90	4	0.225	6.62
Residuals	0.01	133	0.034	
Total	72.03	863		

The effect sizes are shown in Figure 5.27. According to Tutz (2007) describes the effect size the size of a statistical effect. The effect size can be used to clarify the practical relevance of statistically significant results. The single abbreviations seen in Figure 5.27 are: L=effect size of parameter length, H=effect size of parameter height, RH=effect size of parameter relative humidity, S=effect size of parameter support condition; and with L/H=effect size of interaction between length and height, L/RH=effect size of interaction between length and relative humidity, L/S=effect size of interaction between length and support condition, H/RH=effect size of interaction between height and relative humidity, H/S=effect size of interaction between height and support condition, RH/S=effect size of interaction between relative humidity and support condition.

It is clear, that the parameter 'support condition' has a decisive effect on the exceedance of the maximum admisible tensile strengths. According to Figure 5.19, the support condition of the slab supported on three axes causes the main reason of exceedance of the maximum admissible tensile strengths.

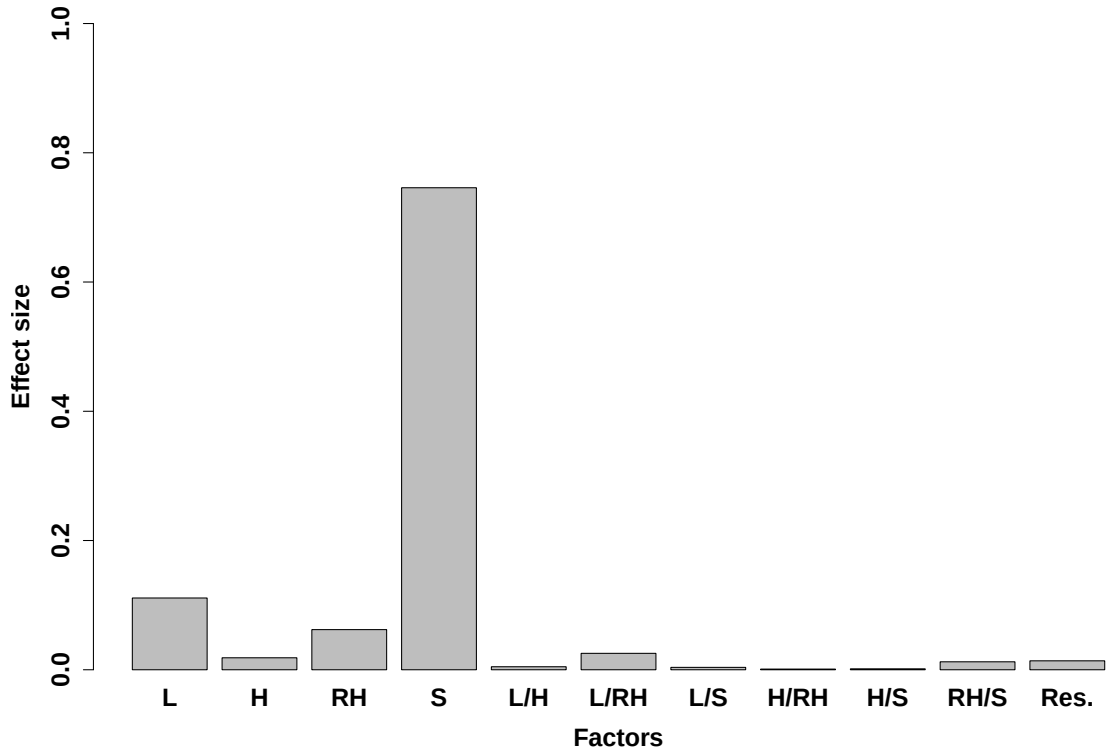

Figure 5.27: Effect sizes 'd' of the respective parameters and interactions for t=43800 hours

5.5 Summary

Within this chapter, a parameter study with four different input parameters (length, height, relative humidity, support condition) was investigated as a function of time. In a first step the times, where the maximum existing tensile strength exceeded the admissible tensile strengths were identified. For the realised parameter study, 43800 hours (five years) was found to be the critical time for the exceedance of the maximum admissible tensile strength.

Furthermore, the time step 43800 hours was looked in detail for the single parameters: length, height, relative humidity and support condition. The existing tensile strengths caused by one single factor in interaction with the factors of the other parameters were again compared with the maximum admissible tensile strength for the time 43800 hours.

Subsequently, the effect of the respective parameter was researched as well as the interaction between the different parameters, to get a qualified assertion of which parameter influences most the existing tensile strengths. Using the analysis of variance it was possible to identify the parameter, here the support condition 'slab supported on three axes'. At the end of the analysis of variance, the effect sizes were given. It became obvious, that the support condition has the main effect size within the parameter study. While regarding the main effects of the parameter 'support condition', the support condition 'slab supported on three axes' could be very clearly identified. Furthermore, the respective effect sizes of the different parameters are determined, which can be used within the design concept as explained in the following Chapter.

The combination of the numerical analysis and the analysis of variance represents a powerful tool while planning a new project with regards to a crack-free cementitious screed.

6 Design concept

A design concept is developed on the basis of the findings from KINTEMP/KINFEST, the findings from the own measurements of shrinkage, the knowledge gained of the self-developed numerical model and the results from the parameter study. The design concept can be used while planning of new screeds. The sequence of the design concept is shown in Figure 6.1.

Input parameters

Initially, the input parameters (hygric and mechanical) of the concrete which will be used have to be defined. Thereby, the evolution of shrinkage as a function of time can be predicted with the analytical approach (see Equation 2.6, Chapter 2.2.3) from DIN EN 1992-1-1:2011-01 (2011). Then, the calculated values of shrinkage are to convert to an equivalent temperature with Equation 4.3 from Chapter 4.3.3. In addition, the required mechanical input parameters have to be defined. For the SOLID185 element, which is used in the numerical simulation of the screed, Young's Modulus and Poisson ration is needed. Furthermore, the tensile strength of the concrete used, which serves as failure-criterion, is to predict. The tensile strength development, as well as the development of Young's Modulus as a function of time, are predicted by the prognosis software KINFEST.

Numerical calculation

The first step for the numerical calculation is the creation of a model. The model is to develop in respect of the planned dimensions and boundary conditions, such as geometry and bearing structure. Successively, every required step of shrinkage, simulated by the equivalent temperature, is applied as a thermal load case. Finally, the results of this calculation serve as a basis to determine the number and position of the expansion-joints.

Output

In a next step, areas with high-stress concentrations can be regarded in detail. Using the element-failure method, crack paths can be calculated, respectively it can be stated if there are critical points such as obstructions or sharp edges in the screed structure. These critical points can be replanned in order to have a crack free screed. Furthermore, to optimize the number and position of the expansion-joints, a parameter-study can be carried out, to identify the parameter, which causes an exceedance of the stresses in the screed.

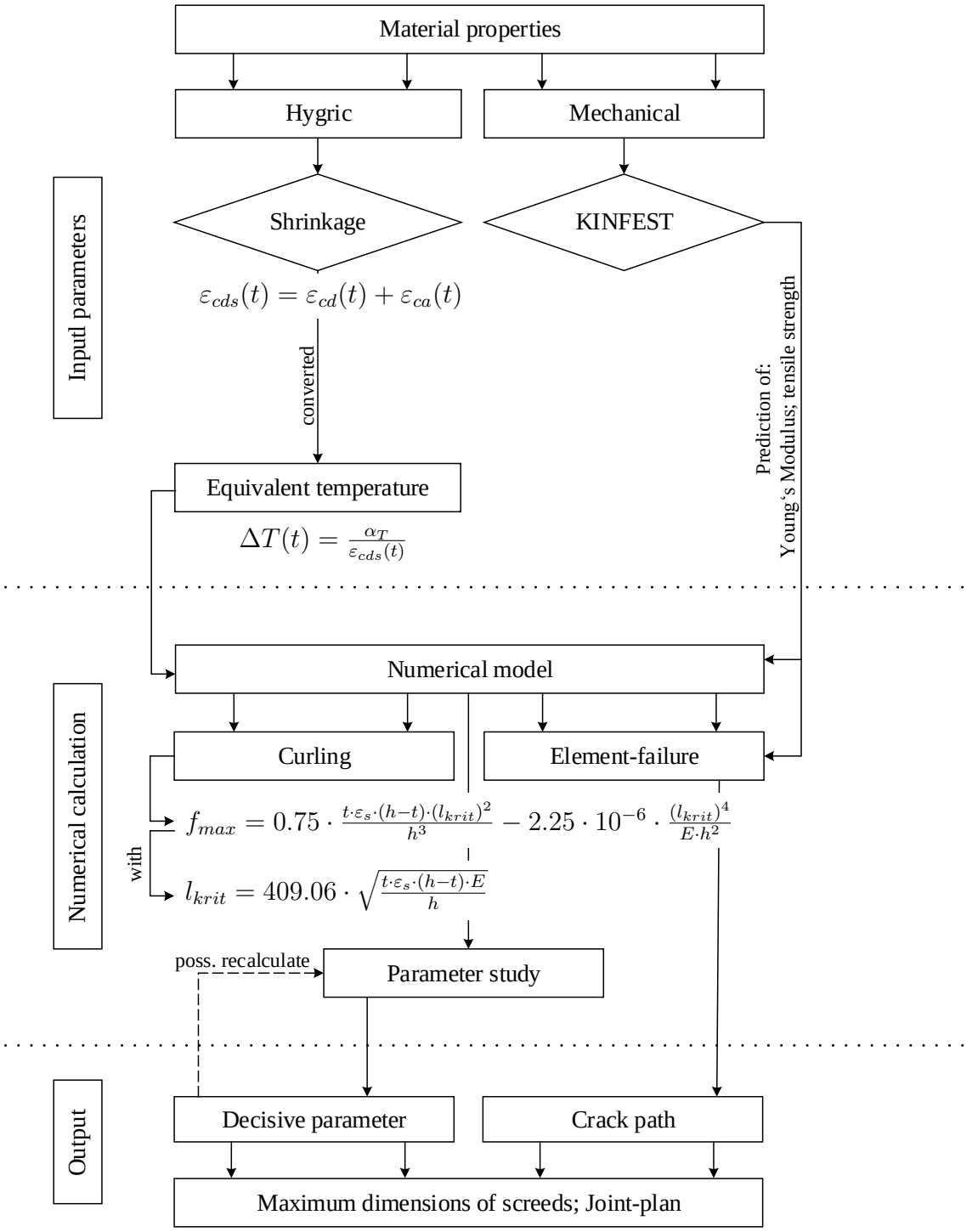

Figure 6.1: Sequence of design concept

6.1 Outlook design concept

In the following, an attempt of a first analytical approach for the design concept is presented. On the basis of the results of the numerical simulation and according to the results of the statistical evaluation, a formula to estimate the stress development in a screed is given. The maximum possible dimensions, as well as the boundary conditions, are arranged according to the dimensions and boundary conditions from the parameter study.

On the basis of the results of the calculation of the maximum tensile stress in X-Z-plane within the numerical analysis, and on basis of the expected tensile strength at the respective time, dimensionless factors α are calculated. Thereby, the factor α is calculated for one single support condition (full support or point support or support on three axes). For the factor α_L for example, the mean value is to determined for all calculated values of length=6000 mm, for each time step. This mean value is divided by the expected tensile strength of the concrete used at the respective time step. The result of this division is a dimensionless factor α. This factor α is then multiplied by the effect size 'd' of the length at the respective time. This procedure is carried out for each factor (length, height, relative humidity, support condition) and then added up. The added up value is finally multiplied by the expected tensile strength of the respective time. The result is the expected tensile stress of the slab $f_{t,\alpha}$ (see Equation 6.1).

$$f_{t,\alpha}(t) = \left(\alpha_{RH} \cdot d_{RH} + \alpha_L \cdot d_L + \alpha_H \cdot d_H + \alpha_{SUPP} \cdot d_{SUPP}\right) \cdot \left((\beta_{cc}(t))^{\alpha} \cdot f_{ctm}\right) \quad (6.1)$$

with

α_{RH}	related stress coefficient of relative humidity
d_{RH}	effect size of coefficient relative humidity
α_L	related stress coefficient of length
d_L	effect size of coefficient length
α_H	related stress coefficient of height
d_H	effect size of coefficient height
α_{SUPP}	related stress coefficient of support condition
d_{SUPP}	effect size of coefficient support condition
f_{ctm}:	medium tensile strength after 28 days [MPa]
$\beta_{cc}(t) =$	$e^{s\cdot[1-\sqrt{28/t}]}$
α:	1 for t $\leq$ 28 days; 2/3 for t $\geq$ 28 days

The results of this first analytical approach for different cases are shown in the following. First, the best case is shown (see Table 6.1). The deviation at the time 1 days is only 5.8%. The predicted value of $f_{t,\alpha}$ underestimates the value of the simulation. The same can be stated for the time 1825 days (5 years), where the predicted value of $f_{t,\alpha}$ underestimates the value of the simulation only of 0.8%. For all the other time steps, $f_{t,\alpha}$ overestimates the values of the simulation many times over. The $f_{t,\alpha}$ values are on the safe side.

Table 6.1: Results of $f_{t,\alpha}$ for full support, a relative humidity of 65.0%, a length of 6000 mm and a height of 80 mm

Time	[days]	1	2	7	28	100	1825
$f_{t,\alpha}$	[MPa]	0.01	0.03	0.06	0.17	0.34	0.91
$f_{t,sim}$	[MPa]	0.01	0.01	0.04	0.10	0.19	0.92
Δ	[%]	-5.8	+155.7	+60.4	+69.0	+81.4	-0.8

For the worst case, as shown in Table 6.2, the deviation at each time step is about 60.0%, whereby the $f_{t,\alpha}$ values always underestimate the values from the simulation.

Table 6.2: Results of $f_{t,\alpha}$ for the support on three axes, a relative humidity of 20.0%, a length of 9000 mm and a height of 50 mm

Time	[days]	1	2	7	28	100	1825
$f_{t,\alpha}$	[MPa]	0.02	0.05	0.14	0.36	0.68	1.44
$f_{t,sim}$	[MPa]	0.06	0.14	0.38	0.97	1.90	3.44
Δ	[%]	-61.4	-64.9	-62.4	-62.7	-64.4	-58.1

For the support condition 'point-support' the results for a screed with a length of 6000 mm, a height of 80 mm and a relative humidity of 42.5 % are given in Table 6.3. The $f_{t,\alpha}$ values underestimate the simulated results at each time step, decreasing from 1 day (-64.3%) to 1825 days (-13.3%)

Table 6.3: Results of $f_{t,\alpha}$ for a point support, a relative humidity of 42.5%, a length of 6000 mm and a height of 80 mm

Time	[days]	1	2	7	28	100	1825
$f_{t,\alpha}$	[MPa]	0.01	0.03	0.07	0.18	0.34	0.94
$f_{t,sim}$	[MPa]	0.03	0.05	0.11	0.25	0.45	1.08
Δ	[%]	-64.3	-42.6	-37.9	-29.0	-24.3	-13.3

Concluding, two Tables are shown (Table 6.4 and Table 6.5) for which the values for length, height, relative humidity and support condition who are residing in midfield. The deviations result predominantly in a minor percentage.

Table 6.4: Results of $f_{t,\alpha}$ for a full support, a relative humidity of 42.5%, a length of 7000 mm and a height of 70 mm

Time	[days]	1	2	7	28	100	1825
$f_{t,\alpha}$	[MPa]	0.01	0.03	0.07	0.17	0.35	0.94
$f_{t,sim}$	[MPa]	0.01	0.02	0.07	0.16	0.31	0.92
Δ	[%]	-5.8	+35.7	-5.4	+7.6	+13.2	+2.7

Table 6.5: Results of $f_{t,\alpha}$ for a full support, a relative humidity of 20.0%, a length of 7000 mm and a height of 60 mm

Time	[days]	1	2	7	28	100	1825
$f_{t,\alpha}$	[MPa]	0.01	0.03	0.07	0.17	0.36	0.96
$f_{t,sim}$	[MPa]	0.02	0.03	0.08	0.20	0.36	0.99
Δ	[%]	-52.9	-9.5	-16.5	-12.6	-0.7	-3.0

6.2 Discussion of the results

In the previous chapter, a first analytical approach for rectangular, unreinforced screeds serving as final surface is developed. The basis for the analytical approach build the results from the parameter study as well as the results from the statistical evaluation. The analytical approach was tested for different boundary conditions (see Table 6.1 to Table 6.5) and compared to the results from the parameter study. For extreme cases which could be very unfavourable conditions as well as very favourable conditions for cracking, the results from the analytical approach differ for some configurations strongly from the results from the parameter study. For cases who are residing in the midfield of the analysed configurations with neither very unfavourable conditions nor very favourable conditions for cracking, the results from the analytical approach gives, compared to the results from the parameter study, acceptable result. All in all the results differ mostly in a small percentage.

The analytical approach is a very promising approach in respect to have an assessment to pre-dimension unreinforced screeds and thus, permits to calculate an order of magnitude of the tensile stresses that must be expected. Though, it should be noted, that extensive research is necessary to verify, to improve and to proof the analytical approach. Furthermore, the analytical approach must be tested for other types of concrete and for different boundary conditions (support conditions, relative humidity, geometrical conditions).

7 Conclusion and outlook

A prognosis tool for unreinforced fairfaced screeds was developed, which is able to predict crack paths in the concrete structure and, in addition, which is able to calculate the stress state in a fairfaced screed. The prognosis tool considers different support conditions, different dimensions of the screed and also different ambient relative humidities. All kinds of cement/concrete can be used.

In the current work, the evolving strengths of the C20/25 concrete as well as shrinkage of the used concrete was taken into account. The challenge was to develop a simple and reliable prognosis tool, which can be used while planning new projects concerning unreinforced fairfaced concrete screeds. Furthermore, the tool will be used in the framework of claims processing. Therefore, a numerical model has been developed which considers the evolving material strengths required as well as the Hygric material behaviour, namely shrinkage and curling of the edges of a concrete floor. Furthermore, a parameter study was carried out, in order to determine the parameter (relative humidity; support condition; height of the screed; length of the screed) which influences most the exceedance of the stresses in the X-Z-plane of the screed.

7.1 Summary

In a first step, all reasons which influence cracking of young concrete (age $\leq$ 28 days) were identified. Besides an inadequate use of the screed, respectively a statical overload of the concrete screed, unplanned form changes within the first days may cause cracks. Furthermore, thermal reasons (hydration heat development and strong changes in the environmental temperature), can lead to cracking. The most important load independent reason which leads to cracking of concrete floors is the shrinkage of the used concrete. Along with shrinkage, the evolving material strengths of the concrete, bears the risk of cracking at an early stage.

To force shrinkage induced cracking, a small H-shaped concrete specimen was developed first. This concrete specimen was obstructed during shrinkage by inserted steel-tubes. In conjunction with the evolving material strengths of the concrete used, cracking could be visually controlled and documented over a period of 43 days. The boundary conditions were controlled insofar, as the specimen was stored in a large climate chamber at a constant temperature and at a constant relative humidity. Thereby, the specimen was fixed on a wooden formwork panel which was covered by a foil to ensure sliding. The foil prevented in addition an interaction of the concrete with the wooden formwork panel. Besides the concrete specimen, shrinkage drains were filled with the concrete used, to measure and to document the shrinkage behaviour. The degrees of shrinkage were compared to the analytical approach from DIN EN 1991-1-1. In addition, concrete cubes and concrete cylinders were produced, to record the evolving material strengths, such as compressive strength and Young's Modulus. These material data were compared to the predicted data of the prognosis tool KINFEST in turn. The comparison of the degree of shrinkage to the analytical approach from DIN EN 1991-1-1 and the comparison of the material data to the predicted data of the prognosis tool KINFEST serves as a basis for a prognosis tool. Thus the prediction of the degree of shrinkage, as well as the prediction of the material strengths gives reliable results, extensive tests may be dispensed to determine the required material parameters. On the basis of the measured and predicted material values, a first numerical model was developed.

For the numerical reproduction of cracking as a function of time from the H-shaped shrinkage specimen, the approach of the element-failure method was chosen. For the element-failure method, a failure criterion has to be chosen first. In the current work, the uniaxial tensile strength, at the respective time was chosen and compared to the existing stresses in X-Z plane within the simulation. The element chosen was the SOLID185, a 3-D structural solid element with eight nodes and three degrees of freedom for each node. The calculation of the crack path is carried out in a loop. An element thus fails, if each node meets the chosen failure criterion. The stiffness of the respective element is set to zero then. The thus damaged model serves as a basis for the next calculation step.

After the numerical reproduction of the crack paths on the small H-shaped shrinkage specimen, using the element-failure method, large-scale tests were carried out, in order to validate the approach of the element-failure method of the self-developed finite elements program. On these large-scale tests, the contact conditions were varied (screed fixed

on foil; screed in direct bound directly to the bearing structure). Again, the material properties (shrinkage; compressive strength; Young's Modulus) were investigated and documented using shrinkage drains, cubes and cylinders. The environmental boundary conditions (relative humidity; temperature) were documented as well. To take into account the contact between bearing structure and concrete and to simulate the different contact conditions, LINK180 elements were used. LINK180 elements are 3D spar elements, consisting of two nodes with three degrees of freedom on each node. While simulating a contact condition, sliding respectively detaching can be simulated. This was realised by assigning a failure criterion to the LINK180 element. The failure criterion chosen for the LINK180 element was the exceedance of a defined elongation. Thus, it was also possible to simulate curling of float mounted concrete floors.

Since the finite element model was developed, calibrated and verified, an extensive parameter study was conducted. In total, four groups of parameters were defined, length, height, support condition of the concrete floor and in addition the ambient relative humidity. Each group consists of three, respectively four parameters, which were investigated at six different time steps. Overall, 864 simulations were carried out. The evaluation of the simulation results took place in a statistical evaluation. Using the analysis of variance (ANOVA) it was possible to identify very clearly the parameter which was responsible for the major exceedance of the stresses in X-Z plane.

7.2 Conclusion and outlook

7.2.1 Conclusion

In the current thesis, a design concept for unreinforced fair-faced screeds, serving as final surface, was developed. As a part of the design concept, a numerical model was created. The numerical model considers the screed and in addition the bearing structure on which the screed is applied. Thereby, two different design variants were taken into account: a direct bond of the screed to the bearing structure and a screed fixed on foil. For the screed in direct bond to the bearing structure, the problem of cracking, which is more important for screeds in direct bond, is considered. Cracking is represented by the element-failure method, which was first time successfully applied on concrete structures. The evolving material properties (Young's Modulus; uni-axial tensile strength; shrinkage) were taken into account. The failure criterion chosen was the uni-axial tensile strength of the concrete used. For screeds fixed on foil, curling of the edge areas of the screed represents an important factor. Here, it was first time possible to simulate the effect of curling of screeds fixed on foil. Besides all types of concrete, all possible geometries can be simulated, the model is not just limited to rectangular geometries. In the framework of this, the research gap, which was mentioned in the beginning of this thesis could be closed. Thus, the self-developed model represents the completest numerical model existing at the moment.

The design concept is completed by a parameter study, with which it is possible to identify the decisive parameter (e.g. length; height; width; geometrical and environmental boundary conditions), which causes cracking in the concrete structure. As a basis for this parameter study serves the self-developed numerical model.

7.2.2 Outlook

The present work can be the basis for further research in the field of numerical modelling and the prediction of damage processes of fair-faced screeds.

As one first point, curling of concrete screeds can be investigated more in detail. The current analytical approaches of curling of concrete floors refers to a two-dimensional elastically bedded beam. Thus, on the basis of numerous tests and measurements on different environmental conditions and on different types of concrete, an analytical ap-

proach for a three-dimensional screed slab can be developed.

Furthermore, the contact behaviour between screed and bearing structure can be the starting point for further research. Thereby, a distinction between screeds fixed on foil and between screeds in direct bond must be made. Static friction as well as sliding friction can be part of extensive practical investigations.

For the design concept, the numerical results of a C20/25 concrete built the basis. To further develop the design concept, the impact of using other types of concrete must be verified. This will need still extensive experimental, numerical and analytical studies which can be realized within a further PhD-thesis.

List of Figures

List of Tables

Nomenclature

Abbreviations

2D	Two-dimensional
3D	Three-dimensional
ANOVA	Analysis of variance
CSH	Calcium-Silicate-Hydrate
CTOD	Crack Tip opening displacement
DIN	Deutsches Institut für Normung
EFM	Element-failure method
EN	Europäische Normen
FE	Finite element
FL	Forklift
XFEM	Extended finite element method

Latin letters

$^{\circ}C$	Celsius
a	Radius of load circle; Crack length
a_0, a_1, a_2	Constant values for the failure-surface by Willam and Warnke
A_c	Cross sectional area
b	Width
B	Thickness of specimen
b_0, b_1, b_2	Constant values for the failure-surface by Willam and Warnke
c_B	Specific heat capacity of concrete
cm	Centimetres
d_H	effect size of coefficient height
d_L	effect size of coefficient length

d_{RH}	effect size of coefficient relative humidity
d_{SUPP}	effect size of coefficient support condition
E	Young's Modulus
E_{cm}	Young's Modulus after 28 days
E_c	Young's Modulus of concrete
F	Force
F	Function of principle stress state
f	Weight of additives
F_{break}	Breaking force
f_{ck}	Compressive strength of concrete
$f_{cm,2}$	Medium concrete strength after 2 days
$f_{cm,28}$	Medium concrete strength after 28 days
f_{cm}	Average cylindrical compressive strength
f_{cm0}	Value of 10 MPa
f_{ctm}	Median tensile strength after 28 days
f_{max}	Degree of curling
f_1	Compressive strength for biaxial pressure
f_2	Compressive strength for uniaxial pressure
f_c	Uni-axial compressive strength
f_cb	Two-axial compressive strength
f_t	Uni-axial tensile strength
$f_{t,\alpha}$	expected tensile stress
g	Weight of gravel; Function for the influence of crack
h	Thickness of floor slab; Hour
h_0	Effective component thickness
H_n	Hydration heat
J	Joule
k	Bedding Modus
K	Kelvin
k_h	Empirical coefficient depending on h_0
K_I	Stress intensity factor
kg	Kilogram
l	Length
l_{krit}	Critical length
l_0	Initial length

m	Metres
mm	Millimetres
MPa	Megapascale
N	Newton
n_{LS}	Number of load steps
p	Contact pressure
Q	Wheel load
$Q_{k,dyn}$	Dynamic characteristic value
Q_k	Static characteristic value
r	Strength development of concrete; Rotation factor
RH	Relative humidity
RH_0	Value of 100%
S	Failure area in the three-dimensional stress space
s	Hardening coefficient of hardening
t	Regarded time; depth of shrinkage
T_{01}	First zero-stress temperature
T_{02}	Second zero-stress temperature
$T_{c,fr}$	Fresh concrete temperature
T_{max}	Maximum temperature
T_{ref}	Reference temperature
T_E	End temperature
T_f	Temperature of additives
T_g	Temperature of gravel
t_s	Age of concrete at the end of post-treatment
T_w	Temperature of water
T_z	Temperature of cement
U	Potential energy
u	Perimeter
w	Weight of water
w	Width of specimen
Z	Edge spacing
z	Weight of cement

Greek letters

α_{ds1}	Coefficient I to considerate a cement type
α_{ds2}	Coefficient II to considerate a cement type
α_T	Coefficient of thermal expansion
α_H	related stress of coefficient height
α_L	related stress of coefficient length
α_{RH}	related stress of coefficient relative humidity
α_{SUPP}	related stress of coefficient support condition
Δl	Length change
ΔT	Temperature difference
ΔT_n	Temperature development
γ	Density of concrete
μ	Coefficient of friction
μ	Poisson's ratio
ν	Poisson's Ratio
ν_{pl}	Plastic component of clip gauge displacement
ρ_B	Density of concrete
σ_{FS}	Flexural stress
$\sigma_{v,M}$	von Mises stress
σ_1	First principle stress
σ_2	Second principle stress
σ_3	Third principle stress
σ_c	Boundary stress
σ_e	Stress in the corner of the plate
σ_h	Hydrostatic stress state
σ_i	Stress in the middle of the plate
σ_n	Representative stress
σ_r	Stress at the edge of the plate
σ_t	Boundary stress of tensile stress
σ_x	Normal stress in X-direction
σ_y	Normal stress in Y-direction
σ_z	Normal stress in Z-direction
τ_{xy}	Shear stress perpendicular to XY-plane
τ_{xz}	Shear stress perpendicular to XZ-plane
τ_{yz}	Shear stress perpendicular to YZ-plane

ε	Strain of concrete
ε_{ca}	Autogenous shrinkage
ε_{cd}	Drying shrinkage
ε_{cds}	Total degree of shrinkage
φ	Dynamic magnification factor
ϑ	Surface temperature of concrete

Appendices

A Annexe

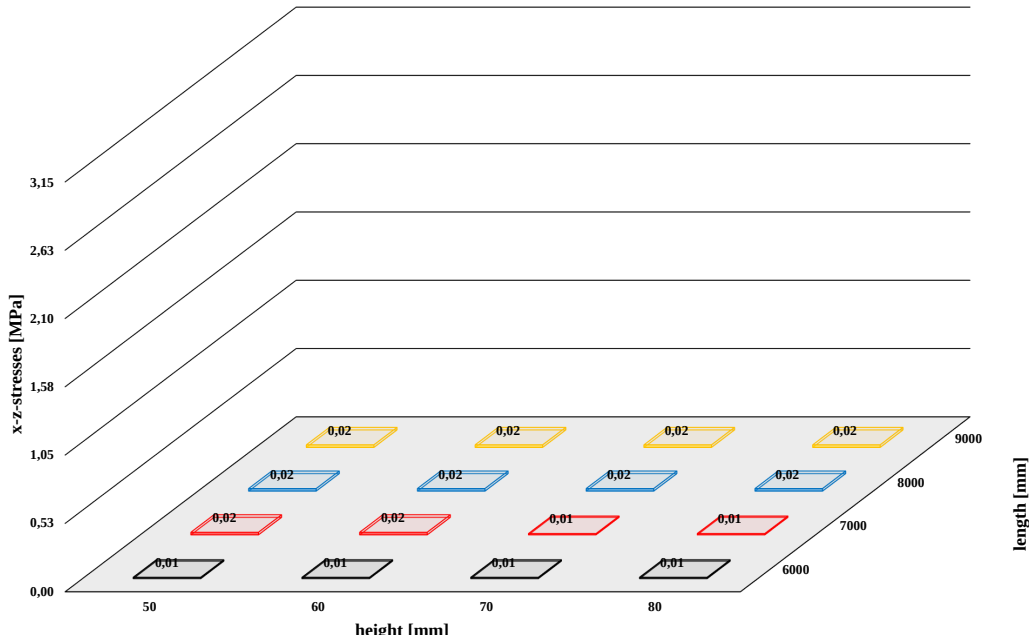

Figure A.1: Result of full supported model; t=24 hours; 20 % relative humidity; $max.f_t = 1.16$ MPa

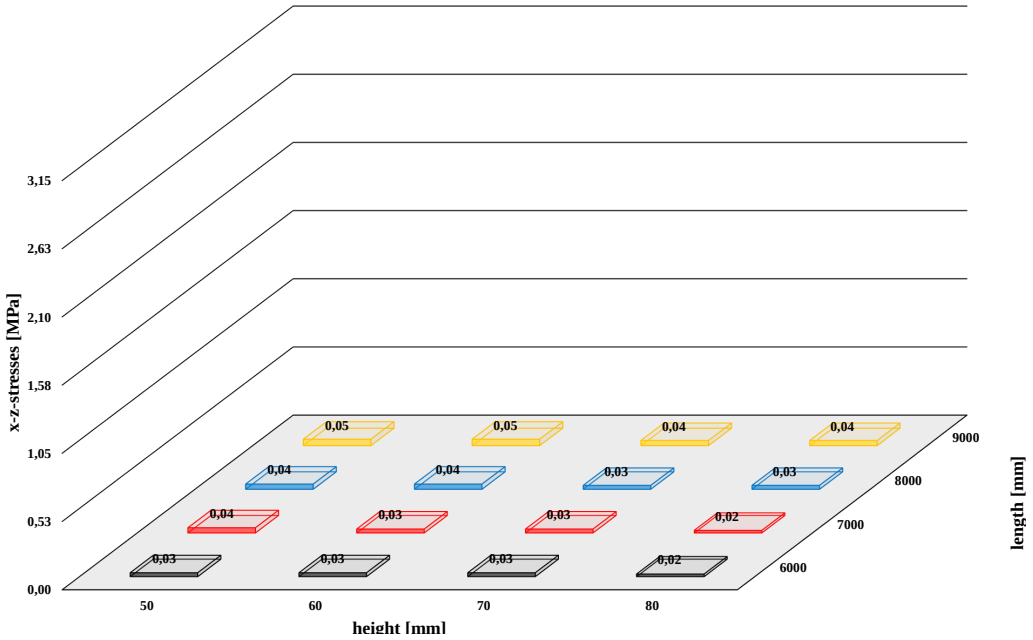

Figure A.2: Result of full supported model; t=48 hours; 20 % relative humidity; $max.f_t = 1.59$ MPa

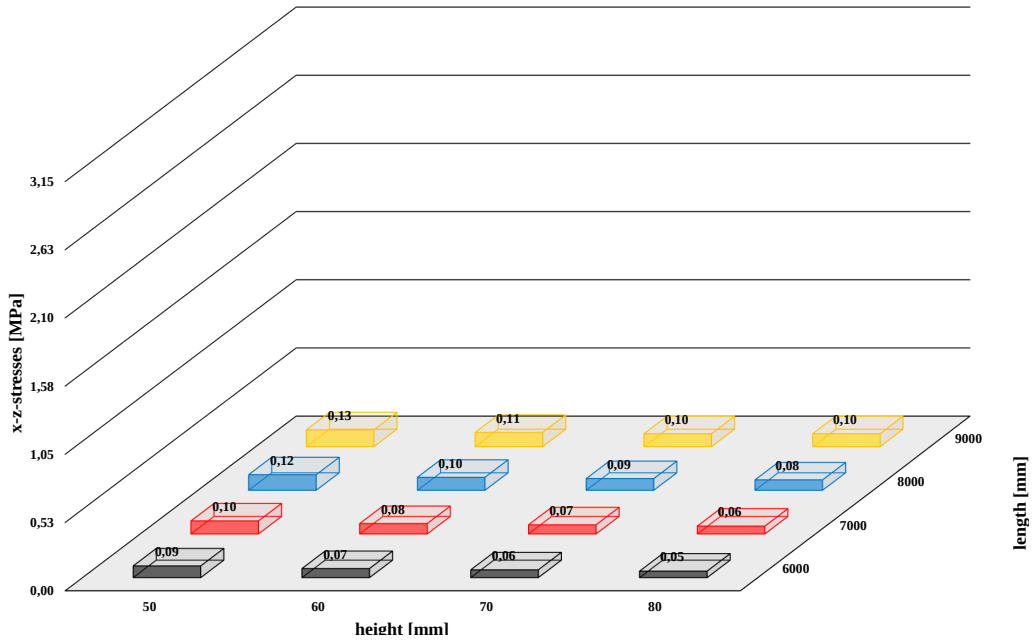

Figure A.3: Result of full supported model; t=7 days; 20 % relative humidity; $max.f_t$ = 1.90 MPa

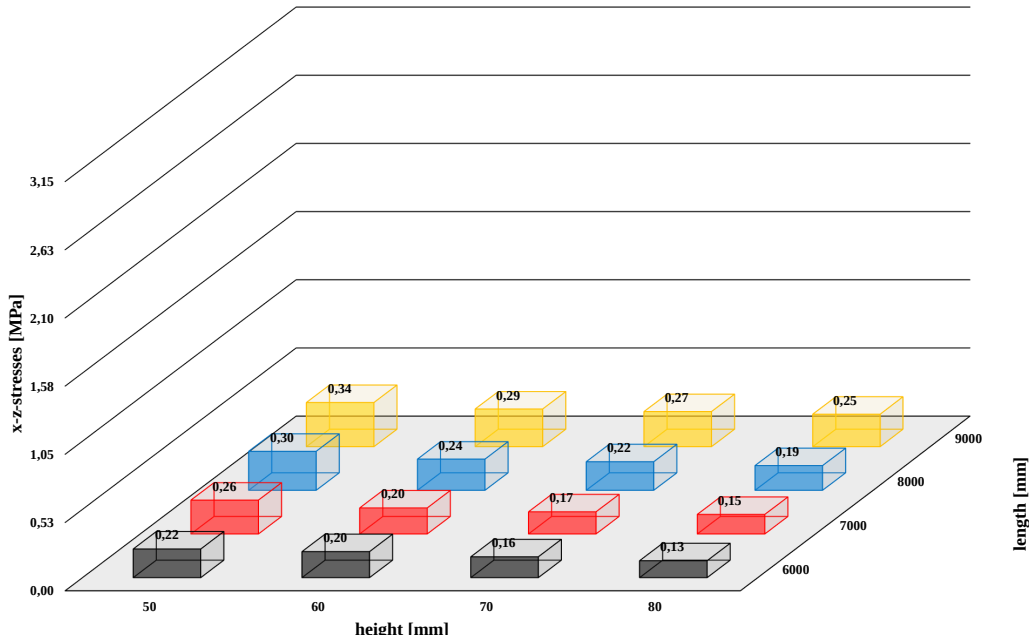

Figure A.4: Result of full supported model; t=28 days; 20 % relative humidity; $max.f_t$ = 2.14 MPa

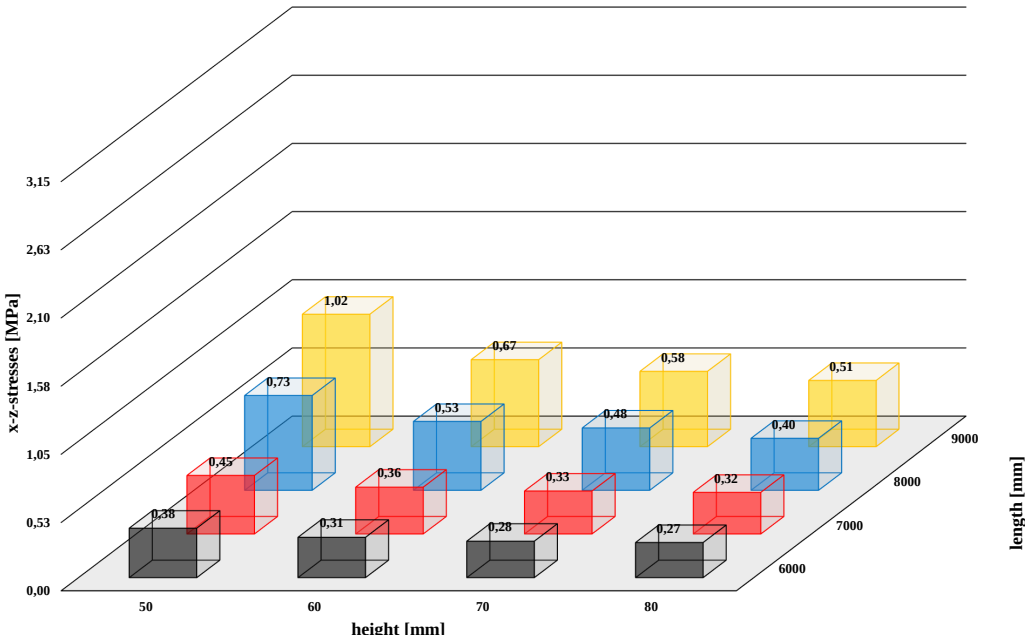

Figure A.5: Result of full supported model; t=100 days; 20 % relative humidity; $max.f_t = 2.47$ MPa

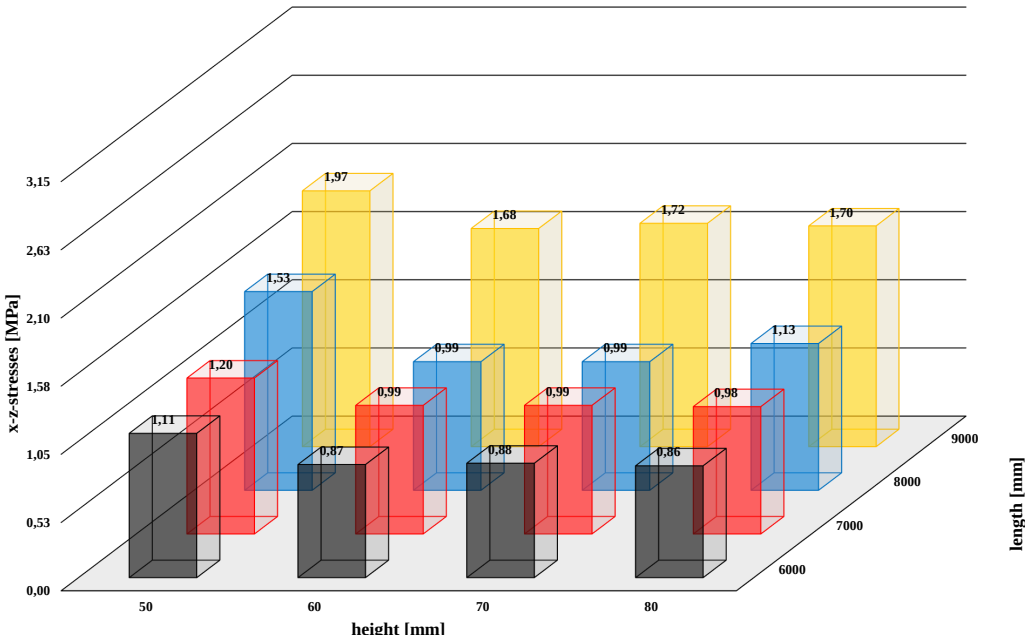

Figure A.6: Result of full supported model; t=5 years; 20 % relative humidity; $max.f_t = 2.82$ MPa

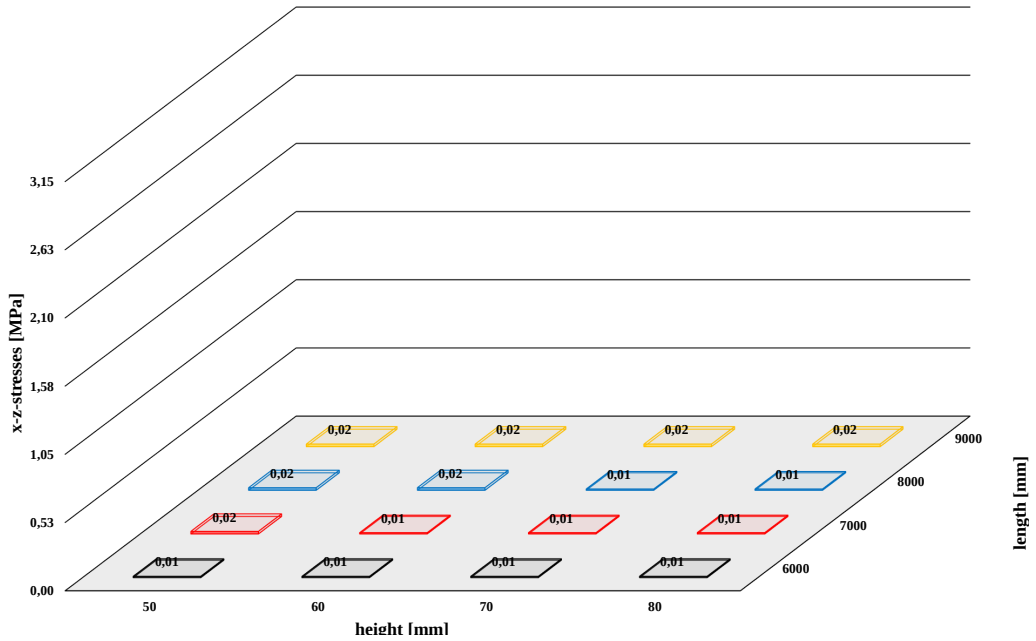

Figure A.7: Result of full supported model; t=24 hours; 42.5 % relative humidity; $max.f_t = 1.16$ MPa

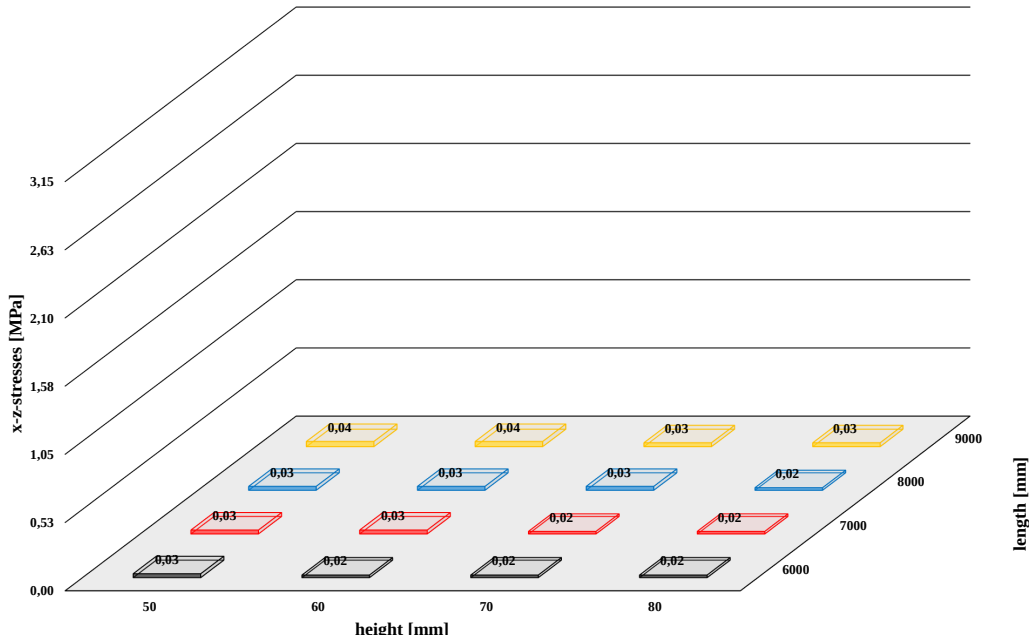

Figure A.8: Result of full supported model; t=48 hours; 42.5 % relative humidity; $max.f_t = 1.59$ MPa

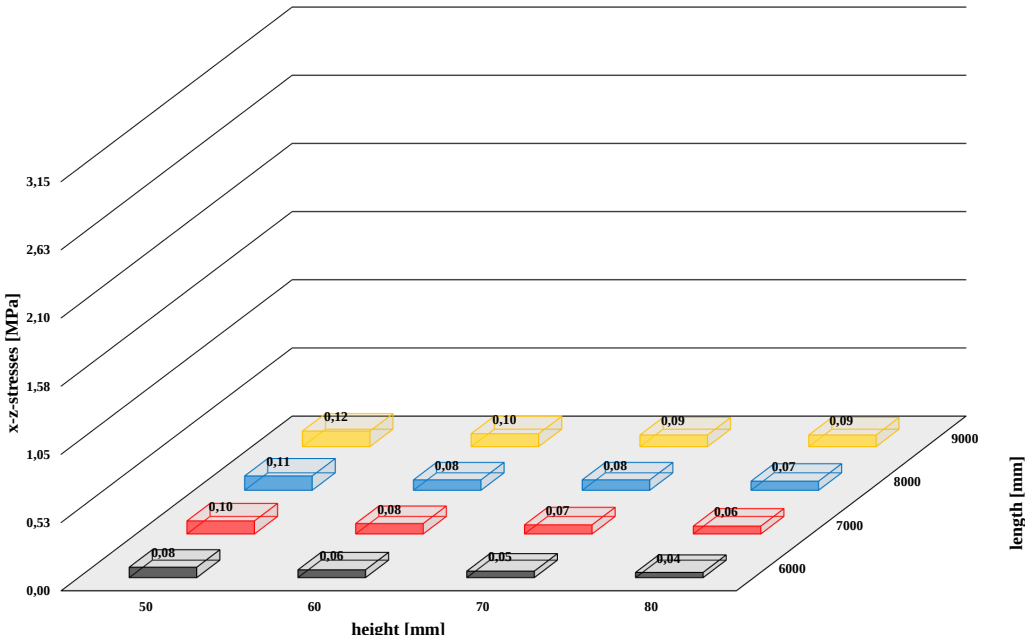

Figure A.9: Result of full supported model; t=7 days; 42.5 % relative humidity; $max.f_t = 1.90$ MPa

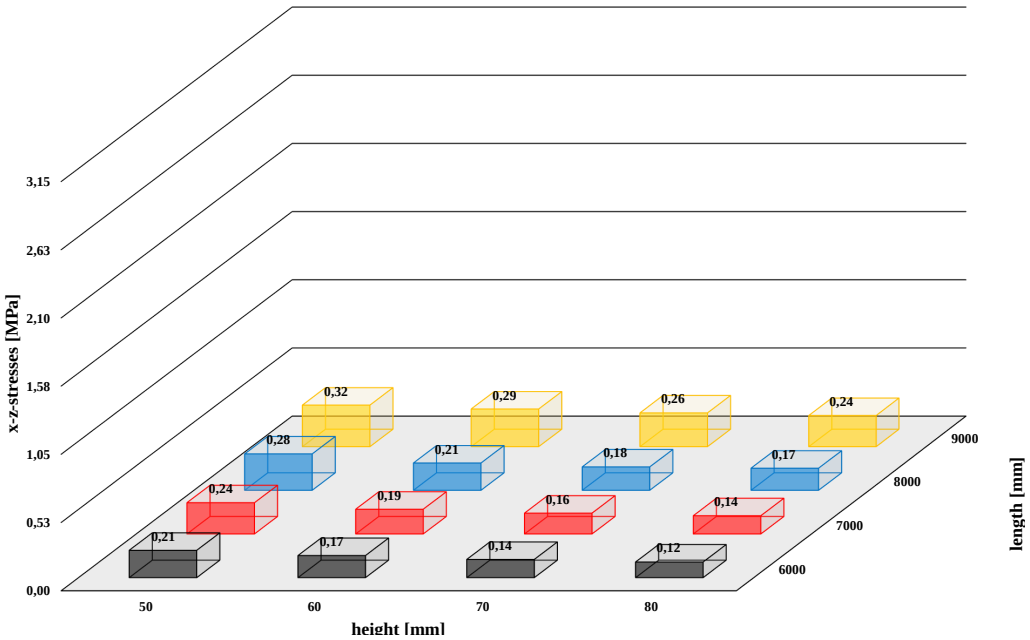

Figure A.10: Result of full supported model; t=28 days; 42.5 % relative humidity; $max.f_t = 2.14$ MPa

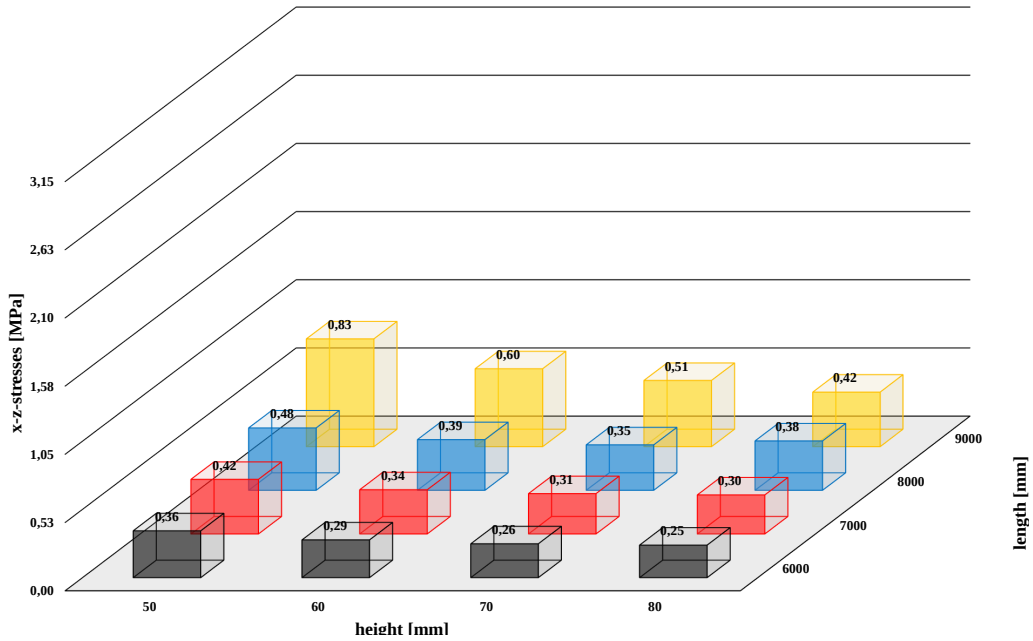

Figure A.11: Result of full supported model; t=100 days; 42.5 % relative humidity; $max.f_t = 2.47$ MPa

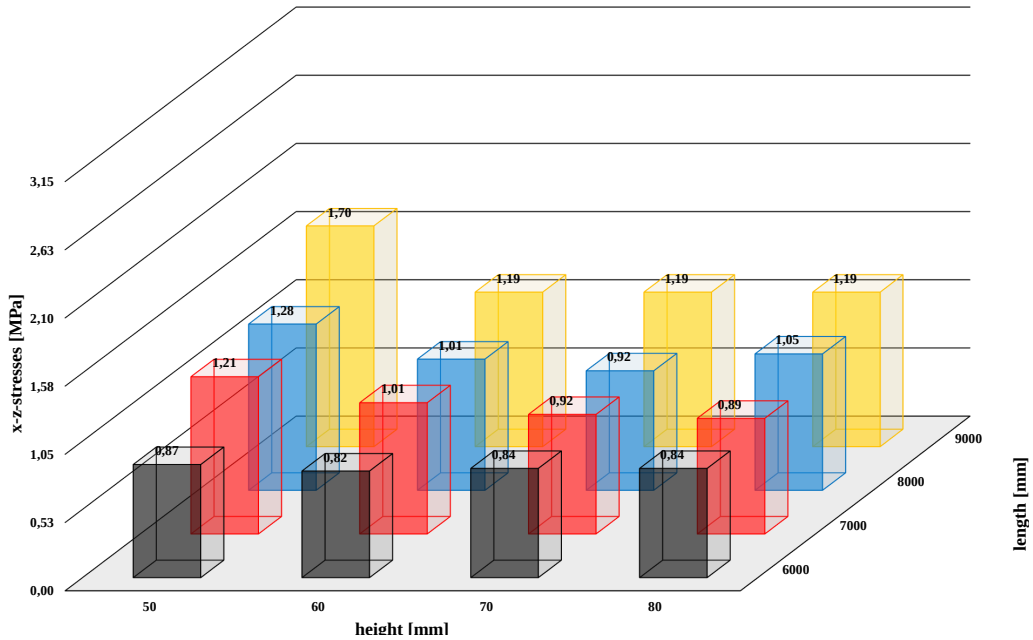

Figure A.12: Result of full supported model; t=5 years; 42.5 % relative humidity; $max.f_t = 2.82$ MPa

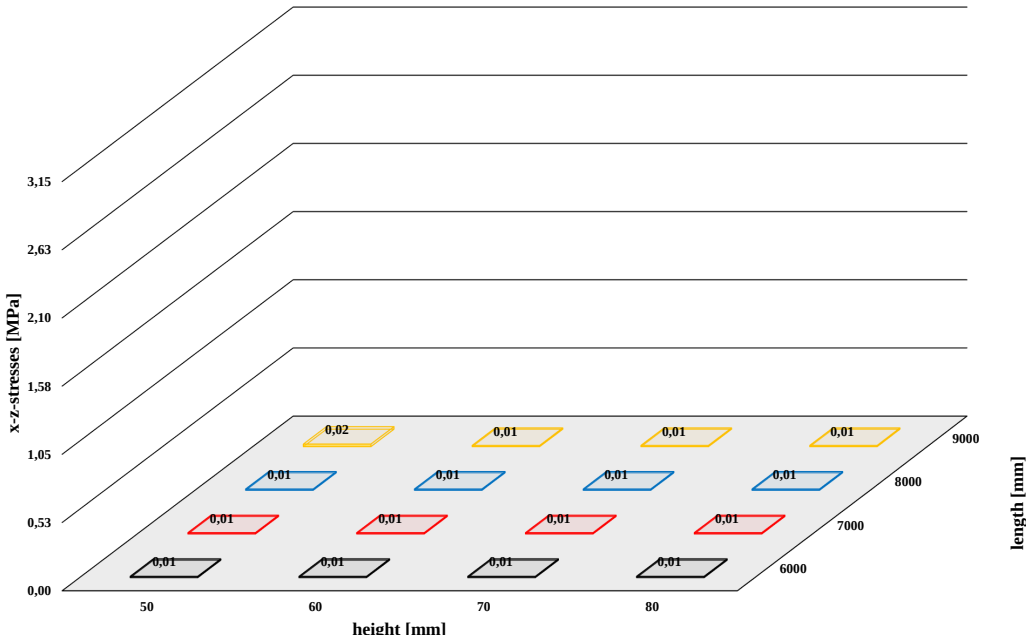

Figure A.13: Result of full supported model; t=24 hours; 65 % relative humidity; $max.f_t = 1.16$ MPa

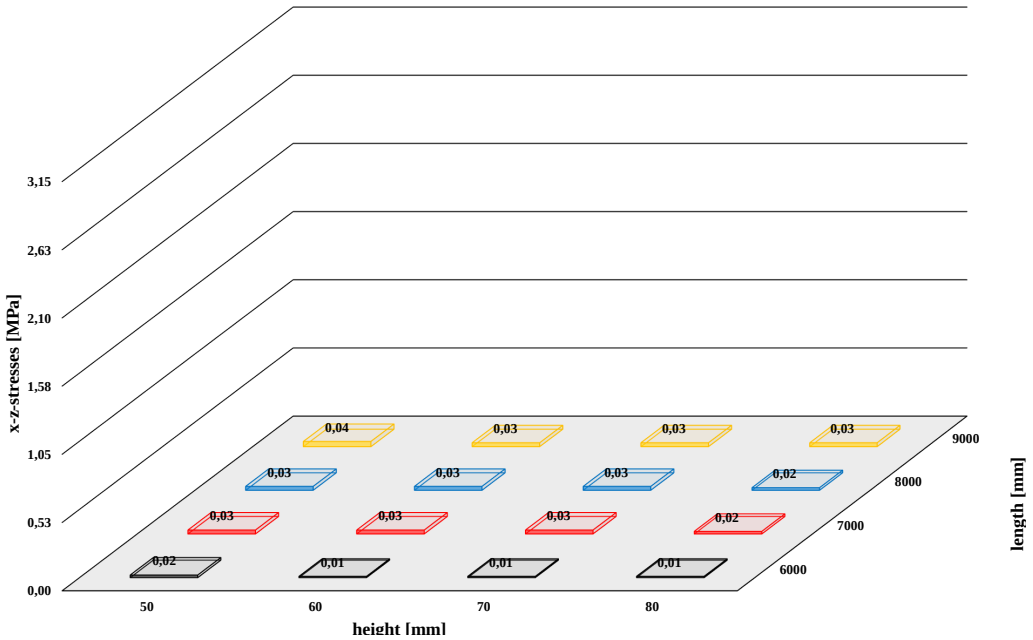

Figure A.14: Result of full supported model; t=48 hours; 65 % relative humidity; $max.f_t = 1.59$ MPa

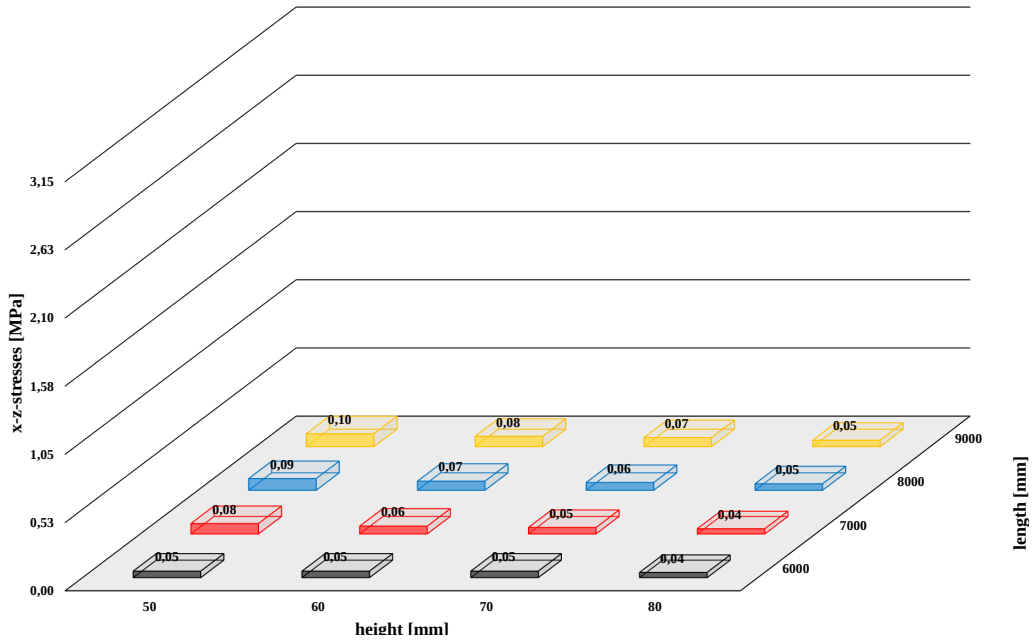

Figure A.15: Result of full supported model; t=7 days; 65 % relative humidity; $max.f_t$ = 1.90 MPa

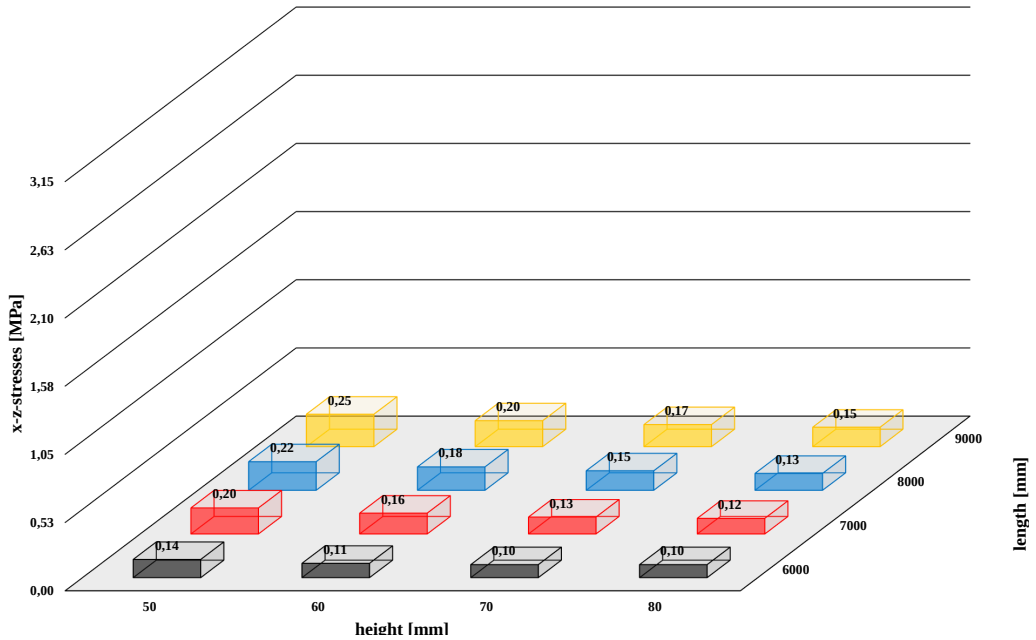

Figure A.16: Result of full supported model; t=28 days; 65 % relative humidity; $max.f_t$ = 2.14 MPa

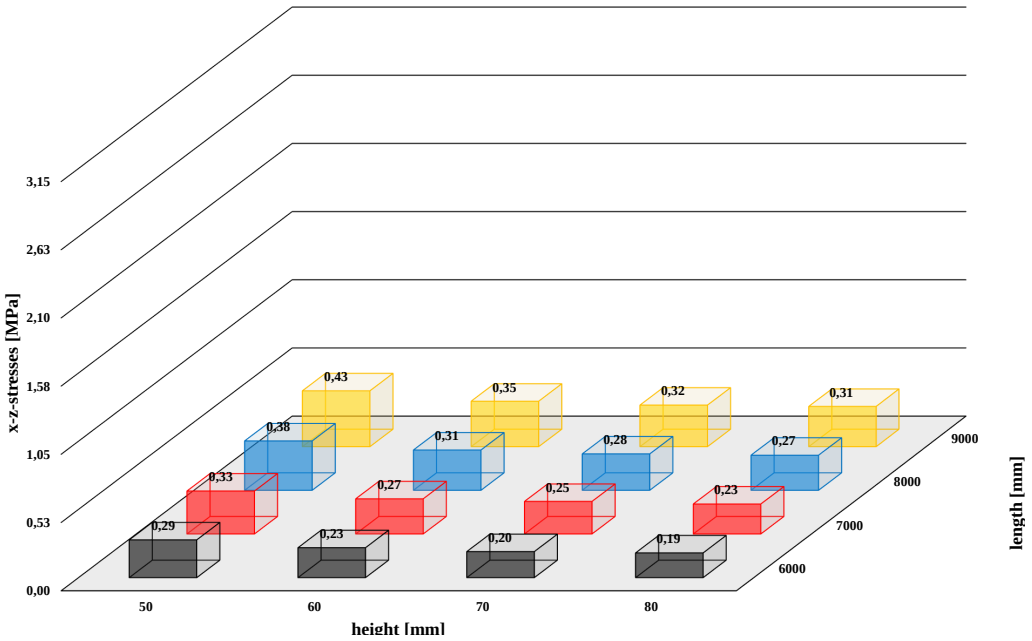

Figure A.17: Result of full supported model; t=100 days; 65 % relative humidity; $max.f_t = 2.47$ MPa

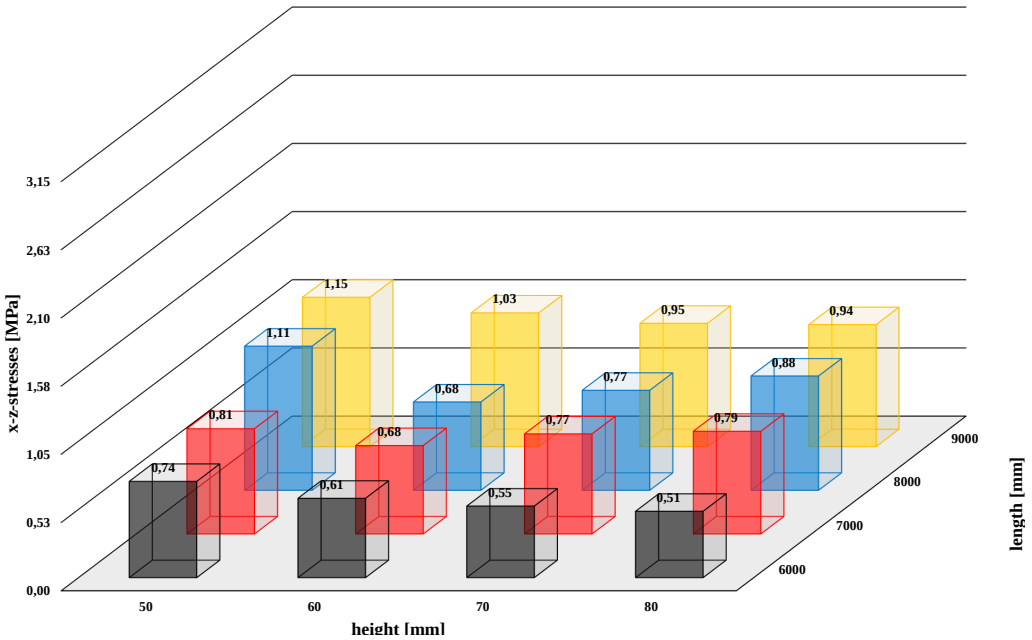

Figure A.18: Result of full supported model; t=5 years; 65 % relative humidity; $max.f_t = 2.82$ MPa

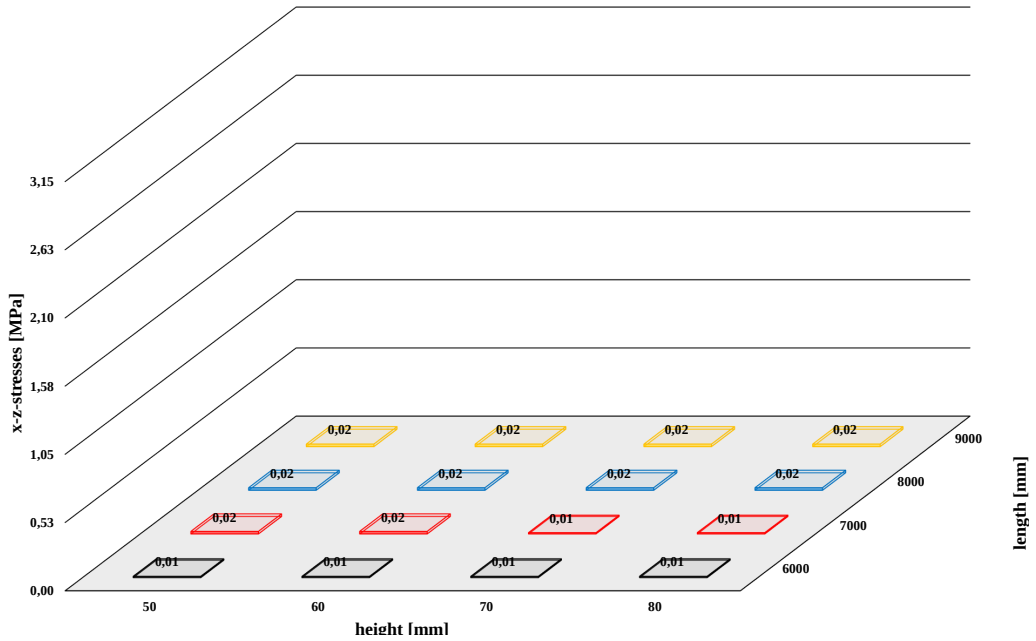

Figure A.19: Result of point supported model; t=24 hours; 20 % relative humidity; $max.f_t = 1.16$ MPa

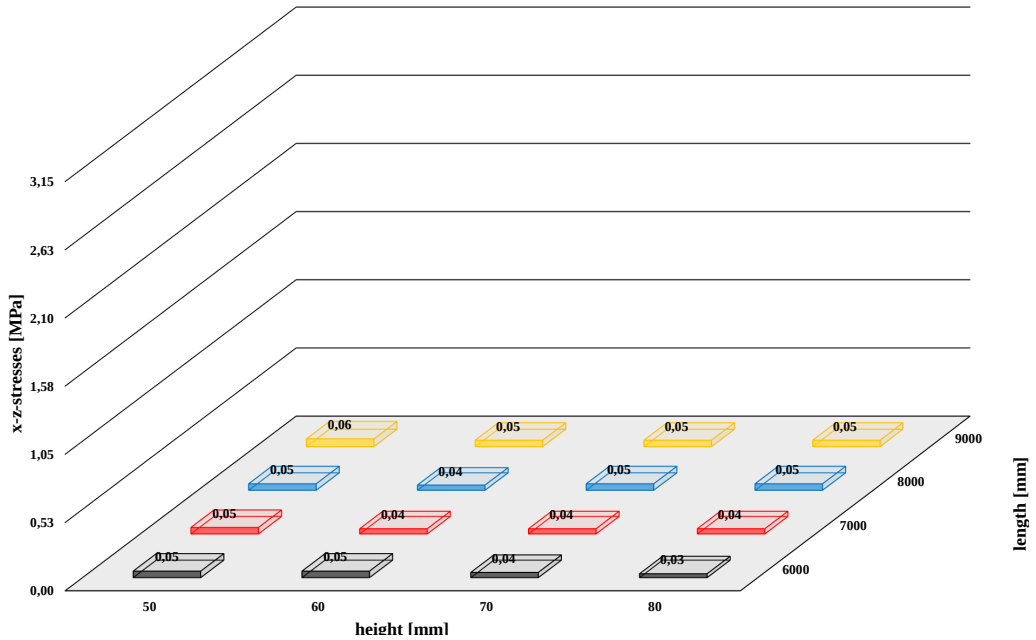

Figure A.20: Result of point supported model; t=48 hours; 20 % relative humidity; $max.f_t = 1.59$ MPa

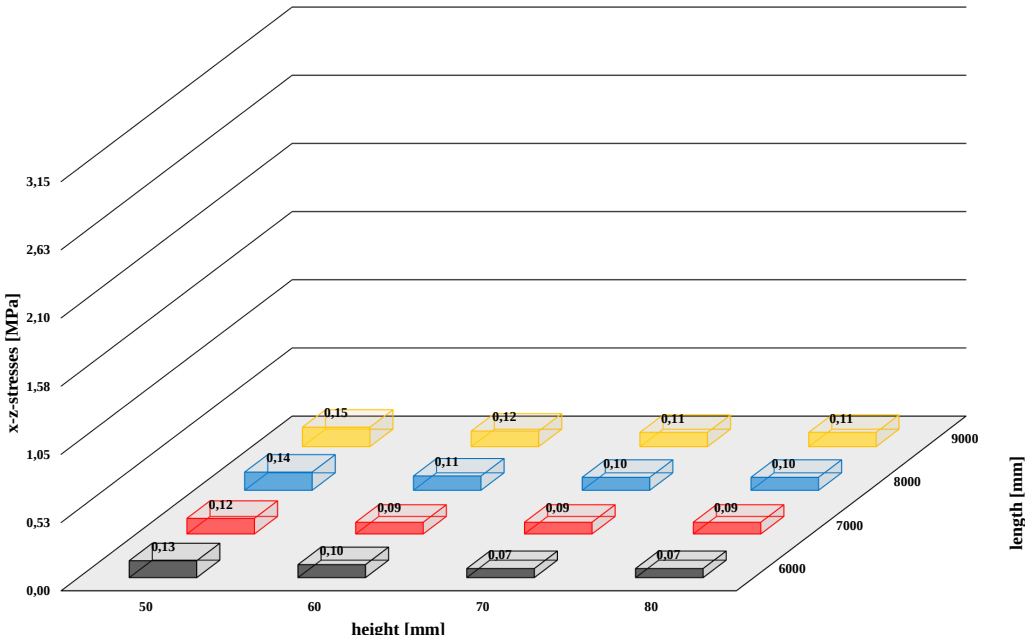

Figure A.21: Result of point supported model; t=7 days; 20 % relative humidity; $max.f_t = 1.90$ MPa

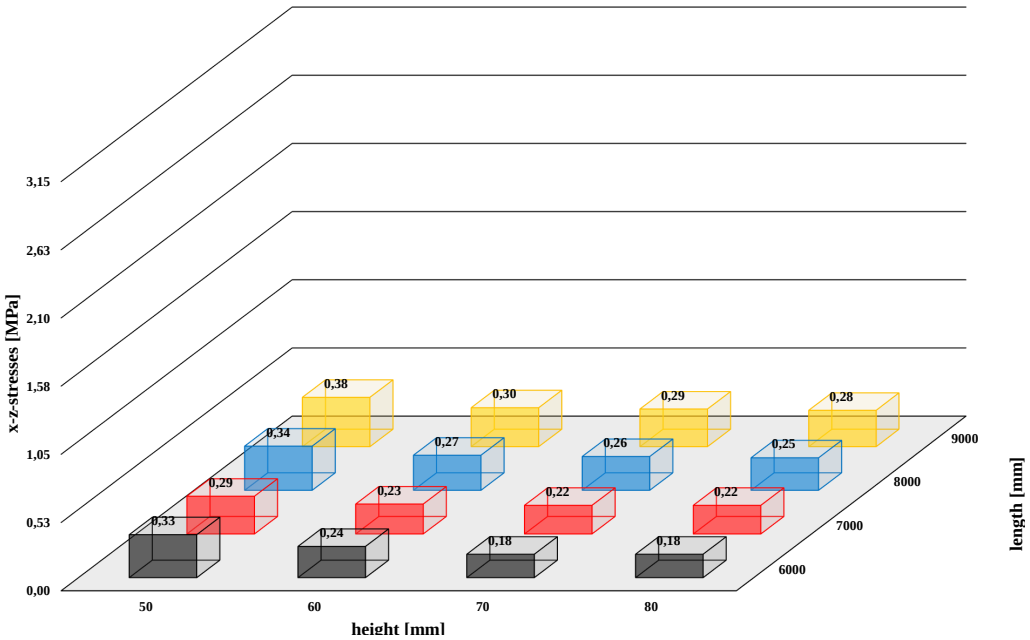

Figure A.22: Result of point supported model; t=28 days; 20 % relative humidity; $max.f_t = 2.14$ MPa

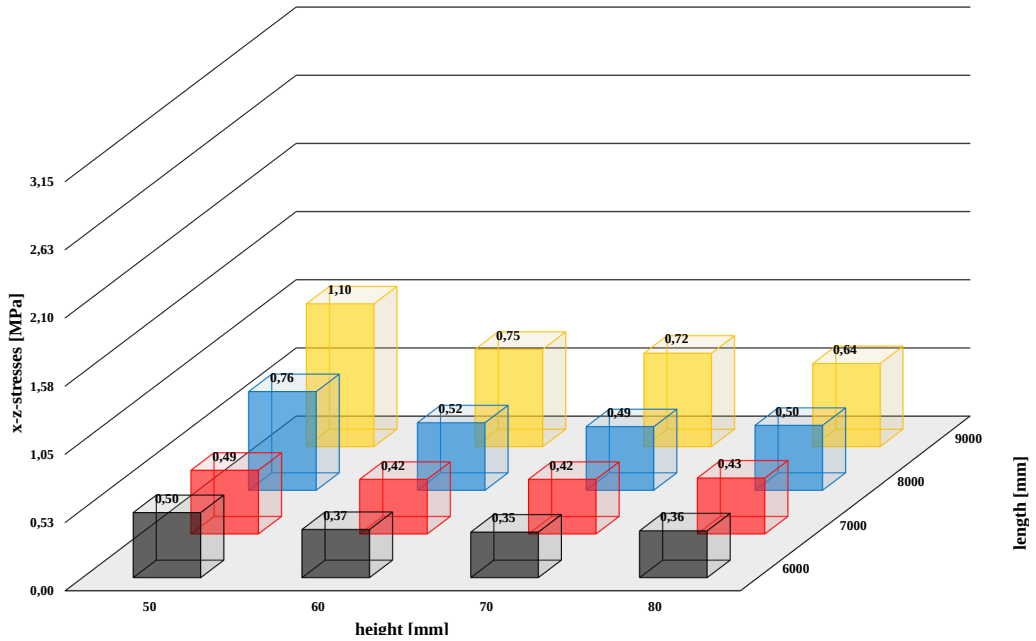

Figure A.23: Result of point supported model; t=100 days; 20 % relative humidity; $max.f_t = 2.47$ MPa

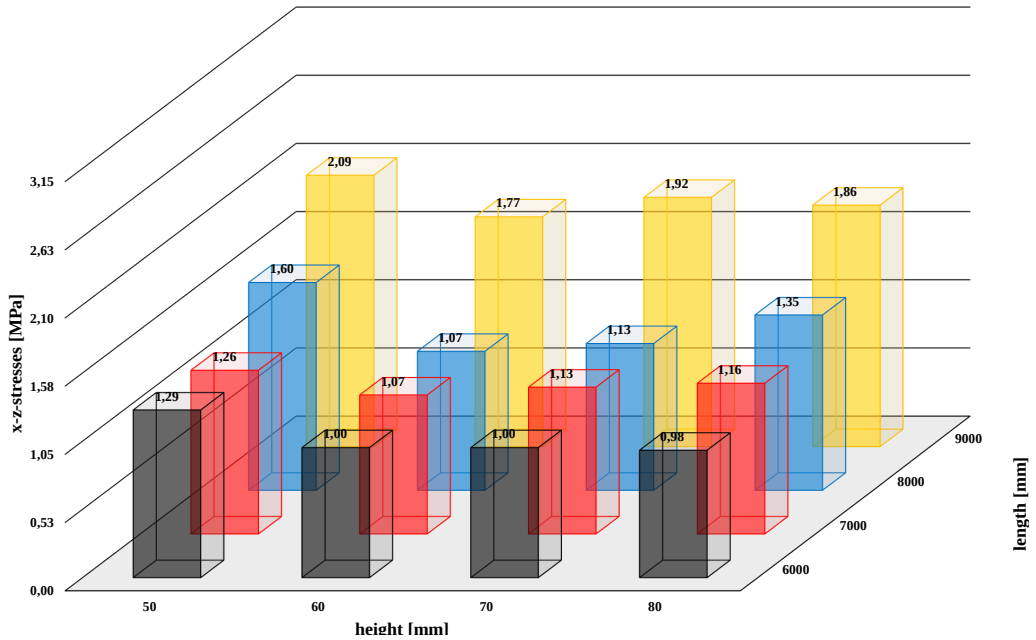

Figure A.24: Result of point supported model; t=5 years; 20 % relative humidity; $max.f_t = 2.82$ MPa

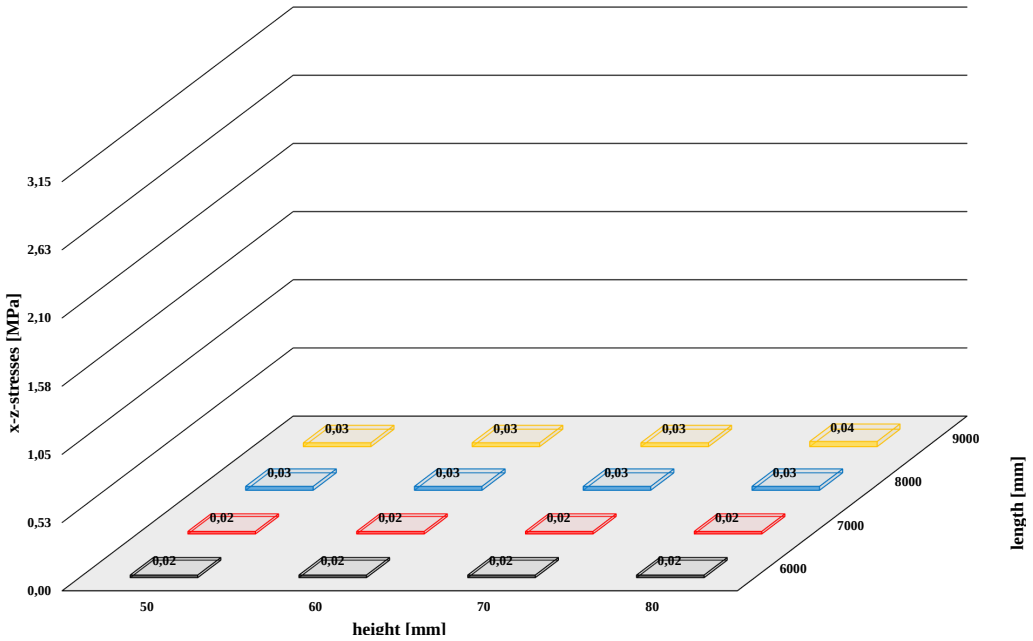

Figure A.25: Result of point supported model; t=24 hours; 42.5 % relative humidity; $max.f_t = 1.16$ MPa

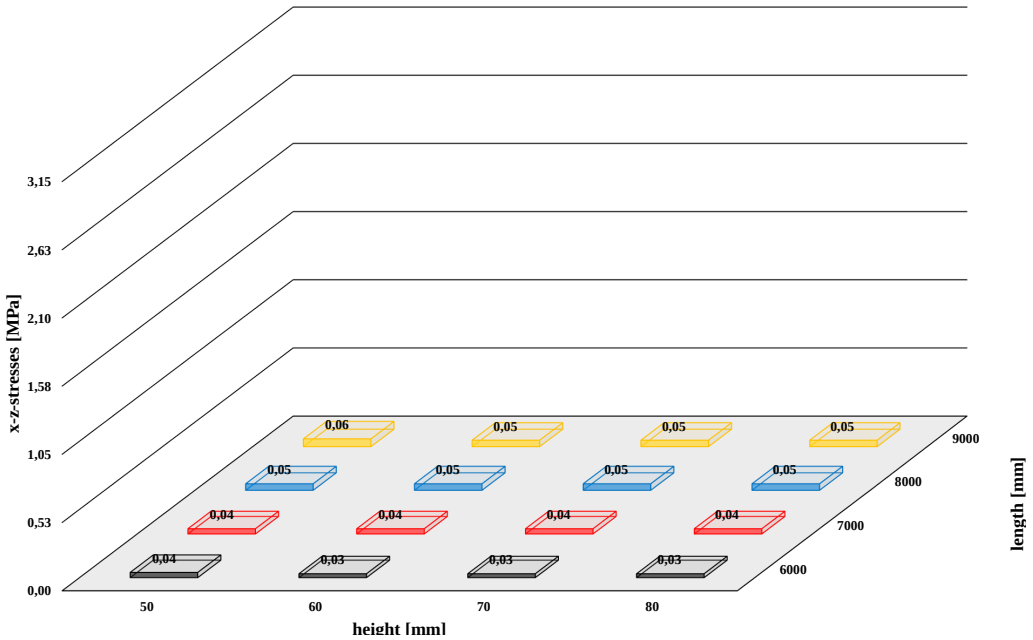

Figure A.26: Result of point supported model; t=48 hours; 42.5 % relative humidity; $max.f_t = 1.59$ MPa

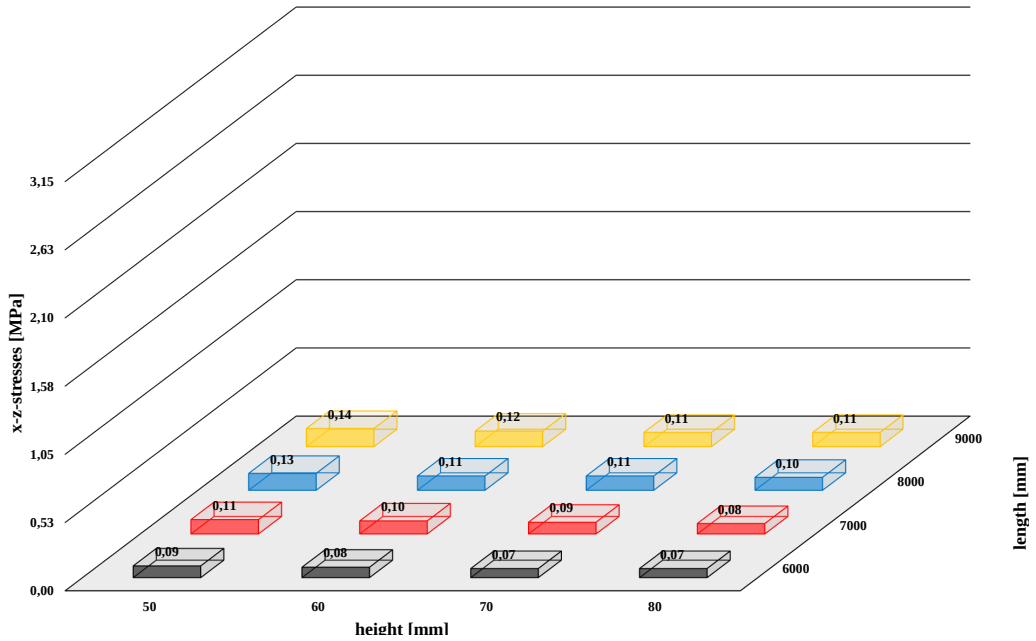

Figure A.27: Result of point supported model; t=7 days; 42.5 % relative humidity; $max.f_t = 1.90$ MPa

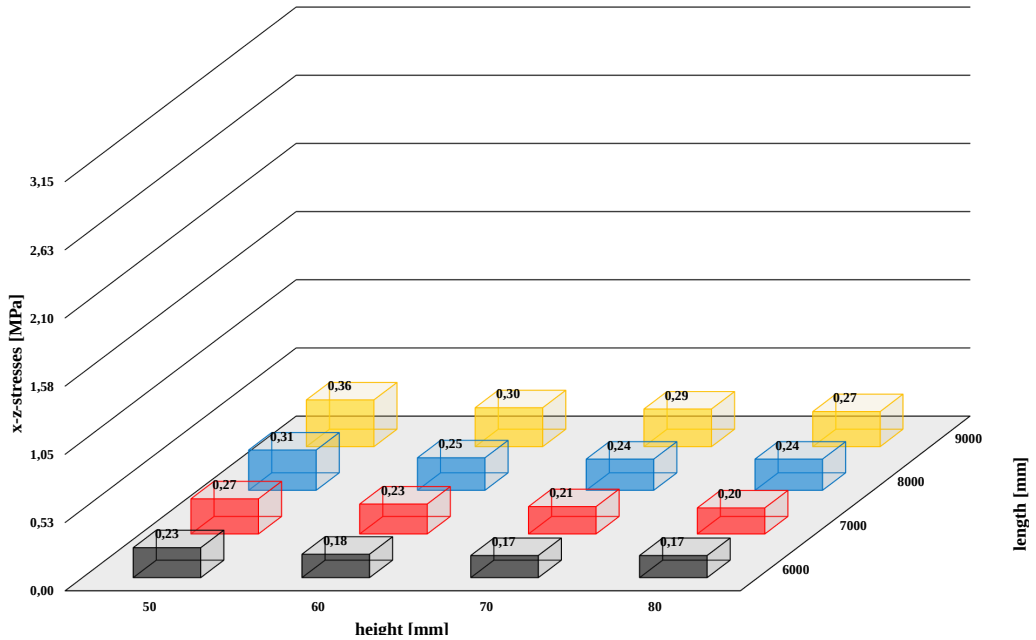

Figure A.28: Result of point supported model; t=28 days; 42.5 % relative humidity; $max.f_t = 2.14$ MPa

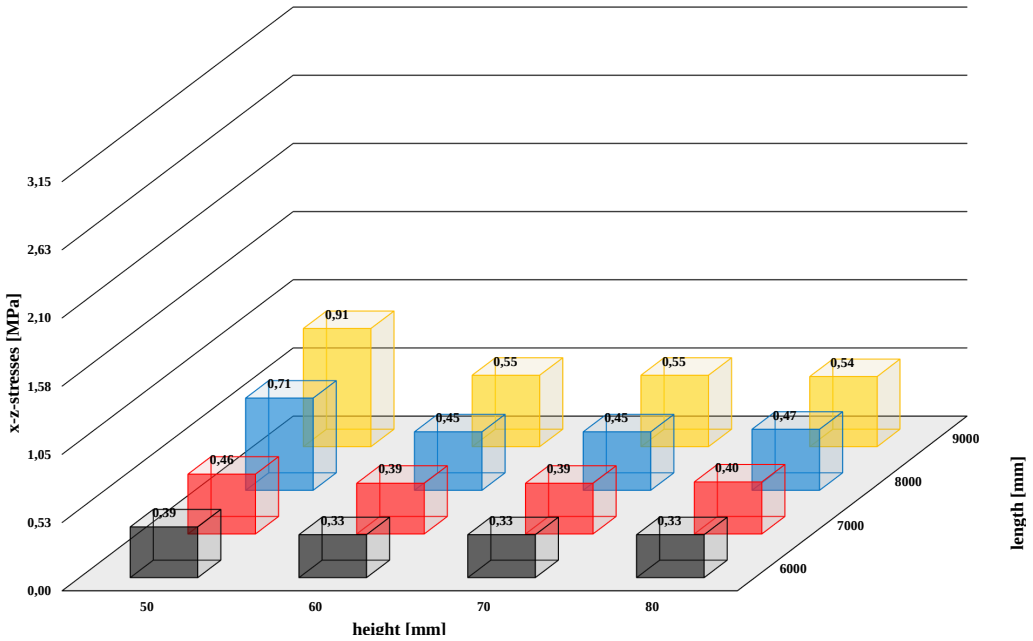

Figure A.29: Result of point supported model; t=100 days; 42.5 % relative humidity; $max.f_t = 2.47$ MPa

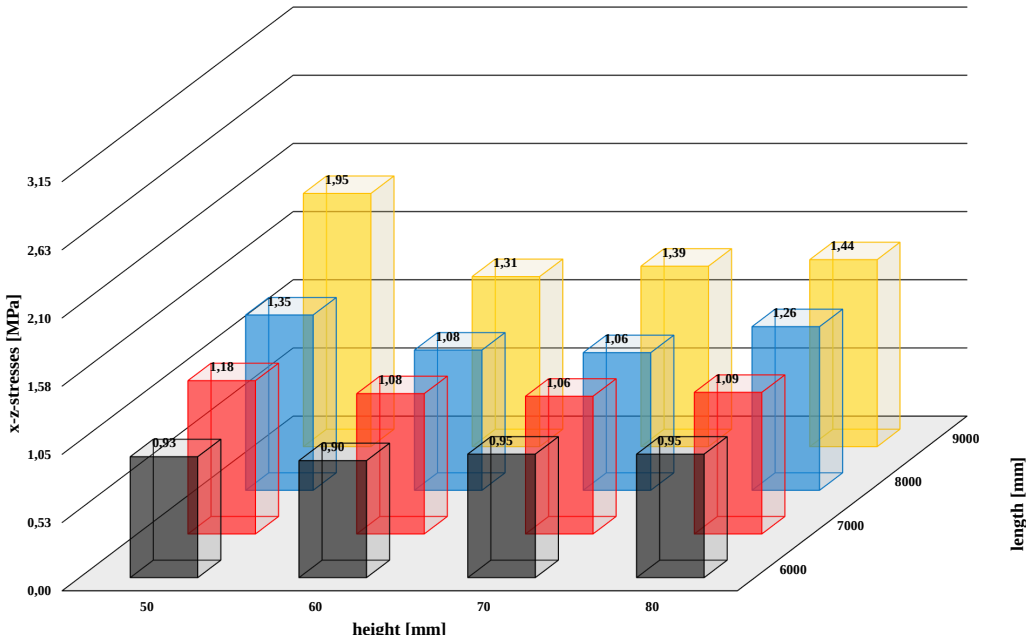

Figure A.30: Result of point supported model; t=5 years; 42.5 % relative humidity; $max.f_t = 2.82$ MPa

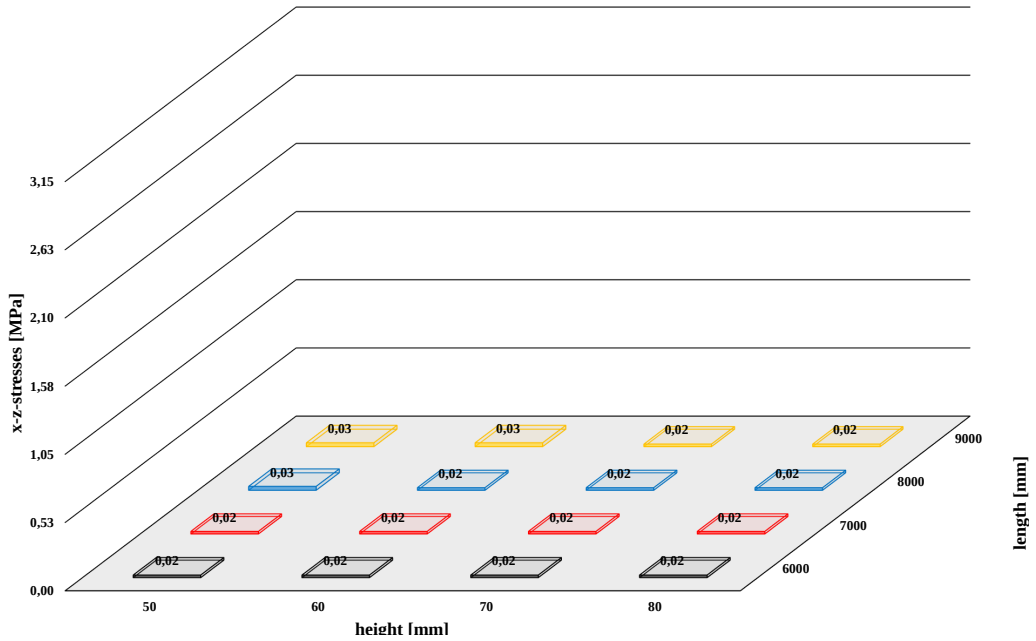

Figure A.31: Result of point supported model; t=24 hours; 65 % relative humidity; $max.f_t = 1.16$ MPa

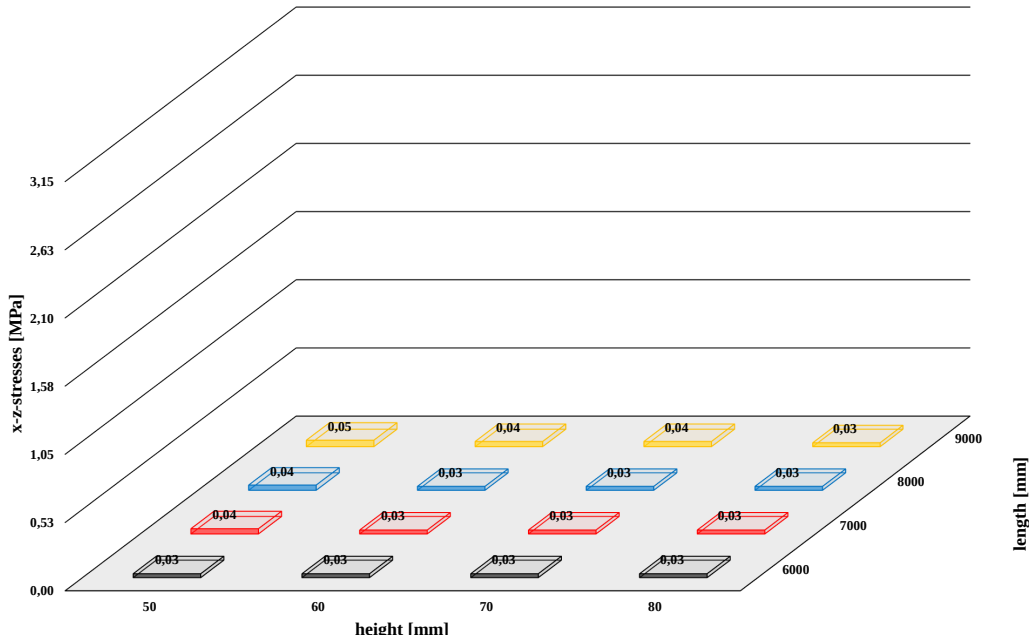

Figure A.32: Result of point supported model; t=48 hours; 65 % relative humidity; $max.f_t = 1.59$ MPa

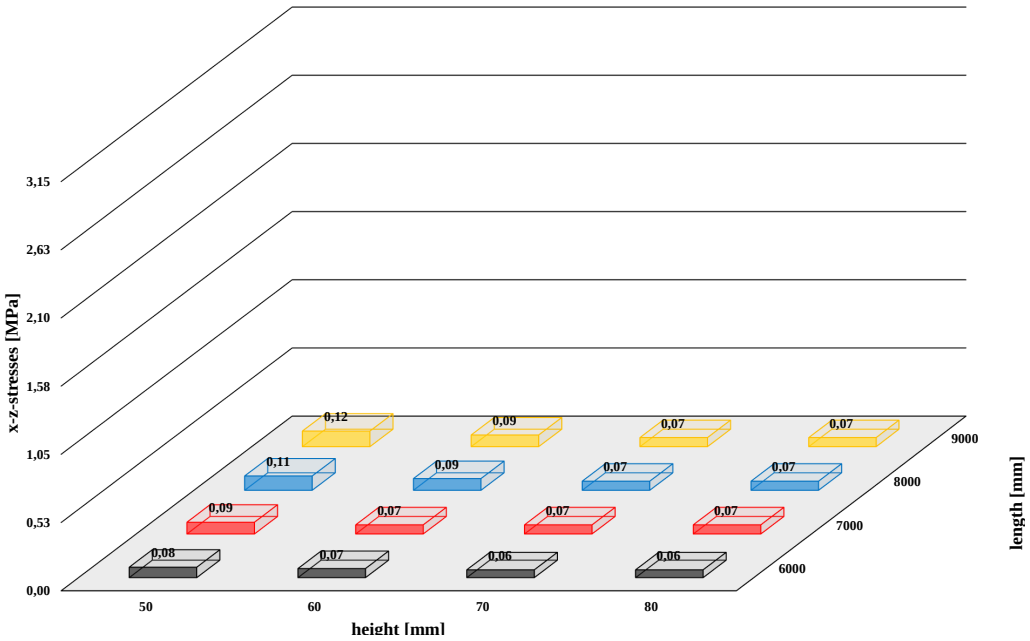

Figure A.33: Result of point supported model; t=7 days; 65 % relative humidity; $max.f_t = 1.90$ MPa

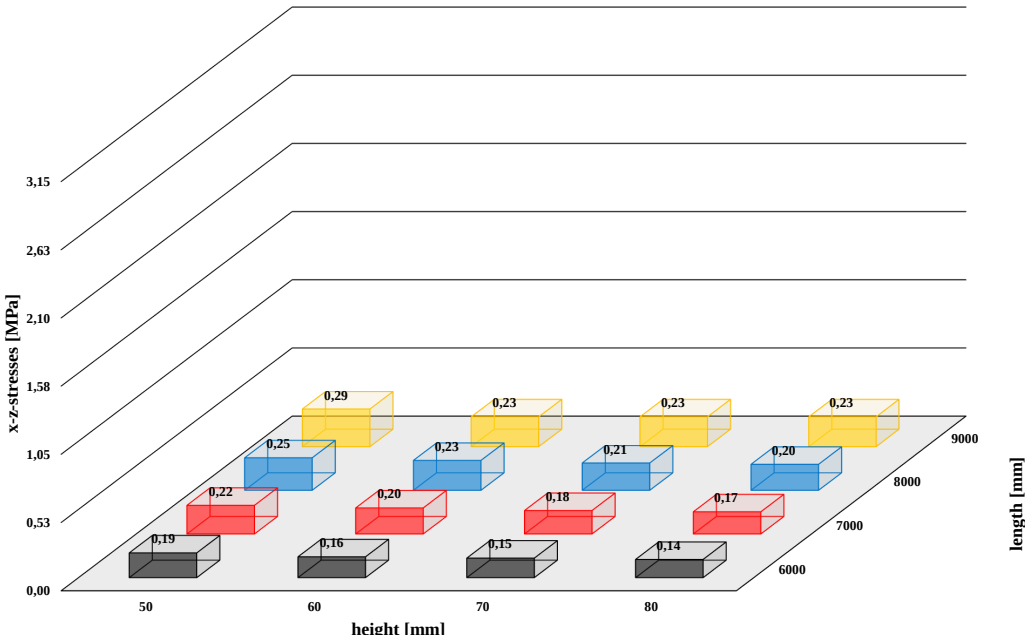

Figure A.34: Result of point supported model; t=28 days; 65 % relative humidity; $max.f_t = 2.14$ MPa

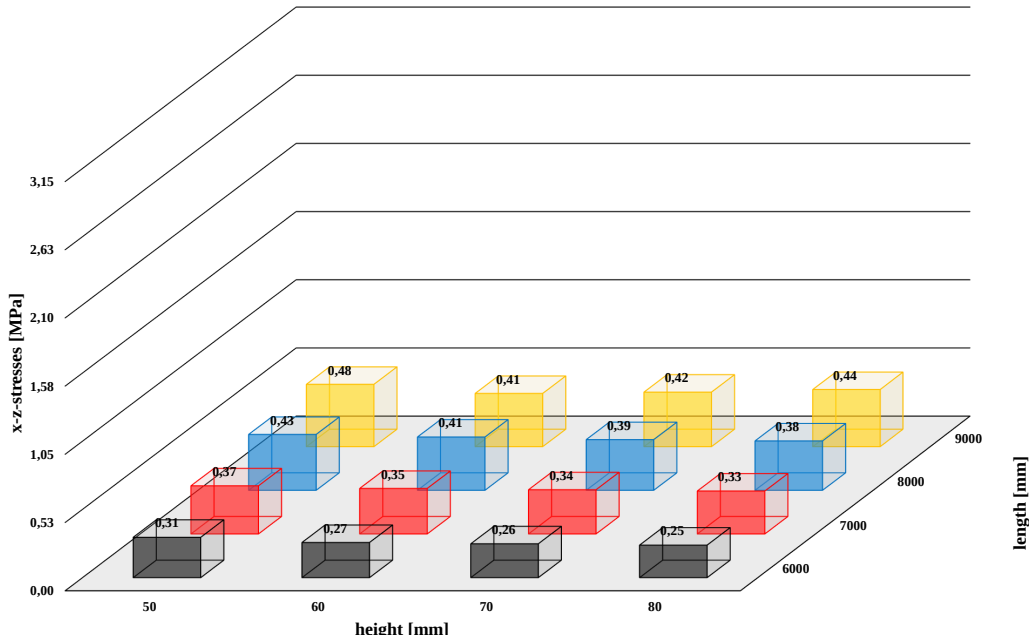

Figure A.35: Result of point supported model; t=100 days; 65 % relative humidity; $max.f_t = 2.47$ MPa

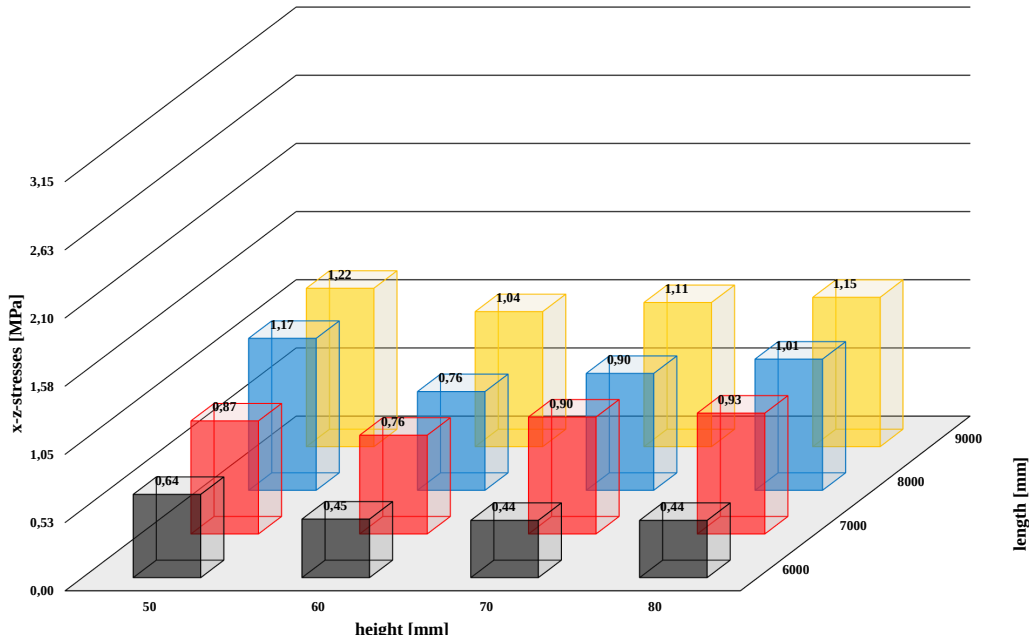

Figure A.36: Result of point supported model; t=5 years; 65 % relative humidity; $max.f_t = 2.82$ MPa

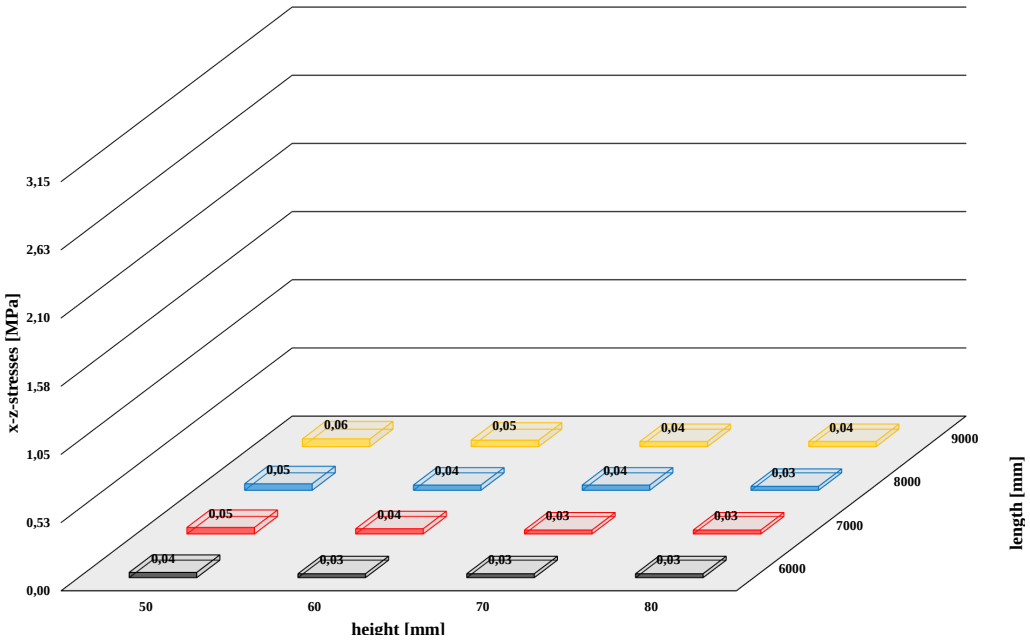

Figure A.37: Result of model with support on three axes; t=24 hours; 20 % relative humidity; $max.f_t = 1.16$ MPa

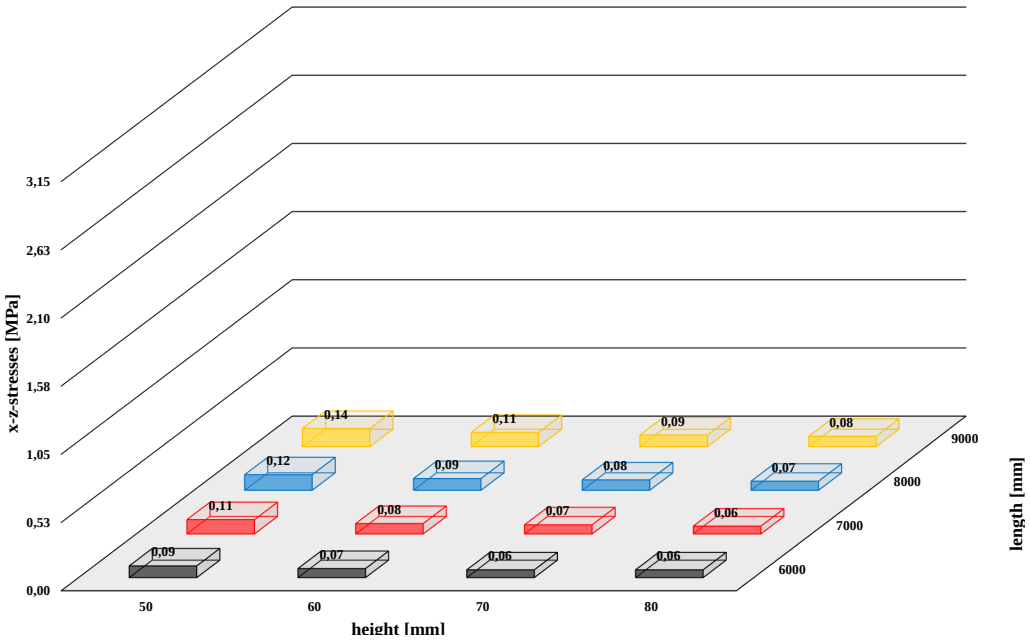

Figure A.38: Result of model with support on three axes; t=48 hours; 20 % relative humidity; $max.f_t = 1.59$ MPa

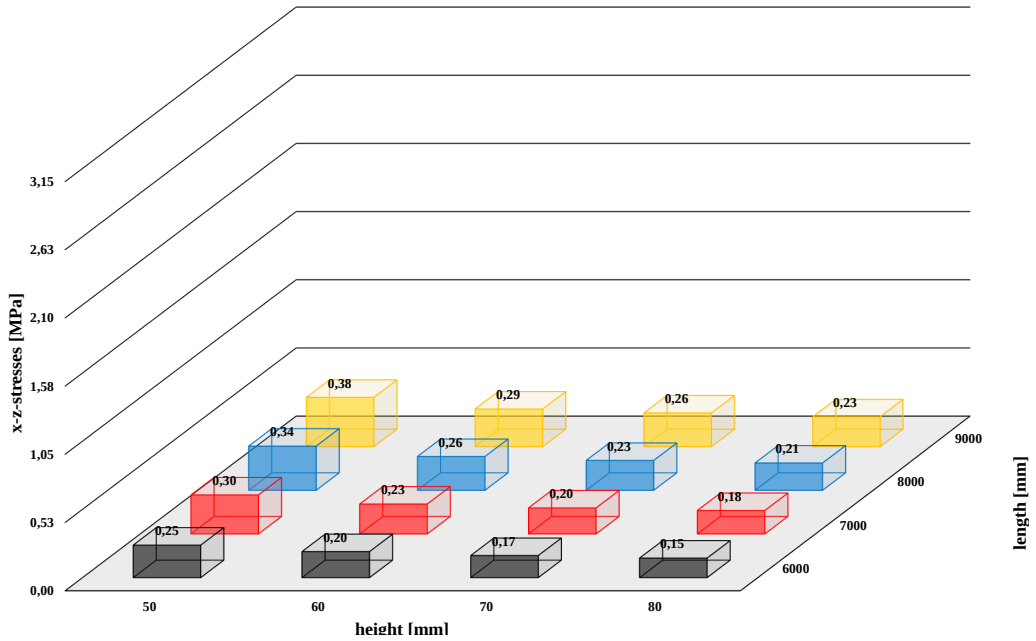

Figure A.39: Result of model with support on three axes; t=7 days; 20 % relative humidity; $max.f_t = 1.90$ MPa

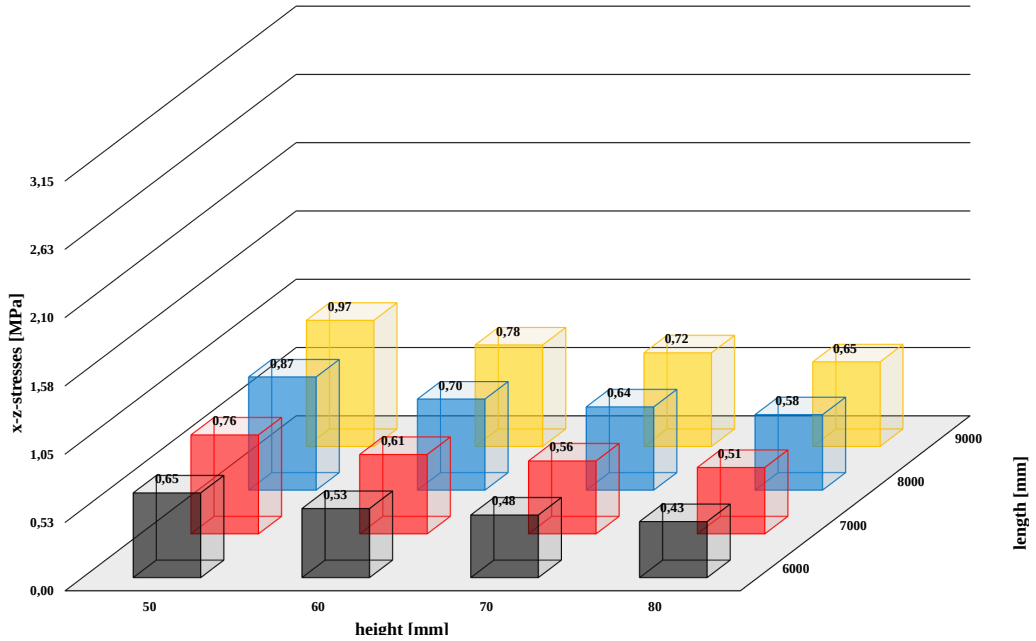

Figure A.40: Result of model with support on three axes; t=28 days; 20 % relative humidity; $max.f_t = 2.14$ MPa

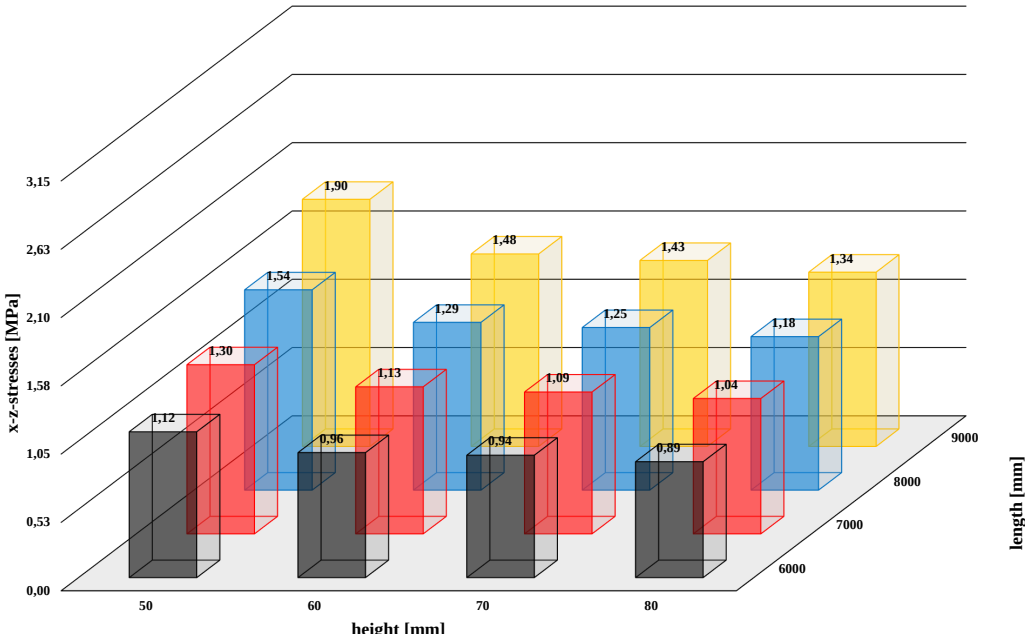

Figure A.41: Result of model with support on three axes; t=100 days; 20 % relative humidity; $max.f_t = 2.47$ MPa

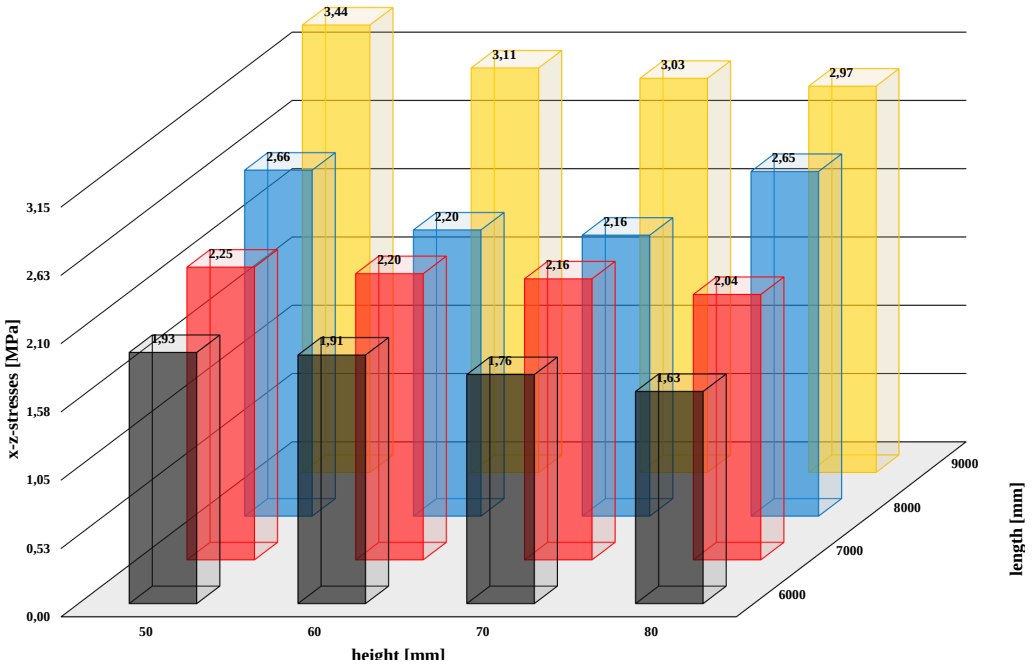

Figure A.42: Result of model with support on three axes; t=5 years; 20 % relative humidity; $max.f_t = 2.82$ MPa

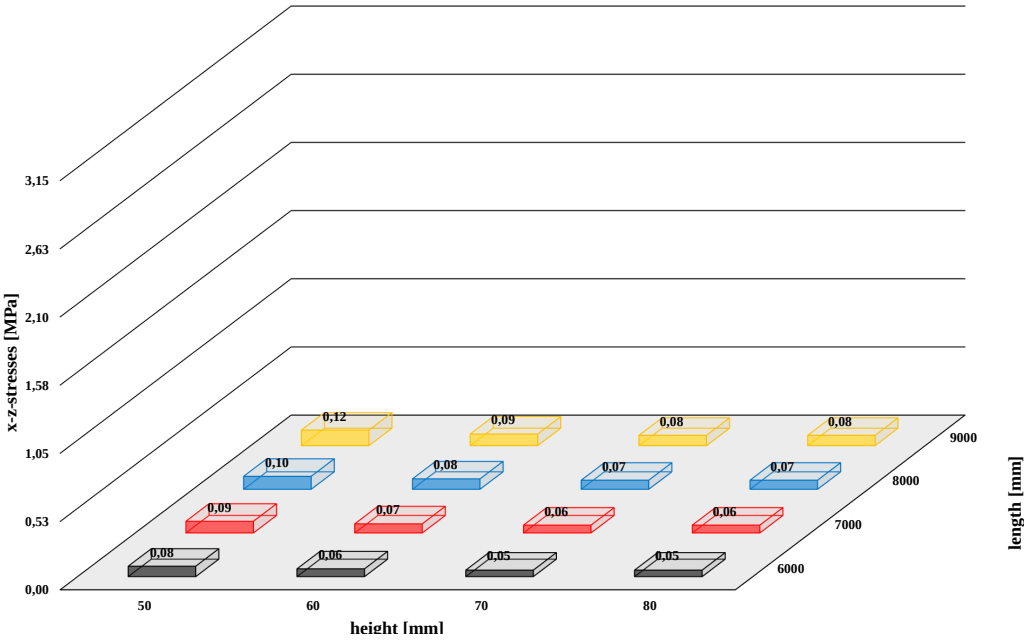

Figure A.43: Result of model with support on three axes; t=24 hours; 42.5 % relative humidity; $max.f_t = 1.16$ MPa

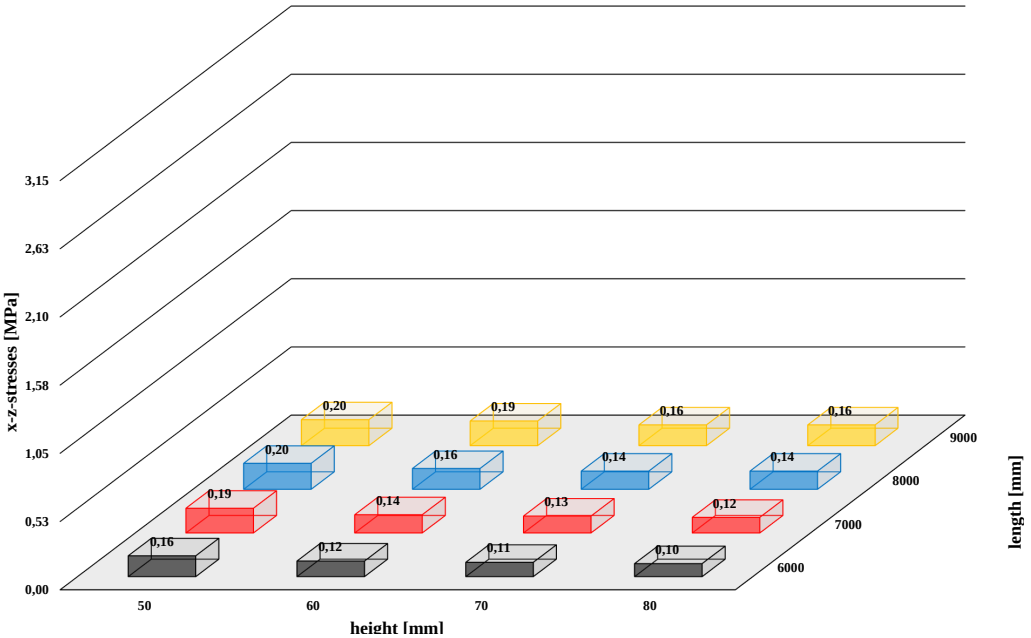

Figure A.44: Result of model with support on three axes; t=48 hours; 42.5 % relative humidity; $max.f_t = 1.59$ MPa

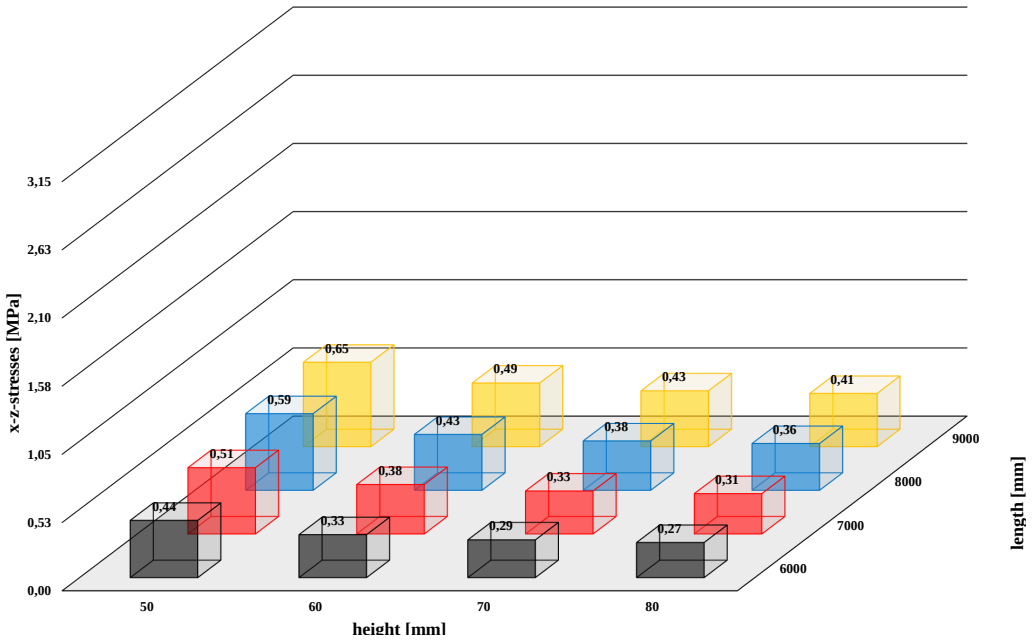

Figure A.45: Result of model with support on three axes; t=7 days; 42.5 % relative humidity; $max.f_t = 1.90$ MPa

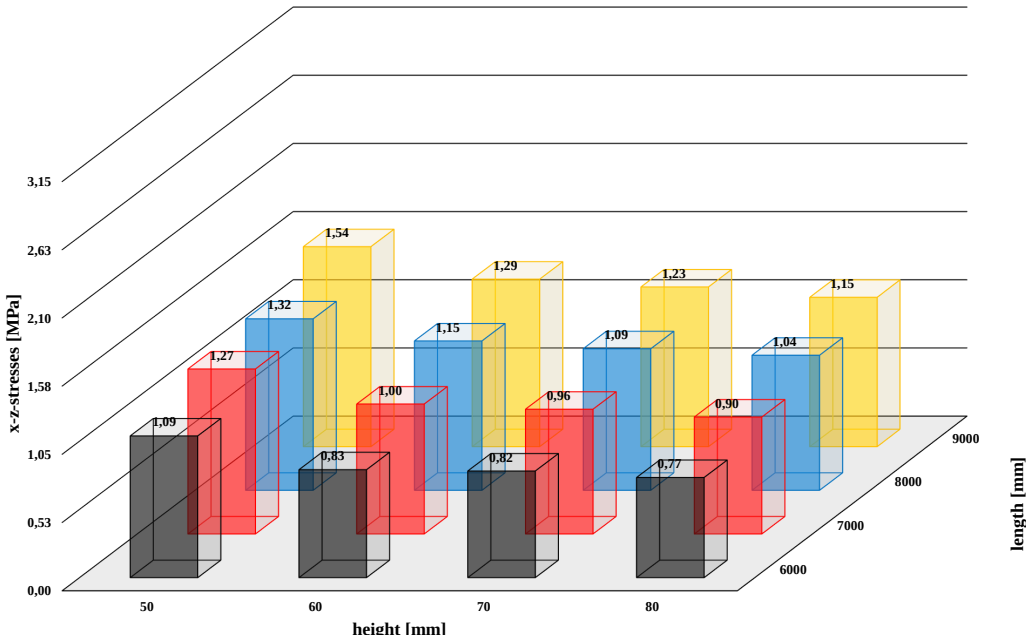

Figure A.46: Result of model with support on three axes; t=28 days; 42.5 % relative humidity; $max.f_t = 2.14$ MPa

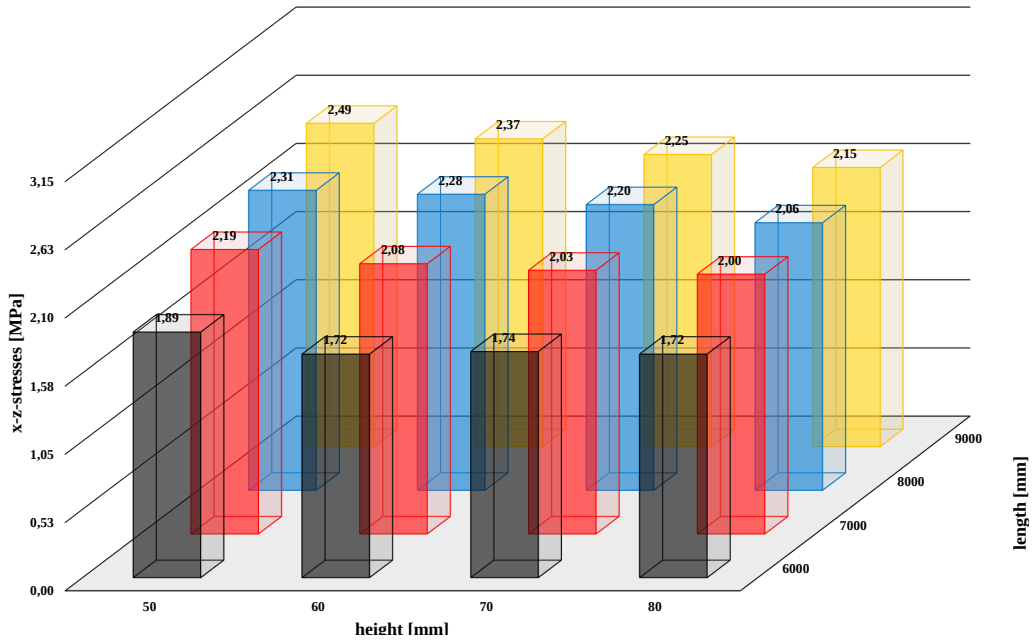

Figure A.47: Result of model with support on three axes; t=100 days; 42.5 % relative humidity; $max.f_t = 2.47$ MPa

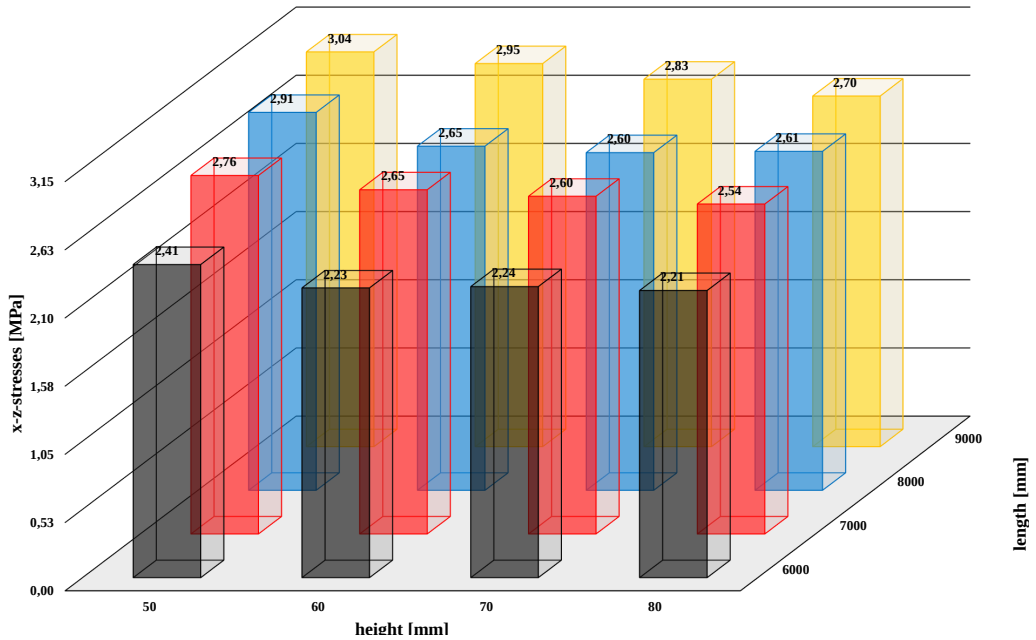

Figure A.48: Result of model with support on three axes; t=5 years; 42.5 % relative humidity; $max.f_t = 2.82$ MPa

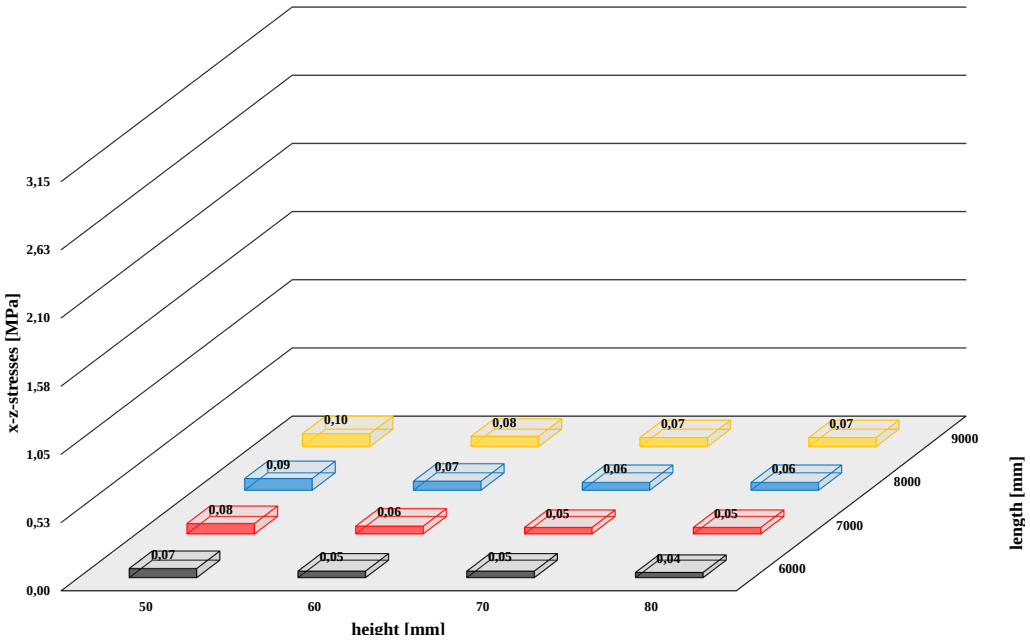

Figure A.49: Result of model with support on three axes; t=24 hours; 65 % relative humidity; $max.f_t = 1.16$ MPa

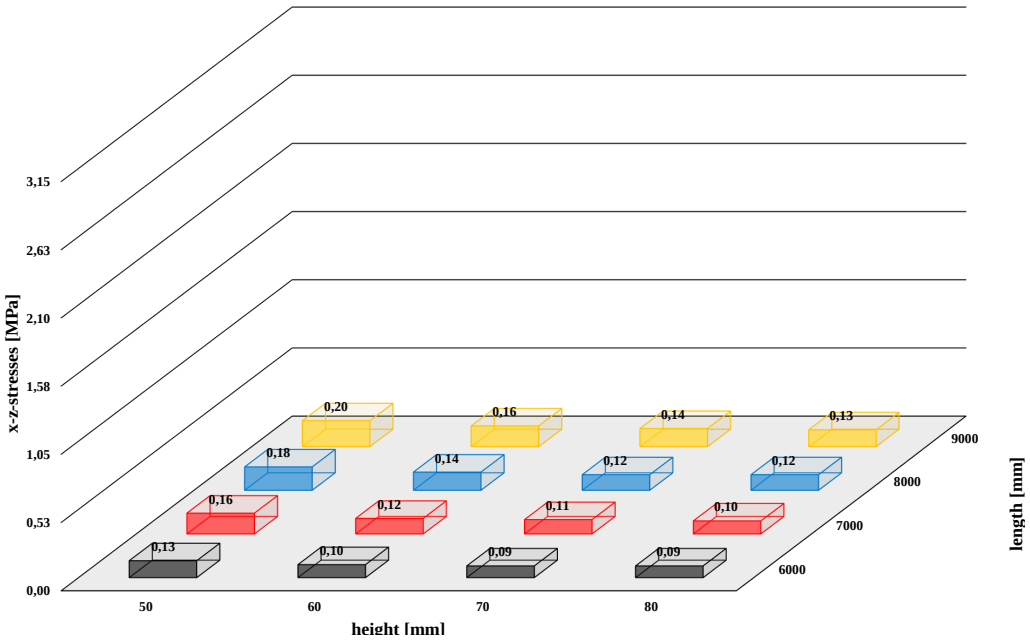

Figure A.50: Result of model with support on three axes; t=48 hours; 65 % relative humidity; $max.f_t = 1.59$ MPa

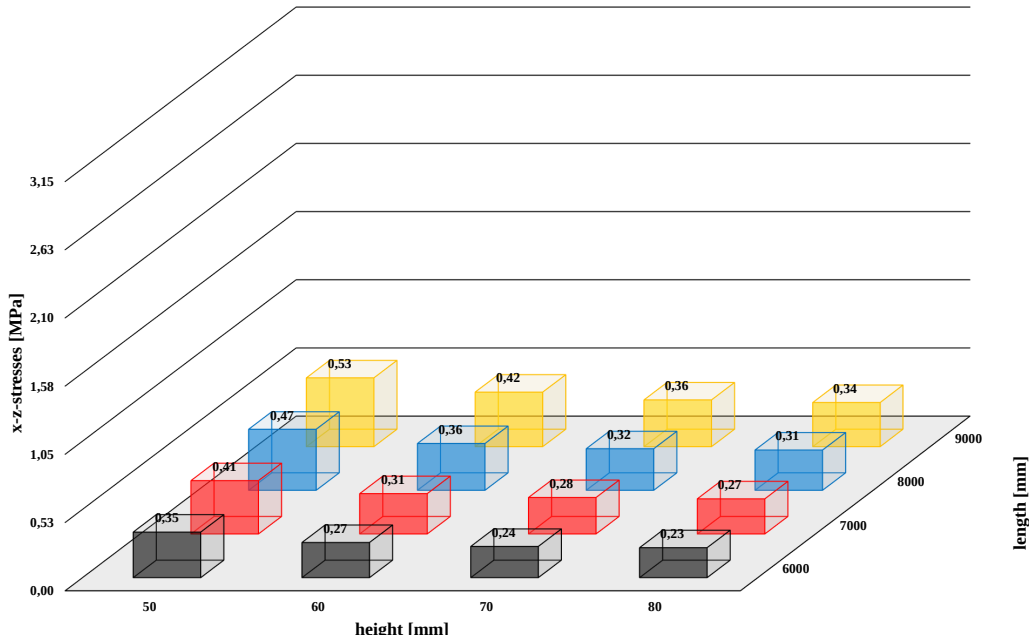

Figure A.51: Result of model with support on three axes; t=7 days; 65 % relative humidity; $max.f_t = 1.90$ MPa

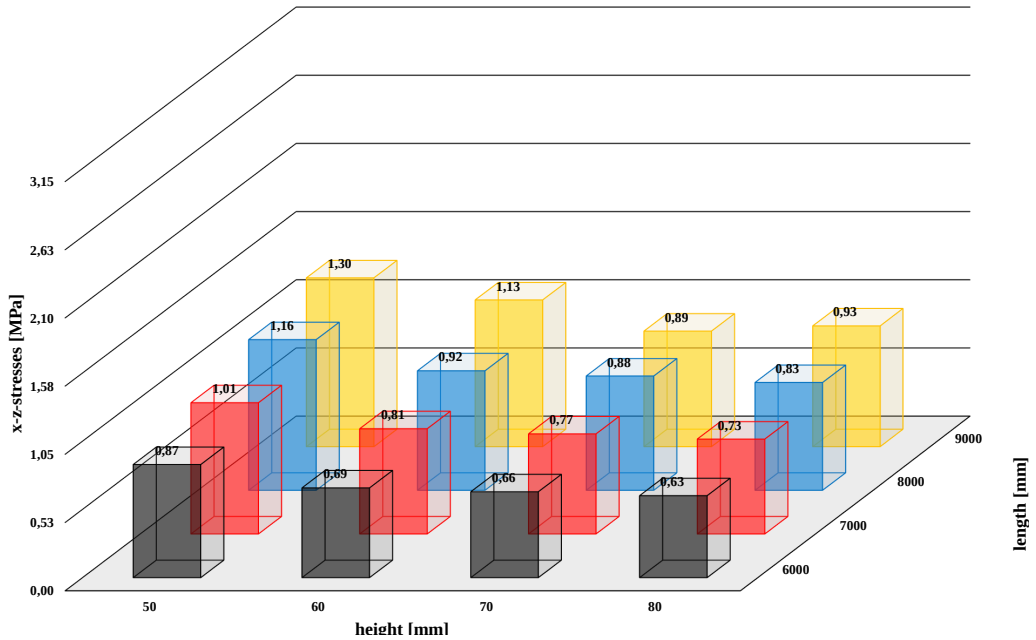

Figure A.52: Result of model with support on three axes; t=28 days; 65 % relative humidity; $max.f_t = 2.14$ MPa

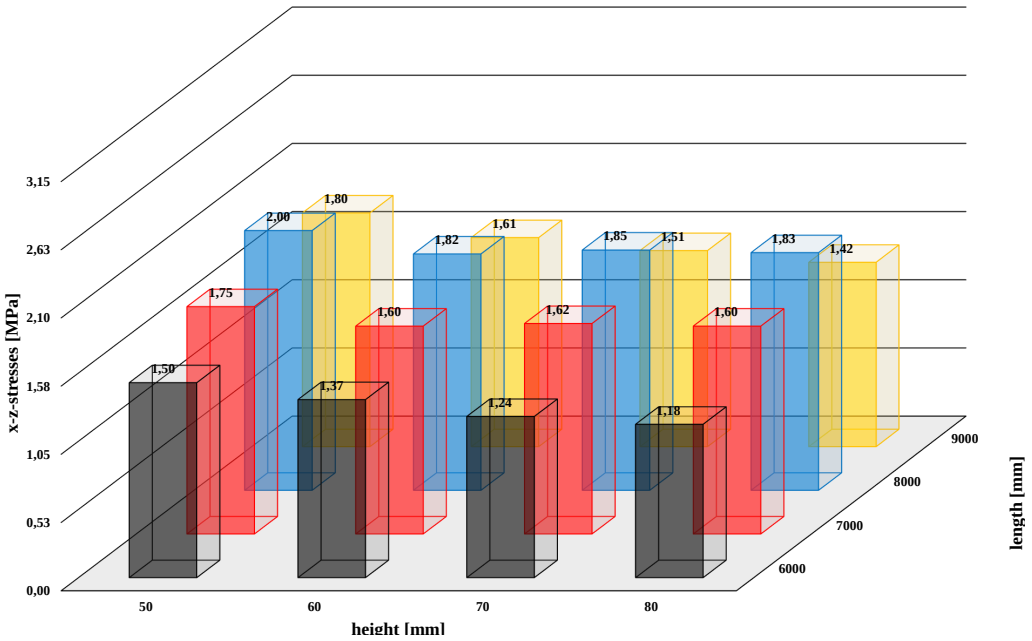

Figure A.53: Result of model with support on three axes; t=100 days; 65 % relative humidity; $max.f_t = 2.47$ MPa

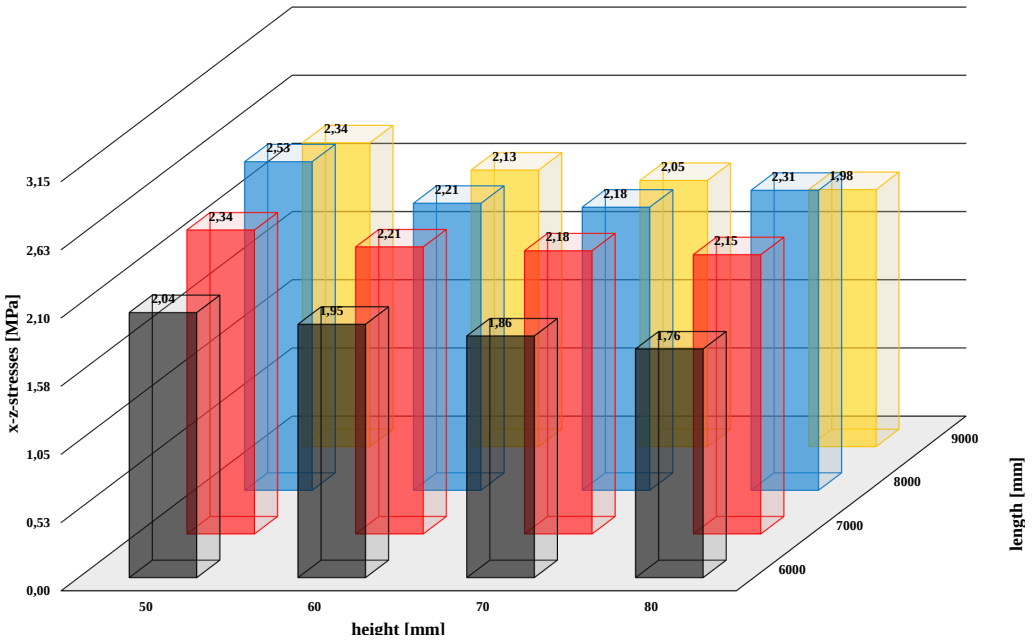

Figure A.54: Result of model with support on three axes; t=5 years; 65 % relative humidity; $max.f_t = 2.82$ MPa

B Annexe

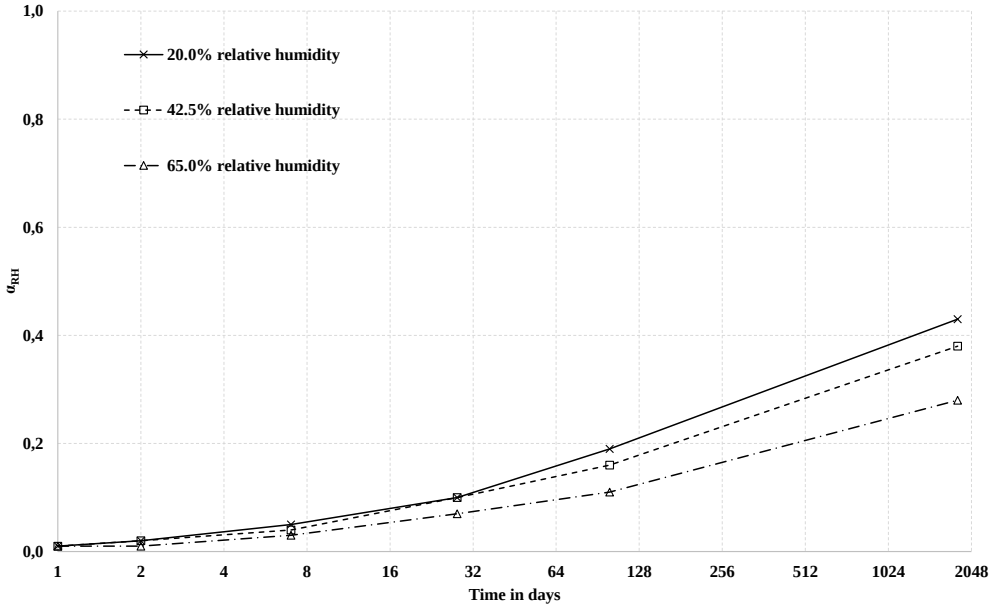

Figure B.1: Related stress development α_{RH} for full support

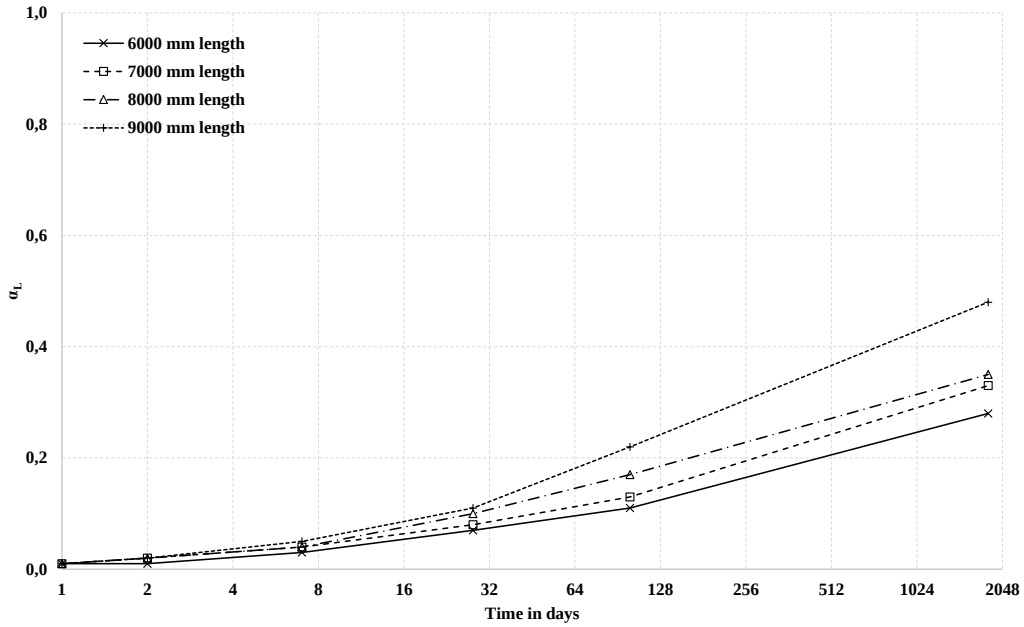

Figure B.2: Related stress development α_L for full support

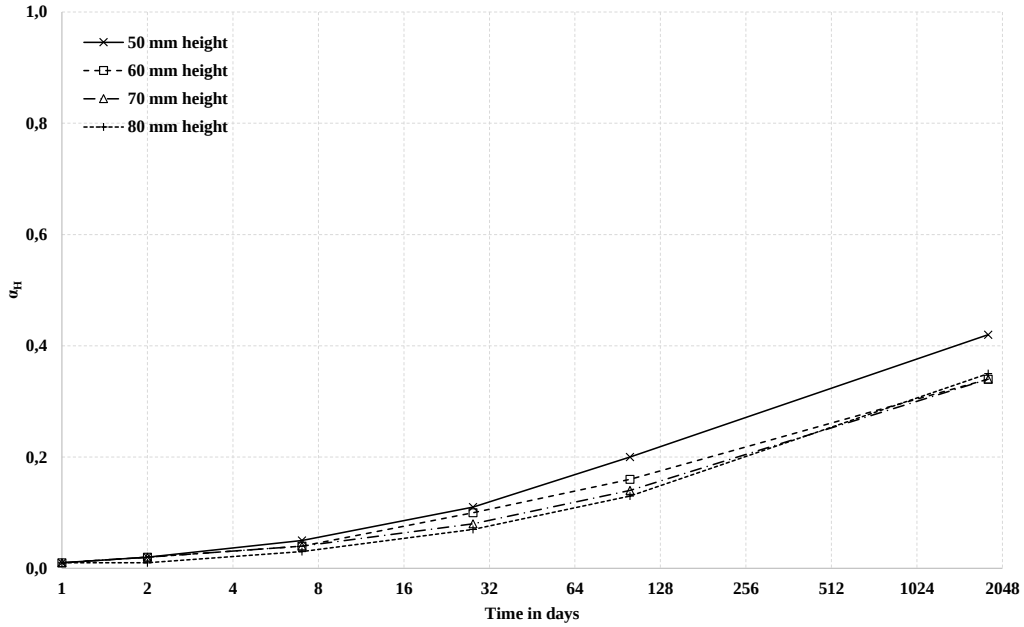

Figure B.3: Related stress development α_H for full support

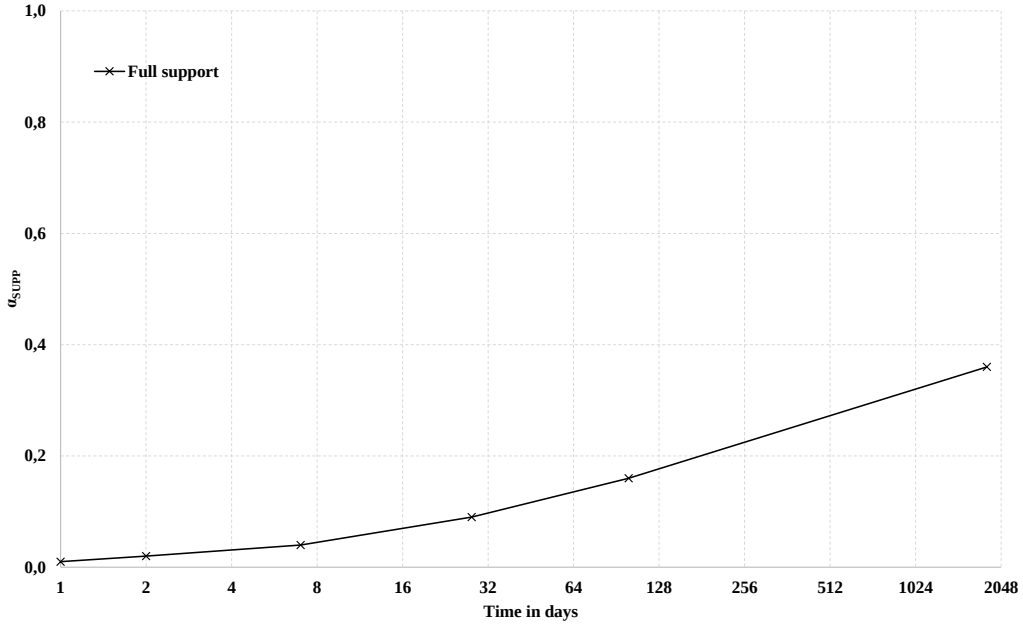

Figure B.4: Related stress development α_{SUPP} for full support

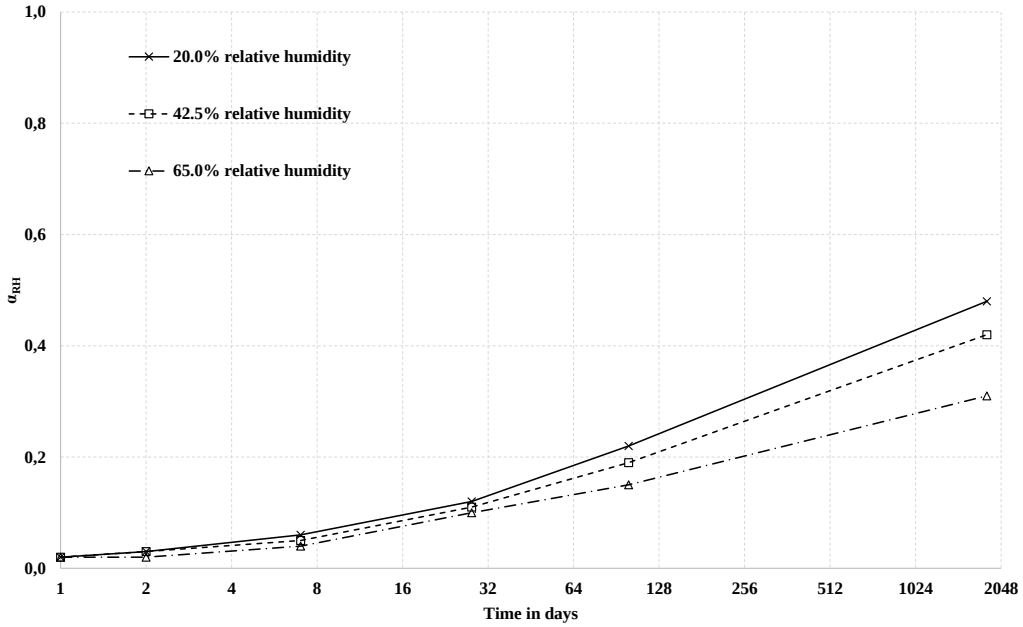

Figure B.5: Related stress development α_{RH} for point support

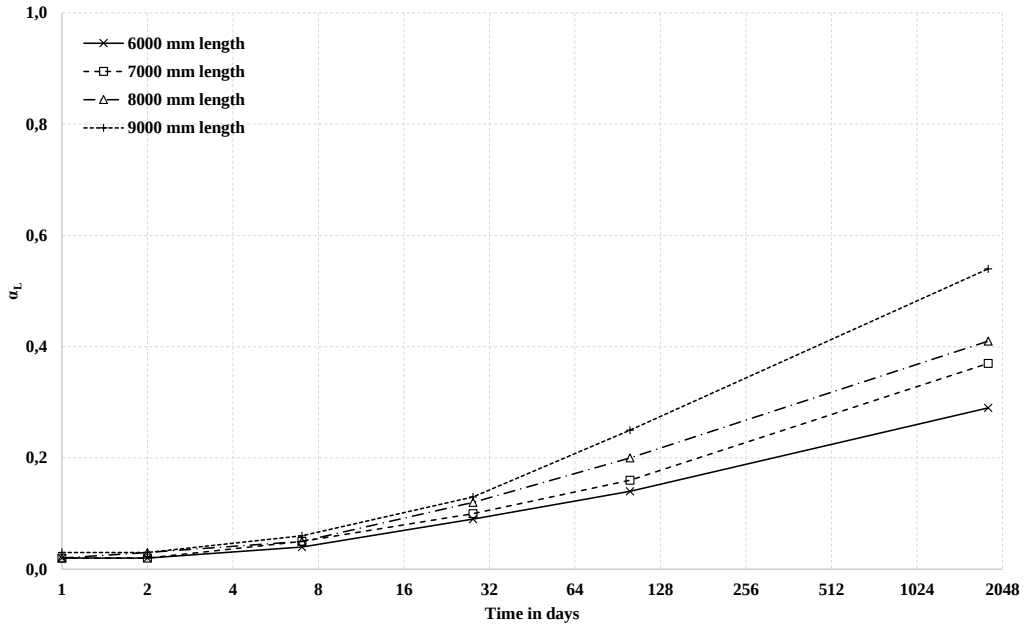

Figure B.6: Related stress development α_L for full support

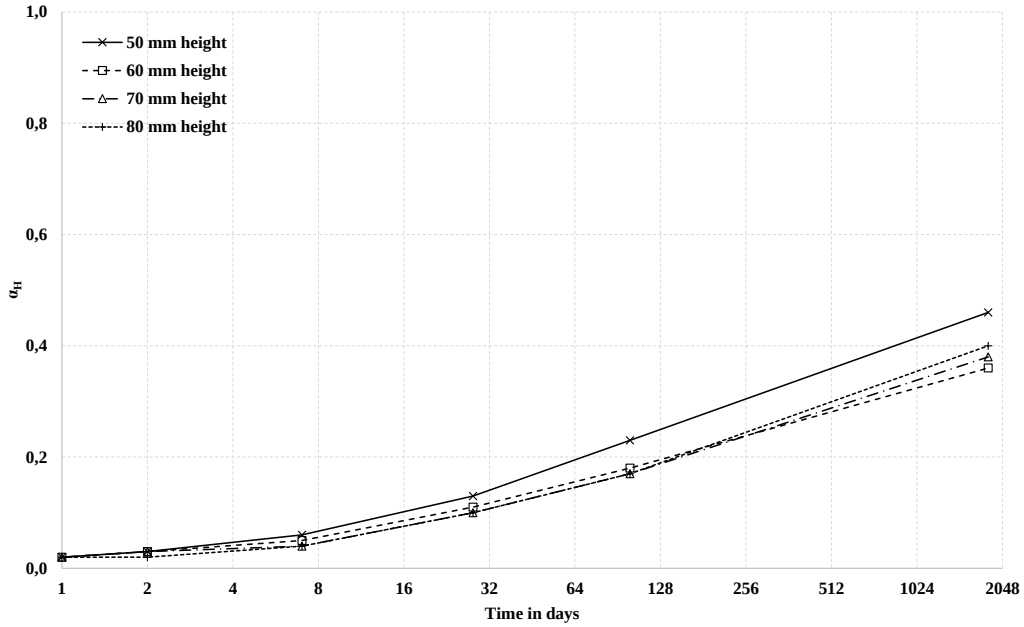

Figure B.7: Related stress development α_H for point support

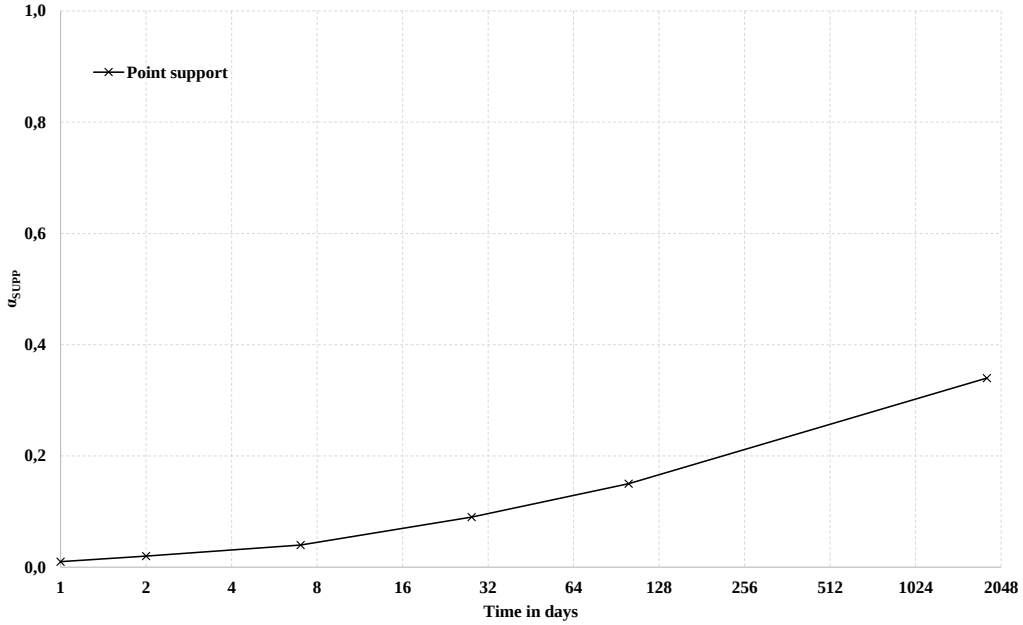

Figure B.8: Related stress development α_{SUPP} for full support

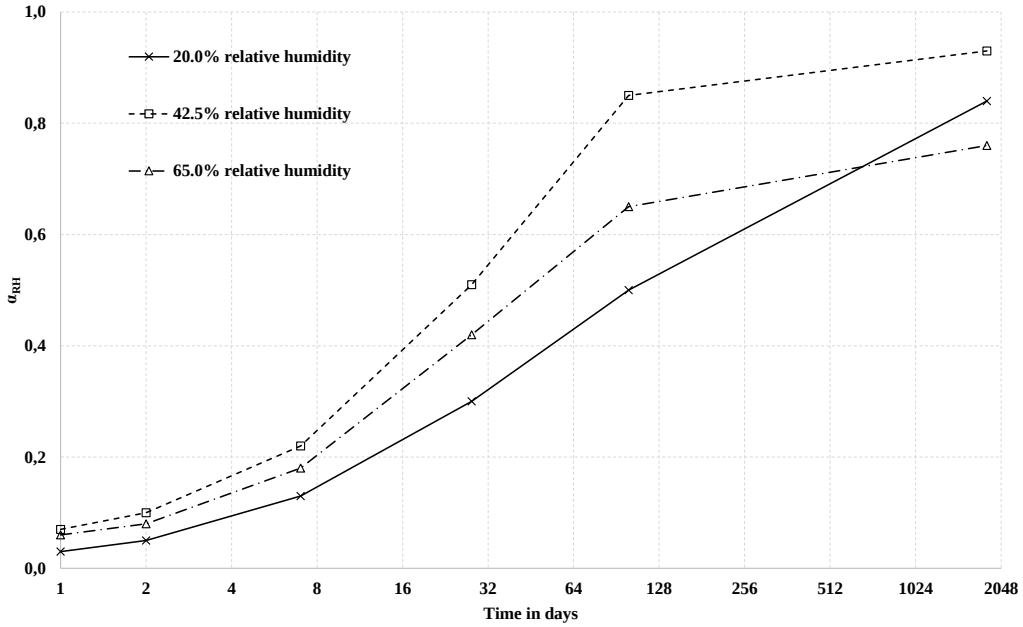

Figure B.9: Related stress development α_{RH} for support on three axes

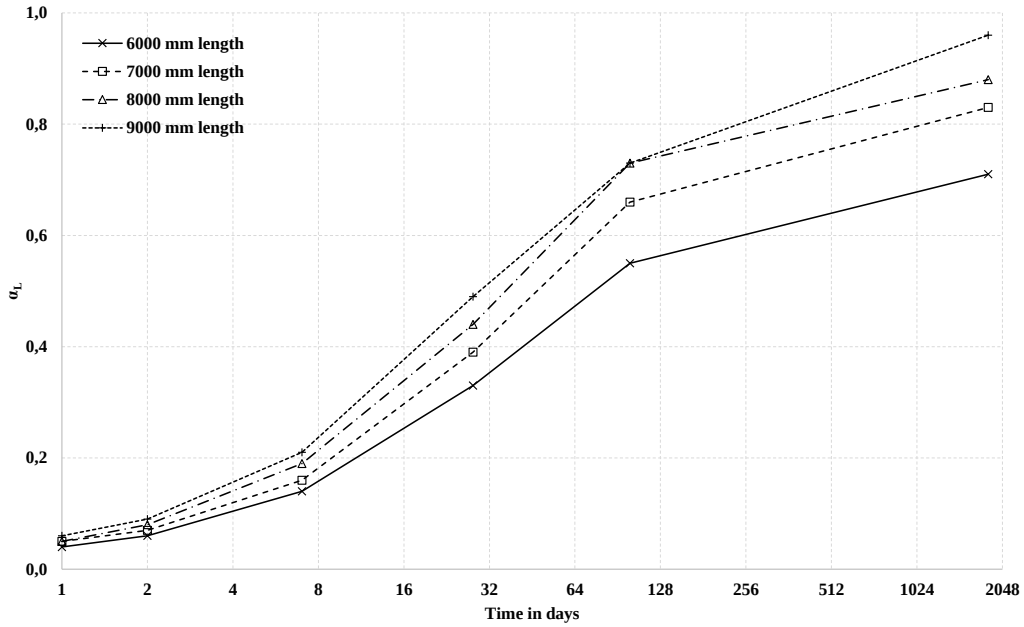

Figure B.10: Related stress development α_L for support on three axes

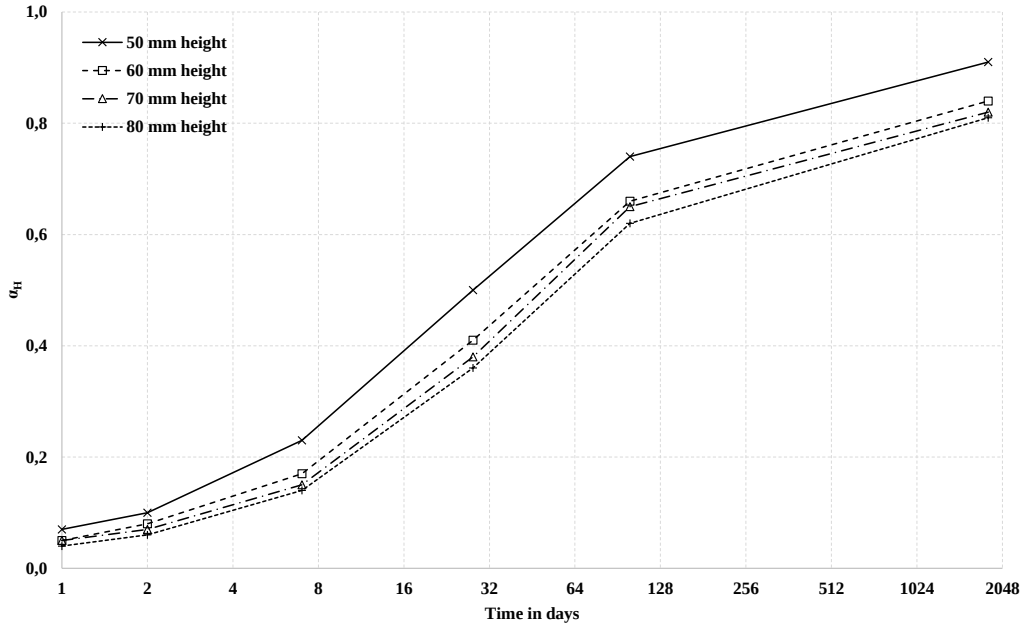

Figure B.11: Related stress development α_H for support on three axes

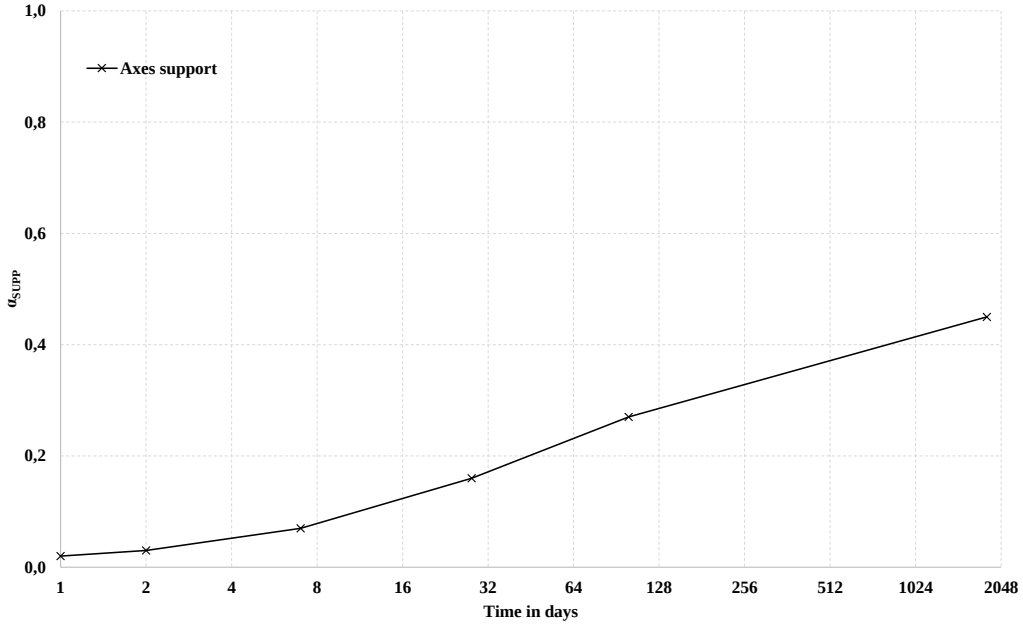

Figure B.12: Related stress development α_{SUPP} for support on three axes

Bibliography

Adams, L. (1976). The measurement of very early hydration reactions of portland cement clinker by a thermoelectric conduction calorimeter. *Cement and Concrete Research*, 6(2):293 – 307.

Šahinagić-Isović, Markovski, and Ćećez (2012). Shrinkage strain of concrete - causes and types. *Građevinar*, 64:727–734.

Akita, H., Koide, H., Tomon, M., and Sohn, D. (2003). A practical method for uniaxial tension test of concrete. *Materials and Structures*, 36:365–371.

Alhussainy, F., Hasan, H. A., Rogic, S., Sheikh, M. N., and Hadi, M. N. (2016). Direct tensile testing of self-compacting concrete. *Construction and Building Materials*, 112:903 – 906.

ANSYS Inc. ANSYS Europe (2013). *ANSYS Theory reference*.

Avak and Glaser (2007). *Spannbetonbau: Theorie, Praxis, Berechnungsbeispiele*, volume 2. Aktualisierte Auflage. Bauwerk, Berlin.

Banthia, N. and Gupta, R. (2006). Influence of polypropylene fiber geometry on plastic shrinkage cracking in concrete. *Cement and Concrete Research*, 36(7):1263 – 1267.

Banthia, N. and Nandakumar, N. (2003). Crack growth resistance of hybrid fiber reinforced cement composites. *Cement and Concrete Composites*, 25(1):3 – 9.

Banthia, N. and Sappakittipakorn, M. (2007). Toughness enhancement in steel fiber reinforced concrete through fiber hybridization. *Cement and Concrete Research*, 37(9):1366 – 1372.

Banthia, N. and Sheng, J. (1996). Toughness of frc composites fracture toughness of micro-fiber reinforced cement composites. *Cement and Concrete Composites*, 18(4):251 – 269.

Beissel, S., Johnson, G., and Popelar, C. (1998). An element-failure algorithm for dynamic crack propagation in general directions. *Engineering Fracture Mechanics*, 61(3–4):407 – 425.

Belytschko, T. and Black, T. (1999). Elastic crack growth in finite elements with minimal remeshing. *International Journal for numerical methods in engineering*, 45:601–620.

Beshara, F. (1993). Smeared crack analysis for reinforced concrete structures under blast-type loading. *Engineering Fracture Mechanics*, 45(1):119 – 140.

Betonstein Handwerk (2011). Merkblatt geschliffene zementgebundene Bodensysteme. Technical report, Betonstein Handwerk.

Biscoping, M. and Beck, M. (2014). Betonieren bei extremen Temperaturen. Technical report, Verein Deutscher Zementwerke e.V., Düsseldorf.

Bonzel, K. W. J. (1961). Festigkeitsentwicklung verschiedener Zemente bei niederer Temperatur. *beton*, 11:35–48.

Bosold, D. and Pickhardt, R. (2014). Zemente und ihre Herstellung. Zement-Merkblatt Betontechnik B1, Verein Deutscher Zementwerke e.V., Düsseldorf.

Bosolt, D. (2014). Risse im Beton. Technical report, Verein Deutscher Zementwerke e.V., Düsseldorf.

Brameshuber, W. (2016). Recommendation of RILEM TC 232-TDT: test methods and design of textile reinforced concrete. *Materials and Structures*, 49:4923–4927.

Bröske, R. (2010). Singularitäten in der FEM und deren Bewertung. pages 1–5.

Bützer, P. (2009). Zementerhärtung. Technical report, Pädagogische Hochschule St.Gallen.

Buffo-Lacarrière, L., Sellier, A., Escadeillas, G., and Turatsinze, A. (2007). Multiphasic finite element modeling of concrete hydration. *Cement and Concrete Research*, 37(2):131 – 138.

Cervera, M., Chiumenti, M., Benedetti, L., and Codina, R. (2015). Mixed stabilized finite element methods in nonlinear solid mechanics. Part III: Compressible and incompressible plasticity. *Computer Methods in Applied Mechanics and Engineering*.

Cervera, M., Faria, R., Oliver, J., and Prato, T. (2002). Numerical modelling of concrete curing, regarding hydration and temperature phenomena. *Computers & Structures*, 80(18–19):1511 – 1521.

Cheng, C., Ge, S., Yao, S., Niu, Z., and Recho, N. (2016). Singularity analysis for a v-notch with angularly inhomogeneous elastic properties. *International Journal of Solids and Structures*, 78–79:138 – 148.

Chern, J.-C. and Young, C.-H. (1989). Compressive creep and shrinkage of steel fibre reinforced concrete. *International Journal of Cement Composites and Lightweight Concrete*, 11(4):205 – 214.

Choi, S.-J., Yang, K.-H., Sim, J.-I., and Choi, B.-J. (2014). Direct tensile strength of lightweight concrete with different specimen depths and aggregate sizes. *Construction and Building Materials*, 63:132 – 141.

Dahms, J. (1978). Herstellung und Eigenschaften von Faserbeton.

de Schutter, G. (1996). Degree of hydration-based description of mechanical properties of early age concrete. *Materials and Structures*, 29:335–344.

de Schutter, G. (2002). Finite element simulation of thermal cracking in massive hardening concrete elements using degree of hydration based material laws. *Computers & Structures*, 80(27–30):2035 – 2042.

Deutscher Ausschuß für Stahlbetonbau (1996). Richtlinie Betonbau beim Umgang mit wassergefährdenden Stoffen. Technical Report 09, Deutscher Ausschuß für Stahlbetonbau.

DIN EN 12390-13:2014-06 (2014). Prüfung von Festbeton - Teil 13: Bestimmung des Elastizitätsmoduls unter Druckbelastung (Sekantenmodul); Deutsche Fassung EN 12390-13:2013. Technical report, Beuth Verlag, Berlin.

DIN EN 197-1:2011-11 (2011). Zement - Teil 1: Zusammensetzung, Anforderungen und Konformitätskriterien von Normalzement. Technical report, Beuth Verlag, Berlin.

DIN EN 1991-1-1:2002 + AC:2009 (2009). Eurocode 1: Einwirkungen auf Tragwerke – Teil 1-1: Allgemeine Einwirkungen auf Tragwerke – Wichten, Eigengewicht und Nutzlasten im Hochbau; Deutsche Fassung EN 1991-1-1:2002 + AC:2009. Technical report, Normenausschuss Bauwesen (NABau) im DIN.

DIN EN 1992-1-1:2011-01 (2011). Bemessung und Konstruktion von Stahlbeton-und Spannbetontragwerken - Teil 1-1: Allgemeine Bemessungsregeln und Regeln für den Hochbau. Technical report, Beuth Verlag, Berlin.

DIN EN 206:2017-01 (2017). Beton - Festlegung, Eigenschaften, Herstellung und Konformität; Deutsche Fassung EN 206:2013+A1:2016. Technical report, Beuth Verlag.

DIN EN 934-2:2012-08 (2012). Zusatzmittel für Beton, Mörtel und Einpressmörtel - Teil 2: Betonzusatzmittel - Definitionen, Anforderungen, Konformität, Kennzeichnung und Beschriftung. Technical report, Beuth Verlag.

DIN Fachbericht 104 (2009). Din Fachbericht 104, "Verbundbrücken,". Technical report, Beuth Verlag, Berlin.

dos Santos, C. C. and Rodrigues, J. P. C. (2016). Calcareous and granite aggregate concretes after fire. *Journal of Building Engineering*, 8:231 – 242.

Drucker, D. C. and Prager, W. (1952). Soil mechanics and plastic analysis or limit design. *Quarterly of applied mathematics*, 10(2):157–165.

Edalat-Behbahani, A., Barros, J., and Ventura-Gouveia, A. (2017). Three dimensional plastic-damage multidirectional fixed smeared crack approach for modelling concrete structures. *International Journal of Solids and Structures*, 115–116:104 – 125.

Eifert, H. (2006). Massige Bauteile aus Beton. Zement-Merkblatt Betontechnik B11, Verein Deutscher Zementwerke e.V., Düsseldorf.

Eisenmann (1996). Bemessung und Konstruktion von Betonstraßen. *Straße + Autobahn*, 12/1996.

Eisenmann and Leykauf (1987). Bau von Verkehrsflächen. *Beton-Kalender*, pages 641–748.

Eisenmann and Leykauf (1991). Hochwölbung der Plattenränder von Betonfahrbahnen. *Straße + Autobahn*, 10/1991.

Fagerholt, Børvik, and Hopperstad (2013). Measuring discontinuous displacement fields in cracked specimens using digital image correlation with mesh adaptation and crack-path optimization. *Optics and Lasers in Engineering*, 51(3):299 – 310.

Fagerholt, Østby, Børvik, and Hopperstad (2012). Investigation of fracture in small-scale {SENT} tests of a welded {X80} pipeline steel using digital image correlation with node splitting. *Engineering Fracture Mechanics*, 96:276 – 293.

Fédération internationale du béton (2013). Code-type models for structural behaviour of concrete. background of the constitutive relation and material in the fib model code for concrete structures 2010. Technical report, Fédération Internationale du Béton, Siegmar Kästl e.K Germany.

Fluckinger, J. (2016). Klassische Bodenprobleme bei Unterlagsböden. Technical report.

Foos, S. (2005). *Unbewehrte Betonfahrbahnplatten unter witterungsbedingten Beanspruchungen*. Phd thesis, Universität Fridericiana zu Karlsruhe (TH).

Francois, R. and Maso, J. (1988). Effect of damage in reinforced concrete on carbonation or chloride penetration. *Cement and Concrete Research*, 18(6):961 – 970.

Fujimoto, T. and Nishioka, T. (2010). Moving finite element analyses for fast crack propagation in sheet metal. *International Journal of Mechanical Sciences*, 52(2):277 – 286. {SPECIAL} ISSUE: Advances in Modeling and Evaluation of Materials in Honor of Professor Tomita.

Gebauer (2016). Grundlagen und Hinweise – KINTEMP und KINFEST.

Georgin, J., Ambroise, J., Péra, J., and Reynouard, J. (2008). Development of self-leveling screed based on calcium sulfoaluminate cement: Modelling of curling due to drying. *Cement and Concrete Composites*, 30(9):769 – 778.

Goris, A. (2010). *Bautabellen für Ingenieure*, volume 19. Werner Verlag.

Graybeal, B. A. and Baby, F. (2013). Development of direct tension test method for ultra-high-performance fiber-reinforced concrete. *ACI Materials Journal*, 110:177–186.

Grube, H. (1991). Ursachen des Schwindens von Beton und Auswirkungen auf Betonbauteile. Technical report, Verein Deutscher Zementwerke e.V, Düsseldorf.

Gruben, G., Fagerholt, E., Hopperstad, O. S., Børvik, T., and Langseth, M. (2014). Numerical simulation of ductile fracture in modified arcan test. *Procedia Materials Science*, 3:661 – 666.

Helm (2010). Neue Richtlinie "Stahlfaserbeton". Fachtagung Stahlfaserbeton.

Hilsdorf, H. and Reinhardt, H.-W. (2000). Beton. *Beton-Kalender*, 1, Section A:1–117.

Hu, S., Lu, J., and Xiao, F. (2013). Evaluation of concrete fracture procedure based on acoustic emission parameters. *Construction and Building Materials*, 47:1249 – 1256.

Jacobs, Hunkeler, Carmine, Germann, and Hirschi (2008). Schwinden von Beton. *Der Bauingenieur*, Heft 3/2008:14–19.

Kamiński, M. and Zielenkiewicz, W. (1982). The heats of hydration of cement constituents. *Cement and Concrete Research*, 12(5):549 – 558.

Karsten, R. (2003). *Bauchemie; Mit Ursachen, Verhütung und Sanierung von Bauschäden.* C.F. Müller Verlag, Hüthing GmbH & Co. KG.

Kashef-Haghighi, S., Shao, Y., and Ghoshal, S. (2015). Mathematical modeling of {CO2} uptake by concrete during accelerated carbonation curing. *Cement and Concrete Research*, 67:1 – 10.

Klischke, M. (2012). Carbonfasern und Polymerdispersion. Untersuchungsbericht, Wilhem Dyckerhoff Institut, Wiesbaden.

Kocur, G. K., Saenger, E. H., Grosse, C. U., and Vogel, T. (2016). Time reverse modeling of acoustic emissions in a reinforced concrete beam. *Ultrasonics*, 65:96 – 104.

Kuna, M. (2010). *Numerische Beanspruchungsanalyse von Rissen.* Freiberg: Vieweg + Teubner Verlag.

Langenberg, P. (2015). Grundlagen der Bruchmechanik. Online.

Lieber, W. (1967). Einfluß von Zinkoxid auf das Erstarren und Erhärten von Portlandzementen. *Zement Kalk Gips*, 20:91–95.

Locher, F. W. (2000). *Zement: Grundlagen der Herstellung.* Bau + Technik.

Lohmeyer, G. and Ebeling, K. (2012). *Betonböden für Produktions-und Lagerhallen. Planung, Bemessung, Ausführung.* Verlag Bau + Technik.

Lorenz, O.-K. and Schmidt, M. (1998). Aufschüsseln auf Trennschicht verlegter Zementestriche. *Estrichtechnik (Sonderdruck)*, 1/1998:2–7.

Lura, P. (2011). Werkstoffe I Schwinden und Quellen. Technical report, EMPA, ETH Zürich.

Martinola, Sadouki, and Wittmann (1996). Numerische Model zur Beschreibung der Eigenspannungen und der Rissbildung in Beschichtungssystemen. In *4. Internationales Kolloquium Werkstoffwissenschaften und Bauinstandsetzen*. Technische Akademie Esslingen.

Mindess, S., Lawrence, F. V., and Kesler, C. E. (1977). The j-integral as a fracture criterion for fiber reinforced concrete. *Cement and Concrete Research*, 7(6):731 – 742.

Oecknick (1996). Computergestützte Analyse der Betonerhärtung in der Baupraxis. pages 66–72.

Oehmischen, S. (2010). Beton – hart, aber tückisch. *Dr. Arnold Chemie-Beratung*.

Ozkan, U., Nied, H., and Kaya, A. (2010). Fracture analysis of anisotropic materials using enriched crack tip elements. *Engineering Fracture Mechanics*, 77(7):1191 – 1202.

Papadakis, V. G., Vayenas, C. G., and Fardis, M. N. (1991). Experimental investigation and mathematical modeling of the concrete carbonation problem. *Chemical Engineering Science*, 46(5):1333 – 1338.

Pathak, H., Singh, A., and Singh, I. V. (2013). Fatigue crack growth simulations of 3-d problems using {XFEM}. *International Journal of Mechanical Sciences*, 76:112 – 131.

Pickhardt, R. and Schäfer, W. (2014). Nachbehandlung und Schutz des jungen Betons. Zement-Merkbkatt B8, Verein Deutscher Zementwerke e.V., Düsseldorf.

Richartz, W. (1969). Über die Gefüge- und Festigkeitsentwicklung des Zementsteins. *Beton*, 19:203–206.

Roziere, E., Cortas, R., and Loukili, A. (2015). Tensile behaviour of early age concrete: New methods of investigation. *Cement and Concrete Composites*, 55:153 – 161.

Saetta, A. V., Schrefler, B. A., and Vitaliani, R. V. (1995). 2 — d model for carbonation and moisture/heat flow in porous materials. *Cement and Concrete Research*, 25(8):1703 – 1712.

Samer, A. (2017). Stress based failure criteria. Online.

Schäfer, W. and Beck, M. (2015). Zementestrich. Zement-Merkblatt Betontechnik B 19, InformationsZentrum Beton GmbH, Erkrath.

Schümann, B. (2006). Wirklichkeitsnahe Berechnung von Stahlbetonstabtragwerken. Studienarbeit, Technische Universität Hamburg-Harburg; Arbeitsbereich Baustatik und Stahlbau.

Schnell, W. (1987). Randverformung bei schwimmenden Estrichen/Heizestrichen - Einflüsse und Folgerungen. *boden-wand-decke*, 10.

Schwarz, P. (2000). [Online].

Shen, D., Shi, X., Zhu, S., Duan, X., and Zhang, J. (2016). Relationship between tensile young's modulus and strength of fly ash high strength concrete at early age. *Construction and Building Materials*, 123:317 – 326.

Song, H.-W., Kwon, S.-J., Byun, K.-J., and Park, C.-K. (2006). Predicting carbonation in early-aged cracked concrete. *Cement and Concrete Research*, 36(5):979 – 989.

Springenschmid, R. and Nischer, P. (1973). Untersuchungen über die Ursache von Querrissen im jungen Beton. *Beton- und Stahlbetonbau*, 68:221–226.

Stark, J. and Wicht, B. (1999). *Zement und Kalk: Der Baustoff als Werkstoff*. Birkhäuser Verlag.

Stark, J. and Wicht, B. (2012). *Geschichte der Baustoffe*. Vieweg+Teubner Verlag.

Staudt, Y., Odenbreit, C., and Schneider, J. (2016). Investigation of bonded connections with silicone under shear loading. In *Challenging Glass 5 - Conference on Architectural and Structural Applications of Glass.*

Stenzel, G. (2005). Beton-Bodenplatten für Hallen-und Freiflächen: Konstruktion und Bemessung. *Beton-und Stahlbetonbau*, 100(4):277–288.

Sun, X., Tan, V., and Tay, T. (2011). Micromechanics-based progressive failure analysis of fibre-reinforced composites with non-iterative element-failure method. *Computers & Structures*, 89(11–12):1103 – 1116. Computational Fluid and Solid Mechanics 2011Proceedings Sixth {MIT} Conference on Computational Fluid and Solid Mechanics.

Tacke, R. (2002). *Feuchte- und Festigkeitsentwicklung hydratisierenden Betons - Modellierung und numerische Analyse*. PhD thesis, Technische Universität Carolo-Wilhelmina zu Braunschweig.

Tay, T., Tan, S., Tan, V., and Gosse, J. (2005). Damage progression by the element-failure method (efm) and strain invariant failure theory (sift). *Composites Science and Technology*, 65(6):935 – 944.

Thienel and Hintzen (1994). Maßnahmen zur Vermeidung von Rissen in Tunnelinnenschalen aus Ortbeton. *Beton*, 44:522–526.

Thienel, K. C. (2015). Werkstoffe des Bauwesens - Festbeton. Technical report, Institut für Werkstoffe des Bauwesens Fakultät für Bauingenieur- und Vermessungswesen Universität der Bundeswehr, München.

Tschernjawski, O. M.-P. W. (1967). Einfluß niedriger Temperaturen auf den Hydratationsprozeß von Portlandzementen. *Silikattechnik*, 18:72–76.

Tutz, L. F. R. K. I. P. G. (2007). *Statistik. Der Weg zur Datenanalyse*, volume 6. Auflage. Springer-Verlag, Berlin / Heidelberg.

van Breugel, K. (1991). *Simulation of hydration and formation of structure in hardening cement-based materials*. PhD thesis, TU Delft.

Venecanin, S. (1989). A discussion of the paper "effect of damage in reinforced concrete on carbonation on chloride penetration" by r. francois and j.c. maso. *Cement and Concrete Research*, 19(6):989 – 990.

Verlag Bau+Technik (2008). Zement-Taschenbuch. Technical report, Verein Deutscher Zementwerke e.V, Düsseldorf.

Wang, C., Xiao, J., Zhang, G., and Li, L. (2016). Interfacial properties of modeled recycled aggregate concrete modified by carbonation. *Construction and Building Materials*, 105:307 – 320.

Wang, Z., Ma, L., Wu, L., and Yu, H. (2012). Numerical simulation of crack growth in brittle matrix of particle reinforced composites using the xfem technique. *Acta Mechanica Solida Sinica*, 25(1):9 – 21.

Weiler, M. and Waldmann, D. (2016). Untersuchung der Rissentwicklung an zementgebundenen Sichtestrichen. *beton*, 66:248–252.

Weise, F. (1996). Erhärtungsverlauf des Betons einer Brücke: Ermittlung der Temperatur- und Festigkeitsentwicklung. pages 732–734.

Weisner, A. and Richter, T. (2016). Massige Bauteile aus Beton. Technical report, InformationsZentrum Beton GmbH, Erkrath.

Wen, L. and Tian, R. (2016). Improved xfem: Accurate and robust dynamic crack growth simulation. *Computer Methods in Applied Mechanics and Engineering*, 308:256 – 285.

Westergaard, H. (1926). Stresses in concrete pavements computed by theoretical analysis. *Public Roads*, 7:25–35.

Willam, K. and Warnke, E. (1974). Constitutive model for the triaxial behaviour of concrete. Technical report, IABSE Reports of the working commisions.

Wischers, G. (1974). Faserbewehrter Beton. *beton*, 24:95/99.

Wischers, G. (1981). Ansteifen und Erstarren von Zement und Beton. pages 145–167.

Wischers, G. and Manns, W. (1972). Ursachen für das Entstehen von Rissen in jugem Beton. In *Technisch-wissenschaftliche Zement Tagung*, Berlin.

Wu, S., Chen, X., and Zhou, J. (2012). Tensile strength of concrete under static and intermediate strain rates: Correlated results from different testing methods. *Nuclear Engineering and Design*, 250:173 – 183.

Yao, W., Li, J., and Wu, K. (2003). Mechanical properties of hybrid fiber-reinforced concrete at low fiber volume fraction. *Cement and Concrete Research*, 33(1):27 – 30.

Zhang, Q. (2016). Mathematical modeling and numerical study of carbonation in porous concrete materials. *Applied Mathematics and Computation*, 281:16 – 27.